Mise en évidence de textures de spin synthétiques par des mesures de transport et de champ microonde

Lauriane Contamin

PSL
UNIVERSITÉ PARIS

THÈSE DE DOCTORAT
DE L'UNIVERSITÉ PSL

Préparée à l'École Normale Supérieure

Mise en évidence de textures de spin synthétiques par des mesures de transport et de champ microonde

Soutenue par

Lauriane Contamin

Le 02 octobre 2019

Ecole doctorale n° 564

Physique en Île-de-France

Spécialité

Physique

Composition du jury :

Jelena, KLINOVAJA Associate Professor, University of Basel	*Rapporteur*
Attila, GERESDI Associate Professor, TU Delft	*Rapporteur*
Dimitri, RODITCHEV Professeur, ESPCI Paris Tech	*Président*
Felix, VON OPPEN Professor, Freie Universität Berlin	*Examinateur*
Matthieu, DELBECQ Maître de Conférence, Sorbonne Universités	*Membre invité*
Takis, KONTOS Directeur de Recherche, Ecole Normale Supérieure	*Directeur de thèse*
Audrey, COTTET Directeur de Recherche, Ecole Normale Supérieure	*Co-directeur de thèse*

ENS | PSL

"Whether or not the Majorana will ever fulfill this promise [quantum information] is a minor detail; its main role is that of a legend, to give hope and move things forward"

Tudor D. Stanescu, Introduction to Topological Quantum Matter and Quantum Computation

"De tout temps, les hommes ont exploité les propriétés des matériaux que la nature mettait à leur disposition"

Henri Alloul, Physique des électrons dans les solides

Abstract

In this thesis, we have studied carbon nanotube-based nanocircuits integrated in a microwave cavity architecture. Our device is compatible with the simultaneous measurement of both the current through the nanocircuit and the frequency shift of the cavity. These two signals give complementary information about the device. In the two experiments presented in this thesis, the carbon nanotube was positioned above a magnetic material containing several magnetization domains. The resulting magnetic stray field's axis oscillates along the carbon nanotube length. For the confined electrons, this is equivalent to both a synthetic spin-orbit interaction and a Zeeman effect.

This synthetic effect is evidenced in two ways. In a first experiment, we have measured the evolution of the nanotube's energy levels when the magnetic material is progressively magnetized by an external magnetic field, thus destroying the oscillations of the stray field. In this experiment, the carbon nanotube had a very transparent contact to a superconducting metal, in addition to the synthetic spin-orbit interaction and Zeeman effect. These ingredients are a pre-requisite to observe Majorana quasiparticles in a one-dimensional nanoconductor. Those quasiparticles are under intense study for their potential use in quantum computing.

In the second experiment, we have realized a double quantum dot in which each dot similarly lays above an oscillating magnetic field. The internal transitions of this DQD are measured with the microwave cavity signal. We evidenced a strong dispersion of the energy of the double quantum dots' internal transitions with a small external magnetic field. This dispersion can be explained by a Zeeman effect in which the Landé factor, g, has been strongly renormalized by the synthetic spin-orbit interaction.

Key words

Quantum electrodynamics, Topological states of matter, Carbon nanotubes, Microwave cavity, Spin-orbit coupling.

Résumé

Dans cette thèse, nous avons étudié des nanocircuits à base de nanotubes de carbone intégrées dans une cavité micro-onde. Notre dispositif permet de réaliser simultanément des mesures de transport et des mesures micro-ondes, qui donnent des informations complémentaires sur le nanocircuit. Dans les deux expériences réalisées durant cette thèse, un nanotube de carbone est placé au dessus d'un matériau magnétique qui présente plusieurs domaines d'aimantation. L'axe du champ magnétique de fuite résultant oscille le long du nanotube. Pour les électrons confinés, il est équivalent à un couplage spin-orbite synthétique et à un effet Zeeman.

Cet effet synthétique est mis en évidence de deux manières. Dans une première expérience, nous avons mesuré l'évolution des niveaux d'énergie de la boîte quantique quand le matériau magnétique est progressivement aimanté par un champ extérieur, ce qui détruit le champ oscillant. Dans cette expérience, le nanotube a un très bon contact avec un métal supraconducteur en supplément des effets spin-orbite et Zeeman synthétique, qui sont les pré-requis pour obtenir des quasiparticules de Majorana dans un nanoconducteur 1D. De telles quasiparticules sont activement recherchées pour leur utilisation pour le calcul quantique.

Dans un second temps, nous avons réalisé une double boîte quantique, dans laquelle chaque boîte est constituée d'un segment de nanotube, situé au dessus du même champ magnétique oscillant que dans la première expérience. Les transitions internes de ce système sont mesurées à l'aide de la cavité micro-onde. Nous avons mis en évidence une très forte dispersion de l'énergie de la transition interne avec un faible champ magnétique extérieur, qui peut être expliqué par un effet Zeeman pour lequel le facteur de Landé, g, a été fortement renormalisé par l'interaction spin-orbite synthétique.

Mots clés

Electrodynamique quantique, Etats topologiques, Nanotubes de carbone, Cavité microondes, Couplage spin-orbite.

Acknowledgements

I would like to start by thanking the member of my commitee for their comment on my work, and the discussion we had during the defence. It is always a great moment to present scientific results to a broader audience that the HQC group, especially when they took some time to obtain. Before switching to french I would also like to thank Magdalena Marganska for her several trips to Paris. We have started discussing how the explicit structure of the carbon nanotube can affect the emergence of Majorana quasiparticles, or of the synthetic spin-orbit effect, and it is extremely motivating to see you tackle this issue with all your computing strength, knowledge and energy. I hope that this exploration brings new insights and new questions about the following of my project.

Je passe maintenant au français, et je voudrais commencer par remercier tous les membres du groupe HQC. En tout premier lieu, Takis et Audrey, pour leur encadrement complémentaire. Takis, toujours enthousiaste et rarement à court d'idée, qui avance les calculs théoriques pendant ses vacances en Crète. Mais aussi présent tous les jours au laboratoire, à débugguer les tables RF, à faire la maintenance de l'évaporateur... J'ai beaucoup apprécié l'équilibre de ma thèse, où j'ai eu l'impression d'avoir beaucoup d'autonomie mais aussi un soutien régulier, qui était bien nécéssaire pour me familiariser avec tous les éléments expérimentaux et théoriques qu'on finit par manipuler ! Audrey, un étage au dessus du laboratoire, tu as toujours été disponible pour des questions théoriques ou une discussion sur les résultats. Tu es toujours très précise et rigoureuse. J'ai été un peu frustrée de ne pas avoir pu prendre plus de temps pour aller plus loin dans certaines réflexions que nous avons eu au cours de ces trois ans, mais il aurait fallu plus de temps ! En début de thèse, j'ai eu la chance d'être formée par Matthieu Desjardins (dit MattMatt), avec qui nous avons trouvé un bon équilibre en salle blanche et dans les mesures. Merci pour cette formation, et pour ton implication dans la rédaction de notre article fleuve. Je te souhaite beaucoup de courage et de réussite pour le projet de startup. Au delà de cette formation, j'ai bien sûr pu échanger des recette de salle blanche et marchanger des multimètres keithley avec tous les autres membres du groupe HQC, en particulier Matthieu Dartiailh (dit Madar) qui écorche toujours mon prénom après 4 ans, Tino Cubaynes qui s'est lancé depuis dans la fabrication d'un appareil combiné four de croissance-agrapheur-MEB (j'imagine qu'il rajoutera à tout cela un cryostat pour plus de simplicité), Federico Valmorra toujours partant pour un verre, Laure Bruhat qui j'espère trouvera comment poursuivre ses convictions, Sébastien Balibar qui oscille entre la physique, l'histoire des sciences et l'écologie. Je leur souhaite à tous une belle carrière, scientifique ou non. Durant ma thèse, le groupe a intégré Matthieu Delbecq, qui s'est directement investi dans le projet Majorana avec un enthousiasme à la hauteur de celui

de Takis, et surtout beaucoup d'énergie. Cela a été très agréable de recommencer à travailler à deux au moment de la transition vers le stapling, qui n'a pas été sans heurt. Je suis aussi heureuse qu'il nous fasse bénéficier de son expérience et de ses talents en code, qui ont rapidement été exploités ! J'espère que tu lanceras tous les projets topologiques que tu as préparés sur papier dans les années à venir. Nous ont aussi rejoint Zaki Leghtas, Raphaël Lescanne et Clarke Smith qui travaillaient dans un cagibi au fond du couloir avant de déménager dans le Yellow Submarine. Je suis sûre que le rapprochement sera bénéfique pour les différents projets de recherche, Zaki n'étant clairement pas à court d'enthousiasme (même quand il s'agit de faire une mesure 4 points). Merci pour les discussions scientifiques, et tout ce que vous nous avez apporté sur les simulations RF. Je quitte maintenant un groupe bien différent, et je souhaite beaucoup de réussite à Marius Villiers et William Legrand qui continuent encore et toujours à lutter avec les nanotubes de carbone.

Durant ma thèse, je me suis retrouvée à travailler avec des textures magnétiques auxquelles je ne comprenaient pas grand chose. Je suis très reconnaissante à Stanislas Rohart et André Thiaville pour le temps qu'ils ont consacré à essayer de nous expliquer ce qu'étaient (et n'étaient pas...) des parois de domaines, et (plus sérieusement) pour leur aide précieuse, à la fois pour fabriquer les textures magnétiques mais aussi pour les caractériser, les simuler, et essayer de les comprendre. Je leur souhaite de continuer cette collaboration de manière fructueuse. Merci aussi à Karim Bouzehouane, Brigitte Léridon et William Legrand pour leur aide dans la caractérisation des textures. J'ai aussi passé un temps non négligeable en salle blanche, et je voudrais remercier Michael, José et Aurélie qui permettent son bon fonctionnement, ainsi que pour leur aide en cas de pépin. Michael, au delà des problèmes techniques, tu es toujours disponible pour me remonter le moral quand la fab ne marche pas (même après 19h) et je t'en remercie. Adoptant une timeline un peu étendue, j'en profite pour remercier Jean-Damien Pillet et Rebeca Ribeiro-Palau pour mon stage à Columbia et pour leur expérience de scientifique. Je tiens aussi à remercier plus largement les membres du département de physique avec qui j'ai eu l'occasion de discuter, de sujets plus ou moins liés à la physique; l'équipe P13, avec en particulier Bernard, Gwendal, Erwann, Holger et David, l'équipe THz avec en particulier Zukhdeep, Juliette, Sylvain et Elisa, l'équipe d'optique, avec Emmanuel, Théo et les anciens de l'équipe Qélec, Danijela, Benjamin, Nathanaël. Zukhdeep et Erwann se sont chargés de mon comité de thèse, et même si ça n'a pas eu lieu d'être, je n'ai aucun doute qu'ils auraient été de parfaits gestionnaires de conflit. J'ai aussi essayé de mon mieux de m'impliquer dans la vie du laboratoire, avec un temps et un succès limité. Cependant je voudrais remercier Camille Aaron et Jean-Marc Berroir qui essayent de faire progresser le pourcentage de femme chercheuse à l'ENS, et Jean-François Allemand qui, assez incroyablement, arrive à gérer l'ED, sa recherche, le CPES

et tous ses anciens élèves croisés au détour d'un couloir.

A l'ENS nous avons la chance d'être très entourés, et je voudrais remercier tous ceux qui aident l'activité de recherche au jour le jour. Tout d'abord, l'équipe administrative, et particulièrement Anne Matignon et Olga Hodges, ainsi que Charlotte Normand et Laura Baron-Ledez. Ensuite, l'équipe cryogénie, avec Olivier et Florent, toujours prêt à faire une démonstration de condensation d'air. Le service informatique, et particulièrement Yann. Les électroniciens, Anne et Philippe. Merci Philippe pour ton aide précieuse quand j'essayai de finir un porte échantillon sous vide très, très contraint. Bien évidemment, l'atelier mécanique et le bureau d'étude: Jean-Michel avant qu'il prenne ses nouvelles fonctions, Jules, Mathieu, Arnaud, Nabil, Georges, José, Pascal, à qui j'ajoute Cyril du magasin matière. Je m'adressais souvent en premier à Jules: merci pour ton aide et ta gentillesse. Enfin l'équipe "travaux" à défaut de connaître un meilleur nom. Didier, Catherine, Célia et Théo: un grand merci pour le magnifique laboratoire que vous nous avez préparé, et votre aide pendant le déménagement. Encore maintenant, vous êtes toujours à l'écoute pour nous dépanner en vitesse au moindre pépin. J'ai abusé de votre gentillesse en demandant parfois un conseil ou un coup de main pour un projet personnel, merci beaucoup.

Au delà du laboratoire, ces quatre années ont été riches en soutien. Merci à mes parents, toujours fiers et souvent intéressés, qui ont suivi de près le feuilleton de la publication de l'article. Merci papa de ton goût pour les sciences, en particulier la biologie (que je partage) et la cosmologie (que je partage moins). Merci maman pour ta fierté, ton attention, et vos fréquentes visites. Merci aussi à mes deux frères et belle-soeurs, toujours là pour me changer les idées soit avec deux petites filles débordantes d'énergies pour Raphaël et Laura, soit avec un chantier jamais achevé pour Antoine et Karen. Merci aussi à la famille de Timothée, c'est toujours un plaisir de passer un moment avec vous pour se changer les idées. Du côté des amis aussi, j'ai été bien accompagnée. A un étage d'écart au plus du laboratoire, les membres du DJFP étaient présentes au moins un déjeuner par semaine (principalement pour évaluer nos directeurs de thèse); merci Sophie, Marylou et Danijela d'avoir partagé avec moi ces années de thèse. Nous accueillions aussi bien volontiers nos collègues biologistes, Judith et France. J'espère faire du yoga (ou juste manger) encore de nombreuses fois en votre compagnie. Dans le cercle parisien, merci à tous les Ronds: Marianne, Vivien, Clémence, Antoine, Jean, Marie, Bertrand, Nicolas, Maxime, Morgane et au projet fou de canoë qui a occupé une partie de mes week-ends, ainsi que des projets manuels divers et de nombreux diners gourmets. Merci Marianne et Vivien pour toutes les vacances partagées. Merci à Adrien et Anne-Emeline pour de nombreux concerts expérimentaux. Merci à Dr. Sophie qui entretient ma garde robe à chaque week-end entre filles avec Amandine (et en option Victor :)) et avec qui je partage de nombreux souvenirs qui me font pouffer bêtement

quand j'y repense. Merci enfin à Timothée, pour la belle fête que nous avons organisé l'été dernier, pour toutes tes questions sur ma thèse et tout ton soutien. Merci d'avoir désynchronisé tes moments de doute et d'exaltation des miens. J'ai hâte de voir ce qui nous attend pour la suite.

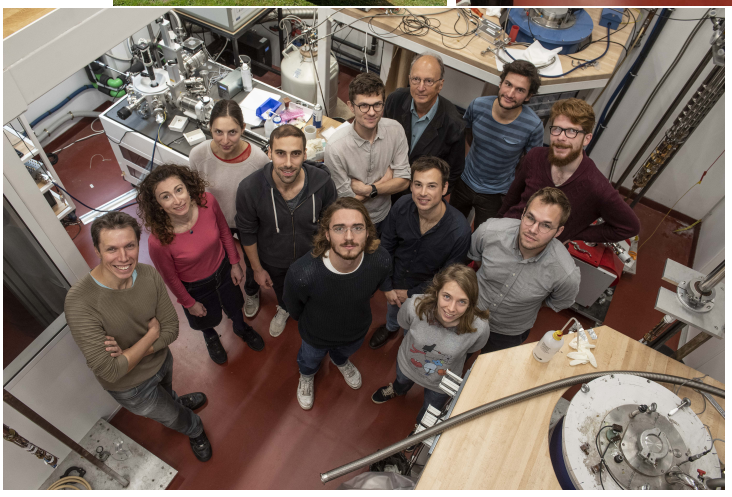

Contents

Acronyms

AC	Alternative current
ADC	Analog-to-digital converter
AFM	Atomic force microscope
AHE	Anomalous Hall effect
AMR	Anisotropic magnetoresistance
AR	Andreev reflection
AWG	Arbitrary waveform generator
B/AB	Bonding/Anti-bonding
CNT	Carbon nanotube
CPR	Current-phase relation
CPW	Coplanar waveguide
cQED	circuit quantum electrodynamics
CVD	Chemical vapor deposition
DC	Direct current
DOS	Density of states
DQD	Double quantum dot
FWHM	Full width at half-maximum
IF	Intermediate frequency
IPA	Isopropanol
JJ	Josephson Junction
LO	Local oscillator
MAR	Multiple Andreev reflection
MBS	Majorana bound state
MFM	Magnetic force microscope
MIBK	Methyl-iso-butyl ketone
MZM	Majorana zero mode
NDC	Negative differential conductance
PCB	Printed circuit board
PMA	Perpendicular magnetic anisotropy
PMMA	Poly methyl methacrylate
QD	Quantum dot
QED	Quantum electrodynamics
RF	Radio frequency
RIE	Reactive ion etching
RMS	Root mean square
sccm	Standard Cubic Centimeter per Minute
SEM	Scanning electron microscope
SMA	SubMiniature version A (microwave connector norm)
SNR	Signal to noise ratio
SOI	Spin orbit interaction
SQD	Single quantum dot
SQUID	Superconducting quantum interference device
SSB	Single side band

STM	Scanning tunneling microscope
SWNT	Single wall carbon nanotube
TEM	Transverse electromagnetic
TRS	Time reversal symmetry
UHV	Ultra high vacuum
VNA	Vectorial network analyser
YSR	Yu-Shiba-Rusinov
ZBP	Zero bias peak
2DEG	Two-dimensional electron gas

Notations

α_{so}	Spin-orbit coupling strength (for a parabolic dispersion relation)
B_{osc}	Magnetic field that is non-uniform in space (stray field of a magnetic texture)
B_{ext}	External magnetic field
δ_{ij}	Kronecker delta
Δ	Superconducting pairing
δ	Quantum dot level spacing
δ_{so}	Spin-orbit energy (for the relation dispersion of a CNT)
e	Electron charge
E_c	Quantum dot charging energy
ϵ_d	Detuning energy between two dots of a DQD
$\epsilon_{L,R}$	Chemical potential of the left/right dot of a DQD
E_{so}	Spin-orbit energy (for a parabolic dispersion relation)
E_z	Zeeman energy
$\eta_{x,y,z}$	Pauli matrice x, y or z acting on the K-K' space for a CNT Hamiltonian
f_{cav}	Resonant frequency of the CPW
f_d	Drive frequency of the CPW
$\Gamma_{S,D}$	Tunneling rate to the source/drain electrode
$\Gamma_{1,\phi}$	Decoherence rate through charge relaxation (1) or dephasing (ϕ)
h	Planck constant
$h.c.$	hermitian conjugate
k_B	Boltzmann constant
κ	Cavity decay rate (or bandwidth)
m	electron mass
μ	chemical potential
μ_B	Bohr magneton
ψ	Electron wavefunction
$s_{x,y,z}$	Pauli matrice x, y or z acting on the spin space
$\sigma_{x,y,z}$	Pauli matrice x, y or z acting on the sublattice space for a CNT Hamiltonian in spinor representation
t	Interdot coupling in a DQD
$\tau_{x,y,z}$	Pauli matrice x, y or z acting on the electron-hole space
v_F	Fermi velocity
V_{rms}	Root-mean square value of the cavity vacuum voltage fluctuations
ω_{DQD}	Pulsation of a DQD internal transition

Introduction

Since the beginning of the XXth century, many technological advances have enlarged the scope of solid state physics, that reversely fostered many new applications. This thesis project grouped elements of four domains of quantum physics: nanotechnologies, superconductivity, quantum light and magnetism.

The discovery of the discrete spectral lines of atoms and molecules (in the XIXth century) was a stepping stone for the development of the quantum physics framework. One particularly illuminating example is the prediction and experimental realization of a laser in the 1960s'. A myriad of applications followed: LEDs, lasers for medical treatments, industrial processes (laser cutting), information processing with CDs... The emission of light at a controlled frequency (combined with the development of high-quality cavities to confine light) also became a fundamental tool to probe solid states with a high energy resolution, and to enquire about the interaction between light and matter.

Starting with the semiconductor-based transistor in the 1940s', technical advances in the domain of electronics enabled the emergence of experimental quantum nanoelectronics. Among these advances, we can give as examples the developement of lithography [1] and metallic thin film deposition techniques to fabricate smaller and smaller circuits, the development of imaging techniques down to the resolution of an atom[1], and the development of molecular beam epitaxy in the 60s' for obtaining pure semi-conducting materials. It is now possible to realize "artificial atoms" in electronic circuits. Indeed, the atoms discrete spectral lines arise from the spatial confinement of the electrons in the electrostatic potential of the nucleus. *Artificial* atoms can be realized by engineering a controlled spatial confinement of a conductor's electrons using electrostatic potentials. The basic rules of quantum mechanics can be studied in details in these tunable quantum systems.

On another front, the development of thermodynamics in the 1850s' enabled the successful cool-down of hydrogen and then helium, until they reached their liquid state[2] in the

[1] The first commercial SEM was developed in the 60s', the AFM was invented in the 80s'.
[2] at 4K, ie $-269°$C for helium.

early 1900s'. This led to the discovery of superconductivity: at low enough temperature, an electrical current flows without resistance in certain metals. This phenomenon has been the object of intense theoretical work, resulting in the BCS theory of superconductivity. The BCS theory established the link between a small attractive interaction between electrons (that can be mediated by the solid's crystalline structure) and the emergence of a macroscopic electronic state where electrons are paired up, and carry current without resistance[3]. The idea of a macroscopic state, where all the electron pairs share a common phase (similarly to photons in a laser) is surprising when considering the number of particles involved, and the fact that this is a quantum phenomenon. Superconductivity has been disconnected from applications for a long time, yet nowadays liquid helium and superconductivity have found several technical applications, such as MRI and metrology. Superconductivity enables the generation of very high magnetic fields (by setting an electrical current in a superconducting material), enriching again fundamental and applied experiments. The perspective of superconductivity at a higher temperature is also a wide field of research, and could make superconducting (dissipationless) circuits economically sustainable.

Our last example will be magnetism which has quite a different history than superconductivity. Indeed, crucial applications of magnetic materials had already been identified before a microscopic understanding of magnetism's rules was achieved, as for example the electromagnet[4]. Quantum theory, and more specifically the notion of spin, was necessary to understand the emergence of ferromagnetic materials that have a permanent magnetization. A ferromagnet can be modeled as a lattice of spins, interacting with one another; each spin carries a certain magnetization, and if they align the material becomes a magnet. Since the 1960s', important work has been done to understand more precisely how to miniaturize a magnetic texture, i.e. a local change in the magnetization of a material. The control over magnetic materials is paramount to the industry of information storage.

Ideal ballistic conductors

As we mentioned before, artificial atoms can be made by spatially confining an electric conductor's electrons. Such a study falls in the domain of mesoscale physics, which studies the intermediate scale, between the atomic and the macroscopic world. In order to observe the effects of confinement, it is necessary to reach a regime where the wave-like nature of conduction electrons becomes relevant: it is necessary to cool down the electrons (to typically $T < 1\,\mathrm{K}$), and to confine them over length scales of the order of

[3] These excitations following a bosonic statistics they do not collide with one another.

[4] An electromagnet consist in a ferromagnetic core that can be magnetized by a small electric current applied in surrounding wires. The magnet can the be used to move other ferromagnetic pieces.

1 µm. It is also necessary to use an electric conductor with a crystalline structure of high quality. If not, the defects act as diffusers that randomize the electrons' trajectories. A very good conductor candidate is the single wall carbon nanotube (CNT), which consists in a tube made out of a rolled-up sheet of graphene. A CNT already provides the electronic confinement in two dimensions.

CNTs can easily be grown using a chemical process with little to no defects. Several recent experimental works have demonstrated precise positioning of a selected CNT over an electrical circuit, to study the artificial atom formed between the source and drain electrodes used to flow a current. One can also increase the complexity of the system and build two artificial atoms in the same CNT, thus forming an artificial molecule. An advantage of a synthetic system is that the typical energy scales can be controlled and changed, as opposed to nature-defined systems. For example, two different regimes concerning the coupling of the artificial atom to the source and drain electrodes can be studied. On the one hand it is interesting to study strongly confined electrons: the resulting system is very isolated and can keep its coherence for a long time. On the other hand, when increasing the coupling between the confined electrons and an electronic reservoir, the reservoir can imprint certain of its properties on the confined electrons. For example, a superconducting reservoir can induce a superconducting pairing in the artificial atom.

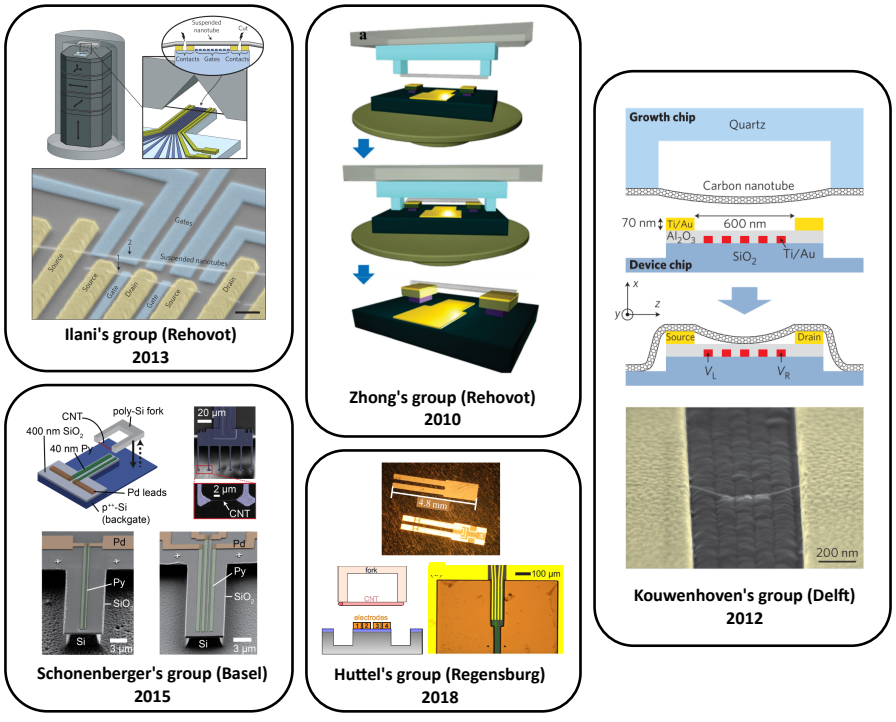

FIGURE 1: Review of several CNT transfer techniques. CNT are grown of a specific substrate, and can then be characterized, using for example Rayleigh spectroscopy. A circuit chip is first prepared, and the CNT is then transferred onto it. Such a transfer technique was also developed in our group and was used during this thesis. Source: [2]

Superconductivity

Superconductivity is a state of matter where electrons in a conductor pair-up at low enough temperature. All the electrons around the Fermi energy E_F pair-up and form a condensate at E_F, which opens a gap in the single-particle excitation spectrum of the superconductor, of width Δ in energy. When there is an interface between a superconductor and a normal conductor, an incoming electron at an energy $E < \Delta$ cannot be transmitted in the superconductor due to the energy gap. If the interface is clean enough, the electron cannot be reflected neither, due to momentum conservation. However, there can be another type of reflection, called Andreev reflection, where the electron is transmitted to the electron-pair condensate, and a hole is reflected. Through this process, the coherence of the superconductor's electron pairs can persist a certain time in the normal conductor.

The standard singlet superconducting pairing involves two electrons with opposite spin. As a consequence, superconductivity can be destroyed by high enough a magnetic field, which changes differently the energy of electrons with opposite spins. In a similar way, if a superconductor is contacted to a ferromagnetic material, the proximity-induced pairing in the ferromagnet is different than in the superconductor. In this thesis, we have studied yet another spin-effect on superconductivity, namely how a spin texture affects the superconductivity induced in a carbon nanotube.

Light-matter interaction

The principle of spectroscopy is to study the properties of matter through its effect on light. In this thesis we have used photons at the microwave frequency (typically $f_c = 6$ GHz) to study our artificial atom-like systems. The photonic signal gives information about the electronic processes at frequencies close to f_c, with a much finer resolution that what is achievable with transport measurement, giving us access to a different energy range. We can distinguish two regimes for the light-matter interaction, depending of whether or not there can be a coherent exchange of energy between light and matter. In order to reach the coherent regime, photons are trapped in cavities to increase their lifetime.

Besides, the photons can probe properties of the system that are not directly visible in transport measurements. For example, in a double quantum dot[5] geometry, they give access to the energies of the inter-dot transitions. It can also give information about the nature of the electronic excitation, for example whether it is spin polarized or not,

[5] An artificial atom is also called a quantum dot; a double quantum dot is the equivalent of an "artificial molecule".

through specific selection rules. During this thesis, we have studied the influence of a spin texture on the wavefunction of an artificial atom using the cavity photons as a high-resolution probe of small energy changes.

This thesis is organised as follows. Chapter one describes how superconductivity and spin-orbit interaction interact to change the nature of the superconducting pairing, and how an additional magnetic field can then favor the emergence of exotic quasiparticles, called Majorana quasiparticles. It also gives an overview of the experimental efforts provided so far to try and generate these quasiparticles. For now the detection methods have focused on the presence of an electronic state at zero energy, without exploiting the more exciting properties of these quasiparticles, such as their self-adjointness.

Chapter two describes a new path to obtain these exotic quasiparticles, which gives more flexibility in the platforms in which they can emerge. Indeed, it shows how a spin-orbit interaction can be autonomously generated in any nanoconductor by using a proximal magnetic field that oscillates along the nanoconductor. We study the emergence of Majorana quasiparticles with this scheme, focusing on the importance of how the superconductivity is additionally induced.

Chapter three gives technical details about key aspects of the project: the design of the microwave cavity, the fabrication techniques for the CNT circuit embedded in the cavity, and the study of the magnetic materials used to create the spin texture.

The next two chapters present original results obtained during this thesis. The interest of these results is summarized below.

Synthetic spin-orbit interaction for Majorana devices

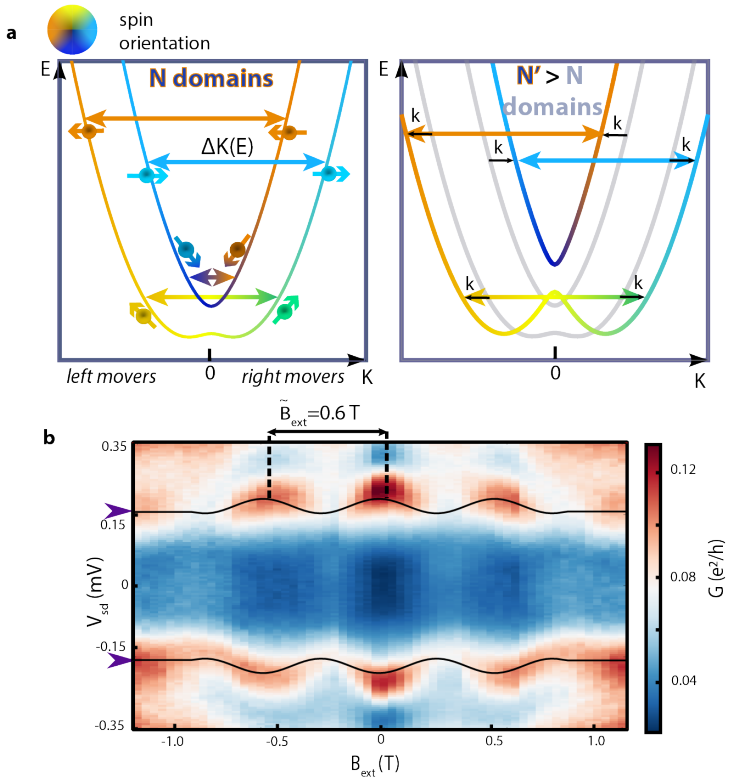

FIGURE 2: (a) Schematic representation of the evolution of a CNT energy bands when subject to a magnetic field rotating in space with N and N' domains, with the allowed interference conditions. The spin orientation is represented by the curves' colors. (b) Conductance map as a function of $V_{sd} - B_{\text{ext}}$ for a CNT placed over a magnetic texture and contacted with superconducting contacts, one of which acts as a probe. Subgap states are measured, which oscillate as a function of a magnetic field. These oscillations occur with a relatively small period of $\tilde{B}_{\text{ext}} = 600$ mT and are due to the change in the confinement-induced interference condition when the magnetic domains are slowly aligned by the external magnetic field.

Chapter four presents the experimental results relative to the interaction of superconductivity with our spin-textured conductor, measured through the current flowing through the device. Below the superconducting gap, the current is carried by electronic levels dressed by the superconducting proximity effect, called Andreev Bound States (ABS). The effect of the spin-texture is visible through the variation of the ABS' energy when an external magnetic field is applied, until the texture disappears for $B_{ext} \gtrsim 0.8$ T. The number of energy oscillations enables us to give an estimate of the spin-orbit energy in our system of about $E_{so} = 1.1$ meV, much larger than in most semiconducting platforms. This high spin-orbit energy opens the way to the observation of exotic excitations, called Majorana quasiparticles.

Sensing spin textures with cavity photons

Chapter five presents another observation of the effect of the spin-texture on the electrons in the absence of superconductivity, this time measured through the cavity in a double quantum dot (DQD) geometry. It shows that the cavity can be a very sensitive detector of small variations of the electronic spectrum in a quasi-isolated conductor. The microwave response is strongly modified when the cavity and DQD are resonant, at $\hbar\omega_{cav} = \hbar\omega_{DQD}$. We have measured strong dispersion of this resonance with an external magnetic field (over a range where the domains are not affected), which points toward large, orbital-dependent Landé factors in the CNT. These large Landé factors could be explained by the synthetic spin-orbit interaction in both dots.

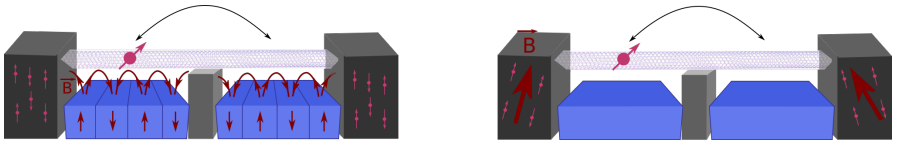

FIGURE 3: Schematic representation of a DQD based magnetically textured qubit (a) and a spin-qubit (b) as studied for the first time in Ref [3]. In device (b), each dot can be described as being spin-polarized by the field of the closest electrode. On the contrary, in device (a), each dot is subject to non-collinear fields.

Chapter 1

Hybrid topological quantum devices

The perspectives of topological superconductivity, and specifically the promises of Majorana fermions for topological quantum information have recently led to multiple experimental works, in a diverse range of systems.

The term Majorana fermions originally comes from the field of high-energy physics, and describes a particle that would be its own antiparticle [4]. It was much later that an analogy was drawn to solid-states physics, where Majorana modes are predicted to appear around vortices in topological superconductors [5], or at the boundaries of a finite 1D system in the famous toy-model by Kitaev [6].

While these proposals are based on materials with exotic properties, it was subsequently realized that they could be engineered by combining more mundane physical ingredients [7–12], either a topological insulator or even a semiconductor in which the spin-rotation symmetry is broken [11, 12], proximitized by "trivial" (s-wave) superconductivity. Since then, numerous physical realizations of mesoscopic systems combining these ingredients have been reported, either with semiconducting nanowires [13–17], 2DEG [18, 19], atomic chains [20, 21] or islands [22]. These experimental realizations drew a lot of attention since it was proposed that Majorana fermions could be paramount for new quantum information schemes [23–25].

In this chapter we will briefly describe the origin of the search for Majorana fermions in solid-state physics (section 1.1), before discussing in more details the method that is followed in this thesis for trying to mimic topological superconductivity (section 1.2) and the experimental signatures obtained so far (section 1.3).

1.1 The quest for Majorana excitations

1.1.1 High-energy physics origin

Majorana fermions were first imagined by Ettore Majorana as hypothetical particles that would be real solutions of the Dirac equation [4]. Although the discussion was held in the field of high energy physics, trying to envision what fundamental particles could exist, an analogy was later drawn between the equations of Majorana fermions and the equations ruling a superconductor [6, 26–29]. To understand this analogy, we summarize here a few key points of the theory behind the Majorana fermions. They are described in more details in the reviews [30, 31].

The Dirac equation describes a fermion field, and reads ($\hbar = c = 1$)

$$(\gamma^\mu p_\mu - m)\Psi = 0$$

with the following notations:

- $\Psi(x)$ is the four-component vector describing the wavefunction of a spin-1/2 particle and its antiparticle (we will drop the x coordinate in the following).
- $p_\mu = (i\partial_t, -\vec{p})$
- $\gamma^0 = \begin{pmatrix} 0 & \hat{s}_0 \\ \hat{s}_0 & 0 \end{pmatrix}$ and $\gamma^\mu = \begin{pmatrix} 0 & \hat{s}_\mu \\ -\hat{s}_\mu & 0 \end{pmatrix}$ for $\mu \in [x, y, z]$
- $(\hat{s}_x, \hat{s}_y, \hat{s}_z)$ are the Pauli matrices and $\hat{s}_0$ is the identity matrix (of dimension 2).

In fact, the definition of γ^μ is not unique and the one given above is called the Weyl representation, found by Dirac. The only constraint is that one should recover the Klein-Gordon equation (the wave equation describing a relativistic particle) when squaring the Dirac equation. E. Majorana proposed an alternative definition of these gamma matrices in which they are purely imaginary (Majorana representation), and the resulting Dirac equation in this representation is real, leading to a real solution Ψ. The reality of Ψ implies that it describes a particle that is equal to its antiparticle. We can already note that a particle that is its own antiparticle is necessarily charge neutral, and thus does not couple to the electromagnetic field (see for example equation (1.1)); we will come back to this point later on.

To go from reality to self-adjointness, one has to calculate the charge conjugation matrix (defined such that its effect on a charged particle is to reverse the sign of the charge). To do so, one can compare the Dirac equations for both a charged particle Ψ and its antiparticle (with opposite charge) Ψ^c in an electromagnetic pseudo-potential A_μ. The Dirac equation becomes $(i\partial_\mu \to i\partial_\mu + eA_\mu)$ [31]:

$$[\gamma^\mu (i\partial_\mu + eA_\mu) - m]\,\Psi = 0 \tag{1.1}$$

$$[\gamma^\mu (i\partial_\mu - eA_\mu) - m]\,\Psi^c = 0 \tag{1.2}$$

We can check that Ψ^c can be written :

$$\Psi^c = C\Psi^* \tag{1.3}$$

where the charged conjugation matrix is $C = i\gamma^y$ in the Weyl representation[1], and $C = \mathbb{1}$ in the Majorana representation. In the Majorana representation, we then conclude that Ψ and Ψ^* describe a particle-antiparticle pair.

[1] It satisfies $-C\gamma^0\gamma^{\mu *} = \gamma^\mu C\gamma^0$ which enables to connect equation (1.1)* and equation (1.2).

To study into more details the interest of the Majorana representation, one can rewrite $\Psi = (\psi_R, \psi_L)^T$, where $\psi_{R,L}$ are two-component spinors that are the right-handed and left-handed projections of Ψ. E. Majorana noticed that for a real solution, the particle is indistinguishable from its antiparticle ($\Psi^c = \Psi$) and the equations on ψ_L and ψ_R decouple:

$$\begin{aligned}(i\partial_t - \vec{p}\cdot\vec{s})\psi_R - im_R\hat{s}_y\psi_R^* = 0\\ (i\partial_t + \vec{p}\cdot\vec{s})\psi_L - im_L\hat{s}_y\psi_L^* = 0\end{aligned} \tag{1.4}$$

From a given set of solutions ψ_L, ψ_R of the Dirac equation, one can form two new four-component spinors that represent two pairs of Majorana :

$$\begin{aligned}\Psi_L = (-i\hat{s}_y\psi_L^*,\, \psi_L)^T\\ \Psi_R = (\psi_R,\, i\hat{s}_y\psi_R^*)^T\end{aligned} \tag{1.5}$$

This condensed summary of the relation between Dirac and Majorana fermions enables us to understand the consequence of the reality constraint: a Majorana fermion is neutral and self-adjoint. If we additionally look for a stationary solution of the equations, it needs to have a zero energy (the particle and antiparticle having opposed energies). Finally, we can note that a pair of Majorana fermions of equal masses such that $\psi_L = i\hat{s}_y\psi_R^*$ forms a Dirac fermion (from equations (1.4) and (1.5)). These properties will help us understand the analogy between Majorana fermions and superconductors physics.

1.1.2 Link to condensed matter physics

In condensed matter, we do not deal with fundamental particles but with electrons in a solid, and more specifically with quasiparticles that are electron-like excitations, effectively acting as independent electrons (quasielectrons) or holes. These excitations take various forms with properties (mass, charge, spin, velocity, statistics...) that can be very different from the ones of a bare electron.

To find a system in which a quasiparticle could mimic a Majorana fermion, we can look at the properties derived in the previous section. Notably, we noted that two well-chosen Majorana fermions are indistinguishable from a Dirac fermion (an electron for example, see equations (1.4) and (1.5)). We can rewrite this relation in term of the creation ($\hat{c}_i^+$) and annihilation ($\hat{c}_i$) operators of a electron in the following way:

$$\hat{\gamma}_{i,1} = \hat{c}_i + \hat{c}_i^+,\ \hat{\gamma}_{i,2} = i(\hat{c}_i^+ - \hat{c}_i) \tag{1.6}$$

where the $\hat{\gamma}_{i,n}$ are self-adjoint operators, or reversely:

$$\hat{c}_i = \frac{1}{2}(\hat{\gamma}_{i,1} + i\hat{\gamma}_{i,2}),\ \hat{c}_i^+ = \frac{1}{2}(\hat{\gamma}_{i,1} - i\hat{\gamma}_{i,2}) \tag{1.7}$$

The canonical anti-commutation relations for the fermionic operators lead to:

$$\{\hat{\gamma}_{i,\alpha}, \hat{\gamma}_{j,\beta}\} = 2\delta_{ij}\delta_{\alpha\beta} \text{ and } \hat{\gamma}_{i,\alpha}^+ = \hat{\gamma}_{i,\alpha} \text{ for } \alpha, \beta \in [1,2] \tag{1.8}$$

The $\hat{\gamma}_{i,\alpha}$ operators represent Majorana fermions. For such operators to describe "natural" excitations of the electrons, we need a system were electrons and holes are superposed. Such a superposition can indeed have a zero charge, as expected for a Majorana fermion. Thus, *superconductors*, that naturally pair electrons, are good candidates. Indeed, the charge is not well defined in the mean field description of a superconductor: only its parity is a good quantum number. Particles coming in or out of the superconducting condensate allowing for variations of the global charge by a multiple of 2e, which bodes well for allowing for Majorana pair annihilation, and for the possibility to superpose an electron and a hole.

If we look more closely at the equations describing a superconductor, we can re-express the hamiltonian of the superconductor in term of Majorana operators [29]. The Hamiltonian of a s-type superconductor, under a mean-field approximation, can be written as:

$$H_{BCS} = \int dx[\sum_{s,\,s'} H_0^{s,s'}(x)\hat{c}_s^+(x)\hat{c}_{s'}(x) + (\Delta(x)\hat{c}_\uparrow^\dagger(x)\hat{c}_\downarrow^\dagger(x) + h.c.)] = \sum_n E_n\hat{\gamma}_n^\dagger\hat{\gamma}_n \tag{1.9}$$

where x is the space coordinate, $H_0(x)$ the Hamiltonian without the pairing term (ie it is a generic Hamiltonian with quadratic terms only), $\Delta(x) \propto \langle\hat{c}_\downarrow(x)\hat{c}_\uparrow(x)\rangle$ the superconducting pairing potential and $\hat{c}_s(x)$, $\hat{c}_s^+(x)$ (resp. $\hat{c}_{ks}$, $\hat{c}_{ks}^+$) the field operators for spin $s = \uparrow, \downarrow$ in real (resp. momentum) space. To diagonalize this Hamiltonian we need to find the eigenvalues E_n and the operators $\hat{\gamma}_n$ (which are not, in general, self-adjoint).

The Bogoliubov de Gennes approach consists in looking for excitations of the following form :

$$\hat{\gamma}_n^+ = \int dx[u_\uparrow^n(x)\hat{c}_\uparrow^+(x) + u_\downarrow^n(x)\hat{c}_\downarrow^+(x) + v_\uparrow^n(x)\hat{c}_\uparrow(x) + v_\downarrow^n(x)\hat{c}_\downarrow(x)], \tag{1.10}$$

or in momentum space

$$\hat{\gamma}_k^+ = u_{k\uparrow}\hat{c}_{k\uparrow}^+ + u_{k\downarrow}\hat{c}_{k\downarrow}^+ + v_{k\uparrow}\hat{c}_{k\uparrow} + v_{k\downarrow}\hat{c}_{k\downarrow}. \tag{1.11}$$

The time-independent Schödinger equation for the mode n then writes (dropping the x index)[32]:

$$h_{eff}\begin{pmatrix} u^n_\uparrow \\ u^n_\downarrow \\ v^n_\downarrow \\ -v^n_\uparrow \end{pmatrix} \equiv \begin{pmatrix} H_0 & \Delta \\ \Delta^* & -\hat{s}_y H_0^* \hat{s}_y \end{pmatrix} \cdot \begin{pmatrix} u^n_\uparrow \\ u^n_\downarrow \\ -v^n_\downarrow \\ v^n_\uparrow \end{pmatrix} = E_n \begin{pmatrix} u^n_\uparrow \\ u^n_\downarrow \\ -v^n_\downarrow \\ v^n_\uparrow \end{pmatrix} \tag{1.12}$$

Looking at the Nambu spinor that is used, we can note that:

$$\Psi(x) \equiv (\hat{c}_\uparrow(x),\, \hat{c}_\downarrow(x),\, \hat{c}^+_\downarrow(x),\, -\hat{c}^+_\uparrow(x))^T = (\psi(x),\, i\hat{s}_y\psi^\dagger(x))^T \tag{1.13}$$

This is the operator version of equation (1.5) and indeed, this spinor satisfies the Majorana condition: $\Psi^c(x) = C\Psi^\dagger(x) = \Psi(x)$[2] (in this basis the charge conjugation operator reads $C = -i\hat{\tau}_y$, where the $\hat{\tau}_i$ are Pauli matrices acting on the electron-hole subspace and $\hat{s}_i$ on the spin subspace).

Finally, with a well chosen unitary transformation we can rewrite h_{eff} as purely imaginary ($h^*_{eff} = -h_{eff}$), and the field operator as self-conjugate, directly mirroring Majorana's work on the Dirac equation [29].

This discussion shows how Majorana fermions can naturally appear in the description of a superconductor. However, the relation (1.13) concerns the quantum field $\Psi(x)$, and does not necessarily lead to anything interesting in the eigenmodes of the system. We can thus go further and look for an eigenstate for which the operator $\hat{\gamma}_n$ fulfills the self-adjointness condition: $\hat{\gamma}_n = \hat{\gamma}^+_n$. Such a mode can only happen at $E = 0$ as noted in section 1.1.1. These modes are called Majorana Zero Modes (MZM) or Majorana Bound States (MBS) in the literature, to distinguish them from the term Majorana fermions.

We can however notice that in an s-wave superconductor with spin rotation symmetry, the spin degeneracy allows us to work in a reduced Nambu space. The excitations of the system can be simply written $\hat{\gamma}_{SC} = u\hat{c}^+_\uparrow + v\hat{c}_\downarrow$, which is always different from $\hat{\gamma}^+_{SC} = u^*\hat{c}_\uparrow + v^*\hat{c}^+_\downarrow$. As a consequence, this symmetry needs to be broken for MZM to appear. Another way to overcome this issue is to consider an effectively spinless system which would still contain superconducting pairing. In this case we could have an excitation of the form $\hat{\gamma}_{spinless} = u\hat{c}^+ + v\hat{c}$, that is self-adjoint provided $u = v^*$. In such a spinless superconductor, the Cooper pair wavefunction needs to be antisymmetric in space (the orbital part of the wavefunction) so that the wavefunction changes sign

[2] This is quickly visible by rewriting $C = \begin{pmatrix} 0 & -i\sigma_y \\ i\sigma_y & 0 \end{pmatrix}$ where $\sigma_y \equiv \begin{pmatrix} 0 & -i \\ i & 0 \end{pmatrix}$ combined with equation (1.13)

under the exchange of its two electron, in accordance with the Pauli principle[3]. Hence an antisymmetric pairing, such as a p-wave pairing is needed.

Indeed, the first superconducting systems to be theoretically shown to host MZM were p-wave topological superconductors either in 1 or 2D: see references [6, 28], among others.

1.1.3 A quick word and some vocabulary about topology

Before looking at an example of topological superconductor into more details, let us summarize a few important notions of topology.

First of all, a topological property is a global property of a system, meaning that it should be independent of small details, and it should not be affected by small (continuous) changes. The first example usually given is the topology of space. Given a closed surface in space, one can easily count how many holes it contains: a spoon contains zero, a ring one, Emmental cheese a lot. One can stretch or twist these objects without changing this value [4]. The number of hole is a topological property of a surface.

One can often define a number (called the topological invariant) that identifies the different possible topological states of the system, or phases (in the previous example, the number of holes). There is no systematic way to know how to calculate a topological quantity, but in the case of space topology, the Gauss-Bonnet number (which is the integration of the curvature of the shape over its surface) does give exactly the number of holes in the volume.

In physics, this notion of topology enables the definition of general properties of a material, that are not affected by small deformations of its Hamiltonian. Indeed, it was shown that beyond the classical phases separated by phase transitions (characterized by the vanishing or the discontinuity of an order parameter), condensed matter ground states can also be classified in terms of topological phases, separated by a topological phase transition (characterized by a change in the topology of the ground state). A topological phase transition comes with a gap closing in the electronic density of states (like any quantum phase transition), that allows for a change in the ground state of the system[5]. Considerations of symmetries allows one to identify universality classes, and to figure out how many topologically distinct phases may exist. For the classical MZM recipes that we will consider, we usually have particle-hole symmetry (if Ψ is an

[3] In s-wave superconductor, the asymmetry comes from the spin part of the wavefunction.

[4] but not cut them; this would not be a "continuous" deformation.

[5] One can picture for example the case of a topological insulator where there are two electronic bands with different topologies around the Fermi energy, and when one invert the valence and the conduction band the semiconductor change phase. At the transition the two bands are degenerate in energy. In finite size systems, the gap does not rigorously close due to the quantization of the energy levels.

eigenvector of H, Ψ^c is also, with a charge conjugation operation such that $C^2 = 1$) but no spin-rotation symmetry, and the system has two distinct possible phases. This identification in terms of symmetries[6] is important because it enables us to specify what are "small perturbations" of the Hamiltonian, that do not change the phase: by that we mean perturbations that do not break the problem symmetries, and keep the energy gap open.

As a consequence, two gapped ground states states are topologically equivalent if one can continuously change the parameters of one to the other without breaking the symmetries of the problem and without closing the excitation gap. A state is called trivial state if it is equivalent to the vacuum state. At the boundary between two topologically distinct phases, there exist zero-energy localized modes, illustrating the inversion of the ground state with an excited state before and after the transition (these states are degenerate at the transition). These localized modes live, for example, around vortices in a superconductor, or at the edge of a quantum hall state.

1.1.4 An example of Majorana Zero Modes

Let us now look at a model of a spinless p-wave 1D topological superconductor (a 1D topological wire) to understand better the peculiarities of the MZM [34] (we take $\hbar = 1$, and Δ real without loss of generality). For a discussion on the tight-binding version of this model, the Kitaev chain, one can look at the pedagogical review of Jason Alicea [35] or the lecture notes of J. Dalibar, where the topological numbers are addressed in more details.

For p-wave pairing, the orbital part of the pairing term needs to be antisymmetric under space reversal as noted in section 1.1.2. We will consider the following hamiltonian:

$$H = \int dx[\hat{c}^+(x)(\frac{p^2}{2m} - \mu)\hat{c}(x) + \Delta(\hat{c}^+(x)\partial_x\hat{c}^+(x) + h.c.)], \tag{1.14}$$

or in momentum space

$$H = \sum_k \xi_k \hat{c}_k^+ \hat{c}_k + i\Delta k \hat{c}_{-k}\hat{c}_k - i\Delta k \hat{c}_k^+ \hat{c}_{-k}^+ \text{ with } \xi_k = \frac{k^2}{2m} - \mu. \tag{1.15}$$

In the spinless Nambu representation $\Psi_k \equiv (\hat{c}_k, \hat{c}_{-k}^+)^T$, the Hamiltonian rewrites:

$$H = \frac{1}{2}\sum_k \Psi_k^+ H_k \Psi_k \text{ with } H_k = \xi_k \hat{\tau}_z + \Delta k \hat{\tau}_y = \vec{b}_k \cdot \vec{\tau}, \tag{1.16}$$

[6] For more considerations on symmetries, one can read Introduction to Topological Quantum Matter and Quantum Computation, T. D. Stanescu or Ref [33].

where we have used the notation $\vec{b}_k \equiv (0,\, \Delta k,\, \xi_k)^T$ where τ are the Pauli matrices acting in the electron-hole space. This Hamiltonian is analogous to the one of a spin $\vec{\tau}$ in a magnetic field $\vec{b}_k$.

We can calculate the dispersion relation by following this analogy, or by squaring this hamiltonian (since particle-hole symmetry ensures a spectrum symmetric in energy, we lose no solution):

$$E_k = \pm|\vec{b}_k| = \pm\sqrt{\xi_k^2 + (\Delta k)^2}. \tag{1.17}$$

This dispersion relation is always gapped, meaning that the lowest energy is strictly positive, except for $\mu = 0$. Sweeping μ from negative to positive values, the energy gap closes and then reopens. This can indicate a topological phase transition, in the sense that the ground state topology can change[7].

To identify which phase is the trivial one, we have to find which phase can be "deformed" into the vacuum phase, meaning that they are topologically equivalent. In fact, taking the limit $\mu \to -\infty$ pushes the bottom of the electronic band to $|E_0| \to \infty$. As a consequence, the $\mu < 0$ band is the trivial phase. This is also visible in the topological invariant associated with this Hamiltonian, which is the winding number of $\vec{b}_k$ around the origin, when k explores all possible values (from $-\infty$ to $+\infty$). The winding of $\vec{b}_k$ in both phases is illustrated in figure 1.1. Panels (a,b) represents $\vec{b}_k$ in the y-z plane (since for this particular Hamiltonian $b_{k,x} = 0$), whereas panels (c,d) represent its orientation $\vec{b}_k/\|b_k\|$, for $k \in [-\infty, \infty]$. In both case, the phase is determined by whether of not the trajectory encloses the origin (for panels (a,b)), or winds around the x-axis (panels (c,d)). Although we have not justified why this quantity represents a topological invariant, the first illustration (panels (a,b)) is particularly instructive. Indeed, the origin corresponds to the existence of a k_0 such that $\vec{b}_{k_0} = \vec{0}$. At this wavevector, the eigenvalues of equation (1.16) are both zero (which is also directly visible in the dispersion relation (1.17)), and there exists a zero-energy mode. Thus there is a phase transition when going from a $\vec{b}_k$-trajectory that does not encircle the origin (b) to one that does (a). The associated winding number will not be affected by small perturbations of the Hamiltonian: it is a topological property of the system.

Now that we have identified the two phases, we can study the boundary between a trivial and a topological phase, for example by considering an infinite 1D wire with a spatially varying chemical potential $\mu = -\alpha x$ where $\alpha \ll m^2\Delta^3$. The Hamiltonian becomes:

$$H = -\alpha x \hat{\tau}_z + \Delta p \hat{\tau}_y \tag{1.18}$$

[7] Such as, for example, when two bands with different topologies invert in energy in a topological insulator phase transition.

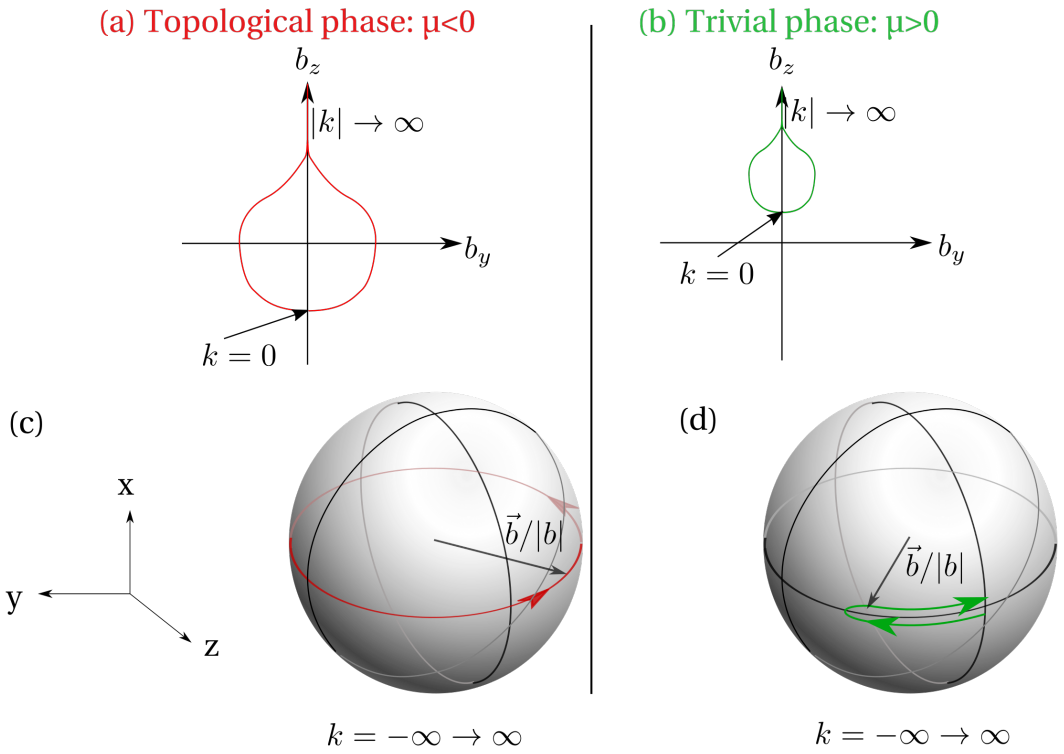

FIGURE 1.1: **Illustration of the topological number in the spinless 1D p-wave superconductor.** With two representation, either in the 2D plane or on the Bloch sphere. Evolution of $\vec{b}$ when k goes from $-\infty$ to $+\infty$ for two situations. For $\mu < 0$ (trivial case, (b) and (d)), the vector does not wind around the origin, whereas for $\mu > 0$ it winds once, as visible in (a) and (c). The direction of rotation depends on the sign of Δ.

As before, we can square it to find the energies of the bound states:

$$H^2 = (\alpha x)^2 + (\Delta p)^2 - \Delta\alpha\hat{\tau}_x \text{ with } [x,\, p] = i \text{ and } \hat{\tau}_z\hat{\tau}_y = -i\hat{\tau}_x \tag{1.19}$$

In the eigenbasis of $\hat{\tau}_x$ (labelled by $\pm$) this represents two harmonic oscillators (one for each of $\hat{\tau}_x$'s eigenvalues), each being associated with a number operator $\hat{n}$. They are shifted by $2\Delta\alpha$ with respect to one another, thus the spectrum is:

$$(E_n^{\pm})^2 = 2\Delta\alpha(n + \frac{1}{2}) \mp \Delta\alpha \tag{1.20}$$

This system admits a zero-energy solution, $E_0^- = 0$. We can foresee that its wavefunction will be of the form $\phi(x) = u_0(x)\begin{pmatrix}1\\1\end{pmatrix} \propto \begin{pmatrix}1\\1\end{pmatrix} e^{-(x/x_0)^2}$ since it needs to be localized around the domain wall (the system being infinite) and it needs to have an equal electron/hole weight to be at zero energy. The corresponding quasiparticle operator is :

$$\hat{\gamma} = \int dx u_0(x)[\hat{c}(x) + \hat{c}^+(x)] \tag{1.21}$$

One can check that this operator is, indeed, self-adjoint. Thus we have found a stationary quasiparticle obeying the Majorana property $\hat{\gamma} = \hat{\gamma}^+$. In the literature, these quasiparticles are called Majorana Zero Mode (MZM) or Majorana Bound State (MBS) to distinguish them from Majorana fermions.

The self-adjoint property has an embarrassing consequence at first sight, which is $\hat{\gamma}^2 = \mathbb{1}$, and as such we cannot define a number operator. However we have already shown that from two Majorana operators we can define a fermionic operator, through the transformation (1.7). We just need to find a second Majorana to complement $\hat{\gamma}$. Actually it is just located at the end of the topological section of the wire, that is bound to exist: the infinite system is not really physical[8]. Provided the wire is long enough ($L \gg x_0$, or the new typical length-scale for the Majorana wave-functions), there will be one localized zero-energy state at both ends of the topological phase, $\hat{\gamma}_1$ and $\hat{\gamma}_2$. The fermionic operator $\hat{c} = \frac{1}{2}(\hat{\gamma}_1 + i\hat{\gamma}_2)$ can have an occupancy 0 or 1: the ground state of the system is doubly degenerate, with either $\hat{c}^\dagger\hat{c} = 0$ or 1. The parity operator can be formally written

$$P = 2\hat{c}^\dagger\hat{c} - 1 = i\hat{\gamma}_1\hat{\gamma}_2 \tag{1.22}$$

Note that in a system with 2N MZM, the ground state has a degeneracy of 2^N corresponding to each pair of 2 MZM being either empty or occupied.

1.1.5 Specific properties of the MZM: the non-abelian statistics

A particularity of localized MZM in 1D or 2D systems is their non-abelian exchange statistics. Indeed, while in 3D particles can only follow the bosonic or fermionic statistics (when exchanging two undistinguishable particles, the global wavefunction stays identical or picks up a minus sign), in 2D a richer behavior can exist[9]. For example, the wavefunction can pick up a phase (anyonic statistic). When the ground state is degenerate, particle exchange can lead to a change in the state of the system, represented by a unitary operation on the wavefunction (non-abelian statistics). The state of a system after several particle exchanges then depends on the order of the exchanges, since the corresponding unitary operations do not necessarily commute.

[8] Note that this is not an issue in the trivial phase since it is equivalent to a vacuum phase.

[9] In 3D, any trajectory that exchange two particles can be deformed into a simple rotation of one around the other; in 2D the trajectories are much more constrained, and thus not all equivalent; for example a particle can rotate several times around another one.

Braiding MZM

As noted just above, a system with 2N MZM has a degenerate ground state, and thus can display non-abelian statistics [36]. The effect of braiding two Majorana quasiparticles was first studied for vortices. One can show that moving one vortex around another affects the Majorana operators $\hat{\gamma}_1, \hat{\gamma}_2$ the following way [37]:

- For clockwise rotation, $\hat{\gamma}_1 \to \hat{\gamma}_2$; $\hat{\gamma}_2 \to -\hat{\gamma}_1$
- For counter-clockwise rotation, $\hat{\gamma}_1 \to -\hat{\gamma}_2$; $\hat{\gamma}_2 \to \hat{\gamma}_1$

This transformation is represented by the unitary evolution $U_{\text{braid cw}} = \frac{1+\hat{\gamma}_1\hat{\gamma}_2}{\sqrt{2}}$[10] (for clockwise rotation) and $U_{\text{braid ccw}} = U^{\dagger}_{\text{braid cw}}$ (counter-clockwise rotation).

Interest to quantum information

The topological properties of MZMs have generated a lot of interest notably in the field of topological quantum information. It was shown that topological states could enable fault-tolerant computing [23]; the idea of fault-tolerant computing being that an error in of the computation will propagate without increasing the total number of errors in the calculation[11].

Additionally, topological states, ie states whose presence depends on the phase of the system will not be destroyed by small perturbations of their environment (as long as they do not break the symmetries of the problem). Indeed if the system is gapped in energy, one cannot change the energy of the zero-mode excitation without closing the gap. By symmetry, if a single zero-energy excitation (in an infinite system) acquires an energy ϵ, then another mode needs to appear at energy $-\epsilon$. The energy of the Majorana mode is thus stable (this stability being related to the size of the energy gap).

Finally, since MZM have a real creation operator they are ideally not sensitive to dephasing (and being at zero energy they ideally do not have a T_1 decay)[12]. To go into more details one has to specify how to form a qubit with such states: the first proposals involved braiding MZM in real space, either vortices in 2D [39], or MZM in nanoconductors networks [40], which is experimentally challenging. Subsequent proposals tried to identify schemes to build qubits and define gate operations without having to finely control the spatial shape of the wave-function [24, 41–46].

[10] With the convention for $\hat{c}$ given in section 1.1.4.
[11] Note that however MZM are not sufficient to build a universal set of gates for quantum computation.
[12] Although temperature fluctuations affect the topological gap and may induce errors [38].

Now that we have briefly reviewed the interest of MZM and the conditions under which they can emerge in condensed matter systems, let us consider more concrete physical realizations.

1.2 Majorana "recipe"

Once the physical effects enabling the formation of Majorana fermions in a solid-state setup were identified (as introduced in section 1.1.2), several theoretical papers offered methods to experimentalists that grouped commonly used ingredients in condensed matter experiments [7–12]. We here introduce one of these methods [11, 12], and discuss the importance of the different ingredients.

1.2.1 Elementary "recipe" and topological transition

In concrete terms, one needs a spinless superconductor to obtain Majorana fermions. Actually, it is sufficient to have one non-degenerate electronic band, with superconducting pairing. Applying a very large magnetic field lifts the spin degeneracy, but the common s-type superconducting pairing does not survive at high magnetic fields. Another way to lift the spin degeneracy is to submit the electron spin to a spin-orbit interaction, non collinear with the Zeeman polarization of a small magnetic field. The combination of these effects on a semiconductors' electronic bands creates a region in energy were there is only one electronic band left, as we see in figure 1.2. This region is called the helicoidal gap; in this gap, right moving and left moving electrons only have one possible spin orientation (that are non collinear) and thus the spin and momentum are locked. s-wave superconductivity can still induce pairing between these two species of electrons since their spins are non-orthogonal.

Thus for now, a promising method to obtain MZM consists in combining the following ingredients [11, 12]:

- a 1D semiconductor
- spin-orbit coupling α
- homogeneous external magnetic field $\vec{B}$, perpendicular to the spin-orbit axis
- proximity-induced superconductivity, with an effectively induced pairing Δ_{ind}[13].

[13] We can choose Δ_{ind} real without loss of generality.

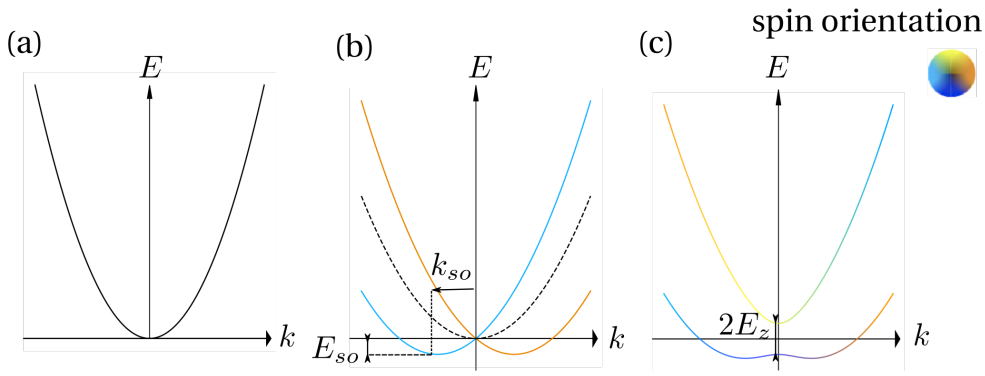

FIGURE 1.2: **Evolution of the electronic bands of a 1D semiconductor** (a) when adding first a spin-orbit energy (b) and a magnetic field (c). Superconductivity is added in figure 1.3. The color-code represent the spin eigenvalue, except when the bands are degenerate in spin with no favored orientation (black).

We develop here the basic properties of this proposal, for the situation where α, B and Δ_{ind} are homogeneous along the semiconductor. The Hamiltonian is:

$$H = \int dx \left[\sum_{s=\uparrow,\downarrow} \hat{c}_s^\dagger(x) \left(\frac{\hat{p}^2}{2m} - \mu + \frac{g\mu_B B}{2}\hat{s}_x + \frac{\alpha}{\hbar}\hat{p}\hat{s}_y \right) \hat{c}_s(x) + \left(\Delta_{ind}\hat{c}_\downarrow^\dagger(x)\hat{c}_\uparrow^\dagger(x) + h.c. \right) \right] \tag{1.23}$$

where we took x as the axis of the semiconductor and of $\vec{B}$, p the momentum and y the axis of the spin-orbit interaction. The Pauli matrices s_i act on the spin.

One can look at the successive effects of each term on the electronic bands to get an insight of how they interact. Starting from a parabolic dispersion relation, degenerate in spin (figure 1.2(a)), the spin-orbit effect splits the bands and shifts them in energy (figure 1.2(b)). Indeed, we obtain from equation (1.23) the eigenenergies:

$$E^\pm(k) = \frac{\hbar^2 k^2}{2m} - \mu \pm \alpha k = \frac{\hbar^2}{2m}(k \pm k_{so})^2 - \mu - \frac{E_{so}}{2} \tag{1.24}$$

$$\text{with } k_{so} \equiv \frac{m\alpha}{\hbar^2} \text{ and } E_{so} \equiv \frac{\hbar^2 k_{so}^2}{m} = \frac{m\alpha^2}{\hbar^2} \tag{1.25}$$

The spin eigenvalue associated with each band is represented in orange (+ band) and light blue (− band).

Adding the magnetic field, (figure 1.2(c)), we obtain the following bands:

$$E^\pm(k) = \frac{\hbar^2 k^2}{2m} - \mu \pm \sqrt{(\alpha k)^2 + E_z^2} \tag{1.26}$$

With $2E_z \equiv g\mu_B B$. The crossing at $k = 0$ opens with a gap $2E_z$, creating the desired "spinless" region: in the gap, there is a single electronic band, thus the spin and momentum of the electrons are locked. This region is called the helical gap. Additionally now the spin eigenvalue depends on the wave-vector k; at large k the spin-orbit energy

dominates and the bands are polarized along the spin-orbit coupling axis (x), whereas at $k = 0$ they are polarized along the magnetic field axis (z).

Adding superconductivity (figure 1.3), we need to add the hole band to the previous picture. The crossings between the electron and hole bands (at zero energy) are lifted by the superconducting pairing. To calculate the bands, the easiest way is to write the Bogoliubov de Gennes hamiltonian as introduced in paragraph 1.1.2, and to diagonalize it. Here we have chosen the Nambu basis $\Psi = \left(\hat{c}^\dagger_{k\uparrow}, \quad \hat{c}^\dagger_{k\downarrow}, \quad -\hat{c}_{-k\downarrow}, \quad \hat{c}_{-k\uparrow}\right)^T$.

$$H_{BdG} = \begin{pmatrix} H_0 & \Delta_{ind} \\ \Delta_{ind} & -\hat{s}_y H_0^* \hat{s}_y \end{pmatrix} \tag{1.27}$$

$$\text{with } H_0 = (\frac{\hbar^2 k^2}{2m} - \mu)\hat{s}_0 + \alpha k \hat{s}_y + E_z \hat{s}_x$$

$$H_{BdG} = \begin{pmatrix} \frac{\hbar^2 k^2}{2m} - \mu & E_z - i\alpha k & \Delta_{ind} & 0 \\ E_z + i\alpha k & \frac{\hbar^2 k^2}{2m} - \mu & 0 & \Delta_{ind} \\ \Delta_{ind} & 0 & -\frac{\hbar^2 k^2}{2m} + \mu & E_z + i\alpha k \\ 0 & \Delta_{ind} & E_z - i\alpha k & -\frac{\hbar^2 k^2}{2m} + \mu \end{pmatrix}$$

Again since the spectrum is symmetric we can square the Hamiltonian without losing eigenvalues and we get the following bands :

$$E_\pm^2 = E_z^2 + \Delta_{ind}^2 + (k\alpha)^2 + (k^2 - \mu)^2 \pm 2\sqrt{(E_z\Delta_{ind})^2 + E_z^2(k^2 - \mu)^2 + (k\alpha)^2(k^2 - \mu)^2} \tag{1.28}$$

Looking at the spectrum, we can see that the system is always gapped except at $E_z = \sqrt{\Delta_{ind}^2 + \mu^2}$. Actually when increasing E_z from zero, the spectrum gap closes and reopens, marking a change in the ground state of the system: see figure 1.3. In the new phase, a pair of MZM exist at both ends of the system.

The criterion for entering the topological phase is thus :

$$E_z > \sqrt{\Delta^2 + \mu^2} \tag{1.29}$$

And the energy gap at $k = 0$ between the MZM and the first energy band is $\Delta E_{k=0} = E_z - \sqrt{\Delta^2 + \mu^2}$.

To find the wave-function associated with the MZM, we can proceed exactly in the same way as in the paragraph 1.1.4, as was done in the first proposal [11]. In this proposal, in the infinite limit, either a linear variation of a parameter - magnetic field ($E_z(x) \propto bx$) or superconducting pairing ($\Delta(x) \propto \delta x$) - was studied, or a step like variation (for the chemical potential μ), and self adjoint excitations at zero energy were evidenced. For a

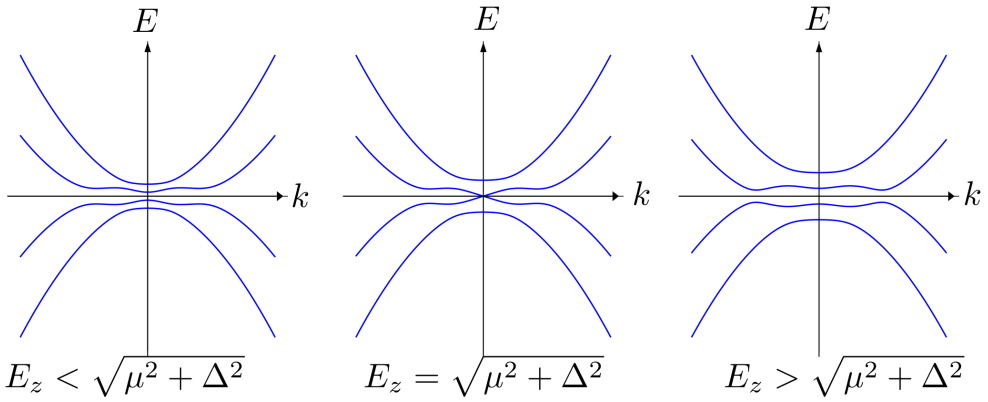

FIGURE 1.3: **Evolution of the energy spectrum in magnetic field**, when increasing the magnetic field (from left to right). At the phase transition (central panel), the energy gap at $E = 0$ closes. There can also be low-energy excitations at higher momentum; the size of the high momentum gap depends on the spin-orbit energy, in contrast to the topological gap.

linear variation of E_z, the ground state wave-function writes $\phi(x) \propto e^{-bx^2/2\alpha}$, giving a localization length of $\sqrt{\frac{2\alpha}{(\partial_x E_z)}}$. For a step-like variation of μ, the wave-function extends in the superconductor (with chemical potential μ_l) over a length $\frac{\alpha/\hbar}{\Delta - \sqrt{E_z^2 - \mu_l^2}}$.

The control of the phase through a variation of μ seems experimentally accessible; we see that in this case α, Δ, μ_l and B influences the localization length; a high magnetic field localizes better the wave-function. This plays an important role in a finite size system, where there are two boundaries between the trivial and the topological phase, and thus one MZM at each boundary. If they are close to one another and their wave-function overlap, they will hybridize, and the energy degeneracy between $P = 0$ and $P = 1$ (P being the parity) is lifted by an energy splitting proportional to this overlap [47].

1.2.2 Importance of the different energy scales

Let us try and understand in more details the importance of all of the energy terms. We can first look at the strength of the effective p-wave pairing in a 1D conductor with all the ingredients introduced above. The eigenvalues and eigenvectors of the Hamiltonian (1.27) are [31]:

$$|e_-\rangle = \frac{1}{\sqrt{2}}(-\gamma_k,\, 1,\, 0,\, 0)^T \quad \text{with } E_{e,-} = k^2 - \mu - E_\Sigma \tag{1.30}$$

$$|e_+\rangle = \frac{1}{\sqrt{2}}(\gamma_k,\, 1,\, 0,\, 0)^T \quad \text{with } E_{e,+} = k^2 - \mu + E_\Sigma \tag{1.31}$$

$$|h_+\rangle = \frac{1}{\sqrt{2}}(0,\, 0,\, \gamma_k,\, 1)^T \quad \text{with } E_{h,+} = -(k^2 - \mu) + E_\Sigma \tag{1.32}$$

$$|h_-\rangle = \frac{1}{\sqrt{2}}(0,\, 0,\, -\gamma_k,\, 1)^T \quad \text{with } E_{h,-} = -(k^2 - \mu) - E_\Sigma \tag{1.33}$$

where we take $\hbar = m = 1$ and note $E_\Sigma = \sqrt{E_z^2 + (k\alpha)^2}$, $\gamma_k = \frac{i\alpha k + E_z}{E_\Sigma}$.

The two lowest energy bands are $E_{e,-}$ and $E_{h,-}$. The coupling induced by the term $\Delta\hat{\tau}_x$ between these two bands is [12]:

$$\Delta_{p,\text{eff}} = \langle h_- | \Delta\hat{\tau}_x | e_- \rangle = \frac{\Delta}{2}(1 - \gamma_k^2) \tag{1.34}$$

We can thus distinguish two situations:

- At large magnetic field $E_z \gg k\alpha$, the pairing reduces to $\Delta_{p,\text{eff}} \approx -i\frac{\Delta\alpha k}{E_z}$ (we recover the result of [34]),
- At large spin-orbit coupling $E_z \ll k\alpha$, the pairing reduces to $\Delta_{p,\text{eff}} \approx \Delta$, and there is another energy gap $E_{gap,k>0}$ at $k \approx \pm k_{so}$.

We can actually rewrite the hamiltonian in the helical basis [31]:

$$\begin{aligned} H = &\int \frac{dk}{(2\pi)} \frac{\Delta_+^p}{2} \left\{ \psi_+^\dagger(k)\psi_+^\dagger(-k) + h.c. \right\} + \frac{\Delta_-^p}{2} \left\{ \psi_-^\dagger(k)\psi_-^\dagger(-k) + H.c. \right\} \\ &+ \Delta^s \left\{ \psi_+^\dagger(k)\psi_-^\dagger(-k) + \psi_-(-k)\psi_+(k) \right\} \end{aligned} \tag{1.35}$$

where ψ_+ are the wavevectors associated with the two lowest energy bands, and with effective gaps:

$$\begin{aligned} \Delta^s(k) &= \frac{E_z\Delta}{E_\Sigma} \\ \Delta_\mp^p(k) &= \frac{\pm i\alpha k\Delta}{2E_\Sigma}. \end{aligned} \tag{1.36}$$

We see that the spin orbit strength, although not apparent in the phase criterion 1.29, affects the strength of the effective p-wave pairing. The stronger the spin-orbit is, the higher the magnetic field can be without destroying the p-wave pairing.

Another important energy scale is the high momentum gap, visible for example in figure 1.3 (at strong spin orbit coupling, it is at $k_{gap} \approx \pm k_{so}$). It needs to be large to separate well the zero energy mode from other low-energy excitations. This gap appears thanks to superconductivity, but is affected by E_z. At $\mu = 0$ it is given by [48]:

$$E_{gap,k>0} = \frac{2\Delta E_{so}}{\sqrt{E_{so}\left(2E_{so} + \sqrt{E_z^2 + 4E_{so}^2}\right)}} \tag{1.37}$$

Finally, we can look at the robustness of both gaps (at zero energy and the high momentum one) when the magnetic field and the spin-orbit axes are not perfectly

orthogonal. For example if there is a small component of the field along the axis y (of the spin-orbit), $B_{y,parasitic}$, it will enter in the band energies through

$$E'_\Sigma = \sqrt{E_z^2 + (k\alpha + g\mu_B B_{y,parasitic}/2)^2} \tag{1.38}$$

which will overall tilt the spectrum. As a consequence, the high-momentum gap reduces at $k < 0$ (for $B_{x,parasitic} > 0$) and can even close.

To summarize, the key points are the following:

- E_z needs to be strong enough to reach the topological criterion, and open an energy gap at $k = 0$,
- A good control of the chemical potential to reach the low μ regime is necessary,
- E_{so} and E_z both need to be of the same order of magnitude in case we cannot control the field orientation too well,
- Δ and E_{so} are important to open an energy gap between the MZM and other excitations (high momentum gap),
- The length of the system L should be as large as possible, staying in the ballistic regime ($L < L_{\text{mean free path}}$).

We can conclude that one should have all the energies of about the same order of magnitude to be able to see the competition between all the effects in presence.

1.3 Physical implementations and experimental signatures

As mentioned in the introduction, several experimental realizations have been proposed to combine the ingredients of the Majorana recipe: nanowires [13, 49, 50], 2DEG [18, 19], atomic chains [20] or islands [22, 51].

So far, experimental signatures obtained in Majorana devices have been mainly transport signatures, ie measurements of the conductance of the device, either local (with STM measurements) or global (by looking at transport through the device). A few experimental setups have also realized devices with a control in magnetic flux (affecting the superconducting phase difference through a Josephson junction) rather than in voltage bias.

Let us summarize more in details the current state of the art.

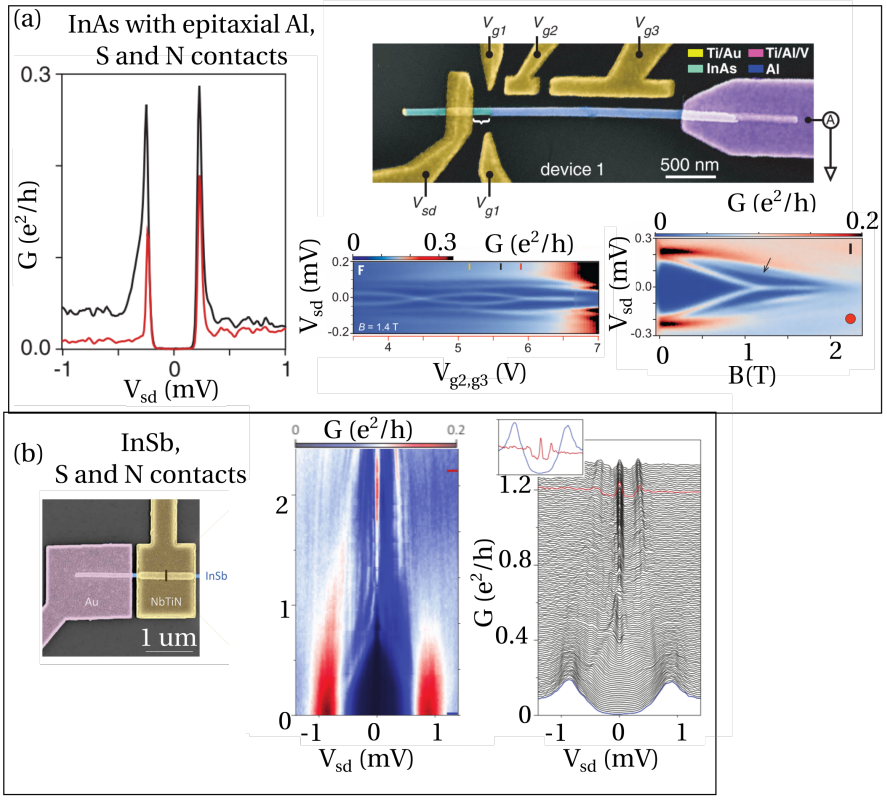

FIGURE 1.4: **Global conductance experimental results** from [15] (a), and [52] (b), showing the ZBP measurement for both a device with epitaxially deposited Al over an InAs nanowire and evaporated superconducting contacts on an InSb nanowire. Panel (a) shows a conductance curve as a function of bias in a region with no subgap state, an SEM image of the device made out of an InAs nanowire with epitaxial Al, contacted with one superconducting and one normal contact, as well as two conductance maps as a function of bias and either gate voltage or magnetic field, showing the evolution of subgap states energies. The data interpretation takes into account the presence of a dot in the uncovered region of the nanowire. Panel (b) shows the experimental device, which consists in an InSb nanowire contacted with a normal and superconducting contact, as well as its conductance as a function of voltage bias and magnetic field (either as a colormap of as a waterfall, each curve being offset by $0.01\frac{e^2}{h}$, from 0 to 2.5 T.

1.3.1 Global conductance measurement

One characteristic of a MZM is that it is pinned at zero energy, independently of the applied magnetic field or chemical potential (once the topological criterion is reached). This is the most easily measured property, although a MZM is only one of the many effects that can give rise to a zero bias peak (ZBP) in a global conductance measurement[14].

Another specificity visible in a global conductance measurement is the quantized value for the conductance of the ZBP, when measuring conductance through a normal - topological superconductor interface. Indeed at the interface, the superconducting

[14]By global, we mean conductance through the whole nanoconductor, as opposed to local measurements with STM techniques

gap prohibits transmission of an incoming electron; it can either undergo a normal reflection or an Andreev reflection where it is retro-reflected into a hole (effectively transferring a charge 2e in the superconductor). The corresponding scattering matrix has a transmission $T = 0$ and reflection matrix (in electron-hole space)

$$R = \begin{pmatrix} r_{ee} & r_{eh} \\ r_{he} & r_{hh} \end{pmatrix}, \tag{1.39}$$

$$\text{with } R(E) = \hat{\tau}_x R(-E)^* \hat{\tau}_x \text{ due to particle-hole symmetry,} \tag{1.40}$$

$$\text{and } R^+ R = \mathbb{1} \text{ since there is no transmission.}$$

In the special case of an incoming electron with energy $E = 0$, the combination of all these properties leads to either a perfect normal reflection (and no conductance measured; this is the trivial phase) or perfect Andreev reflection $|r_{eh}| = 1$. Hence, in principle, the measured conductance is quantized at $G = \frac{2e^2}{h}$ (for the case of one effectively spinless channel, as expected in the topological phase). Tunneling through a symmetric two barrier system (N-TS-N) is equivalent to the above case of an N-TS interface. However, several effects can reduce the height of the peak, as will be discussed later on.

First measurements with InSb or InAs nanowires

The first papers to interpret a ZBP as a signature of a MZM studied InAs [14] or InSb nanowires [13, 53, 54] with superconducting contacts.

In Ref [13], the device under study was an InSb nanowire of diameter 110 ± 10nm contacted to an extended NbTi superconducting contact (about 2 μm) on one side, with a gap of about $\Delta = 250$ μeV, and to a normal contact on the other. This nanowire was selected for its high g-factor (estimated at 50 here, typical values are in the range 35-50), and an expected spin orbit energy of typically $E_{so} = 50$ μeV, corresponding to $l_{so} = 200$ nm (with a very small effective mass m^*).

A zero bias peak is observed at a conductance $G_{\text{diff}} \sim 0.05\frac{2e^2}{h}$ above a background conductance of $G_{\text{diff}} \sim 0.1\frac{2e^2}{h}$. It is pinned at zero energy over a range of magnetic field of about 200 mT, and a range of gate voltage corresponding to a few level spacings as given by the observed Coulomb blockage peaks. The peak width at half maximum is about 20 μeV. The authors also studied the influence of the field angle: the ZBP disappears at certain magnetic field angles, which is interpreted as the situation where the magnetic field is applied along the spin-orbit direction. The peak disappears at a temperature $T = 200$ mK.

In such a geometry, the authors propose that the coupling between the superconductor and the nanowire is homogeneous, and thus there is a topological phase (at high magnetic field) over the whole section of the nanowire that is covered by the superconducting contact. Two MZM are localized at both ends, one of which overlaps with the normal contact used for the conductance measurement.

After these first results, many questions were raised, notably about the interface between the superconductor and the nanowire, and the effect of disorder (which will be discussed in section 1.3.2). Subsequent experiments tried to reduce the quasiparticle weight below the superconducting gap and to build a more complete picture of the condition in (μ, B) for the emergence of the ZBP [55, 56]. In reference [52], the authors also observed a well developed ZBP over a larger range of magnetic field than the previous experiments (over 1T), as reproduced in figure 1.4 (b). From the conductance measurement at large bias, they infer a mean free path of 10 µm, larger than the device size (1 µm), as required for the interpretation in term of MZM. They also managed to obtain a much better superconducting gap, with almost no conductance below the gap before the appearance of the peak.

Nanowire with epitaxially grown Al superconductor

A new geometry of devices was also studied after the first experimental signatures were reported, consisting in InAs nanowires with an epitaxially grown shell of aluminum [15, 57, 58]. The nanowire can then be contacted to normal (or superconducting) electrodes to measure conductance.

In such devices, "hard" superconducting gap were obtained as one can see in figure 1.4 (a) and 1.5. A better control of the transport regime was also achieved. A side effect of this new fabrication technique is the presence, in the measured device, of a dot on the side of the nanowire that is not covered in Al. Possible influences of this dot will be discussed in the paragraph 1.3.2. Finally in Ref [58], the authors measured a ZBP of higher conductance than previous devices, up to the theoretically predicted value of $G = 2e^2/h$[15], over a range of 2 mT (before the closing of the gap at 1 T). Signature of gate jumps however blur this measurement. A trivial ABS is also measured when tuning a gate voltage, and when at zero energy it also appears stable over a range of 0.2 T before splitting.

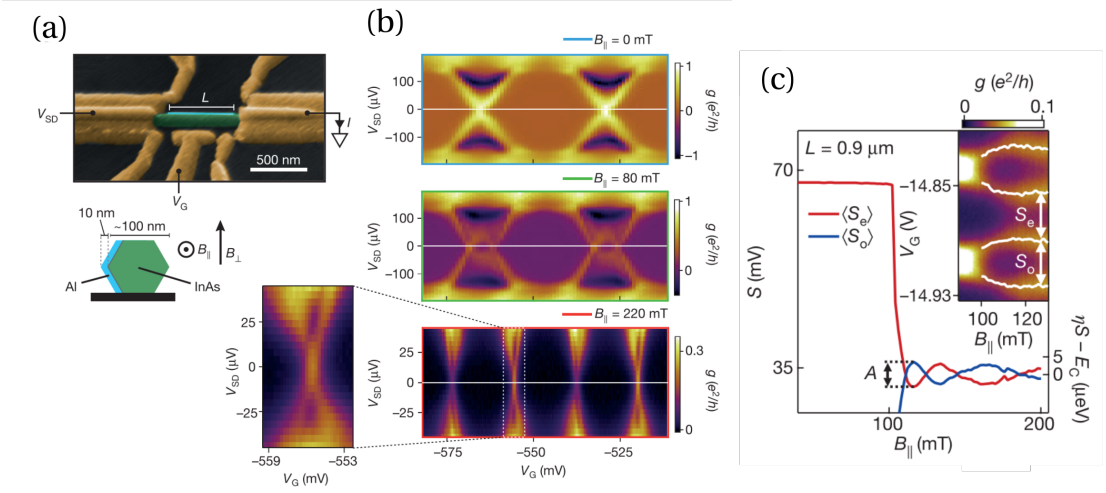

FIGURE 1.5: **Experimental results from [49] on a superconducting island**. (a): SEM image and schematics of the device. (b) Conductance map as a function of bias V_{sd} and gate V_g for three values of the external magnetic field, $B = 0$ mT, 80 mT, 220 mT (from top to bottom). The Coulomb diamond evolve from a 2e to a 1e periodicity when increasing the magnetic field. (c) Oscillations of the even-odd spacing (in gate) of the Coulomb peaks as a function of B.

Another device geometry: superconducting island

In the experiments described above, the Al shell is contacted to an electrode used for the conductance measurement. Another possibility is to leave the shell floating. Then in the island formed by the Al-covered nanowire the total charge Q is a good quantum number. One can thus observe even-odd population effects in the island: assuming the semiconductor is fully proximitized, an unpaired electron has an energy cost of Δ_{ind}. This was observed decades ago in superconducting islands [59]: the energy of a state with N electrons on a superconducting island of charging energy E_c, as a function of gate potential V_g (with gate capacitance C) is:

$$E_{N,\,\text{odd}}(V_g) = E_c\left(\frac{CV_g}{e} - N\right)^2 + E_0 \text{ if N odd} \tag{1.41}$$

$$E_{N,\,\text{even}}(V_g) = E_c\left(\frac{CV_g}{e} - N\right)^2 \text{ if N even} \tag{1.42}$$

where E_0 is the lowest energy for a quasiparticle. An external magnetic field can change the energy E_0, without affecting $E_{N,\,\text{even}}$ (apart from the effect of B on the superconductivity). In Ref [49], such an effect is observed: at $B = 0$, the measurement of Coulomb diamonds shows a $2e$ periodicity below the superconducting gap, but the energy spacing between $E_{N,even}$ and $E_{N,odd}$ reduces up to a point where a $1e$ periodicity is reached, indicating the existence of a $E_0 = 0$ quasiparticle state in the island (around $B = 200$ mT).

[15] Although several effects can supress this quantization, as will be discussed later on.

Close to this point, the authors measured E_0 (through the energy spacing between Coulomb peaks), and interpret its dependence on B and the island length L as a measure of the localization of MZM. This system was studied more in details in Ref [60, 61].

New devices and techniques

Other materials ? In the last few years various geometries have also been developed as Majorana devices: gated 2D heterostructures with InSb [62] or InAs with epitaxially grown Al [19], as well as SiGe nanowires [63].

Among theoretical proposals, the more exhaustive description of the superconductor-semiconductor system has also led to new proposals, for example in the geometry of the Al shell [64].

Additional characterization of the spectrum RF measurement were performed on epitaxially grown InAs-Al devices, in a regime where no MZM are expected, to study more in details the devices [65, 66]. These experiments' modeling is discussed in more details in reference [67].

1.3.2 Critiques of the measurements and further modeling

After the first experimental measurements, several discrepancies between the theory and experiments were put forward, as well as other possible interpretation of a ZBP [68].

The main criticisms were the following:

- The height of the conductance peak was much lower than the $2e^2/h$ expected for an N-Topological Superconductor interface (except for one device),
- The appearance of the Majorana zero energy peak was over a small magnetic field range,
- No splitting of the peak was observed, even in short devices where it was expected,
- There were no oscillations of the ZBP at high magnetic fields[16],
- There was no signature of the gap closing and reopening at the potential topological phase transition,

[16] Whereas it is expected due to the change in the coherence length of the MZM with the magnetic field [47].

- There was a high quasiparticle weight in the superconducting gap (problem of the "soft gap"): for instance in Ref [13], the ZBP emerges from a background conductance of $0.1\frac{e^2}{\hbar}$.

Although subsequent experiments worked on these issues, notably on trying to improve the superconductor-nanowire interface, some of these criticisms still hold, and additional signatures of the specificities of MZM are still looked for.

Differences between the first theoretical model and the actual experimental setup there can explain why the measurements do not accurately reproduce the theoretical predictions. A lot of theoretical work was done to try and refine the understanding of the experimental results. For example, a varying spin-orbit coupling [69], one stronger than expected [70] or Coulomb interactions [71] can explain the absence of oscillations of the MZM at high magnetic field (after the topological phase transition). A large tunnel coupling to the normal probe used to measure the conductance can reduced the height of the conductance peak, lower than the expected quantized value [72]. The large width of the measured conductance peak can be explained in a multisubband scenario [73]. The presence of multiple subbands can also blur the signal of the gap closing [74]. Finally, a smooth variation of the physical parameters, such as the confinement potential, can lead to the formation of trivial ZBP [75, 76].

We now review in some details the theoretical work that has been done to describe more accurately the actual physical implementations of a Majorana device.

Various approximations of the model compared to the real system

Actual physical realizations are usually more complex than the sum of the "recipe" ingredients, and a more complex theory is required to fully interpret the current measurements. In this section we will discuss four questions: the effect of inducing superconductivity, of multiple subbands, of Coulomb interactions, and of the neighboring dot in epitaxial devices.

First of all, in the above equation superconductivity was added as an effective induced pairing in the 1D nanoconductor, but in realistic systems it is induced by connecting the nanoconductor to a superconductor of superconducting gap Δ_s: at $E < \Delta_s$, electrons of the nanoconductor impinging on the interface are retro-reflected as holes through Andreev reflections, which induce correlations between electrons in the nanoconductor. However the strength of the induced superconducting pairing, and the impact of the interface of the characteristics of the nanoconductor must be considered.

Second, no nanoconductor is purely one-dimensional. Its cross section determines the subband spacing, which can go from the eV for carbon nanotubes (whose diameter can be smaller than 1 nm) to tens of meV for nanowires of diameter 100 nm. Hence, depending on the chosen nanoconductor, it may be hard to reach the one-subband occupancy.

Third, the electrostatic environment of the system affects the localization of the electronic wave-function. It can be either the screening effect of the different metals involved in the experimental realizations, or more simply disorder in an imperfect device.

Finally, Coulomb repulsion is present in low-dimensional systems, and can affect the emergence of MZM. Besides, when implementing the Majorana "recipe" the nanoconductor is usually coupled to one or several contacts, either superconducting (to induce superconductivity) or normal to probe the density of states of the system. If the coupling is too strong, a weak tunneling picture does not hold anymore. Many-body effects such as a Kondo peaks can be observed.

Inducing superconductivity: how to relate Δ_{ind} to Δ_s, and undesired effects

The different descriptions of the coupling between a 1D nanoconductor and a bulk superconductor is described in details in reference [35]. At first order, one can calculate proximity-induced pairing by considering the superconductor to be unperturbed by the interface to the nanoconductor. One then obtains an induced gap $\Delta_{ind} \propto \Gamma^2$ where Γ is the single-electron tunneling between the two materials (in the limit $\Delta \gg \Gamma$).

A more complete approach consists in solving the hamiltonian problem for both systems before integrating out the parent superconductor's degrees of freedom. This way, the electronic wavefunctions' extension in both system is described.

A lot of efforts have been put recently to try and improve the modeling of the nanowire-superconductor systems studied experimentally. References [77–80] performed both analytical calculations and numerical simulations[17], highlighting parasitic effects that could hinder the transition to a superconducting topological phase: renormalisation of the spin-orbit interaction when the coupling to the superconductor is strong, effect of a gate potential on the spin-orbit interaction...

On the experiments side, in reference [81] the authors showed that the confining potential can strongly affect the coupling strength between the superconductor and the nanoconductor, complicating even more the control on the emergence of MZM.

[17] Notably numerically solving in a self-consistent way both the Shrödinger and Poisson equations to describe the wavefunction localization across the 1D section for a nanowire covered by a thin superconductor.

The multisubbands case

Most realistic systems do not realize perfectly *one-dimensional* conductors; nanowires or nanotube have a certain width, and the quantization of the wave-function along this width defines conduction bands[18]. It is not always possible to tune the system in a single subband occupation regime (notably if the chemical potential is renormalized [82]). One can then wonder how the system behaves when there are N subbands occupied.

Naively, one can say that the N subbands implement N repetitions of the ideal 1D system: if N is even, the N Majoranas at each end hybridize and form $N/2$ trivial fermions; if N is odd, there is one unpaired MZM at each end.

Actually the validity of this picture depends on the energy gap between the bands. If it is not greater than Δ, there can be proximity-induced hybridation between subbands, as described in references [83–85] and reviewed in Ref [86]. In this regime, the induced superconducting gap can be greatly modified by the presence of the subbands.

Finally, the presence of multiple bands can also strongly modify the MZM signature, such as the width of the conductance peak [73].

In this regard, carbon nanotubes are very confined materials, where transport occur through four channels only (due to both the spin and valley degree of freedom). Experimentally, they can be grown and transferred on electrical circuits. Several groups have reported a very good tunability of the circuit parameters as well as the detection of a semiconducting gap[19].

Effect of disorder

Disorder in the system can be studied from two point of views: does it affect the emergence of MZM ? Can it explain the presence of trivial ZBP ?

Let us first discuss how the Majorana physics is affected. This was studied for example in Ref [88], where a 1D nanoconductor presents multiple topological and trivial regions, due for example to spatial variations in the chemical potential or in the induced superconducting pairing. In this situations several MZM can appear and overlap. However if not too many MZM are present, and there is an odd number of topological regions, the system can still exhibit a quantized ZBP in conductance. Of course, the localization length, and the possibility to do more complex operations are affected.

[18] We will assume that the width of the system is still smaller than the electronic coherence length

[19] For semiconducting CNTs, or metallic ones with a mini-gap possibly due to strain, curvature... [87].

Another question is whether other disorder-induced effect can explain the presence of a ZBP. Several works studied the effect of disorder in such devices. Disorder can give rise to constructive interferences at zero-bias appearing as ZBP in the conductance [89, 90][20], or induce pair-breaking that enables the presence of localized, low energy states near the wire end [68].

Effect of Coulomb interaction

The effect of interaction was studied in more details in references [91, 92]. They conclude that interactions tend to reduce the topological gap (which is rather intuitive, since they tend to suppress pairing). However, they also enhance the magnetization in the nanoconductor, increasing the size of the topological phase in parameter space[21].

In the regime of strong interactions, where the Kondo effect arises, it was also proposed that new signatures of MZM emerge [93–95].

A competing effect to generate a ZBP: the Kondo effect. When the coupling between a nanoconductor and its reservoir(s) is large[22], a many-body state can form between a localized electron in the conductor and the electrons of opposite spin in the fermi sea of the reservoir: this is a Kondo effect [96, 97]. It can be observed as a conductance peak at zero energy (at the energy degeneracy between the electron and the fermi energy in the reservoir). The effect requires an isolated spin and so only appear for certain occupancies of the nanoconductor.

The interplay between the Kondo effect and superconductivity was first observed in a CNT [98, 99]; depending on the values of Γ and E_c with respect to the superconducting gap Δ, the ground state of the nanowire (at the charge degeneracy point, ie at detuning $\epsilon_\delta = 0$) can be either a doublet (an unpaired electron, favored by the Kondo effect and a strong charging energy) or a singlet state (favored by superconductivity). The transition from one ground state to another, for example as a function of an external magnetic field translates as a ZBP in the transport measurement, that can extend over a certain range of gate voltage, as studied in Ref [100] (whose results are reproduced in figure 4.1 (e)).

The Kondo effect is sensitive to an external magnetic field since it requires an energy degeneracy between the two spin orientations to form the many-body state. As a

[20] This is called an anti-localization effect, and is due to the presence of spin-orbit interaction.

[21] The picture offered is that electrons can avoid the energy cost of the Coulomb repulsion by aligning their spins

[22] More precisely when $\Gamma \sim E_c \gg k_B T$, where Γ is the coupling to the leads and E_c is the charging energy

function of magnetic field, the transport ZBP will split in energy when $g\mu_B B_{ext} > k_B T_K$ where T_K is the Kondo temperature; still at low enough magnetic field the peak can appear fixed at zero energy.

This effect was measured in an InAs/InP nanowire by Lee et al. [101], showing how a ZBP could appear in a regime where MZM are not expected. They proposed that the uncertainty between Kondo and Majorana physics could be lifted by suppressing the quasiparticle weight below the superconducting gap. In a subsequent experiment, they again show the appearance of a ZBP linked to a zero-energy crossing of energy levels of the S-QD-S device [100][23].

In a later paper with InSb nanowires contacted with Nb, the transport ZBP was measured over several Coulomb blockade peaks [102], showing no even/odd distinction, excluding the Kondo effect as the source of the ZBP (for which the peak would be present in the odd diamonds only).

A similar study as the one presented in reference [99] was conducted in InSb nanowires [103] . The different types of ground states are be distinguished notably by the evolution under magnetic field; the singlet ground state splits due to lifted degeneracy.

Effect of the neighboring dot, in devices with epitaxially grown superconductor

In references [15] and [104], the authors show that a dot forms in the uncovered section of the nanowire, by detecting dot levels that they can tune in and out of resonance. The authors try to use this dot as a local "perturbation", and look for its hybridization with a potential MZM. Other works similarly studied the dot-nanowire setup, showing that the dot can be used to measure the local spin polarization of the zero-bias state [105][24], or the non-locality of the MZM in a more complex setup [106].

However, it was also shown that a trivial ABS localized in such a dot could mimic the observed peaks interpreted as MZM, even if the conductance appears to be $\frac{2e^2}{h}$ [107, 108]. The authors still put forward some ways to use the dot as a probe of the ZBP, or point out that the trivial ABS in the dot would be less robust to changes in all the system parameters (couplings, chemical potentials, magnetic field).

[23] This crossing can in theory evolve into a MZM for a longer nanconductor
[24] Thanks to Pauli spin blockade

1.3.3 Other experimental setups

In addition to the conductance measurement described above, other physical systems or other geometries were also studied. Josephson junction can be made out of topological superconductors, or alternatively using a helical weak link, and the supercurrent can have specific features as a function of the phase difference across the junction. Atomic systems, 1D chains or islands can be fabricated and their density of state locally measured using STM techniques, enabling a spatial resolution of the electronic wavefunction.

Josephson effect and phase-biased devices.

Specific signatures of MZM can be obtained in a phase-biased Josephson Junction (JJ) [6, 109]. If we consider a junction made out of two topological superconductors separated by a weak link, the current-phase relation (CPR) is distinctively different from that of a JJ made out of trivial superconductors [6]. This is due to the presence of MZM at both ends of the weak link (there are four in total, one at each end of the two topological superconductor, as shown in figure 1.6 (b)).

In a tight-binding picture (the centermost sites being $\hat{c}_{L,N}$ for the left superconductor and $\hat{c}_{R,1}$ for the right one, as represented in figure 1.6 (a)), the phase difference between the two superconductors ϕ can be integrated into the tunneling element, $t = |t|e^{i\phi/2}$. The tunnel coupling between the two superconductors is written:

$$H_J = \left(t\hat{c}^{+}_{L,N}\hat{c}_{R,1} + h.c.\right)$$

In the basis of $\hat{\gamma}_{L,i}$, $\hat{\gamma}_{R,i}$ for $i \in [1,2]$ (corresponding to the systems' 4 lowest-energy modes), it reduces to[25]:

$$H_J = \frac{it}{2}\cos\left(\frac{\phi}{2}\right)\hat{\gamma}_{1,L}\hat{\gamma}_{2,R} = t\cos\left(\frac{\phi}{2}\right)\left(n - \frac{1}{2}\right) \tag{1.43}$$

where $\hat{\gamma}_{1,L}$ and $\hat{\gamma}_{2,R}$ are the two internal MZM and n is the number operator for the corresponding fermionic degree of freedom.

As a consequence, the energy of the junction is given by

$$E(\phi) = \pm\sqrt{T}\Delta\cos(\phi/2) \tag{1.44}$$

[25] One can rapidly observe this by considering the Kitaev toy model; in the topological phase, the usual transformation (1.7) of the fermionic operator of the last/first site of the chain $\hat{c}_{1/N} = \frac{1}{2}(\hat{\gamma}_{1/N,1} - i\hat{\gamma}_{1/N,2})$ can be understood as the combination of one isolated Majorana associated with a zero-energy mode ($\hat{\gamma}_{N,2}$ or $\hat{\gamma}_{1,1}$) and half a fermion associated with a non-zero energy mode.

where $T = |t|^2$ is the normal state transmission of the junction, which gives

$$I(\phi) = \frac{-2e}{\hbar}\frac{\partial E}{\partial \phi} = \pm I_c \sin\left(\frac{\phi}{2}\right) \tag{1.45}$$

whereas the "usual" current-phase relation is $I = I_c \sin(\phi)$. Hence for a topological superconductor, the periodicity in ϕ is 4π, versus 2π for a trivial superconductor. This is called the fractional Josephson effect. Intuitively, it can be understood by the change in the charge transferred across the weak link, from $2e$ in a trivial superconductor-based JJ to $1e$ in presence of MZM. Indeed, the phase dependence appears through the tunneling element t, and the periodicity depends on which order of t appears in the spectrum.

In addition to the 4π periodic signature in the CPR, the scaling of the critical current with the normal transmission T of the junction changes from T to $\sqrt{T}$ as the superconductors become topological (still due to the change of the charge transferred across the junction) [110]. Finally, under RF-irradiation or an AC current excitation, the JJ device displays Shapiro steps. The energy spacing at which they appear (that depends on the RF excitation frequency) is expected to double in the topological case.

In realistic systems, two effects can strongly affect the detection of the fractional Josephson effect: quasiparticle poisoning (the possibility for the charge of the weak link to be subject to a charge jump) and finite size effects that hybridize the two remaining MZM at the end of the junction to the central ones. As a consequence, the 2π periodicity is recovered, but with a sawtooth-like CPR (see figure 1.6 (c)).

Experimental results In 2012, there was a first claim to have observed missing Shapiro steps in the AC Josephson effect in an 1D JJ made out of a gated InSb 2DEG covered with Nb (except at the weak link) [18]. However this first measurement could not discriminate MZM and trivial Andreev states with energy close to zero [76].

A subsequent experiment studied the photon emission of a voltage-biased Josephson junction made out of an InAs nanowire with an Al shell, the Al shell being removed locally to form the weak link. The photons were detected through photo-assisted current in a nearby detector made out of a trivial JJ [111]. The dependence of the emission peak as a function of the nanowire bias enables to distinguish between an effective charge e (for topological superconductors) or $2e$ for trivial superconductors (through the relation $e_{eff}V_{NW} = hf_{emission} = 2\Delta_{det} - eV_{det}$ where Δ_{det} and V_{det} are the superconducting gap and the voltage bias on the detector). The authors show measurement of a few devices, which they claim to tune in the topological regime by applying a magnetic field $B_c = 175 - 190$ mT depending on the device, giving effective g-factors of the order of

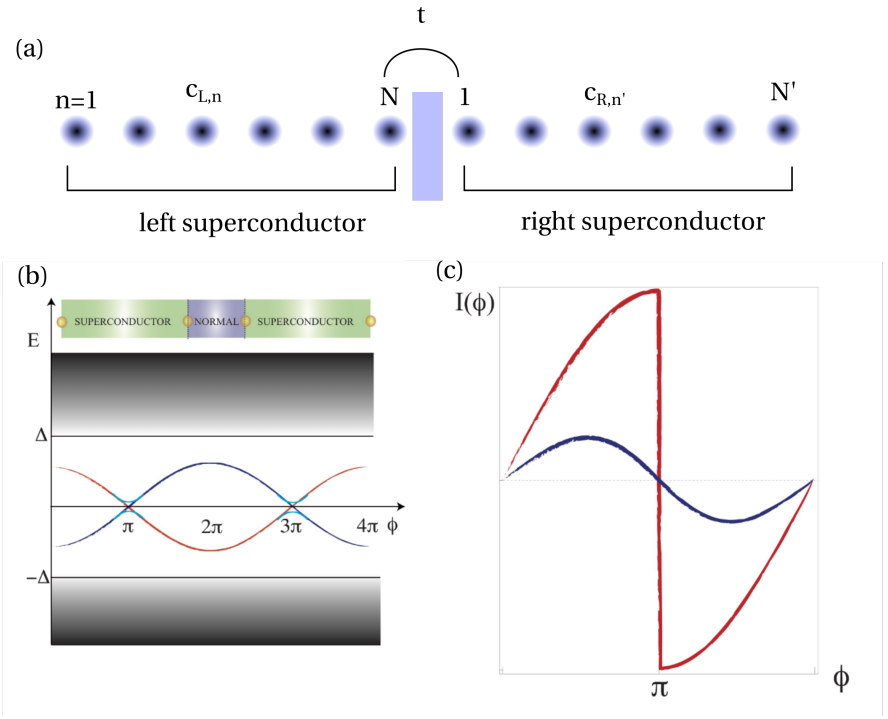

FIGURE 1.6: **Schematics and characteristics of the TS-N-TS junction.** The system consists in two topological superconductors separated by an insulating weak link. (a) Tight-binding description. (b) Schematics, showing the presence of 2 MZM at each end of the topological superconductors, as well as the low-energy spectrum of the Josephson junction containing Majorana modes as a function of superconducting phase difference ϕ (the red and blue curves denote different fermionic parities). Hybridization between the external and internal MZM due to finite size effects results in residual splittings (at $\phi = \pi$ and 3π). (c) The equilibrium supercurrent in realistic Majorana junctions is always 2π periodic, but with a sawtooth shape (red) as opposed to a sinusoid (blue) for trivial JJ. Adapted from [31].

11-35. The effect subsists over a magnetic field range of 300 mT. Finally, the onset of the effect is sensitive on the gate voltages.

Another system to potentially host MZM is a Bi nanowire. Bi nanowires can transport current through bulk states, surface states and edge states. However, it was shown that when superconductivity is induced in an S-NW-S geometry, the transport is dominated by two ballistic edge states at opposite edges of the nanowire [112]. These nanowires are expected to have a spin-orbit coupling much stronger than the other platforms, and thus to potentially host topological edge states [16].

A recent study coupled such a nanowire (contacted with W) to a microwave resonator [50]. Here the geometry of the device is slightly different since the authors do not aim at realizing a topological superconductor - weak link - topological superconductor junction, but rather a Josephson junction with a weak link that can have a helical gap, to characterize the nanowire. A signature of this helical gap is that the states are spin-momentum locked, preventing backscattering. Thus even at a finite transmission, ABS

formed in the weak link will cross in energy at a phase difference $\phi = \pi$, whereas in a normal SNS junction they would anticross.

The authors studied the dependence of the resonator resonant frequency and quality factor as a function of the flux bias across the JJ. They observe peaks in the quality factor of the resonator around a phase difference π, indicating a channel of dissipation. At this phase difference, either there are anti-crossing energy levels or protected crossing (in the helical gap). If the levels are anticrossing with an energy difference larger than that of the cavity (about 4 GHz = 16 μeV), the dissipation should disappear at low temperature, $T \to 0$, in stark contract with the observed behavior.

During the writing of this thesis, a new geometry was studied in the context of Majorana physics, labelled planar Josephson Junctions, consisting in a SQUID geometry, where the weak link in one of the JJs is made out a 2DEG with spin-orbit interaction [113–115].

Local conductance measurement

Another way to obtain a 1D conductor is to build a chain of atoms on an atomically flat surface, which is probed by scanning tunneling microscope (STM). STM gives a measure of the density of states, resolved is space and energy. The paramount advantage of this measurement technique is that it can directly measure the localization length of potential MZM, and distinguish them from excitations that are delocalized over the whole chain. Using a spin-polarized tip can give indications about the spin polarization of the state [116], while using a superconducting tip can measure the relative electron and hole weight of superconductivity-induced state. MZM are expected to have an equal electron and hole weight.

To group all the necessary ingredients, it was suggested to use a superconducting substrate with a strong spin-orbit coupling, and to use magnetic atoms to build the chain.

The magnetic moment of an individual magnetic atom over a superconducting substrate lead to the formation of bound states below the superconductor gap energy, called Yu-Shiba-Rusinov (YSR) states, and were studied for example in Mn impurities over a Pb substrate [117, 118]. When forming a chain of such magnetic atoms, these states overlap to form two electronic bands with spin-degeneracy being lifted. In such a chain, the magnetic moment of the atoms are expected to order magnetically[26]. If the magnetic atoms are not perfectly polarized, the s-wave superconductor induces p-wave like pairing

[26] Several possibilities have been discussed for this ordering, notably ferromagnetic ordering or spin helix.

terms, and the system implements a Kitaev chain[27]. As a consequence, the chain can host Majorana fermion at its ends [119–121]. Its topological phase depends on the superconducting gap, the magnetic moment of the impurities, the magnetic order and the strength of the interatomic coupling.

The first experiments studied a Fe chain over a Pd substrate displayed a ZBP at the end of the chain probed with a normal tip [20, 21], as well as a superconducting [122] and spin-polarized one [123], to get an additional signature of MZM. On the other hand, Ref [124] studied a similar setup with Co atoms instead of Mn. No ZBP is detected, which is interpreted as the possibility that the Co chain is equivalent to two Kitaev chain.

Other experiments taking advantage of the local measurement enabled by STM techniques in a 2D system studied Co islands over a Pb substrate [22, 125], or Bi crystals in contact to a Fe cluster over a Nb substrate [51].

The main limitation of these systems is the control over their fabrication and their integration in more complex devices. In the following, we will focus on the circuit experiments, probed by transport measurement.

1.3.4 Going beyond the current limitations

We have shown the current experimental results in the search for Majorana Zero Modes, with a particular focus on global conductance measurements in 1D nanowires. Some experimental signatures are consistent with the presence of such a MZM, but not all of them, whereas alternative scenarii for the emergence of a conductance zero-bias peak remain plausible. As a consequence, there is a need for a better understanding and control of the current devices under study. This can be achieved by a more realistic modeling of the devices, or by studying alternative devices, where important parameters such as the spin-orbit coupling strength do not depend on gating or tunnel coupling to the superconductor. In parallel, measurements beyond the conductance measurement are needed to characterize more fully the observed ZBP.

Need for new detection schemes. There is a continuous transition from ABS to MZM (both in field and in system length, since they control the modes overlap). As a consequence, numerous works have tried to explore this transition from "partially separated ABS" to MZM [76, 126–129] to better understand the experimental observations. The conductance measurement alone does not give an exact information on the separation

[27] Even when the magnetic atoms are fully polarized, there can be parallel spin pairing in the chain in the limit of a dense atom chain. In this limit, the YSR bands cross the fermi energy and the electronic wavefunction can partly delocalize into the superconductor thanks to spin-orbit coupling.

of the zero-energy states: depending on the probing method, it may be hard to establish how well a MZM is localized without looking at specific properties such as the non-abelian exchange statistics. This information is paramount for evaluating the potential of MZM as qubits.

More critically, in the measurements presented above not all of the expected signatures of MZM were detected, such as the closure and reopening of the excitation gap at the transition. Since numerous physical phenomena can give rise to ZBP in a system without Majorana quasiparticles, new detection methods are needed to unambiguously identify MZM.

Among the other experimental setups readily available, one could spotlight the possibility to mimic an actual Kitaev chain by building an array of quantum dots coupled to superconductors, as studied by several theory papers [130–132]. A first step in this direction is to control double or more dots with superconducting proximity effect [17].

The first advanced experiments to have been theoretically proposed involved fusion [24] or braiding of MZM, in real space using electrostatic potentials or through a series of measurements [44, 133, 134].

Several alternative methods were put forward in the literature, such as detecting the spin polarization of the MZM [105, 135], detecting the effect of the helical gap on Josephson effect [136], measuring noise characteristics [137–139], controlling the MZM hybridization with a quantum dot [46], coupling the MZM to photons in cavity [140–143].

Need for a richer fabrication toolbox. The constraint of a strong spin-orbit interaction have limited so far experimentalists to the use of a very limited number of semi-conductors, for which the naive picture of a single parabolic electronic band does not hold anymore. Numerous effects must be better understood and taken into account, such as the renormalization of the energy scales due to the coupling to the superconductor, the change of g factor and spin-orbit coupling strength with gating, the number of channels participating in transport, disorder in the interface between the nanoconductor and metallic leads or islands. In light of these complexities, experiments based on other material could give new insight into the search for MZM.

Both the study of new platforms and the observation of additional specific properties of MZM in advanced experiments would take forward the understanding of the hybrid systems used to engineer them.

Chapter 2

Synthetic SOI in a cQED architecture

We have seen in the previous chapter how one can engineer topological superconductivity by combining spin-orbit coupling, spin polarization and s-type superconductivity. We will start by discussing quickly the origin of spin-orbit coupling in section 2.1. The combination of spin-orbit coupling and polarization opens a gap in the electronic band structure where only one flavor of electron remains, called the helical gap. In this region the proximity effect reproduces a p-wave superconducting pairing. The experimental efforts so far have been focused on semiconductors with a relatively strong intrinsic spin-orbit interaction[1].

Another road to obtain a helical gap in a nanoconductor is to synthesize the spin-orbit interaction, lifting the constraint on the choice of semiconducting material. In this chapter, we will first discuss the possibility to synthesize a spin-orbit interaction using a rotating magnetic field, in section 2.2.

We will then discuss how superconductivity-induced states emerge in the nanoconductor, and how they evolve when we add the necessary ingredients for topological superconductivity in a regime slightly different than the simple one studied in 1.2. Indeed we cannot experimentally obtain a homogeneous coupling of a superconductor to our carbon nanotube over a long region, and we rather induce superconductivity "on the side". We thus theoretically investigate the effect of a superconducting contact on the side of the nano-conductor with a tight-binding formalism in section 2.3.

Finally, we discuss in section 2.4 the possibility to detect specific properties of MZM beyond the zero-bias conductance peak, by looking at the coupling of a circuit supporting MZM with photons trapped in a cavity.

2.1 Spin-orbit interaction

In the previous chapter, we have considered a 1D realisation of a topological superconductor, by combining a nanoconductor with spin-orbit interaction, induced superconductivity and a magnetic field. In the model studied in section 1.2, we have used a Rashba-type spin orbit effect [144] in the effective low-energy hamiltonian of a semiconductor. However, depending on the material under study, there can be a variety of couplings between the spin and orbital degree of freedom. We here briefly discuss the origin of spin-orbit coupling, and its possible measurement.

[1] Although they are among the materials with the strongest instrinsic spin-orbit interactions, it remains small compared to other energy scales such as the superconducting gap for example.

2.1.1 Origin of the spin-orbit coupling

Spin-orbit effect refers to a relativistic effect that changes the energy of a moving electron in a spatially varying electrostatic potential according to: $H_{so} = \frac{\hbar}{4m^2c^2}(\vec{\nabla}V(\vec{r}) \times \vec{p}) \cdot \vec{s}$ where $V(\vec{r})$ is an electrostatic potential, and m, $\vec{r}$, $\vec{p}$, $\vec{s}$ are the mass, position, momentum and spin of the electron (this term is derived from the Dirac equation, in a non-relativistic approximation called the Pauli equation).

In atomic physics, $V(\vec{r})$ is the electrostatic potential of the atomic core, and the energy levels of the electrons bound to the atoms are deeply modified by this effect; this is called the Pauli spin-orbit interaction. On the other hand, in semiconductor physics, the electrostatic confinement is integrated in the formation of the bands. H_{so} then results in an energy term that lifts the spin degeneracy without an external magnetic field (at $B = 0$)[2] in the low-energy effective model for the "free electrons" of a given semiconductor [145]. This term is called the spin-orbit coupling. Since it is still related to the atomic potential, it is more important in materials made out of heavy atoms.

For a crystalline lattice that is symmetric in space and time, electronic and hole states are spin degenerate (space reversal transforms $\vec{k}$ in $-\vec{k}$ whereas time additionally flips the spins, giving $E_+(k) = E_-(k)$). This degeneracy can be lifted by a magnetic field that breaks time reversal symmetry, or alternatively at $B = 0$ by breaking the space inversion symmetry. The band structure then acquires a texture in spin that can depend on the wave-vector k[3].

The space inversion symmetry is broken when the lattice structure of the crystal forming the considered semiconductor is asymmetric, for example for the zinc blende structure; this is called bulk inversion asymmetry (BIA) or Dresselhaus term in the specific resulting hamiltonians. In semiconducting heterostructure or confined structures such as quantum wells, an asymmetry of the confinement potential can also lift the spin degeneracy; it is called structure inversion asymmetry (SIA), or Rashba term (in the hamiltonian). In the same idea, external electric field can also give rise to spin-orbit coupling. InSb and InAs, which were discussed in subsection 1.3, have such both a BIA and a SIA emerging from a confining potential without rotational symmetry. The corresponding Dresselhaus term is often neglected, being lower than the Rashba term.

These terms are derived in most semiconductors by integrating the spin-orbit interaction at the level of the band structure. In lower dimension systems such as carbon nanotubes, one can already take into account the different orbitals at the level of the base atom (that have different orbital momenta $\vec{L}$) when calculating the band structure. The coupling

[2] And without breaking the time-reversal symmetry.
[3] As is the case for example for the Rashba wire studied in Chapter 1.

between the electronic spin and this angular momentum gives rise to the energy term $H_{so,atomic} = \Delta_{so,atomic}\vec{L}\cdot\vec{S}$ (this is the Pauli spin-orbit interaction mentioned before). It can in turn lead to a new spin-orbit coupling, depending on how the atomic orbitals couple to form the bulk conductor: In CNTs for example, the rolling of the graphene sheet enables the coupling of different orbitals in neighboring atoms, yielding a stronger spin-orbit interaction than in graphene.

External factors can also induce a spin-orbit interaction in the material: curvature or strain in the material (studied experimentally in a CNT in [146]), external electric fields [147], or non-collinear magnetic fields [148] as we will discuss later on. The orbital effect of a large external magnetic field can also modify the spin-orbit coupling [149].

Finally, in a hybrid system such as a nanoconductor in contact with another material, the bare values of the spin-orbit coupling is renormalized by the leakage of the electronic wave-function in the other material [78–80]. In return, one can induce spin-orbit coupling by "proximity effect" in a material with no intrinsic spin-orbit interaction (SOI).

To conclude, the spin-orbit interaction present in the low-energy hamiltonians of semiconductors has various sources, but can be usually traced back to an asymmetry in an electric field felt by the electrons.

2.1.2 Spin-orbit coupling in CNTs

In the rest of the thesis, we present experimental results on carbon nanotubes (CNTs) based circuits. Spin-orbit coupling strength in the specific case of a CNT was discussed in several papers (see the review [150]). References [151] and [152] (among others) present tight-binding calculations to study the effect of the atomic spin-orbit effect[4]. In reference [147], the effect of an external electric field perpendicular to the CNT is also included, giving rise to a spin polarization perpendicular to the applied field (as expected for an electric-field induced spin-orbit coupling).

The conclusion is that spin-orbit coupling depends on the diameter of the carbon nanotube, its chirality and on the electronic density. There is (at least) two effective terms that shift the energy bands of the spin, with a shift dependent on the valley degree of freedom [150]. The spin-orbit coupling partially lifts the four-fold degeneracy at zero-magnetic field[5].

By looking at the dispersion of excited states in the single electron regime [153, 154] or successive energy levels [155], previous experiments estimated spin-orbit couplings of

[4] In carbon nanotube, the rolling of the graphene flake couples different p orbitals of carbon, giving rise to an atomic spin orbit coupling that is absent in graphene.

[5] The Kramers pair K,s and -K,-s stay degenerate

the order of a few hundreds of μeV (mainly for the first electronic levels; the effect is expected to be reduced at large filling factor). Reference [155] has reported values as high as the meV, higher than expected by the various modelings. These experimental results are summarized in table II of reference [150].

2.1.3 Measurement of the spin-orbit coupling

Beyond theoretical predictions, it is convenient to experimentally measure the spin-orbit coupling. In this regard, bulk values for semiconducting materials have been the subject of extensive study. Chapter 6 of Ref [145] provide several references. However in nanowires or patterned 2DEG made out of semiconductors, the spin-orbit interaction strength vary from the bulk value (at least due to the change in the confinement potential), and has to be measured for each specific geometry.

Among the possible detections that were used in 2D or 3D semiconductors, optical measurements are still available in reduced dimensions (such as Raman spectroscopy [156]). Weak antilocalization and Shubnikov-de-Hass oscillations, however, are mechanisms that depend on the spin-orbit interaction but can only be observed in 2D systems[6]. Another way to measure spin-orbit coupling in 1D systems is by transport spectroscopy of a confined ballistic segment of conductor, in the Coulomb blockade regime. It was used in a carbon nanotube-based quantum dot as shown in the previous paragraph.

Among recent experiments, spectroscopic measurement of an InAs wire inside a microwave spectrometer was also used to extract a value for E_{so} of $E_{so} = 24$ μeV [65] or for a coupling strength of $\alpha_{so} = 32 - 38$ meV $\times$ nm [66].

More indirectly, Bommer *et al.* [157] studied the evolution of a superconducting gap with a InSb nanowire-based device under a magnetic field. They observe a very different behavior depending on the orientation of the field, which can be traced back to the axis of the spin-orbit coupling and its strength. They point out that the spin-orbit axis depends on the gating of the device and its geometry, with extracted value in the range $\alpha_{so} = 15 - 35$ meV $\times$ nm.

One could also hope to detect the helical gap in the band structure of the nanoconductor [158]. This is what is claimed to be done in Ref [159], however the spin-orbit energy extracted is much higher than expected for the material (6.5 meV for an InSb nanowire), which is not understood.

[6] Or disordered wires with a finite section for weak antilocalization, which is not the regime sought-after.

2.2 Magnetic texture with a semiconductor

As mentioned above, spin-orbit coupling emerges due the atomic electric field, converted in a magnetic field in the moving frame of the electron. One can show that a spin-orbit coupling is equivalent to an oscillating magnetic field [160][7]. Given that, there are several ways to synthesize such an interaction: one can apply a spatially dependent electric or magnetic field, or rely on an RKKY interaction.

In general, the electric field required to induce spin-orbit interaction needs to be both strong and inhomogeneous over a short length, making it experimentally challenging to realize: Ref [161] gives for example a value of 50 V/300 nm to enhance the spin-orbit interaction of a graphene sheet by a factor 7. In the same idea, atomic-scale "impurities" can be used to create fast varying electrical fields; this was done experimentally with gold atoms below graphene [162]. Finally, in certain situations an electric field can have a stronger effect than expected with this simple picture, as was shown theoretically in Ref [163] for SiGe nanowires, and measured through magneto-conductance in Ref [164, 165]. However it would be challenging experimentally to tune simultaneously the chemical potential and the spin-orbit interaction strength with gate voltages.

A magnetic field oscillating in space is another possibility to induce spin-orbit interaction. It can either be generated by localized magnetic moments that order through the Ruderman-Kittel-Kasuya-Yosida (RKKY) mecanism, thanks to their coupling to conduction electrons. This was studied both in atomic chains [119, 121, 166] and in ^{13}C carbon nanotubes [167, 168]. Or it can be the stray field of a nearby magnetic material (either a ferromagnet with domains, an array of magnets or an array of magnetic tunnel junctions) [148, 169–173].

In the experiments conducted during this thesis, the last option was chosen and our nanoconductor was placed in proximity to a ferromagnetic material presenting magnetization domains. An interesting aspect of this choice is that one can in theory control the domains and thus the effective spin-orbit interaction, either by applying a magnetic field or by flowing a current through the ferromagnet [174].

2.2.1 Effect of a magnetic field oscillating in space

In this section, we will present how a magnetic field oscillating in space implements a synthetic spin-orbit interaction in a 1D nanoconductor, first considering a parabolic dispersion relation for the electrons and then with the low-energy hamiltonian of a CNT.

[7] In addition to a constant magnetic field, so that time-reversal symmetry is not broken. This is more evident when considering the transformation presented in section 2.2.1.

Calculation

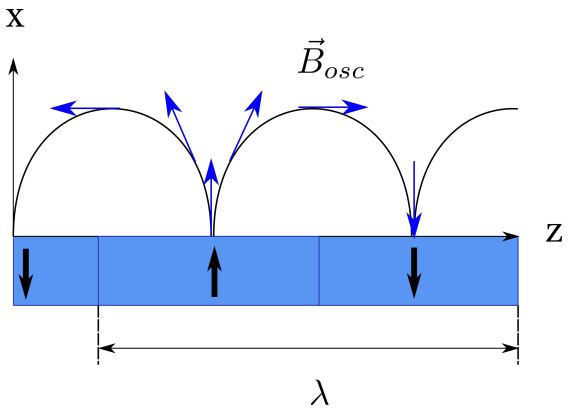

FIGURE 2.1: **Schematics of a magnetic texture's stray field** Oscillating magnetic field considered in the calculation. For a succession of domains (or nanomagnet, drawn in blue), the field lines follow the black curve. At a given altitude x (close to the surface), one can in first approximation consider that the amplitude of the oscillating field B_{osc} is constant along z, with an oscillation of its direction. The period of this oscillation is λ, corresponding to two domains/magnets with opposite magnetization.

Let us consider a 1D semiconductor along the z direction, subject to a space-dependent magnetic field $\vec{B}(z)$. For simplicity, we take a parabolic dispersion relation, following Ref [170].

Defining $\cos(\Phi) \equiv \frac{\vec{B}\cdot\vec{z}}{B}$ and $\hat{s}_{xy} \equiv \frac{(\vec{B}\times\vec{z})\cdot\vec{s}}{\|\vec{B}\times\vec{z}\|}$,

$$H = \left(\frac{\hat{p}_z^2}{2m} - \mu\right)\hat{\tau}_z + \frac{1}{2}g\mu_B\vec{B(z)}\cdot\vec{\hat{s}} + \Delta\hat{\tau}_x \tag{2.1}$$

can be transformed to $\tilde{H} \equiv UHU^\dagger$ with

$$U \equiv e^{i\Phi\hat{s}_{xy}/2} = \cos(\Phi/2) + i\hat{s}_{xy}\sin(\Phi/2), \tag{2.2}$$

with the following effect:

$$\vec{B(z)}\cdot\vec{s} \to \|B\|\hat{s}_z \tag{2.3}$$

$$\frac{\hat{p}_z^2}{2m}\hat{\tau}_z \to \frac{\hat{p}_z^2}{2m}\hat{\tau}_z - \frac{\hbar^2}{2m}U^\dagger\partial_z^2 U\hat{\tau}_z - \frac{i\hbar}{m}U^\dagger\partial_z U\hat{p}_z\hat{\tau}_z \tag{2.4}$$

For a helical field as shown in Figure 2.1, we have more precisely

$$\vec{B} = (-B_{osc}\sin(\Phi),\, 0,\, B_{osc}\cos(\Phi))^T \text{ with } \Phi = \frac{2\pi z}{\lambda} \tag{2.5}$$

hence $\hat{s}_{xy} = -\hat{s}_y$, $\partial_z U = \frac{-i\pi}{\lambda} U \hat{s}_y$, and

$$\tilde{H} = \left[\frac{\hat{p}_z^2}{2m} - \mu + \frac{\hbar^2}{2m} \left(\frac{\pi}{\lambda} \right)^2 \right] \hat{\tau}_z + B_{osc} \hat{s}_z + \frac{h}{2m\lambda} \hat{p}_z \hat{s}_y \hat{\tau}_z \tag{2.6}$$

$$= \left(\frac{\hat{p}_z^2}{2m} - \mu + \frac{E_{so}}{2} \right) \hat{\tau}_z + B_{osc} \hat{s}_z + \frac{\alpha}{\hbar} \hat{p}_z \hat{s}_y \hat{\tau}_z \tag{2.7}$$

We thus see that the oscillating magnetic field is equivalent to *both* a constant Zeeman effect of amplitude B_{osc} and a synthetic spin-orbit interaction with perpendicular quantization axes. The spin-orbit coupling strength is

$$\alpha = \frac{\pi h^2}{m\lambda}, \tag{2.8}$$

the corresponding spin-orbit energy being $E_{so} = \frac{m\alpha^2}{\hbar^2} = \frac{h^2}{4m\lambda^2}$[8]. The synthetic spin-orbit interaction also shifts the chemical potential to $\tilde{\mu} = \mu - E_{so}/2$, which in turns shifts the position of the helical gap in energy.

Both spin-orbit terms (those containing the term α) can actually be combined into a simple spin-dependent shift of the wave-vector k by $k_{so} = \frac{\alpha m}{\hbar^2}$, so that the hamiltonian (2.7) factorizes into:

$$\tilde{H} = \left[\frac{1}{2m} \left(\hat{p}_z + \frac{\alpha m}{\hbar} \hat{s}_y \right)^2 - \mu \right] \hat{\tau}_z + B_{osc} \hat{s}_z \tag{2.9}$$

The specific case of carbon nanotubes

We now consider the effect of a rotating magnetic field for the band structure of a carbon nanotube. A strength of carbon nanotubes is their relative simplicity (in terms of geometry), allowing calculations of their band structure. In addition, CNTs are a almost perfectly one-dimensional nanoconductors; their strong lateral confinement enables measurements where four conduction channels only participate in transport.

Several theory papers have already studied the specific case of carbon nanotubes for the emergence of topological properties, relying on a strong electric-field- or curvature-induced spin-orbit interaction [175, 176], or a strong intrinsic one, combined with a very large magnetic field, in ref [177]. For such systems, the valley degeneracy must be lifted to reach a regime with MZM.

The specific influence of a spatially varying magnetic field was studied in Ref [171]. In addition to generating a strong spin-orbit coupling, the rotating magnetic field breaks

[8] Note that for $\lambda \leq k_F$, this description falls short. This situation is described for example in Ref [160].

the K-K' degeneracy through its orbital effect. The authors show specific phase diagrams (depending on the chirality of the CNT and the spatial dependence of the field) where MZM can be obtained in the system by solving numerically the hamiltonian.

In the case of the helical field that we consider, its effect is equivalent to the following terms in the hamiltonian (written in spinor notation, with σ, s, τ, η the Pauli matrices operating in A/B sublattice, spin, electron-hole and K/K' valley space):

- A Zeeman effect on the spin: $g\mu_B B_{osc}\hat{s}_z$
- An orbital Zeeman effect $\propto \hat{\eta}_z\hat{\sigma}_x\hat{\tau}_z$
- An effective spin-orbit:

$$\delta_{so}\hat{\sigma}_y\hat{s}_x\hat{\tau}_z \text{ with } \delta_{so} = \frac{hv_F}{2\lambda} \tag{2.10}$$

We can compare the effective spin-orbit term with the kinetic energy term in the CNT hamiltonian, $\hbar v_F k\hat{\sigma}_y\hat{\tau}_z$, and see that in this case again the spin-orbit part of the transformation is equivalent to a shift of the k wavevector, by $k_{so} = \frac{\delta_{so}}{\hbar v_F}$.

Comparison of both calculations

We can wonder to which extend one can compare the energy scales for the spin-orbit interaction in the two situations of a linear or a parabolic dispersion relation. We have seen that in both cases the helical magnetic field is equivalent to a Zeeman effect and a spin-dependent shift of the wave-vector:

- $k_{so} = \frac{\delta_{so}}{\hbar v_F}$ for the linear case,
- $k_{so} = \frac{\alpha m}{\hbar} = \frac{\sqrt{mE_{so}}}{\hbar}$ for the parabolic one.

It is certain that E_{so} and δ_{so} are not equivalent. However, we can look at how they relate around the helical gap.

To compare the effect of the spin-orbit coupling in both calculations one can look at the resulting dispersion relation. In the model with parabolic dispersion relation, the bands are given by equation (1.26) with the replacement $\mu \to \tilde{\mu} = \mu - \frac{E_{so}}{2}$:

$$E^{\pm}(k) = \frac{\hbar^2 k^2}{2m} - \mu + \frac{E_{so}}{2} \pm \sqrt{(\alpha k)^2 + E_z^2} \tag{2.11}$$

For simplicity, in the linear dispersion relation case (CNT), we place ourselves in the situation $\Delta_{KK'} = 0$ so that the two valleys are degenerate, and we neglect both the Zeeman and the orbital effect of the field since we want to compare the spin-orbit terms.

The nanotube Hamiltonian then reads [171]

$$H_{CNT} = (\hbar v_F k \hat{\sigma}_y + E_g \hat{\sigma}_x - \mu + \delta_{so} \hat{\sigma}_y \hat{s}_y)\, \hat{\tau}_z, \tag{2.12}$$

which gives the dispersion relation:

$$E_{\sigma,s}(\kappa) = \sigma \sqrt{(\hbar v_F \kappa - s\delta_{so})^2 + E_g^2} - \mu \tag{2.13}$$

Note that here κ denotes the component parallel to the nanotube of the vector $\delta\vec{k} \equiv \vec{k} \pm \vec{K}$ with $\pm\vec{K}$ the wavevector at the K/K' points of the nanotube (the perpendicular component is quantized due to the boundary condition imposed by the rolling of the tube). The Fermi velocity is noted v_F.

First let us consider a semi-conducting carbon nanotube. Close to the bottom of the band, $\hbar v_F \kappa - s\delta_{so} \ll E_g$:

$$E_{+,s}(\kappa) \sim E_g + \frac{1}{2E_g}((\hbar v_F \kappa)^2 + \delta_{so}^2 - 2s\hbar v_F \kappa \delta_{so}) - \mu \tag{2.14}$$

This dispersion relation is equivalent to the parabolic one (equation (2.11)), with the matching

$$\alpha \leftrightarrow \frac{\hbar \delta_{so}}{m^* v_F},\ E_{so} \leftrightarrow \frac{\delta_{so}^2}{E_g} \text{ with } m^* \equiv \frac{E_g}{v_F^2} \tag{2.15}$$

Applying this matching to equation (2.8), that relates α to the field period λ (for free electrons) is in agreement with equation (2.10) that relates δ_{so} to λ (for the CNT).

Then we consider a metallic carbon nanotube, with the dispersion relation

$$E_{\sigma,s}(\kappa) = \sigma \hbar v_F \kappa - \mu + s\delta_{so} \tag{2.16}$$

We note k_{so} the Fermi wave-vector at the bottom of the band (for the nanotube, it is the Fermi wave-vector where the band cross $E = 0$), and we compare the dispersion relation close to the bottom of the band:

- For the parabolic dispersion, $k_{so} = \pm\frac{m\alpha}{\hbar^2} = \pm\frac{\pi}{\lambda}$
  and $E_s(k_{so} + q) \sim \frac{E_{so}}{2} - \tilde{\mu} + sE_{so} + \alpha q(1 + s) = E_{so} - \mu + sE_{so} + \alpha q(1 + s)$
- For the linear dispersion, $k_{so} = \sigma\frac{\delta_{so}}{\hbar v_F} = \sigma\frac{\pi}{\lambda}$
  and $E_{+,s}(k_{so} + q) = \delta_{so} - \mu + s\delta_{so} + \hbar v_F q$ (upper band)

We see that the spin-orbit energies defined in both situations, $E_{so} = \frac{m\alpha^2}{\hbar^2}$ and $\delta_{so} = \frac{hv_F}{2\lambda}$ are equivalent in the two dispersion relations at the bottom of the band. To push the

comparison, one has to express the Fermi velocity in the parabolic case $v_F = \frac{1}{\hbar}\frac{dE}{dk}|_{k\sim k_{so}} = \frac{\hbar}{m}(k + sk_{so})$. Around the bottom of the band, we can roughly say that it will be of the order of $v_F \sim \frac{\hbar k_{so}}{m}$. Then again, both transformations of the rotating field are in agreement, with this time the equivalence

$$E_{so} \leftrightarrow \delta_{so} \tag{2.17}$$

Finding the gap

We have studied above the transformation of an helicoidal magnetic field for both a linear and a parabolic dispersion relation. It is equivalent to a spin-dependent shift in the electron wave-vector, and a Zeeman effect.

Compared to the effective hamiltonian studied in section 1.2, the band structure evolves differently with the spin-orbit strength (evidenced by the shift in the chemical potential coming from the transformation: $\mu \to \mu - E_{so}$, in the parabolic case). As a consequence, the opening of the helical gap does not occur around $E = 0$, but is shifted in energy. One can note that the situation is different in the case of the RKKY: since the magnetic order emerges due to an interaction with the electrons, it is directly tuned at a period $1/k_F$ and the gap opens around the Fermi energy [168].

The amplitude of the synthetic spin-orbit interaction does not, in itself, depend on the amplitude of the oscillating magnetic field, which can appear surprising. However, in the limit of $B_{osc} \to 0$, the helical gap in the dispersion relation goes to zero. There remains the spin-depend shift in the wavevector k, but it has no physical consequence. Indeed, in this case ($B_{osc} = 0$), we can simply reverse the unitary transformation given by equation (2.2), and we get back a simple degenerate parabolic band, without any shift nor oscillating field. In the end this synthetic effect is effective as long as temperature does not close the helical gap.

The condition for the opening of a gap in a graphene nanoribbon (similar to that of a CNT), in the limit E_z, $\Delta_{KK'} < \delta_{so}$ is given by (Ref. [148]):

$$k_B T < E_z \text{ for a semiconducting nanoribbon} \tag{2.18}$$

$$k_B T < \frac{\Delta_{KK'} E_z}{\delta_{so}} \text{ for a metallic one.} \tag{2.19}$$

This second line is due to the fact that in the metallic case, the K/K' degeneracy needs to be lifted for a helical gap to appear, as noted above.

Effect of disorder, or other spatial dependences for the magnetic fields

In the previous sections, we described the effect of an ideal oscillating magnetic field, with a periodic spatial modulation described by equation (2.5), for two different dispersion relation. However in the experiments, the shape of the magnetic field may deviate from this ideal case.

The effect of deviations can be studied in two ways. In some theory paper, a weak disorder was considered: in Ref [148] it is shown that for rotating magnetic field or linearly oscillating field (in one direction only), disorder has little effect since from Fourier decomposition, each period opens a gap at slightly detuned chemical potential. One just needs a sufficient weight of the Fourier component at a given frequency.

Ref [178] studied the effect of disorder in a different setup, the one of the atomic chain. The magnetization of each atom is random with a given correlation strength between neighboring atoms. It is shown that changing the correlations between atoms does not suppress the topological regime but rather alters the phase diagram (as long as they are not completely aligned).

On the other hand, one can also study numerically the effect of a realistic experimental magnetic field, as was done in references [170, 173, 174]. In the latter paper, the authors studied several magnet configurations over a gated defined Si nanowire in a 2DEG (with low g-factor $g = 2$), and tried to optimize the induced topological gap over the possible configurations. They compared the optimal configurations with an ideal helical field, yielding similar amplitudes for the topological gap. They finally studied the effect of disorder in physical implementations for the most promising geometries.

2.2.2 Oscillating magnetic field in a finite system, with the scattering formalism

One could also wonder how the equivalence found in the previous section holds in a finite size system. A convenient formalism to re-express the problem is the scattering formalism, which enables us to discretize the space into segments of constant magnetic orientation, forming an angle $\theta(z)$ to the vertical axis. The amplitude of the magnetic field is constant along the system.

Let us calculate the transfer matrix of the interface between two such segments, as pictured in Figure 2.2(a). It relates the wave-functions in the left and right region, ψ_L and ψ_R, written in the spin up/down basis. The wave-functions can be written as:

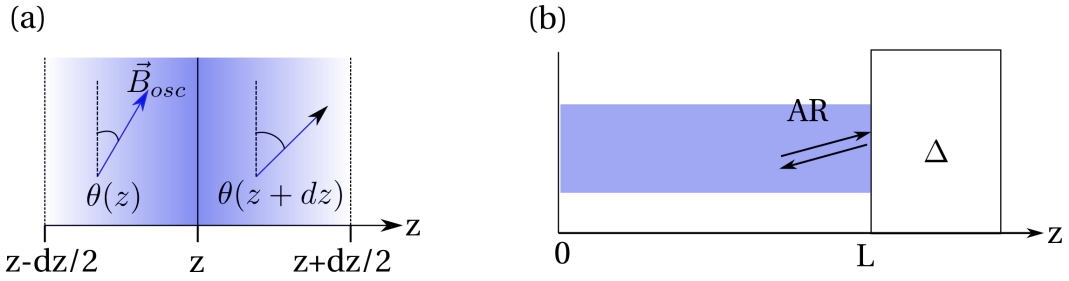

FIGURE 2.2: **Support for the scattering calculation** (a) Schematics of the "unit cell" used to describe the magnetic texture in scattering formalism. (b) Finite size effects can then be taken into account by adding two interfaces around a segment of texture of size L, for example here a hard wall on the left, a superconductor of gap Δ on the right. With a superconducting interface, electron are subject to Andreev reflections (AR) at the interface.

$$\psi_L(z) = \frac{1}{\sqrt{k_\uparrow}} \begin{pmatrix} \cos[\theta(z)] \\ \sin[\theta(z)] \end{pmatrix} \left(A e^{ik_\uparrow z} + B e^{-ik_\uparrow z} \right) + \tag{2.20}$$

$$\frac{1}{\sqrt{k_\downarrow}} \begin{pmatrix} -\sin[\theta(z)] \\ \cos[\theta(z)] \end{pmatrix} \left(C e^{ik_\downarrow z} + D e^{-ik_\downarrow z} \right) \tag{2.21}$$

$$\psi_R(z) = \frac{1}{\sqrt{k_\uparrow}} \begin{pmatrix} \cos[\theta(z')] \\ \sin[\theta(z')] \end{pmatrix} \left(A' e^{ik_\uparrow z} + B' e^{-ik_\uparrow z} \right) + \tag{2.22}$$

$$\frac{1}{\sqrt{k_\downarrow}} \begin{pmatrix} -\sin[\theta(z')] \\ \cos[\theta(z')] \end{pmatrix} \left(C' e^{ik_\downarrow z} + D' e^{-ik_\downarrow z} \right) \tag{2.23}$$

where $z' = z + dz$ and $k_{s=\uparrow,\downarrow}$ are the wave-vectors associated with spin up and down, independent of the orientation of the magnetization.

Defining the following matrices:

$$R(\theta) = \begin{pmatrix} \cos(\theta/2)/\sqrt{k_\uparrow} & -\sin(\theta/2)/\sqrt{k_\downarrow} & \cos(\theta/2)/\sqrt{k_\uparrow} & -\sin(\theta/2)/\sqrt{k_\downarrow} \\ \sin(\theta/2)/\sqrt{k_\uparrow} & \cos(\theta/2)/\sqrt{k_\downarrow} & \sin(\theta/2)/\sqrt{k_\uparrow} & \cos(\theta/2)/\sqrt{k_\downarrow} \\ \cos(\theta/2)\sqrt{k_\uparrow} & \sin(\theta/2)\sqrt{k_\downarrow} & -\cos(\theta/2)\sqrt{k_\uparrow} & \sin(\theta/2)\sqrt{k_\downarrow} \\ \sin(\theta/2)\sqrt{k_\uparrow} & \cos(\theta/2)\sqrt{k_\downarrow} & -\sin(\theta/2)\sqrt{k_\uparrow} & -\cos(\theta/2)\sqrt{k_\downarrow} \end{pmatrix} \tag{2.24}$$

$$\text{and } S(dz) = \begin{pmatrix} e^{ik_\uparrow dz} & 0 & 0 & 0 \\ 0 & e^{ik_\downarrow dz} & 0 & 0 \\ 0 & 0 & e^{-ik_\uparrow dz} & 0 \\ 0 & 0 & 0 & e^{-ik_\downarrow dz} \end{pmatrix},$$

the continuity of the wave-function and its derivative yields the transfer matrix τ for the segment, with

$$\tau(z, dz) = S\left(\frac{dz}{2}\right) R^{-1}[\theta(z+dz)] R[\theta(z)] S\left(\frac{dz}{2}\right). \tag{2.25}$$

This transfer matrix contains the propagation through the two short segments represented in figure 2.2 (a) and the rotations corresponding to the change in the field axis. One can now establish the differential equation followed by τ [179]:

$$\frac{d\tau}{dz} = \left(i\kappa + \frac{d\theta}{dz}\frac{\mathcal{A}}{4}\right)\tau(z) \tag{2.26}$$

with the notations

$$\mathcal{A} = \frac{1}{\sqrt{k_\uparrow k_\downarrow}} \begin{pmatrix} 0 & k_\uparrow + k_\downarrow & 0 & k_\uparrow - k_\downarrow \\ -(k_\uparrow + k_\downarrow) & 0 & k_\uparrow - k_\downarrow & 0 \\ 0 & k_\uparrow - k_\downarrow & 0 & k_\uparrow + k_\downarrow \\ k_\uparrow - k_\downarrow & 0 & -(k_\uparrow + k_\downarrow) & 0 \end{pmatrix} \tag{2.27}$$

$$\kappa = \begin{pmatrix} k_\uparrow & 0 & 0 & 0 \\ 0 & k_\downarrow & 0 & 0 \\ 0 & 0 & -k_\uparrow & 0 \\ 0 & 0 & 0 & -k_\downarrow \end{pmatrix} \tag{2.28}$$

For a constant variation of the magnetization angle, $\frac{d\theta}{dz} \equiv k_\alpha$, over a section of nano-conductor of length L, this equation yields

$$\tau(L) = \exp\left(i\kappa L + k_\alpha \frac{\mathcal{A}}{4} L\right) \tag{2.29}$$

Now that we have calculated this transfer matrix, we can terminate the conductor subject to an oscillating field by two potential barrier, or by superconducting contacts and calculate the transmission of such a confined structure (the details are given in appendix B). This is what we will study below, but first we will compare the scattering calculation and the unitary transformation of section 2.2.1.

Link to the unitary transformation

To recover the calculation for an infinite system, one can diagonalize this transfer matrix and obtain the "equivalent" dispersion relation of the system (equivalent to moving to

the rotating frame in the unitary transformation). As in the previous section, we consider a parabolic dispersion relation:

$$k_{s=\pm1} = \sqrt{\frac{2m}{\hbar^2}(E + \mu + s\frac{1}{2}g\mu_B\|B_{osc}\|)} \tag{2.30}$$

The four eigenvalues of $\kappa + k_\alpha \frac{A}{4i}$ are

$$k^{\pm}_{s=\pm1} = \pm\sqrt{\frac{2m}{\hbar^2}\left(\frac{E_{so}}{2} + E + \mu + s\sqrt{2(E+\mu)E_{so} + \left\|\frac{1}{2}g\mu_B B_{osc}\right\|^2}\right)} \tag{2.31}$$
$$\text{with } E_{so} = \frac{\hbar^2 k_\alpha^2}{4m}.$$

We recognize the wave-vectors associated with a system with both spin-orbit coupling and constant Zeeman (compared to the notations of section 1.2, here $k_\alpha = 2k_{so}$), where the dispersion relation is:

$$E_\pm(k) = \frac{\hbar^2 k^2}{2m} - \mu + \frac{E_{so}}{2} \pm \sqrt{\left(\frac{1}{2}g\mu_B B_{osc}\right)^2 + \frac{\hbar^2 k^2}{m}E_{so}} \tag{2.32}$$

An energy gap of size $g\mu_B B_{osc}$ opens at $k = 0$ for $\mu - \frac{E_{so}}{2} = 0$.

2.2.3 Different regimes with the scattering formalism

We have shown how a magnetic field rotating in space, and more specifically a helicoidal field along a nanoconductor is equivalent to both a Zeeman effect and a synthetic spin-orbit interaction for the electronic bands. We now move on to a concrete discussion of which transport measurement could reveal such a synthetic spin-orbit effect.

Transmission as a function of the chemical potential

A first idea could be to directly measure the helical gap in the band structure of our nano-conductor. The associated measurement is illustrated in figure 2.3.

In this figure, we plot the transmission of a segment of nanoconductor with a helicoidal magnetic field $\vec{B}_{osc}$, confined by two barriers (of equal transmission t for simplicity) as sketched in panel (a). The parameters are the length of the conductor L, the chemical potential μ, the amplitude B_{osc} of the oscillating field and the total rotation θ of the field over L (see appendix B for the exact formula, and the definition of the reduced units k, L and b_{osc}). The infinite nanoconductor would have a dispersion relation of

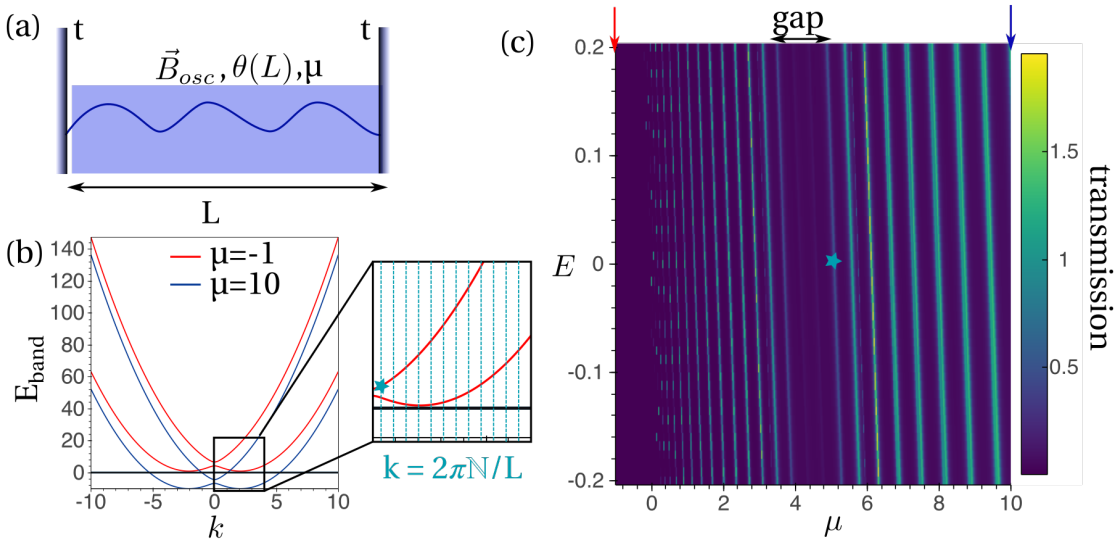

FIGURE 2.3: **Detection of the helical gap in the transmission as a function of μ.** (a) Schematics of the system studied, with represented the conductor of length L, chemical potential μ, subject to an helicoidal field $\vec{B}_{osc}$ of total rotation $\theta(L)$, confined by two barriers of transmission t. (b) Equivalent band structure, at $\mu = -1$ (in red) and $\mu = 10$ (in blue, as shown by the arrow in panel (c)). The black line indicates the level $E = 0$. Insert: discretization of the band structure in a confined structure of length L. The first level of the upper band is identified by a star, and related to a transmission peak in (c). (c) Transmission of the segment subjected to a helicoidal field, as a function of the energy E and chemical potential μ. Looking at the transmission at energy $E = 0$, we can see the bottom of the bands at $\mu = 0$, and a reduction of conductance around $\mu = 5$, corresponding to the position of the helical gap. The reduced parameters for this plot are $L = 25$, $b_{osc} = 1.2$, $\theta = 4.2$, $t = 0.3$.

E_{band} given by equation (2.32), represented in panel (b), whereas in a finite size system the wavevector k is quantized (as represented in the insert by the dashed blue lines).

We can see in panel (c) the transmission signal, that reveals the resonant levels emerging in the confined structure. The helical gap in the band structure is noticeable by the reduction of the transmission around $\mu = 5$. In the experiments, such a reduction will be measurable if the level spacing in the system is smaller than the width in energy of the gap. The effect is thus more easily visible in long ballistic devices, but their length is limited by the electronic mean-free path in the CNT[9]. At large transmissions, the peak are broadened by the coupling to the leads thus enabling the detection of a small reduction in conductance around the helical gap, even if the level spacing is slightly larger that $g\mu_B B_{osc}$. In our case it would be complicated to reach this parameter regime, given the low g-factor for carbon nanotubes[10].

[9] Which is estimated at about $1 - 2$ µm in our devices.

[10] For $g = 2$, $B_{osc} = 1$ T corresponds to a gap of 60 µV, whereas typically the level spacing in our devices is $\delta \sim 1$ meV).

Transmission as a function of the spin-orbit energy

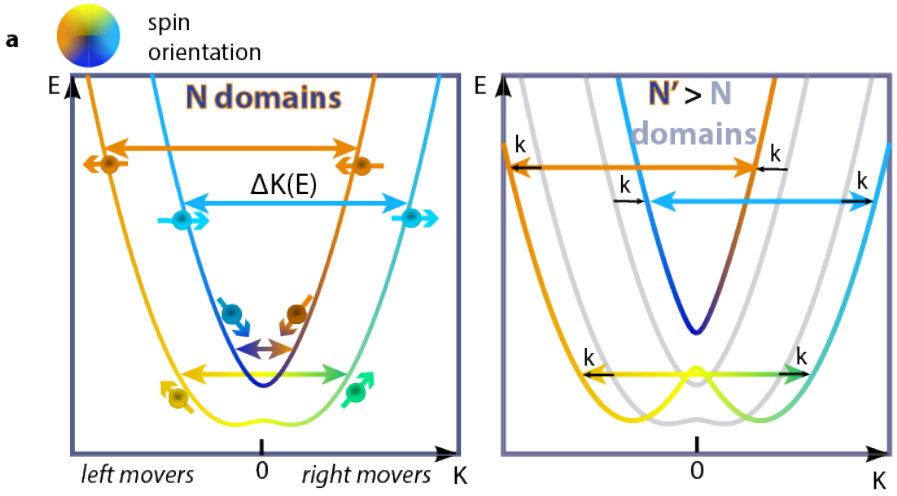

FIGURE 2.4: **Band structure for a conductor with a helicoidal field for two values of the field period.** (a) Energy bands as given by equation (2.31). The color indicates the spin eigenvalue for each band. At high energy, the two bands have opposite spins and a right-moving electron can only be reflected onto the same band (giving rise to an interference condition containing the wave-vector difference ΔK). On the contrary, at the bottom of the bands additional trajectories are allowed, as shown by the additional arrows. (b) Similar band structure for a smaller magnetic field period (here noted as a higher number of domains N' in a finite-size structure). The bands are shifted by k, which leaves the interference condition identical at high energy (where the shifts compensate) but not at low energy.

Another way to detect the effect of the helicoidal field is to change its structure (such as the domain period, orientation), for example by applying an external magnetic field, and to look at the changes in the transmission signal.

Applying a magnetic field on a magnetic texture can have various effects depending on the magnetic anisotropies and the orientation of the field. It can change the domains size, the magnetization axis of the domains and of the domain walls. The change in the axis in turn can change the strength of the stray field above the structure. This will be discussed in more details in chapter 3, in the specific case of the texture chosen for the experiments presented in chapters 4 and 5. At the very least, the structure has a saturation field where it is completely magnetized parallel to the applied field, thus destroying the synthetic spin-orbit effect.

For now, we can quantitatively study the evolution of the spectrum as only one parameter changes, the period of the oscillating field (ie the size of the magnetic domains). As we have seen in the calculation, the spin-orbit effectively shifts the wave-vector of the electron at a given energy; a change in the synthetic spin-orbit will thus modify the interference condition in a finite size system. This effect is represented in figure 2.4, where the band structure for an infinite system is plotted for two periods of the helicoidal

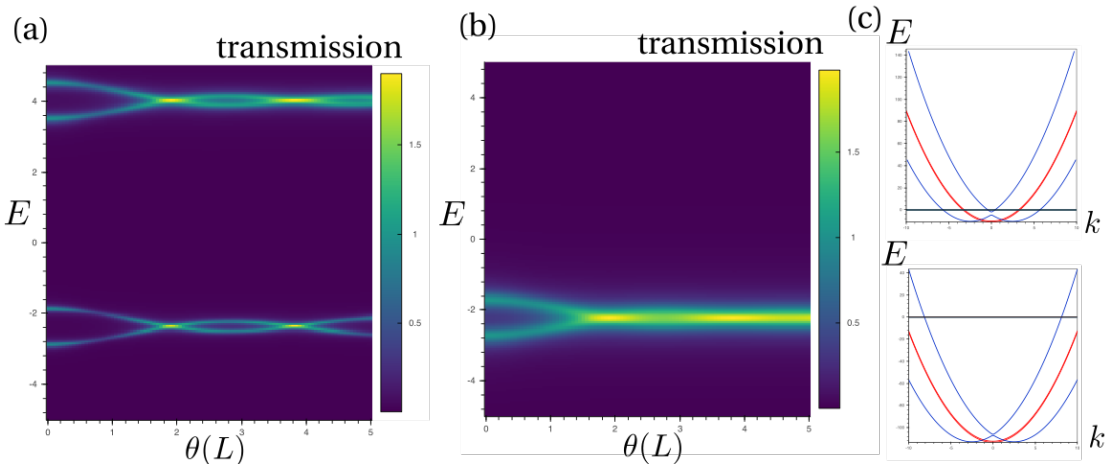

FIGURE 2.5: **Transmission of the device depicted in figure 2.3, as a function of the energy and the total magnetic field rotation** $\theta(L)$, at low chemical potential (a), and high chemical potential (b). The energy of the electronic levels oscillate with $\theta(L)$ in both cases, but these oscillations are strongly damped in the second case. (c) Corresponding band structure, where the black level indicates the chemical potential at which the transmission is plotted, and the red (blue) bands correspond to the initial (final) value for $\theta(L)$. The reduced parameters for these plots are $L = 3.3$, $b_{osc} = 0.5$, $t = 0.05$, $\mu = 10.6$ (a) and $\mu = 112.8$ (b).

magnetic field. The change in the spin-orbit strength also changes the spin eigenvalue associated with each band, which will determine whether the bands are orthogonal or not (at a given energy), and whether they can interfere as represented by the colored arrows.

The corresponding effect on the transmission of the segment is represented in figure 2.5: we look at the evolution of the transmission as a function of energy and $\theta(L)$ (the total rotation of the magnetic field), for two values of the chemical potential. Close to the bottom of the band (panel (a)), the energy levels oscillate as a function of $\theta(L)$, whereas these oscillations are damped when we increase the chemical potential (panel (b))[11].

We see that large variations of the spin-orbit energy at the bottom of the band result in oscillations of the energy levels with a period corresponding to the matching condition $2k = \frac{2\pi}{L}$ (given that for a confined structure, the constructive interferences yield $\Delta K = \frac{2\pi n}{L}$, $n \in \mathbb{N}$) In this expression, k indicates the shift of the band structure as noted in figure 2.4, and is equal to $k = k_{so}^{N'} - k_{so}^{N}$ when the texture evolves from N domains to N'. The visibility of these oscillations is greater at low chemical potential, and at high magnetic field B_{osc}[12]. The period of the oscillations is controlled by the variation of the spin-orbit energy compared to the level spacing in the nanoconductor. We will show an

[11] Note that in (b) only one level can be seen due to the higher level spacing at large chemical potential for a parabolic dfispersion relation.

[12] Interestingly, for this detection method low tunnel couplings are favorable, contrary to the detection as a function of the chemical potential. The chosen method can thus be adapted to the experimental parameter regime.

estimate in section 4.2.3, as well as simulations showing that a full oscillation is visible provided we can change the number of magnetic domains along the nanoconductor by about 2.

The parameters used in figure 2.5 do not represent a very realistic implementation of a CNT device with a magnetic texture ; the Zeeman energy is too high. Indeed, we can roughly measure the level spacing δ in reduced units in panel (a) and notice that $b_{osc} \sim \delta/10$. In realistic devices, $\delta \sim 1$ mV. Given $\mu_B \sim 60$ μeV/T, it corresponds to $B_{osc} = 1.7$ T for $g = 2$[13].

An interesting effect that can change the visibility of these oscillations, notably at lower values of B_{osc}, is a polarized region in the nano-conductor, that can appear due to the remanent field of the magnetic texture, or due to the fast alignment of the domain walls with the external magnetic field (depending on the characteristics of the texture). To highlight this effect, we consider a slightly more complicated structure, as shown in figure 2.6, and compare the evolutions of the energy levels in $\theta(L)$ with or without polarization in the external regions. In presence of this effect, the oscillations display anti-crossings which makes it easier to detect them in transport measurements, even at magnetic fields as low as about 400 mT. This is the order of magnetic field expected in our devices, as will be described in more details in section 4.2.3.

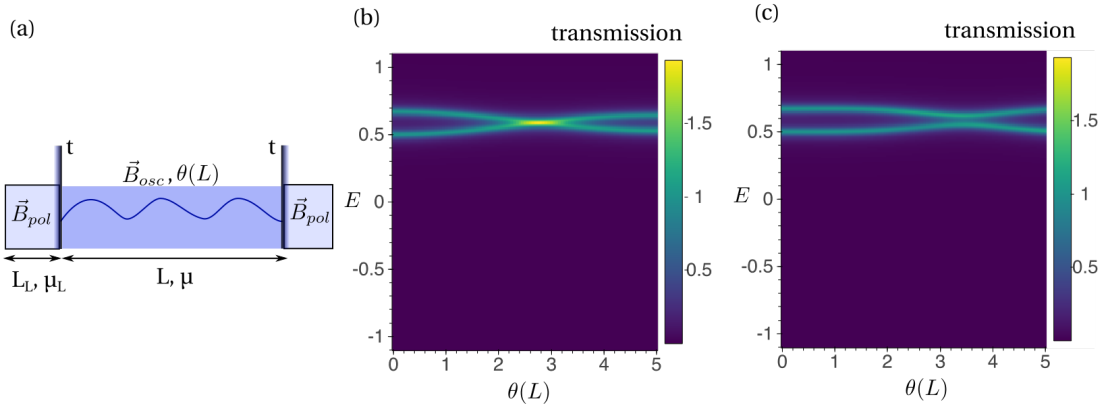

FIGURE 2.6: **Simulations of the effect of a helicoidal field with polarized sections** (a) Schematics of the second structure studied, made out of a central region subject to an oscillating field surrounded by two polarized regions of chemical potential $\mu_{L,R}$ and length $L_{L,R}$ subject to a field $\vec{B}_{pol}$. (b, c) Transmission of the device as a function of the energy and the total magnetic field rotation $\theta(L)$, at low chemical potential, for $b_{pol} = 0$ (b) and $b_{pol} = b_{osc}$ (c). The reduced parameters for these plots are $L = 1.6$, $b_{osc} = 0.15$, $t = 0.05$, $\mu = 4$, $\mu_{L,R} = 2$ and $L_{L,R} = 0.5L$.

To conclude, in this section we have compared two possible measurements to evidence the effect of the synthetic spin-orbit interaction. The effect could be visible in the transmission as a function of the chemical potential μ, but for very long ballistic devices

[13] Although the Landé factor for CNT can be larger due to the orbital effect of the magnetic field.

which is challenging (in our CNT circuits, we usually estimate a mean-free path of a few micrometers). On the other hand, looking at the evolution of the transmission as a function of the domain size (which can be modified by an external magnetic field for example) gives a visible signature of the effect, even for magnetic fields as low as 400 mT (as we will show in chapter 4). This detection method requires a good control over the chemical potential μ to tune the conductor to the band bottom, which is usually attainable with carbon nanotubes [180–185].

Adding superconductivity to complete the recipe

To finish implementing the "recipe" for the emergence of MZM, we also need to add superconductivity to the system. It can be either added as superconducting contacts on one or both sides of the two-terminal normal segment.

The SNS junction: In presence of two superconducting contacts to the normal segment, the equations for superconductivity-induced bound states (called Andreev Bound States in all generality) are given by [186]:

$$\det\left[\mathbb{1}-\exp\left(-2i\,\mathrm{acos}\left(\frac{E}{\Delta}\right)\right)\begin{pmatrix}e^{-i\delta/2}&0\\0&e^{i\delta/2}\end{pmatrix}S(E)\begin{pmatrix}e^{i\delta/2}&0\\0&e^{-i\delta/2}\end{pmatrix}S^{*}(-E)\right]=0, \tag{2.33}$$

where $S(E)$ is the scattering matrix of electrons in the normal segment (the scattering matrix for the holes is given by $S^h(E) \equiv (S^e(-E))^*$) and δ is the phase difference between the two superconductors of identical gap Δ.

The SN junction terminated by a hard wall: On the other hand, if the normal segment is connected to only one superconducting contact and a hard wall on the other side (as is the case, for example, with a tunnel barrier), the bound states energies are now given by the Andreev Billiard equation [187]:

$$\det\left[\mathbb{1}-\exp\left(-2i\,\mathrm{acos}\left(\frac{E}{\Delta}\right)\right)S'(E)S'^{*}(-E)\right]=0. \tag{2.34}$$

where $S'(E)$ is the scattering matrix of the closed normal region, relating the incoming and outgoing modes at the superconducting interface. It can be formally expressed by combining the normal region scattering $S(E) \equiv \begin{pmatrix}S_{11}&S_{12}\\S_{21}&S_{22}\end{pmatrix}$ and the hard wall reflection (incoming waves are reflected with a phase factor of π):

$$S'(E) = S_{11} - S_{12}(1+S_{22})^{-1}S_{21}. \tag{2.35}$$

We recognize the formula for a Fabry-Pérot interferometer, illustrating the possible electronic trajectories in the closed normal region. The full ABSs equation re-expresses a constructive interference condition, where the elementary trajectory consists in two round trips inside the normal region (once as an electron, once as a hole, as visible by the presence of the $S_{12}S_{21}$ factor in $S'(E)$). In contrast, in the S-N-S junction, the bound states equation is equivalent to constructive interferences over one round trip only.

We will not study here the influence of superconductivity on the visibility of the synthetic spin-orbit effect in more details. In chapter 4, we will present numerical calculations of the evolution of bound states in an SN-hard wall system, and show that the variation of the synthetic spin-orbit coupling is measurable using realistic parameters for a CNT circuit.

2.3 New geometries for the generation of MZM

In most theoretical models, an effective superconducting gap is considered homogeneous along the 1D conductor. In the scattering formalism developed above, on the contrary, superconductivity is added as an interface between a superconductor and the helical region. However, in the actual physical devices, the situation is slightly different since superconductivity can be induced in an inhomogeneous manner along the device. Here, we study in more details a device where superconductivity is added on a segment of the nanoconductor, and we investigate how superconductivity induced-bound states (Andreev Bound States, of ABS) can evolve into MZM in such a system, notably when the band structure of the superconductor correspond to a trivial topological phase. For this study, we use a tight-binding description of the nanoconductor, enabling us to gain access to the spatial dependence of its density of states.

We will also study the situation where not only the superconducting pairing is non-homogeneous, but also the spin-orbit coupling or the Zeeman effect. Our motivation to do so is to describe more accurately two experimental situations: experiments where the superconducting contact renormalizes the Landé factor and spin-orbit strength in the nanoconductor below the contact, and experiments where the spin-orbit is induced by an oscillating field that does not extend to the superconducting region. We will see that when no region of the nanoconductor regroups all the Majorana “ingredients”, the localization of the zero-energy mode is improved in an SNS geometry compared to the NS junction.

2.3.1 Tight-binding formalism

We use the same model as the one introduced in Ref [143]. We consider the following discrete hamiltonian for a chain coupled to a superconductor:

$$\begin{aligned} H = & \sum_{n\in[1,N]} \hat{d}_n^\dagger(-\mu(n)\hat{s}_0 + B_{osc,z}(n)\hat{s}_z + B_{osc,x}(n)\hat{s}_x)\hat{d}_n \\ & - t(n)(\hat{d}_n\hat{d}_{n+1}^\dagger + \hat{d}_n^\dagger\hat{d}_{n-1}) + (t_k(n)\hat{d}_n^\dagger\hat{c}_k + h.c.) \\ & - i\hat{d}_n^\dagger\Lambda(n)\hat{s}_y(\hat{d}_{n+1} - \hat{d}_{n-1}) + H_s \end{aligned} \tag{2.36}$$

where $s_{i=0...3}$ are the Pauli matrices acting on the spin, $\hat{d}_n^+ = \left(\hat{d}_{n\uparrow}^\dagger, \quad \hat{d}_n^\dagger\right)^T$ (resp. $\hat{c}_k^\dagger = \left(\hat{c}_{k\uparrow}^\dagger, \quad \hat{c}_k^\dagger\right)^T$) the creation operator of an electron at site n (resp. in the superconductor, with momentum k), and H_s is the hamiltonian of the superconductor (of gap Δ and Dynes parameter Γ_n). The magnetic field at site n along the axis i is written $B_{osc,i}(n)$, the hopping parameters are $t(n)$ (between sites) and $t_k(n)$ (to the superconductor) and the chemical potential at site n is $\mu(n)$. The intrinsic spin-orbit coupling term at site n is $\Lambda(n)$. In general, all terms can be site dependent.

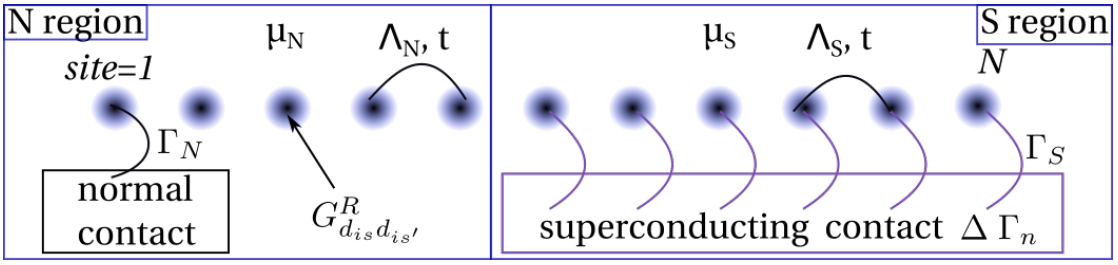

FIGURE 2.7: **Description of the tight-binding parameters** Schematics of the chain of N sites described using tight-binding formalism. There are two regions in the chain, a normal region (N) with parameters μ_N, t, Λ_N and a "superconducting region" (S) where the sites are coupled to a superconductor, with parameters μ_S, t, Λ_S.

In the following, we will either use a uniform parametrization, or define two regions as represented in figure 2.7, labeled N (N_1 sites) and S ($N-N_1$ sites) with possibly different parameters:

$$\Delta(n) = \Delta\Theta(n - N_1) \tag{2.37}$$

$$\Lambda(n) = \Lambda_N\Theta(N_1 - n) + \Lambda_S\Theta(n - N_1) \tag{2.38}$$

We calculate from this hamiltonian the retarded Green's function in the Nambu spin space at each site, which allows us to obtain electronic density of states at energy ω, $N_s(\omega)$ through

$$\tilde{G}^R_{\hat{d}_s,\hat{d}_{s'}}(t) = -i\theta(t)\langle\{\hat{d}_s(t), \hat{d}_{s'}(t)\}\rangle \tag{2.39}$$

$$N_s(\omega) = -\frac{1}{\pi}\,\mathrm{Im}\left[G^R_{d_s,d_s}(\omega)\right] \tag{2.40}$$

with $\tilde{G}^R$ the Fourier transform of G^R and θ the Heavyside function.

In the study that follows, the parameters are given in reduced units, which are defined in Appendix B.

2.3.2 MZM in an homogeneous NS chain: Influence of the normal segment

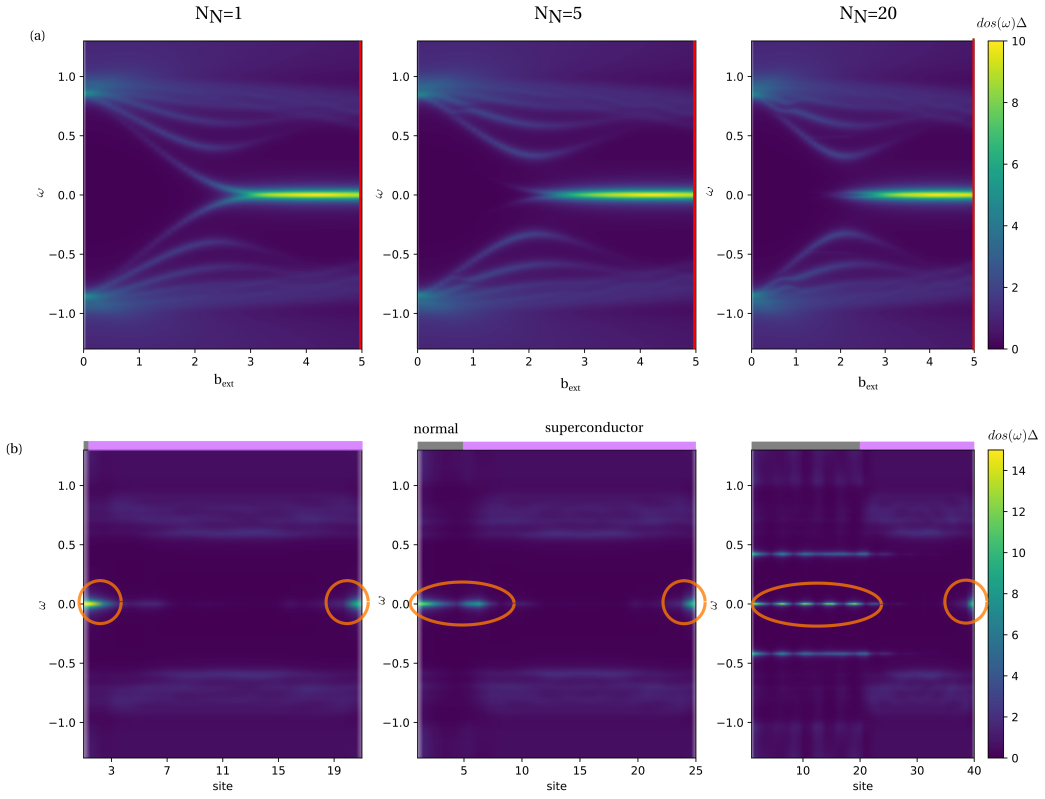

FIGURE 2.8: **Effect of a normal region on the emergence of two MZM** Density of states $dos(\omega)\Delta$ at the last site of the chain as a function of energy ω and external magnetic field b_{ext} (a), and density of states as a function of energy and site (b) when varying the length of the normal region. Panel (b) is taken at $b_{ext} = 5$ as shown by the red line in (a). The length of the normal region is $N_N = 1, 5$ and 20 sites (from left to right), in addition to 20 sites proximitized by a superconductor, as indicated by the grey and purple lines. Two MZM appear at the end of the chain, as highlighted by the orange circles. The left one extends over the normal region. The magnetic field and spin-orbit coupling ($\Lambda = 5$) are homogeneous along the chain. The parameters are $\mu_N = 6$, $\mu_s = 6$, $t = 2.5$, $\Delta = 1$, $\Gamma_N = 0.001$, $\Gamma_S = 5.5$, $\Gamma_n = 0.1$.

We first use this formalism to consider the effect of an inhomogeneous superconducting proximity effect in the chain. We consider an "NS chain", made out of two regions, a normal region (N) and a region proximitized by superconductivity (S). The parameters are homogenous in each region, as shown in figure 2.7. We study the transition from a chain with superconductivity induced everywhere and a chain with two regions in figure 2.8. In a first time, we consider that the spin-orbit energy and the external magnetic field are the same in both the N and S regions.

As the size of the normal segment is increased, the ZBP at the interface to the normal region spreads over all the normal sites. we go from a situation where we have two localized Majorana modes at the end of the chain to a situation where one Majorana is delocalized along the helical normal wire, and the second one stays localized in the superconductor as previously described in Ref [188]. Note that the state localized in the normal segment is still separated from the other excitations, not by a superconducting gap but by the confinement-induced gap (as visible for example in figure 2.8).

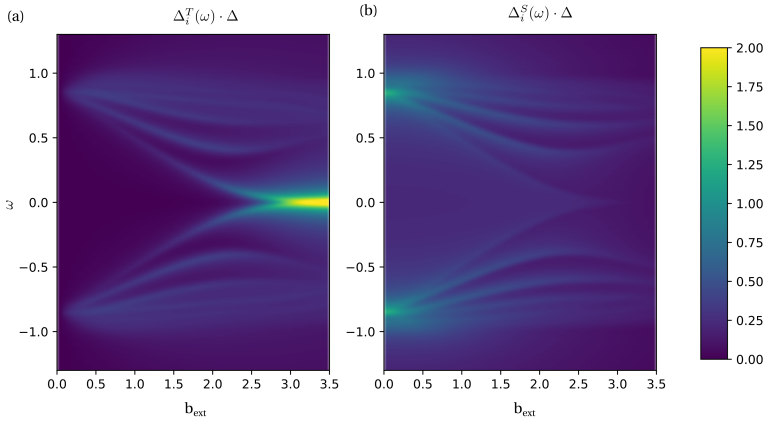

FIGURE 2.9: **Different superconducting pairing intensities in the homogeneous Majorana chain** Triplet pairing intensity Δ_d^T (a) and singlet pairing intensity Δ_d^S (b) as a function of energy ω and magnetic field b_{ext}, at site $N = 1$, for a chain with a homogeneous superconducting proximity effect (as well as homogeneous spin-orbit interaction). The parameters are the ones of figure 2.8 (with one normal site).

The presence of MZM here is indicated by the presence of a localized zero-energy state when the magnetic field and chemical potential are tuned to enter the topological regime. However, one can also look at more specific properties of the MZM wavefunction. In a Hamiltonian formalism, given the eigenfunctions in the Nambu basis $\gamma = (\psi_1, \psi_2, \psi_3, \psi_4)$, several measures of the excitation properties were proposed. One can plot the charge $\rho = |\psi_1|^2 + |\psi_2|^2 - |\psi_3|^2 - |\psi_4|^2$ and quasiparticle density $Q = |\psi_1|^2 + |\psi_2|^2 + |\psi_3|^2 + |\psi_4|^2$. Comparing both quantities, a MZM can be identified as carrying no charge (see for example [188]). Another parameter, labeled Majorana polarization was proposed in ref [189] to similarly discriminate between ABS and MZM.

Here we consider an open system, and thus we do not have access to the explicit eigenfunctions. However, we can directly look at the induced superconducting pairings on the chain. There are three possible triplet spin pairing (for which the spin exchange is antisymmetric): $|\uparrow,\uparrow\rangle$, $|\downarrow,\downarrow\rangle$, $\frac{1}{\sqrt{2}}(|\uparrow,\downarrow\rangle + |\downarrow,\uparrow\rangle)$, and one singlet spin pairing (for which the spin exchange is anti-symmetric): $\frac{1}{\sqrt{2}}(|\uparrow,\downarrow\rangle - |\downarrow,\uparrow\rangle)$.

We can investigate the nature of the electron-electron pairing by looking at the local Green function coupling different spins. The symmetric and antisymmetric contributions can be distinguished and we can compare Δ_i^S, indicating a s-type pairing at site i and Δ_i^T indicating an antisymmetric pairing.

$$\Delta_i^S = \frac{1}{\sqrt{2}}\left|\mathrm{Im}\left[G^R(d_{i\uparrow}^\dagger, d_{i\downarrow}^\dagger)\right] - \mathrm{Im}\left[G^R(d_{i\downarrow}^\dagger, d_{i\uparrow}^\dagger)\right]\right|, \tag{2.41}$$

$$\begin{aligned}(\Delta_i^T)^2 = \frac{1}{2}&\left|\mathrm{Im}\left[G^R(d_{i\uparrow}^\dagger, d_{i\downarrow}^\dagger)\right] + \mathrm{Im}\left[G^R(d_{i\downarrow}^\dagger, d_{i\uparrow}^\dagger)\right]\right|^2 + \left|\mathrm{Im}\left[G^R(d_{i\uparrow}^\dagger, d_{i\uparrow}^\dagger)\right]\right|^2 \\ &+ \left|\mathrm{Im}\left[G^R(d_{i\downarrow}^\dagger, d_{i\downarrow}^\dagger)\right]\right|^2.\end{aligned} \tag{2.42}$$

These quantities can be identified as spectral pairing functions (i.e. with an energy resolution) by coming back to the BCS theory definition of the superconducting pairing parameter Δ_i, here taken at site i:

$$\Delta_i \propto \left\langle \hat{d}_{i\downarrow}^\dagger \hat{d}_{i\uparrow}^\dagger \right\rangle \tag{2.43}$$

$$\text{here, } \left\langle \hat{d}_{i\downarrow}^\dagger \hat{d}_{i\uparrow}^\dagger \right\rangle = \frac{1}{\pi}\int d\epsilon f_{FD}(\epsilon)\,\mathrm{Im}\left[G^R\left(d_{i\uparrow}^\dagger, d_{i\downarrow}^\dagger\right)\right] \tag{2.44}$$

where f_{FD} is the Fermi-Dirac distribution. For the triplet component, we have summed on all possible triplet pairings. We can see in figure 2.9 that in the textbook case of a chain with homogeneous parameters, the zero-energy state has no singlet pairing and a maximal triplet pairing, as opposed to the precursors ABS or the high energy ABS.

2.3.3 MZM in an NS chain - influence of the spin-orbit and Zeeman energies in the superconductor

In the previous section, we have considered the spin-orbit coupling and the external magnetic field to be homogeneous along the chain. The appearance of MZM in an SNS geometry with homogeneous spin-orbit and magnetic field was studied in several works [126, 188, 190–192]. However, to our knowledge, the chain parameters (with the exception of the chemical potential) are usually considered constant. We will instead study an inhomogenous scenario, in the regime where the spin-orbit coupling and the Zeeman energy in the superconducting region are smaller than in the normal region. A first motivation to do so is to describe more accurately an experimental

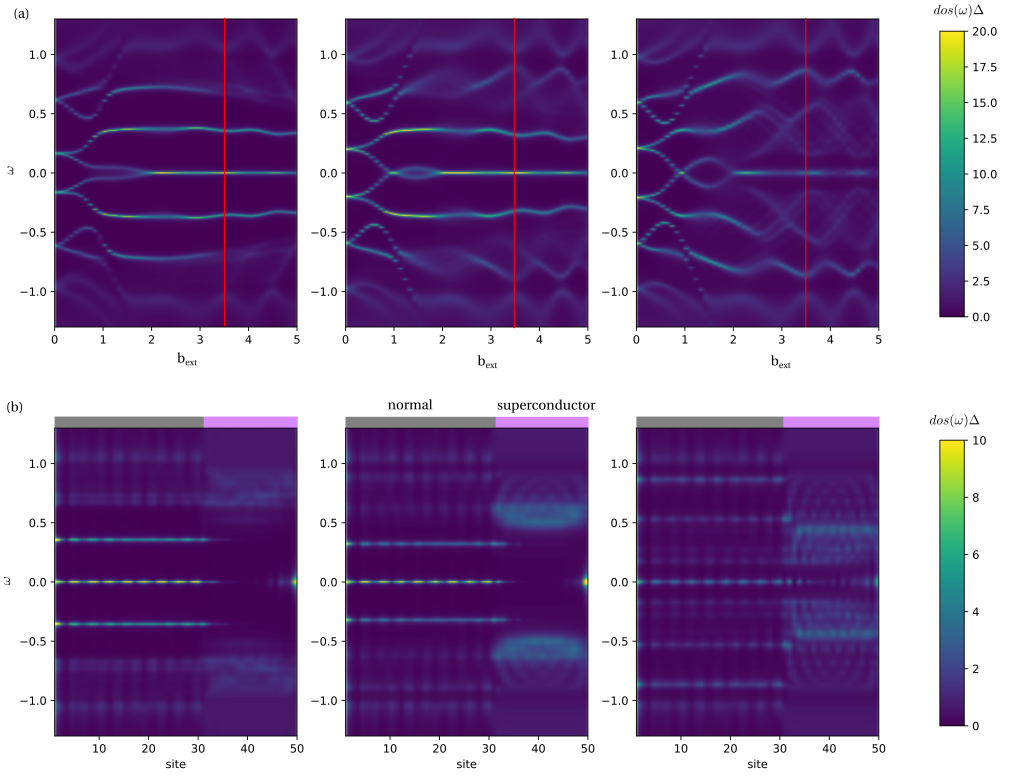

FIGURE 2.10: **Evolution of the MZM in a NS junction with a varying Λ_S** (a) Density of states of the first site of the chain as a function of energy ω and external magnetic field b_{ext}, and (b) density of states as a function of energy and site when varying the spin orbit interaction strength in the superconducting section. Panel (b) is taken at $b_{ext} = 3.5$ as shown by the red line in (a). The parameters are $N = 50$, $\mu_N = 6$, $\mu_S = 5$, $t = 2.5$, $\Delta = 1$, $\Gamma_N = 0.001$, $\Gamma_S = 5.5$, $\Gamma_n = 0.1$, $\Lambda_N = 5$ in the normal region, and a spin-orbit coupling $\Lambda_S = 5, 2.5, 0.5$ in the superconducting region (from left to right). The superconducting region extends over 20 sites, as shown by the purple and grey lines. The level spacing is modified by the change in the spin-orbit energy (notably through the chemical potential shift), as visible in the number of levels below the gap in (b).

setup where the spin-orbit is synthetically induced by a magnetic texture, which cannot necessarily extend onto the superconductor. A second motivation is linked to recent theory papers showing that in proximitized nanowires the coupling to the superconductor can renormalize the spin-orbit energy in the conductor [82]. Finally, the presence of the superconductor can screen the effect of an external magnetic field (below the superconductor).

We start by studying the same NS junction as in the previous section. Figure 2.10 illustrates the effect of a decrease in spin-orbit coupling, and figure 2.11 the effect of the screening of the field in the superconducting region. The results of the NS chain with homogeneous parameters still hold when decreasing the spin-orbit coupling in the S region. However when screening the external magnetic field, the density of states is different: the zero-energy mode does not extend into the superconductor. It appears

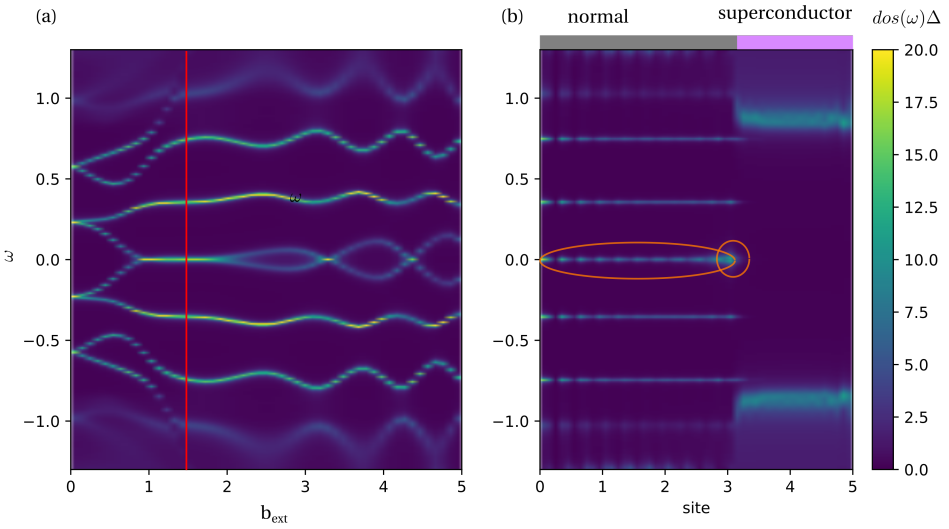

FIGURE 2.11: **SN chain subject to an external magnetic field, screened by the superconductor**. In this scenario, the magnetic field is fully screened inside the proximitized region of the nanoconductor. The normal and superconducting regions are indicated by the grey and purple lines. (a) Density of states as a function of energy and magnetic field. (b) Density of states as a function of energy and site, at $b_{ext} = 1.5$ as indicated by the red line. The parameters are the one of figure 2.10 with $\Lambda_S = 0.$, $\mu_S = 3$. In panel (b), we can see that the previously separated MZM now seem to overlap at the N/S interface, as highlighted by the orange circles.

that the weight that was previously at the end of the chain (figure 2.10) is shifted to the NS interface. This indicates that the end of the topological region in the chain has moved, as expected when we screen the field in the superconducting region. In such a setup, it may be harder to isolate two MZM. One way to try and localize these states better is to consider an SNS chain.

2.3.4 MZM in an SNS chain

In the homogeneous NS chain described above, the Majorana that is located in the normal region is delocalized over the chain. As a consequence, we can expect that in an SNS chain, there will be four Majorana modes, two of which will hybridize (in the central normal region) and two will remain localized in the S regions. This way, we can obtain two well separated MZM.

This idea is illustrated in figure 2.12. First, on the left column (chain 1), the density of states as a function of external magnetic field (top line) and site (bottom line) is plotted for a chain with a spin-orbit coupling (although reduced) in the superconducting region and without any screening of the field. We see that we obtain two Majorana modes at the end of the chain. Here we use the same parameters as the ones of figure 2.10. The two remaining columns (chains 2 and 3) describe chains where there is no spin-orbit coupling

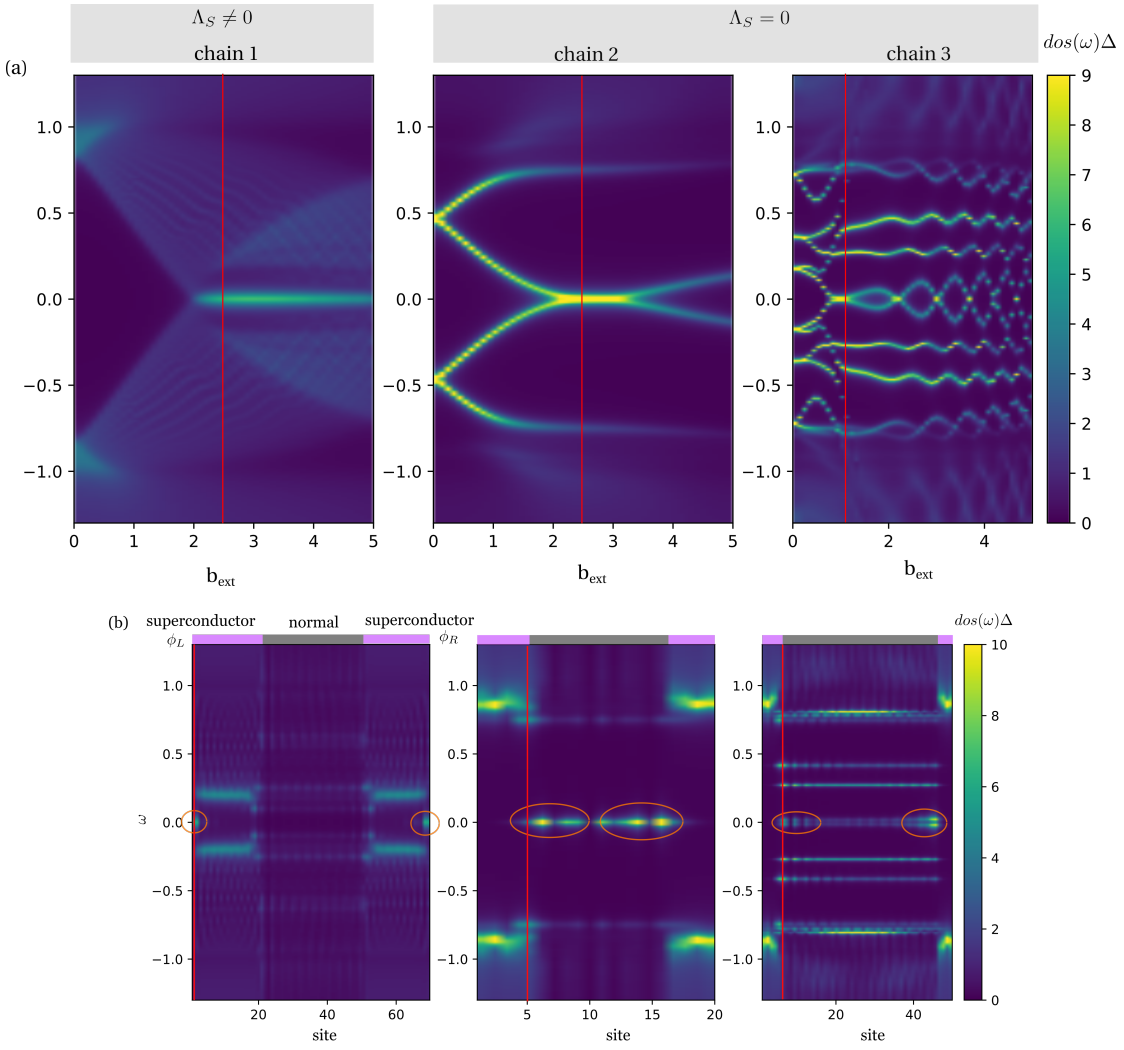

FIGURE 2.12: **Localized modes in an SNS chain**. Density of states as a function of energy and magnetic field at site i_0 (a) and density of states as a function of energy and site at field b^0_{ext} (b) for three different SNS chains. In presence of two superconductors, the phase difference $\phi_L - \phi_R$ affects the density of states. Here we take $\phi_L - \phi_R = 0$. These plots show how the partially localized modes obtained in the previous geometry hybridize and lead to new zero-energy modes (highlighted by the orange circles). In presence of a spin-orbit coupling in the superconducting region (chain 1), a zero energy mode exists, separated into two localized peaks at both end of the system as we would obtain in a fully proximitized system. When there is no spin-orbit coupling in the superconducting region, these two peaks are not fully separated (chains 2 and 3). The specific parameters are the following. Chain 1 corresponds to a chain with a reduced spin-orbit coupling in the superconducting region (with the same parameters as in figure 2.10), with the left superconducting region duplicated to the right: $N = 70$ with 20 proximitized sites on each end, $\Lambda_S = 0.5$, $\Lambda_N = 5$, $\mu_S = 5$, $\mu_N = 6$, $b^0_{ext} = 2.5$, $i_0 = 0$). Chains 2 and 3 describe chains with no spin-orbit coupling nor magnetic field inside the superconductor, for two sets of parameters, corresponding to two different chain length. The parameters are $N = 20$ with 5 proximitized sites, $\mu_N = 6$, $\mu_S = 3, \Lambda_N = 10$, $b^0_{ext} = 2.5$, $i_0 = 5$ (chain 2) and $N = 50$ with 5 proximitized sites, $\mu_N = 4$, $\mu_S = 3, \Lambda_N = 4, b^0_{ext} = 1.2$, $i_0 = 5$ (chain 3). The remaining parameters are the same as for figure 2.8. The field values used for panel (b) and site index used for panel (a) are show with a red line.

in the proximitized region, and in addition the magnetic field is screened. We see that we still obtain zero energy modes, however they are not fully localized, as we could foresee from the NS study. Indeed, already in the NS chain we observed that the spatial distribution of the zero-energy mode then does not extend into the superconductor, but stays partially spread in the normal region, and partially pinned at the interface. Increasing the length of the chain seem to localize them more. Surprisingly, in spite of the overlap between these states, their energy is fixed at zero over a certain range of magnetic field (a).

To conclude, in this section we have studied the emergence of zero-energy modes for inhomogenous systems. We first considered an inhomogeneity in the proximity effect. The zero-energy state is partially localized in the superconductor, partially spread over the normal region. When the spin-orbit coupling and Zeeman effect in the normal region are suppressed, these two states are not well separated anymore. In an SNS geometry, it is possible to separate them more efficiently.

2.4 Spectroscopy of Majorana pairs with cQED methods

Up until now, the majority of experiments made with nanoconductors potentially hosting MZM were transport measurement. However, the measurement of the density of states alone does not reveal the specific properties of a MZM, and notably its self-adjointness. One way to try and observe this property is to use a microwave cavity, capacitively coupled to the circuit.

Indeed, it has been shown experimentally that the microwave signal of a cavity coupled to a mesoscopic system can reveal properties that are not accessible through current measurement, as well as provide new means to manipulate quantum states [193]. In the case of Majorana Zero Modes, the use of microwave signal to probe the topological phase was studied in references [140–143]. It was also proposed that microwave photons can be used to braid MZM or to build a qubit gate [194–196].

We briefly discuss how to couple our system to a cavity, and the possible information one can extract from the measurement of the cavity signal.

2.4.1 Light-matter coupling

General coupling

A general description of the light-matter coupling in mesoscopic circuits can be found in Ref [193]. Here we will quickly introduce a few notions developed in this paper to discuss the coupling to MZM.

To couple a quantum circuit to a microwave cavity, one can use a capacitive coupling, by bringing the electric AC potential of the cavity close to the circuit. The circuit is then subject to a spatially varying electrostatic potential $V_\perp(\vec{r})$.

The coupling between the cavity and the circuit (described as an ensemble of orbitals, of creation operator $\hat{c}_n$)[14]) is expressed as

$$\hat{h}_{\text{int}} = \sum_{\text{n orbitals}} g_n \hat{c}_n^\dagger \hat{c}_n (\hat{a} + \hat{a}^\dagger) \tag{2.45}$$

The prefactors g_n are geometric factors, that depend on the spatial dependence of the cavity mode and of the energy orbital n:

$$g_n = -e \int \mathrm{d}r^3 \, |\varphi_n(\vec{r})|^2 \, V_\perp(\vec{r}) \tag{2.46}$$

The effect on the cavity signal depends on the charge susceptibility of the nano-conductor. The transmission b_t/b_{in} of the cavity can be written [193]:

$$\frac{b_t}{b_{\text{in}}} = \frac{2\sqrt{\Lambda_L \Lambda_R}}{\omega_{\text{RF}} - \omega_0 + \mathrm{i}\Lambda_0 - \Xi(\omega_{\text{RF}})} \tag{2.47}$$

with

$$\Xi\left(\omega_{\text{RF}}\right) = \sum_{n,n'} g_n g_{n'} \chi_{n,n'}\left(\omega_{\text{RF}}\right) \tag{2.48}$$

and

$$\chi_{n,n'}\left(t - t'\right) = -\mathrm{i}\theta(t) \left\langle \left[\hat{c}_n^\dagger(t) \hat{c}_n(t), \hat{c}_{n'}^\dagger\left(t'\right) \hat{c}_{n'}\left(t'\right) \right] \right\rangle_{\hat{h}_{\text{int}}=0} \tag{2.49}$$

With the following parameters: the L/R port contributions to the cavity linewidth $\Lambda_{R,L}$, the measurement pulsation ω_{RF}, the resonance pulsation ω_0 (and linewidth Λ_0) of the cavity. The global charge susceptibility of the nano-circuit $\Xi\left(\omega_{\text{RF}}\right)$, regroups all the terms $\chi_{n,n'}\left(t - t'\right)$ that describe how the occupation of level n responds at first order to a classical modulation of the energy of level n', in stationary conditions (the subscript $\hat{h}_{\text{int}} = 0$ indicates the situation with no coupling between the circuit and the cavity).

[14] These orbitals correspond to electronic states in both the CNT and its electrodes

Two distinct cases

Depending on the geometry of the circuit, we can identify two distinct situations.

In the first case, $V_\perp(\vec{r})$ varies along the CNT circuit; then g_n depends on the circuit orbital n and the cavity can reveal informations on the internal degree of freedom of the system. The easiest geometry to have different couplings for different orbitals is to use a double quantum dot circuit where the cavity is mainly coupled to one dot. In this scenario, the interaction Hamiltonian (2.45) effectively modulates the chemical potential of one dot with an amplitude proportional to g_n and the number of photons. In this case, the charge susceptibility is strongest at ω_{DQD}, the transition energy of the DQD [193]:

$$\Xi\left(\omega_{\mathrm{RF}}\right) \propto \frac{1}{\omega_{\mathrm{RF}} - \omega_{\mathrm{DQD}} + \mathrm{i}\Gamma_2^*} \tag{2.50}$$

where Γ_2^* is the decoherence rate of the DQD transition.

In the second case, $V_\perp(\vec{r})$ does not vary in the CNT (in which case g_n will be equal for all the CNT orbitals), but is different in the CNT circuit and in its leads. In this situation, the cavity can be used to reveal the dynamics of the tunneling into the leads [197, 198][15]. In the simple situation of a QD coupled to a normal lead, the susceptibility is proportional to the admittance of the QD, and the cavity signal will change around $\epsilon = 0$. This is schematically represented on figure 2.13.

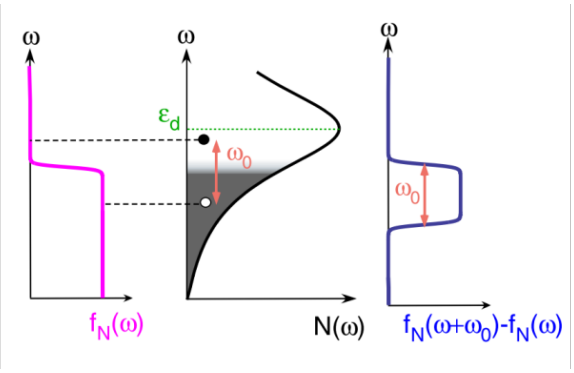

FIGURE 2.13: **Lead-dot coupling**: Physical picture of the coupling between a lead and a QD. The cavity can induce the formation of electron-hole pair in the dot density of states if the difference in fermi function between ω and $\omega - \omega_{cav}$ is non-zero. The signal is strongest for the dot detuning $\epsilon_d = 0$. Source: [193].

2.4.2 Implications of the self-adjointness

In the previous paragraph, we have discussed the interest of coupling a mesoscopic circuit to a cavity in the general case. We will now consider the specific case of a system hosting

[15] Provided the g in the leads are small; we take it equal to zero for simplicity

MZM. For simplicity, we use the ideal model of a nano-conductor with homogeneous spin-orbit coupling, Zeeman and s-type superconducting pairing along its length. In this system, there exists a pair of MZM with an energy splitting ϵ that vanishes at large enough magnetic field.

The hamiltonian when the two MZM $\hat{\gamma}_{i,1}$ $\hat{\gamma}_{i,2}$ weakly hybridized is written, in the Majorana operator basis (1.7),

$$H_{\text{merge}} = \frac{i}{2}\epsilon\hat{\gamma}_{i,1}\hat{\gamma}_{i,2} = \epsilon\left(\hat{c}_i^\dagger\hat{c}_i - \frac{1}{2}\right) \tag{2.51}$$

On the other hand, the general form for the coupling between the MZM pair and cavity photons can also be rewritten in the Majorana operator basis in the following way (dropping the i index) [143]:

$$H_{\text{coupling}} = ig\hat{\gamma}_1\hat{\gamma}_2\left(\hat{a} + \hat{a}^\dagger\right) \tag{2.52}$$

where g is real due to $\hat{\gamma}_{1,2}^\dagger = \hat{\gamma}_{1,2}$ and $\hat{\gamma}_{1,2}\hat{\gamma}_{1,2}^\dagger = \frac{1}{2}$ [141]. As mentioned before, it is a geometric factor that depends on the spatial form of the cavity mode and of the MZM wavefunction. For non-overlapping MZM, we expect $g \to 0$ as a Majorana fermion does not couple to the electro-magnetic field (since it carries no charge).

Comparing both Hamiltonians, we see that they commute, which means that the coupling does not induce transitions between the Majorana doublet but can only change its energy, and there will be no effect on the cavity resonant frequency[16]. This is equivalent to a longitudinal coupling in term of Bloch sphere representation. In fact, one can show that this is simply linked to a selection rule preventing the cavity from exciting two modes with different fermionic parities.

We can note that for a different reason, non-degenerate ABS with opposite spins are not coupled to the cavity photons due to a selection rule stating that the photon cannot reverse the spin. Thus cavity photons can discriminate between degenerate and non degenerate ABS, but not between well separated MZM and non-degenerate ABS. Measuring at the same time the transport and cavity signal can provide complementary information.

Two concrete proposals

We develop in more details two proposals to observe MZM with cavity measurements.

In order to get a cavity signal, one can tune the chemical potential along the nano-conductor to engineer more than two MZM (for example, by creating a central trivial

[16] In the stationnary regime; if one can modulate g the resonant frequency may shift

region in the nanoconductor with a piano of gates). With four MZM, there can exist a transverse coupling between the cavity and the nano-conductor, due to a term that couples two MZM associated with two different fermionic degree of freedom. This can lead to a readable effect either as a small cavity shift, or as a non-linear effect at high number of photons, that depends on the chemical potential of the topological phase (more precisely, on how far the system is into the topological phase) [141].

Another way to measure MZM properties with a cavity is to take into account additional states, either higher energy states in the conductor or states in the leads. Although the cavity photons do not couple to transitions between a Majorana doublet, they can couple to transitions between one of the MZM and one of these state [143]. One can then measure the cavity dispersive shift, identify the transitions that couple to the cavity and deduce the forbidden transitions, as shown in figure 2.14 (line 1 and 2 are visible in the cavity signal, but not P). It seems that the short length regime, where a Majorana doublet is present over a larger range of magnetic field is more favorable to identify such a signal.

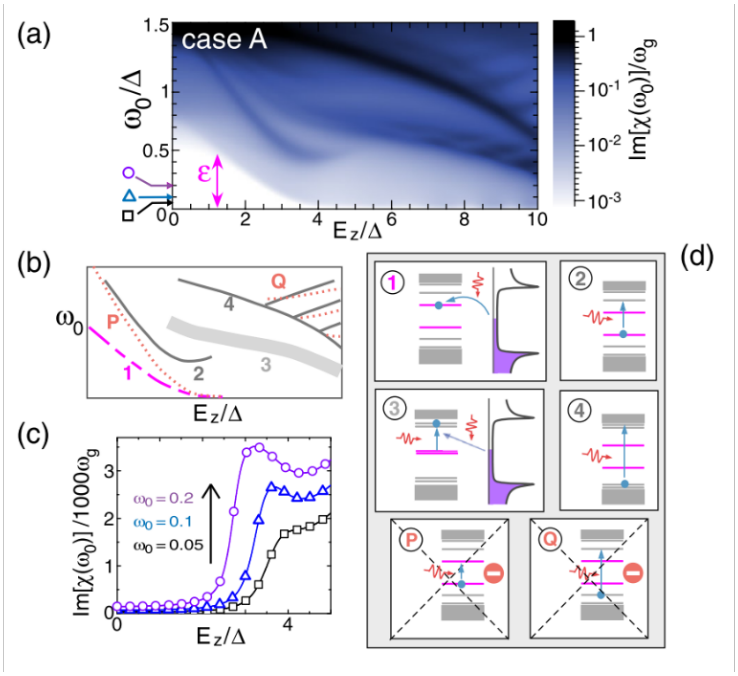

FIGURE 2.14: **Proposal for detecting the self-adjoint property of MZM through cavity photons** (a) Charge susceptibility of the system as a function of an external magnetic field (E_z) and cavity resonant frequency (ω_0). The cavity signal is subject to a frequency and linewidth shift that is proportional to the real and imaginary part of the charge susceptibility. (b) Scheme of the features appearing in (a) Charge susceptibility as a function of E_z for different cavity frequencies, as shown in (a). (d) Processes contributing to the features of panel (b), and forbidden processes P and Q. P is the transition inside the Majorana doublet. Q couples to non-degenerate ABS with opposite spins. Source: [143]

.

Chapter 3

Experimental methods

In this chapter, we give some details on the various techniques that are used to fabricate the mesoscopic devices presented in this thesis. Special emphasis is put on the fabrication and characterization of the magnetic texture used in the experiments presented in chapter 4 and 5 (section 3.3). We will also discuss the new CNT transfer technique (the "stapling") used at the end of this thesis, and the possibility to obtain superconducting contacts to the CNT in sections 3.2 and 3.4. The influence of the new device geometry needed for the stapling technique on the microwave cavity resonance is studied in section 3.1. Finally, the general processes for the circuit fabrication and measurement are described in sections 3.5 and 3.6.

3.1 cQED methods

An important specificity of our experimental technique is that we combine a mesoscopic circuit with a microwave cavity, to study the electronic system through both its transport characteristics and the change in the microwave signal when the circuit is coupled to the cavity. Such dual measurements can reveal complementary properties of the electronic state, as introduced in section 2.4.1.

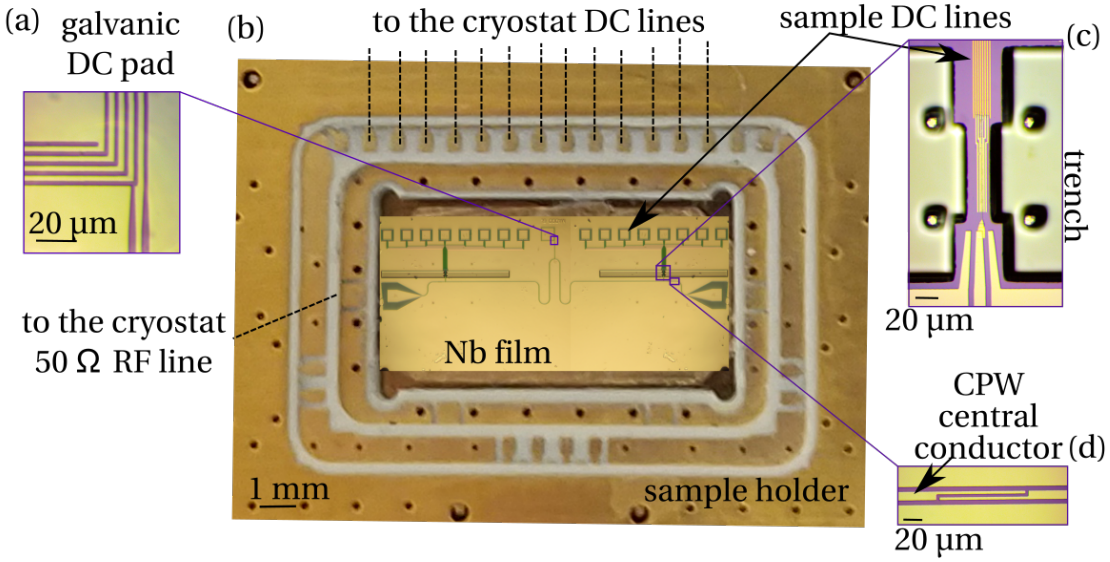

FIGURE 3.1: **Image of a microwave cavity in the sample holder:** (b) Picture of a device combining a coplanar waveguide (CPW) and DC lines for the stapling technique, inside the sample holder (the PCB of the sample holder is visible in gold). The sample holder DC lines and radiofrequency (RF) lines ends are visible. Wire bonding is needed to connect the sample to the cryostat. (a) Zoom-in on the DC pad directly connected to the cavity central conductor (labeled galvanic DC pad). (c) Zoom in on the ground plane opening in the CPW, where the mesoscopic circuit is visible. It is surrounded by trenches needed for the transfer of a CNT with the stapling technique. (d) Zoom-in on the coupling capacitances of the CPW to the RF ports.

3.1.1 Cavity geometry

The microwave cavity is a $\lambda/2$ 2D coplanar waveguide (CPW) fabricated by etching Nb deposited onto a Si/SiO_2(500 nm) high resistivity substrate. The CPW consists in a strip of Nb (typically $100 - 150$ nm thick), that we will call the central conductor of the cavity, interrupted by two capacitances that couples the cavity to two input/output lines, and surrounded by two "infinite" ground planes (figure 3.1(d)). The electromagnetic field propagates in a quasi-transverse electromagnetic (TEM) mode. On the same sample, DC pads and lines are prepared for the CNT circuit, as visible in figure 3.1 (b) and (c). In the rest of this discussion, we will call "CNT circuit" the metallic lines that are used for the transport measurement, labelled sample DC lines in the picture. The smallest part of these lines (in the 100 µm × 100 µm ground plane opening), which are done separately during the fabrication process, will be called the "microscopic CNT circuit".

The cavity geometry can be chosen using a simple model of the distributed impedance of the strip, which is a function of its width and height, of the width of the surrounding insulating gaps and of the permittivity of the dielectric [199]. This impedance matches the one of our RF equipments at $Z = 50\ \Omega$. The resonant frequency then depends on the length of the strip [199]. A figure of merit of the CPW is the resonance quality factor, defined as $Q = \frac{f_c}{\Delta f}$ with f_c the resonant frequency and Δf the FWHM of the amplitude of the signal[1]. The quality factor depends on both the internal losses (linked to the Nb kinetic inductance, the quality of the Nb film and the SiO_2 substrate, as well as the cleanliness of the process), and to the capacitive coupling to the RF ports [200].

In order to couple a CNT circuit to the microwave cavity, a metallic line is connected to the central conductor of the CPW at a antinode of the electric field (of the resonant mode). This way, the CPW mode extends to the circuit region close-by (as shown in figure 3.1(c)). The DC electrostatic potential of this metallic line can be left floating, or alternatively controlled by a DC pad that is directly connected to the central conductor of the CPW, at a node in the electric field (figure 3.1(a)). The CPW mode is partially protected by the presence of a long thin metallic line, yielding a large inductance between the pad and the cavity central strip. This DC contact to the cavity gives more flexibility in the design of the electron-photon coupling: it can be used either as an electrode of the mesocopic circuit (galvanic coupling), or as a floating gate (capacitive coupling).

However, connecting metallic lines onto the central conductor of the cavity can greatly modify the resonant mode, and reduce its quality factor, for both capacitive and galvanic coupling. To highlight these effects, we have first measured the influence of a capacitive

[1] Δf is related to the lifetime of the photon in the cavity; Q is thus an indication of the number of times the photons can bounce back and forth in the cavity before being dissipated or exiting in the RF ports.

coupling between the mesoscopic circuit and the cavity on the resonance quality factor. We have then simulated the effect of a galvanic connection on the central conductor of the CPW.

3.1.1.1 Influence of a capacitance to a DC line

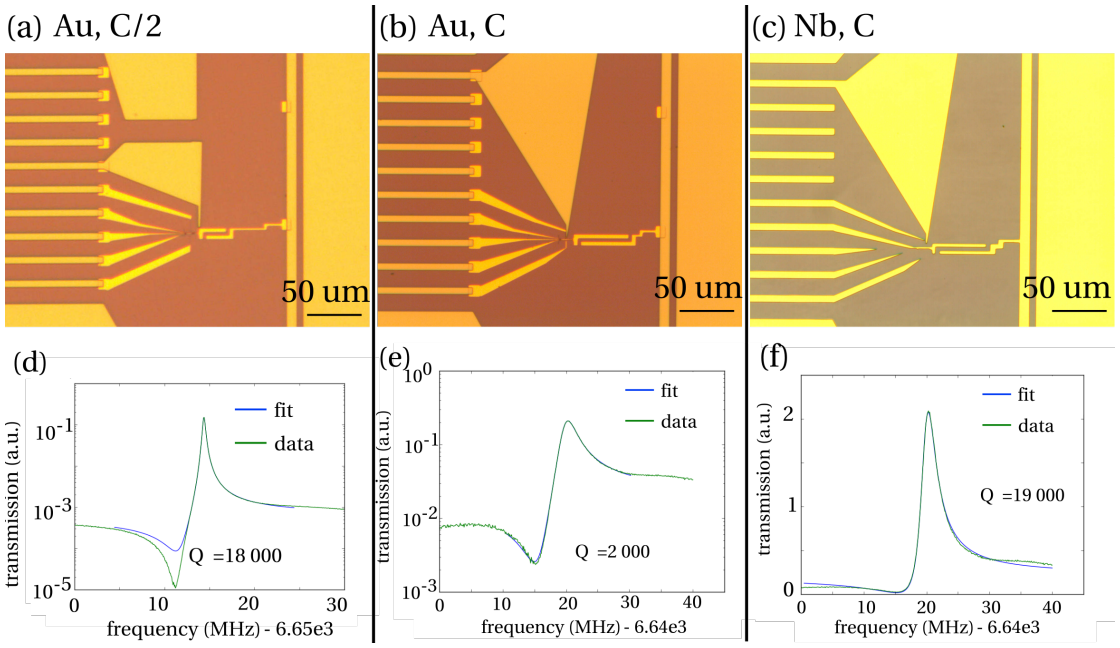

FIGURE 3.2: **Impact of a capacitive coupling to DC lines on the cavity:** (a, b, c) Picture of the three test devices, with a capacitance connected to the central conductor of the cavity. (a, b) correspond to two capacitances made out of gold, of respectively (d, e, f): Transmission amplitude (in linear scale, arbitrary units) as a function of the probe frequency (green line), with a fit using a Fano transmission (blue). The fit equations can be found in M.C. Dartiailh PhD thesis [201]. The measurement method is described in section 3.1.3.

To study the influence of a capacitive coupling on the quality factor, we have fabricated several samples with a capacitance between a DC line and the CPW central conductor. The chosen capacitance value is similar to the capacitance C of the input/output ports of the cavity: C is made out of two metallic lines of length 50 µm and height 150 nm facing each other, separated by a gap of 3.5 µm. The label $C/2$ refers to two lines of half this length, as can be seen in figure 3.2 (a,b,c). One of this line is connected to the central conductor of the cavity, the second to a DC line in the cryostat. The capacitance C is either made out of a dissipative (normal) metal, gold, or a superconducting[2] metal, niobium.

The resulting transmissions are shown in figure 3.2 (d,e,f). The quality factors have to be compared to the ones of a similar resonator with no capacitance to a DC line,

[2] at the measurement temperature, 300 mK.

$Q \sim 40\ 000$. We see that for both (e) and (f), the quality factor is reduced to about $Q = 18000 - 19000$, but is still high enough for our experiments[3]. However, for a large, dissipative capacitance (c), the quality factor is strongly reduced, at $Q = 2000$. Finally, we can note that for the gold capacitances, the resonance has a Fano shape, indicative of a coupling to a parasitic 3D mode, which can contribute to the depreciation of the quality factor.

This measurement is particularly relevant in light of the development of the stapling technique, the new CNT transfer technique that was developed in the group during this thesis. It will be described in more details in section 3.2. For the stapling, one needs to fabricate sufficiently long electrodes (at first, we were typically using electrodes of length 70 µm). In ref [185], in the presence of such a large capacitance (made out of superconducting aluminum) between the cavity and the surrounding DC gates, the quality factor was 4200. It will become all the more important to understand and take into account this effect when designing more and more complex circuits. Indeed, they can require adding more elements in the ground plane opening of the cavity, which risks increasingly perturbing its resonance.

3.1.2 Influence of a galvanic DC contact on the cavity

We now focus on the effect of a galvanic connection of a DC line onto the central conductor of the resonator, as shown in figure 3.1(a). This DC line is positioned at a node in the electric field. The dissipative cryostat circuit is separated from the cavity central conductor by an inductance (a long, thin Nb line). Cavities with such DC bias typically have lower quality factor, in the order of 1000, up to 10 000 [202].

A first test was made without the microscopic CNT circuit. The inductive line is adapted to a 70 Ω impedance, while the cavity is adapted to 50 Ω. The transmission[4] as a function of the probe frequency is represented figure 3.3, corresponding to a quality factor of 5100.

To gain more insight into the impact of the DC circuit, and how to best design the cavity, it can be accurately simulated using Ansys HFSS (High Frequency Structure Simulator), a 3D electromagnetic simulation software relying on finite element modeling of the structure, and numerical solving of the Maxwell equations.

In order to simulate the full CPW geometry, we first have to model the connection of the sample DC lines to the instruments, through the sample holder and the cryostat lines. In the cryostat, the DC lines are connected to low-pass filters as described in figure 3.4

[3] A rule of thumb can be that we want a cavity linewidth much smaller that the coupling to the leads
[4] the line amplification and attenuation is not compensated in this value

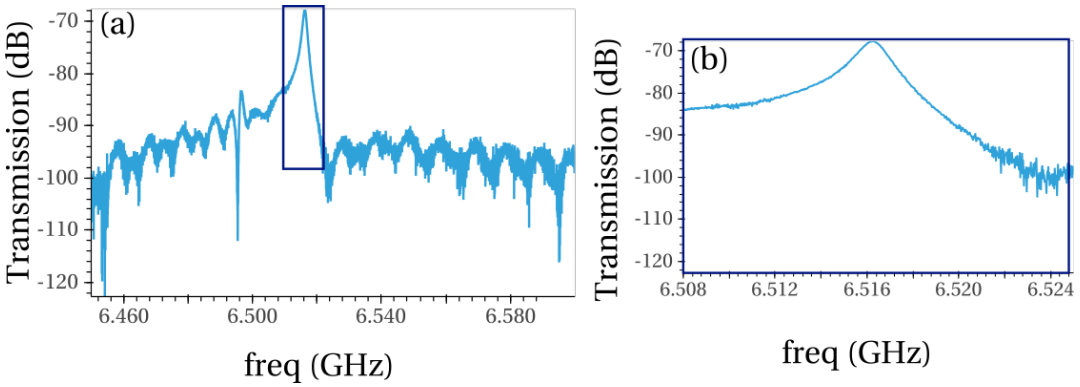

FIGURE 3.3: **Resonance of a CPW with a galvanic DC pad:** Transmission of a CPW with an inductive line, as a function of the input tone frequency on two different range of frequency (the lines amplification/attenuation offset is not removed). The resonant frequency is $f_c = 6.52$ GHz, and the quality factor $Q = 5100$. The cavity geometry for this measurement is shown in figure 3.1.

(a), but we do not know exactly the values of the inductance and resistance of the lines from the sample to the filter at the expected resonant frequency (around 6.5 GHz) .

In HFSS, we can model these lines by connecting the DC bonding pad to the ground through a lumped RLC circuit (noted as a Z impedance). A figure of merit to check that the modeling is realistic is to look at the quality factor of the resonant mode, and compare it with experimental results. We tested different modeling on a simple design of a cavity with no inductance, which has been measured several times with quality factors of the order of 50 000. We found that only taking into account an inductance of the order of 1 nH (expected for the bond wire) yielded unrealistic quality factors compared to our measurement, of more than 10^5. Describing the circuit as an effective resistance of $R = 50\ \Omega$ gave a quality factor of 42 000, much closer to our empirical expectations. For the CPW with the inductance and no DC circuit, the simulations with $R = 50\ \Omega$ gave an expected quality factor of 4100, also very close to the actual measurement presented in figure 3.3.

As a consequence, this convention was taken for the subsequent simulations: the DC lines are all connected to a $R = 50\ \Omega$ resistance to the ground. This is represented in the simulation drawing of figure 3.4 (b) by the dark blue blocks connected to the DC pads.

Several geometries were tested to study the influence of the cavity DC pad, both with and without the microscopic CNT circuit (the simulation parameters are detailed in Appendix C). The optimal geometry is shown in figure 3.5. The cavity drawing is shown in panel (a), and the magnitude of the electric field of the CPW resonance mode is plotted in different regions of the resonator in panels (b), (c) and (d). For this resonance, the quality factor is $Q = 5000$, at frequency $f_c = 6.4$GHz. A second parasitic

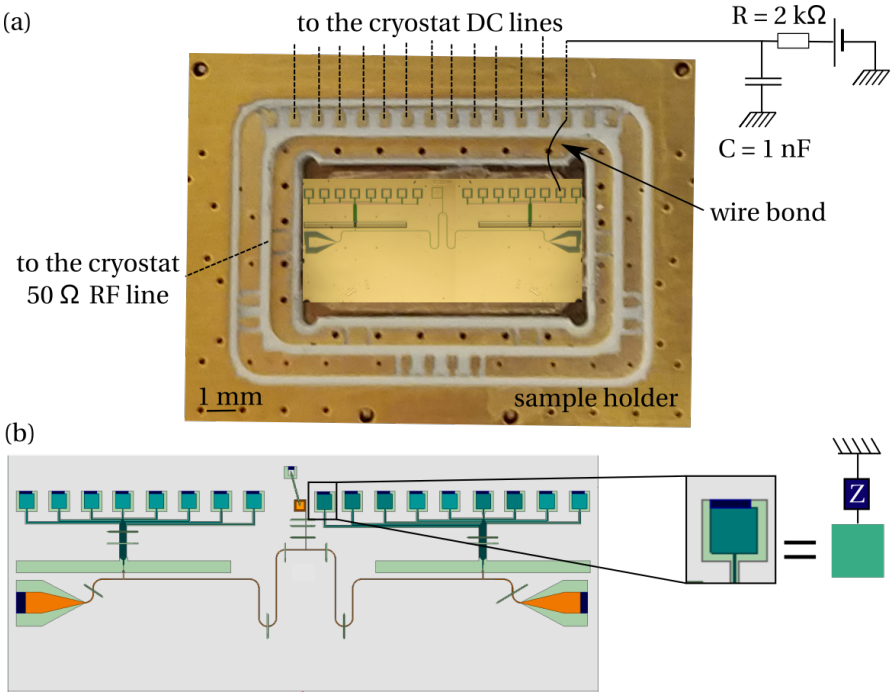

FIGURE 3.4: **Modeling of the fridge lines in HFSS:** (a) Picture of the sample holder and schematics of the circuit on the DC lines in the cryostat (the ones that connect to the sample holder). (b) Corresponding cavity drawing for HFSS simulations. On each DC line, the fridge circuit is represented by a Z impedance to the ground.

mode exists at $f_{\text{para}} = 7$ GHz (with the electric field magnitude distribution shown in panels (e) and (f), concentrated in the DC lines and galvanic DC pad). Given its quality factor ($Q = 24$), it is supposed to be well separated from our CPW mode. However HFSS cannot calculate Q very accurately; the order of magnitude is so that this mode could couple to the CPW mode and degrade its quality. Simulating the same geometry with a larger capacitive coupling between the cavity and the DC lines reduced the quality factor to $Q = 3300$ (see panel (g)), as experimentally measured in a different geometry in section 3.1.1.1.

Geometry	f_c (GHz)	simulated Q	Measured Q
No galvanic DC pad, no DC circuit	6.8	42 000	$\sim$ 50 000
Large 50 Ω DC pad, no DC circuit	7.0	2 700	
Large 70 Ω DC pad, no DC circuit	6.7	4 100	5 000 (fig 3.3)
Small 70 Ω DC pad (of fig 3.5, no DC circuit)	6.4	6 100	
Small 70 Ω DC pad (of fig 3.5 (with DC circuit)	6.4	5 000	

TABLE 3.1: Quality factor Q and resonant frequency f_c for some of the cavity geometries tested.

The result of some of the simulations is summarized in table 3.1. In addition, we have observed that the cavity resonance has a higher quality factor when the inductance has

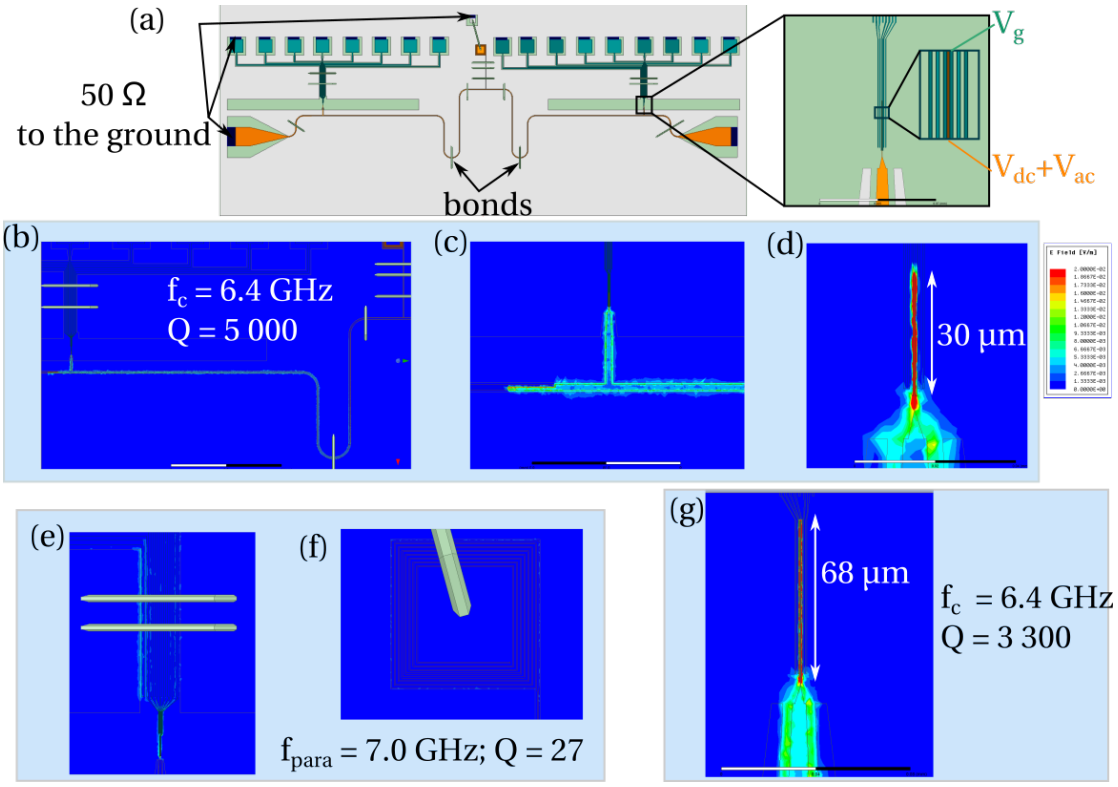

FIGURE 3.5: **Simulations of the influence of a galvanic DC pad on the cavity mode:** (a) Large-scale drawing of the best cavity geometry tested. The ground plane are represented in light green, the SiO_2 in light green, the DC lines in green and the cavity central conductor and input/output ports in orange. (b) Electric field magnitude for the CPW mode (f_c = 6.4GHz, Q = 5000), on several regions : the center of the cavity, the input capacitance and the CNT circuit. (e, f) Parasitic mode at f_{para} = 7 GHz, oscillating in the DC lines. (g) CPW mode for the same geometry, with a larger coupling capacitance between the DC circuit and the cavity.

the following characteristics: the center pad is small[5], and the inductive line between the cavity central line and the DC pad is not adapted to a 50 Ω impedance (the impedance tested on these parts is 70 Ω, similar to the value for the CPW measured in figure 3.3). These results are slightly dependent on the specific dimensions of the microscopic CNT circuit, notably the width of the electrode connected to the cavity (we observed a variation of Q of 15%), and as stated before on the modeling of the fridge circuit. Finally, in these simulations all the metals were considered as ideal metals (perfect conductors), which is true for the superconducting Nb sheet but not for some metals of the CNT circuit.

In the end, these simulations are very helpful to identify trends in the impact of the geometry on the CPW resonance quality factor, but only the actual transmission measurement can really give the quality factor of a given design. The strong dependence of the simulation result on the cryostat line modeling is an indicator that the cavity resonant

[5] we compared two pad: the "large pad" of width 200 µm, and the "small pad" of width 100 µm (bonding pad and snail)

mode is not protected enough from these dissipative lines. More work could be done to improve its isolation, for example adding lumped-elements filters or stub on the DC lines.

Evaluation the circuit-cavity coupling A small side note can be made here about another potential interest of these simulations: they enable us to see how the mesoscopic circuit can couple to the cavity. Here we did not plot the good metrics to study this effect. Indeed, the coupling to the cavity was discussed in section 2.4.1. It was shown that the coupling strength to one circuit element depends on the electrostatic potential of the CPW mode at this element, in equation (2.46). The visibility of transitions between two circuit elements depends on the change in coupling strength between these two elements, thus on the variation of the electrostatic potential along the mesoscopic circuit[6].

In order to know how the CNT circuit will couple to the cavity photons, we can extract from the measurements the evolution of the electrostatic potential V along the CNT circuit. If the CNT axis is x, one should plot

$$V(x,y) = \int_{\text{CNT circuit}} E_x dx \tag{3.1}$$

3.1.3 Cavity transmission measurement

Our microwave cavity resonant frequency is typically around $f_c = 6.5$ GHz. Since we cannot acquire and measure a signal at this frequency fast enough, we modulate an input microwave signal (called the local oscillator, LO) by multiplying it with a $f_{IF} = 20$ MHz signal (generated by an AWG, and called the intermediate frequency, IF) using a single side band mixer (SSB) before sending it to the cavity input. After passing through the cavity, the signal is down-converted by multiplying it with the LO signal, resulting in a signal at f_{IF}. We use an I/Q mixer that returns both quadratures of the signal. An analog-to-digital converter (ADC) collects several traces of this signal (typically 10000) with a sampling rate of 1 Gs/sec[7], and averages them. We can then extract the I and Q quadrature by multiplying the averaged trace by $2\cos(\omega_{IF}t)$ and $2\sin(\omega_{IF}t)$ [8]. Knowing I and Q, we calculate the phase and amplitude of the output signal using:

$$A = \sqrt{\frac{I^2+Q^2}{2}} \qquad \varphi = -\arctan\left(\frac{Q}{I}\right)$$

[6] In the two simple cases described in section 2.4.1, we had a DQD with $g \neq 0$ for one dot only, and a SQD coupled to a lead with $g \neq 0$ in the dot, $g = 0$ in the lead.

[7] The sampling rate is expressed in giga sample per second, meaning that we collect one data point each nanosecond.

[8] the factor 2 compensates for the $\frac{1}{2}$ average value of a $\cos^2$ or $\sin^2$ function.

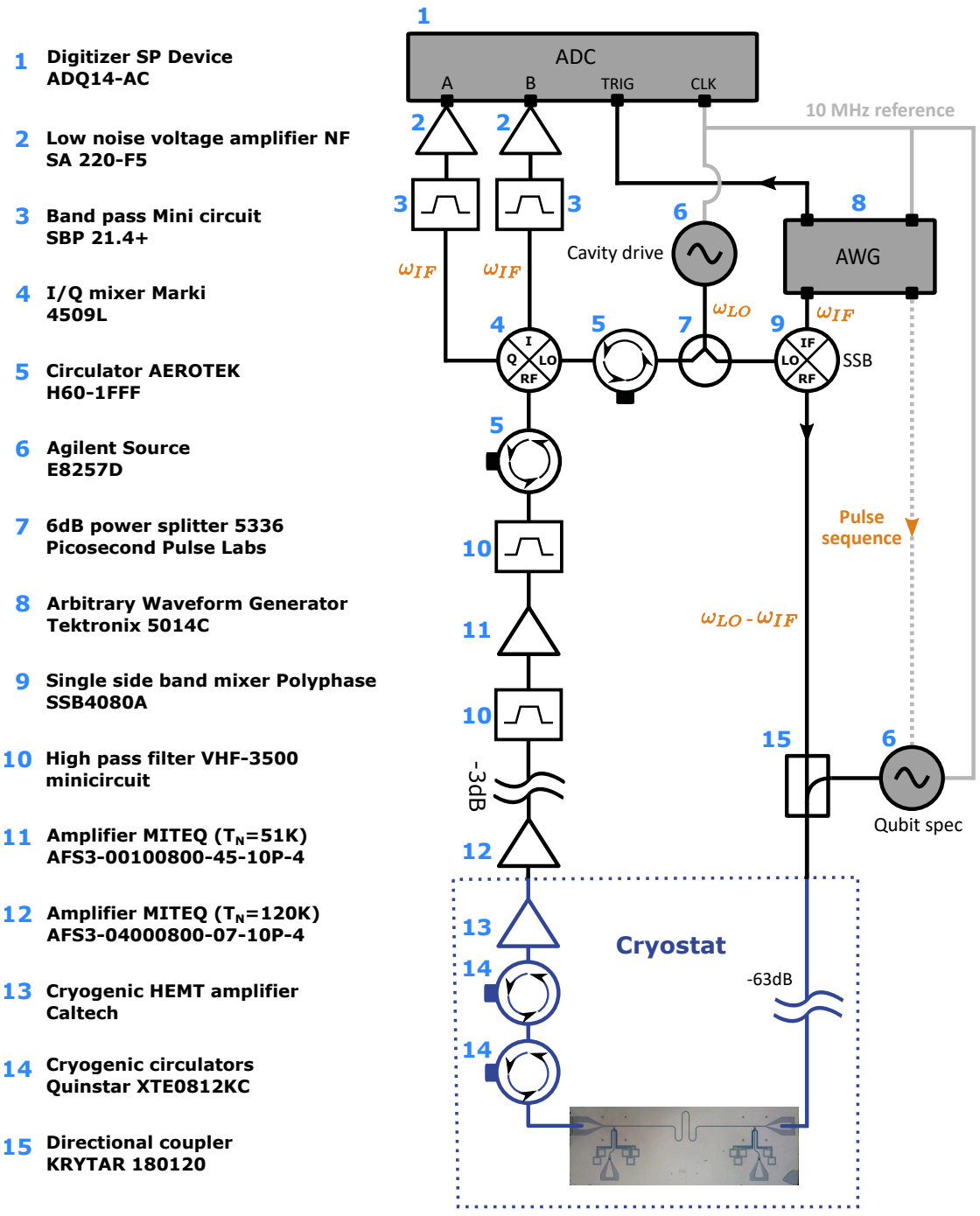

FIGURE 3.6: **Schematic of the RF measurement setup**

The precise measurement setup used in this thesis is presented in figure 3.6.

3.2 Carbon nanotubes

We use a carbon nanotube (CNT) as a nanoconductor for building quasi-one dimensional circuits. Carbon nanotubes have the advantage of being rather simple material, that can be fully modeled without the need for effective band approximations [203, 204].

CNTs can be grown by chemical vapor deposition (CVD). To obtain CNTs, we deposit a catalyst containing iron nanoparticles on the growth chip (either the quartz pillars for the stamping or the comb for the stapling, as will be explained later on), in low density in order to avoid the formation of bundles of CNTs[9]. The chip is positioned in a furnace, and heated up to 900°C under a mixed flow of H_2 and CH_4. The specific steps of the CNT growth are given in section 3.2.2. We here describe how to embed these CNTs into a microwave cavity. We then discuss the possibility to characterize the CNTs with other tools than the transport measurements.

3.2.1 CNT transfer techniques

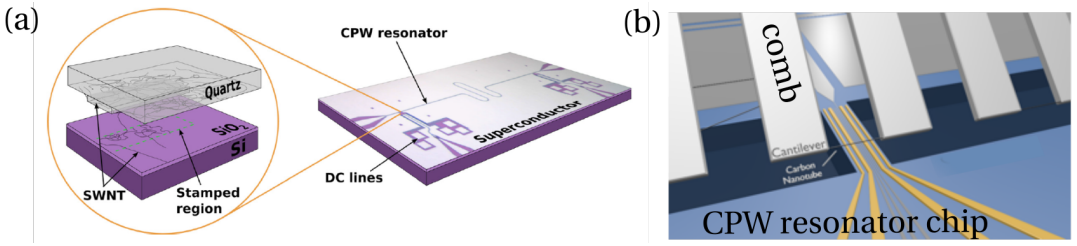

FIGURE 3.7: **The two transfer techniques used during this thesis:** (a) the stamping technique consists in randomly depositing CNTs grown over quartz pillars in a selected area of the CPW chip. (b) the stapling technique enables a transfer of a specific CNT, selected on a comb of cantilevers. The transfer can be done at the very last step of the fabrication. In the image, the comb chip is held above the CPW chip. Adapted from [236] and [2].

The fabrication of a CNT circuit inside a microwave cavity is a constrained problem. On the one hand, the growth results in a variety of CNTs, not a single type (even though the growth conditions can be tuned to affect the diameter and number of walls of the CNTs obtained, as well as the probability of forming bundles). On the other hand, one has to pay attention to the evolution of the quality of the microwave cavity during the fabrication of the CNT circuit: the CNT growth at 900°C cannot be done on the same chip as the one used for the microwave cavity without destroying the CPW resonance

[9] A bundle occur when a CNT is rolled up with one or several other CNTs

(because of dislocations and impurities, that affect the high frequency properties of the superconductor).

To circumvent these issues, we use a growth chip different than our cavity chip. We then image the grown CNTs and select a "good" one. The rest of the circuit can then be drawn around the selected CNT, or the chosen CNT can be transferred onto an already prepared circuit. The two approaches where used during this thesis: first the existing stamping technique was used for the device of chapter 4, then a new stapling technique was developed, tested and used for the device presented in chapter 5 (as well as two of the control devices of chapter 4).

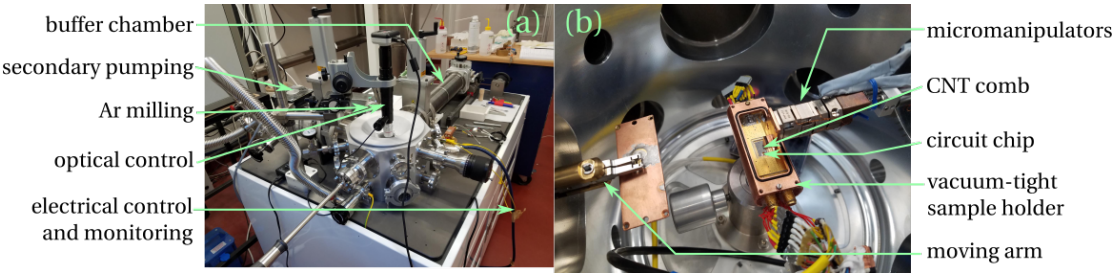

FIGURE 3.8: **Photograph of the stapler:** (a) large scale of the stapling machine. We can see the optical microscope, the Ar milling gun, the electrical wires for the monitoring of the stapling. The comb is retracted in the buffer chamber during the Ar milling. (b) Zoom-in on the vacuum chamber, where the sample holder is visible as well as the micromanipulators used for displacing the comb when stapling. The stapling is done under vacuum, then the sample holder is sealed with the cover held in the moving arm.

Figure 3.7 presents the difference between those two fabrication techniques. The first local transfer technique, called stamping technique, was developed by J. J. Viennot [205]. Two chips are prepared, a microwave cavity with a ground plane opening and a quartz chip with etched pillars. CNTs are grown over the pillars before the two chips are aligned one above the other with a mask aligner and brought into contact. CNTs are transferred randomly in the ground plane opening of the cavity, imaged using an SEM, and then contact electrodes are lithographically defined. Details of the fabrications can be found in M. M. Desjardins's PhD thesis [206]. The drawback of this technique is that this last lithography step can introduce defects in the CNT, due in particular to resist residues[10]. As a consequence, this technique had a low yield, and the resulting devices were not always very tunable.

In order to improve these aspects, the second transfer technique, called stapling technique was developed, largely due to the work of T. Cubaynes [2]. Inspiring ourselves from several recent works [183, 207–209], we designed a new transfer machine, shown in figure 3.8; its usage is described in more details in 3.5.2.2. This technique enables

[10] In addition, theelectron-beam exposure directly on the CNT may also introduce defects in the lattice.

an accurate positioning of one given CNT, which can be deposited onto its electrical circuit, and does not undergo any post-transfer processing. If the height of the contact electrodes is sufficient, the CNT can be suspended which enables a much better control on its electrostatic environment.

The main steps of this transfer technique are as follows. On the one hand, a cavity chip is processed to contain the microwave cavity and the metallic electrode needed for the CNT circuit. Trenches of depth of about 10 µm are etched around these electrodes. The cavity chip is then positioned in a sample holder in the transfer chamber, and electrically connected to a monitoring rack. On the other hand, CNTs are grown over a comb of cantilevers, and imaged after growth. The comb is positioned in a mobile section of the transfer chamber, and the segment containing the most promising CNT is aligned over the cavity chip using attocube micro-manipulators with optical microscope monitoring, under vacuum (at pressure in the 10^{-7} mbar range). The comb is then lowered below the level of the contact electrodes into the trenches, until an electrical contact is detected between the circuit electrodes. The CNT ends are cut using outer electrodes made for this purpose. The comb is retracted, and the sample holder is sealed, still under vacuum, using a moving arm. The sample holder can finally be transferred to a cryostat and cooled down.

A new sample holder was designed to withstand vacuum, thus reducing the risk of a chemical reaction of the CNT (when the stapler-cryostat transfer is done under atmospheric condition, the CNT often worsen during transfer; when done with a nitrogen flow, a change was less frequent; transferring under vacuum is the ideal situation), as shown in figure 3.8 (b). This sample holder is made of several pieces that are glued together using epoxy glue, which is also used to fill-in the vacancies around the SMA and DC electric cables. Although the SMA connectors in themselves are not vacuum tight, tightened SMA cables are (we use here the Astrolab 16301 minibend cables). Finally, a rubber gasket enables to seal the cover onto the sample holder. Such a sample holder can be pumped down to 6×10^{-5} mbar in 10 minutes, and after 10 minutes in static vacuum the pressure has only increased to 2×10^{-2} mbar. However the thermal cycles tend to degrade the epoxy resist; future developments of this sample holder would benefit from being made out of a smaller number of separated pieces.

Overall, the stapling technique has greatly improved the success yield of the fabrication process. Resonators can now be measured beforehand, and besides a given circuit can be used multiple times, with different CNTs. These advantages open the way to more complex devices, as well as the use of better characterized CNTs as we will now discuss.

3.2.2 Carbon nanotube fabrication and characterization

The CNTs obtained with a given growth recipe can be characterized by TEM measurements, giving us access to the distribution of diameters and the ratio between SWNT and MWNT.

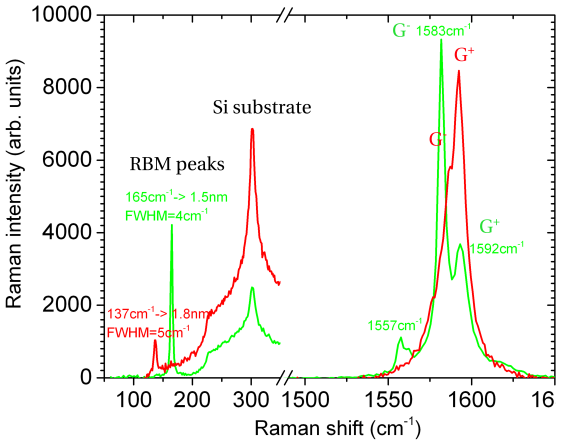

FIGURE 3.9: **Raman spectroscopy of the sample MU9TRd**. Two traces are represented, corresponding to measurements with two lasers, a red (red curve) and green (green curve) one.

On the other hand, a specific CNT can also be characterized by various techniques. Thanks to the development of the stapling, it is becoming possible to exhaustively characterize a CNT before transferring it to a mesoscopic circuit. Among the tools available, there are the AFM which gives an estimate of the CNT diameter, Raman spectroscopy, for establishing the presence of defects [210], and which can give information on the tube structure and character (metallic or semi-conducting) [211, 212], and Rayleigh spectroscopy which can directly reveal the chirality of a single wall carbon nanotube [213, 214]. Rayleigh spectroscopy however is more restrictive since one needs the CNT to be suspended, but it is fully compatible with the growth on combs of the new stapling technique.

For now, we have tried to develop Raman spectroscopy of our CNT, combined with AFM measurement of the diameter. Raman spectroscopy can enable us to distinguish between a single wall, a multi-wall or a bundle of CNTs, and also, for a single tube, between a semi-conducting or a metallic one. Indeed, the Raman spectrum of a SWCNT will show two peaks around 1600 cm^{-1}, called the G^+ and G^- peak, associated with the vibration of the C-C bound. The G^- peak position and width depends on diameter and character of the tube (although for metallic CNT, the G^- peak can be very broad): the spacing between the two peaks can be used to extract to the diameter of the CNT. For a bundle or a multi-wall CNT, there will be as many G^- peaks as NT, and the G^- peak energy can be renormalized by the interaction with the other NT, making the interpretation of

a spectrum more complicated. A D peak at around 1350 cm^{-1} can be seen when there are defects in the CNT [210]. Finally, if the energy of the laser is close to the energy of the electronic transitions of the CNT, we can observe an additional peak between 50 cm^{-1} and 400 cm^{-1}, also directly linked to the diameter of the tube.

In figure 3.9 the Raman spectrum of the CNT in sample MU9TRd is shown (the magnetic sample that will be presented in chapter 4), for two lasers (red and green). It was measured by Aurélie Pierret of the LPENS. We interpret this spectrum as follows. We observe the signal associated with two CNTs, a metallic one, which gives a broad signal around the G peak and a RBM signal at 137 cm^{-1}, corresponding to a diameter of 1.8 nm (seen with the red laser), and a semi-conducting CNT, which gives two peaks at high shift (1583 cm^{-1} and 1592 cm^{-1}) and a RBM signal at 165 cm^{-1} corresponding to a diameter of 1.5 nm (seen with the green laser). The peak at 300 cm^{-1} corresponds to the Si substrate. No D peak is detected, indicating a good quality of the CNT.

For now these new characterization techniques have only been used as post-processing of our electrical circuit. This could already help us to detect trends in the CNTs growth and transfer. In a foreseeable future, Raman spectroscopy, or even more so Rayleigh spectroscopy will enable us to select a CNT knowing its exact structure, prior to its stapling.

3.3 Magnetic texture

During this thesis, we have fabricated mesoscopic circuits to study the effect of an oscillating magnetic field on confined electrons in a CNT, as theoretically studied in chapter 2. The oscillating field is generated by a ferromagnetic gate containing several magnetization domains, placed below the CNT. The magnitude of the stray field at the position of the CNT needs to be large enough to induce a Zeeman splitting of the electronic bands. Additionally, the smaller the domains the stronger the synthetic spin-orbit coupling, as shown in section 2.2.1. We present here as a magnetic texture a Co/Pt multilayer, and its characterization. We compare different magnetic characterization tools, MFM, SQUID and Hall bar, their advantages and limitations.

3.3.1 Formation of a magnetic texture

Bulk ferromagnetic materials have a exchange interaction that tends to align neighboring spins; thus they can present a uniform magnetization[11] below the Curie temperature

[11] At external magnetic field $B_{ext} = 0$, this is only true locally.

(that depends on the strength of this interaction). This temperature is about 1400°C for Co, much larger than the temperatures at which we work (300 K for some characterizations, 4 K or below for the measurements). Depending on the material crystalline structure, the spin orientation can have a favored direction, called the anisotropy axis. In finite structures, the magnetic ground state also depends on the demagnetizing field, i.e. the magnetic field generated by the magnetic moments ordering inside the material (which generates an energy term called the demagnetizing energy E_d). The shape of the surfaces will affect the shape of the demagnetizing field. For example, in planar magnetic thin films, the shape anisotropy K_d makes it less energetic for the magnetization axis to be in-plane. In more complex structures, several domains can form depending on the energetic cost of the domain wall compared to the demagnetizing energy.

For the synthetic spin-orbit effect, we want to use a structure with several magnetic domains, thus we need to understand how to favor complex equilibrium magnetic structures over a homogeneous magnetization in thin films. Several physical effects can induce an out-of-plane anisotropy K, that competes with the shape anisotropy; if the two are of the same order of magnitude, domains can form. The figure of merit to determine the magnetic ground state when the two anisotropies compete is the quality factor $Q = K/K_d$[215]. The effective anisotropy, $K_{eff} = K - K_d$, roughly represents the cost of having domain walls. Several scenarii can be distinguished:

- If $Q = 0$, the magnetization is uniform, in plane,
- If $Q \ll 1$, the magnetization is mostly in plane, but there can be a critical thickness from which a fraction of the magnetization is out-of-plane and oscillates (this is called “weak stripes”),
- If $Q \sim 1$, there can be periodic domains,
- If $Q \gg 1$, the magnetization is uniform, out-of-plane.

Several effects can provide an out-of-plane anisotropy. First, strain can provide enough out-of-plane anisotropy to induce spontaneous oscillations of the magnetization in certain ferromagnetic material. This is the case for Ni [216]: in Ni nanostructures, the out-of-plane component of the magnetization oscillates along the smallest dimension. However only a fraction of the total magnetization oscillates, which will give a low value for the oscillating magnetic field (scenario $Q \ll 1$). Second, epitaxial growth of alloys on specific seeding layers, yielding controlled crystalline structures can give rise to domains formation in several magnetic materials (scenario $Q \sim 1$): for example, CoPt, or FePt have been studied extensively in the spintronics community [217–221][12]. Third, an

[12] Here the crystalline anisotropy is out-of-plane

interface between a ferromagnetic material and a metal with strong spin-orbit interaction provides an interfacial anisotropy term, that will be strongest when the ferromagnetic layer is thin (scenario $Q \sim 1$)[13]. It can can be enhanced by fabricating multilayered structures alternating a magnetic material and a heavy metal [222, 223]: for example, Co and Pt. This is the path that was chosen for our experiments. It is relatively easy to adapt to our fabrication technique (since it does not require an epitaxial deposition), and the anisotropies can be adjusted by changing the parameters of the multilayered structure.

3.3.2 Choice of the magnetic texture

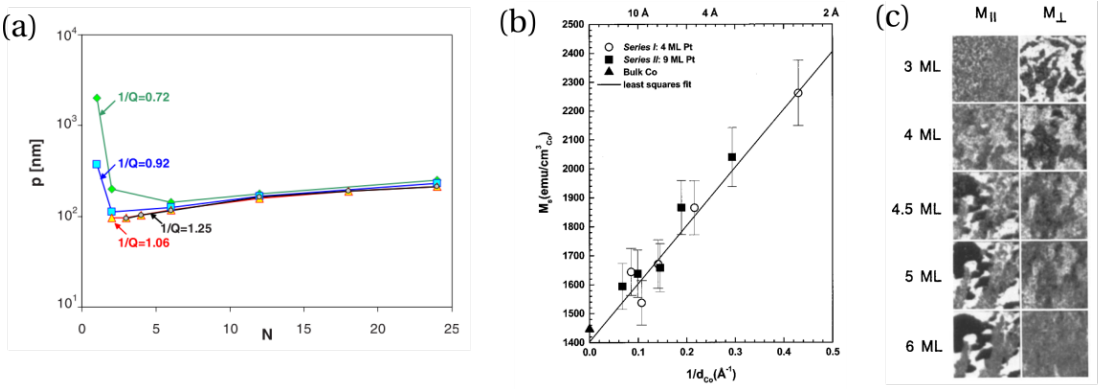

FIGURE 3.10: **Influence of several parameters on the domains** (a) Calculation of the evolution of the domains period p with number of repetition N, plotted for different quality factors $Q \propto K_d t_{Co}/K_s$. Source: [224]. (b) Measurement of the saturation magnetization M_s of a Co/Pt multilayered structure as a function of the Co thickness d_{Co}. Source: [217]. (c) Spin polarized SEM of a Au/Co thin film. The perpendicular and parallel magnetization is shown for several Co thickness, given in monolayers (ML, with 1 ML $\sim$ 0.23 nm. Source: [225].

We now describe how a specific magnetic texture was chosen. The parameters that are important to us when choosing the magnetic texture are, first of all, the presence of domains and their size. The thickness of each layer, and the total number of layers in the multilayered structure will influence these parameters: a large number of layer repetition reduces the domain size, as shown in figure 3.10 (a). The Co thickness t_{Co} affects the interface anisotropy ($K = K_s/t_{Co}$, where K_s is a surface energy density), thus also changes the domain period. The domain formation as a function of Co thickness is shown for example in a simple Au/Co structure in figure 3.10 (c).

We also require a strong in-plane[14] saturation field, that gives us some flexibility in the parameter space in the experiments. This depends on K_s/t_{Co}: the stronger the

[13] $K = \frac{K_s}{t_{FM}}$ where K_s is the interfacial term and t_{FM} is the ferromagnetic metal thickness

[14] Other experimental constraints, notably the presence of superconductivity forces us to apply the external magnetic field in-plane, as will be seen in chapter 4.

magnetization is out-of-plane (ie the stronger the interfacial anisotropy is), the harder it will be to rotate it. Thin layers of Co are thus favorable. Here we can mention that having domains require a *small* effective anisotropy K_{eff} which is usually synonymous of a small saturation field. Indeed, in the simple picture of one domain with an easy axis, the saturation field B_{sat} corresponds to the energy to pay to compensate for not aligning along the easy axis: $K_{eff} = \mu_0 M_s B_{sat}$ where μ_0 is the Bohr magneton and M_s the saturation magnetization. In a multilayered structure with many repetitions, this saturation field can be higher, as the dipolar energy is not minimized through the shape anisotropy but through the flux closure via the formation of domains.

Finally, it is also important to know what is the amplitude of the magnetic field above the texture. Co (or Fe) are materials with strong magnetization, and are good candidates to obtain a large amplitude of magnetic field. Thin Co layers can have their magnetic moment enhanced by the interaction with the Pt layer [217], as shown in figure 3.10 (b).

It was first decided to fabricate a

$$\text{Ta(40 Å)/Pt(48 Å)/[Co(15 Å)/Pt(10 Å)]}_{\times 10}\text{/Pt(38 Å)/Alox}$$

multilayered structure in the Laboratoire de Physique des Solides (Orsay). In future samples, we could fabricate multilayered structures with three metals, such as Pt/Co/Au, and rely on DMI interaction to reduce the domain wall cost [226–228] (thus increasing the saturation field), to optimize these parameters.

3.3.3 Characterization of the magnetic texture

We have characterized this magnetic structure, and notably the important parameters listed above: the size of the magnetic domains, the amplitude of the field oscillations, the in-plane saturation field. We have also tried to understand how the magnetic texture evolves with an external magnetic field, to evaluate which control we can have over the strength of the synthetic spin-orbit interaction.

Unfortunately, these informations are not necessarily easy to measure. We will present here various characterization tools that we have used to try and estimate these parameters.

Magnetic force microscope (MFM) measurement

The principle of the MFM is the same as the atomic force microscope, except that the tip is covered with a magnetic material. It will thus be sensitive to a magnetic field $\vec{B}$. More precisely, the tip has a total magnetic moment $\vec{M}$ that is subject to a force

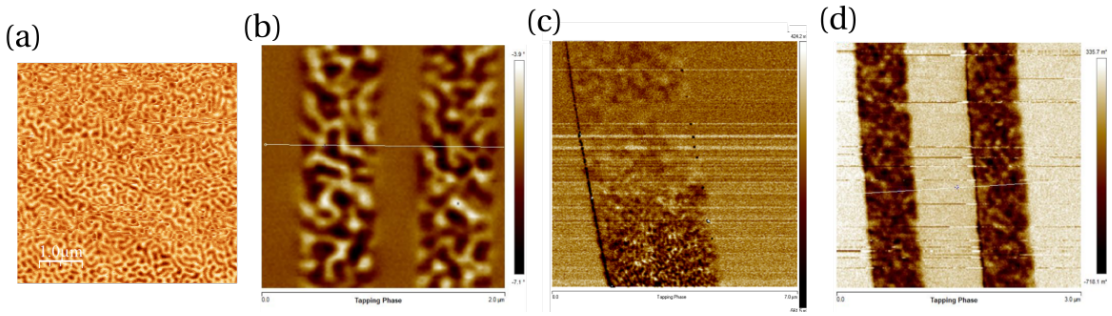

FIGURE 3.11: **MFM characterization of the magnetic texture:** MFM phase signal of three different samples, using tips with a high saturation field and out-of-plane magnetization. Plain chip (a) and nano-structured lines (b, c) of Co/Pt with the first deposition technique, corresponding to Ta(40 Å)/Pt(48 Å)/$[$Co(15 Å)/Pt(10 Å)$]_{\times 10}$/Pt(38 Å)/Alox. In image (c), we see the tip degrading during the scan, greatly reducing the visibility of the domains. (d) Nano-structured gates of Co/Pt with the same recipe, using a second deposition technique.

$F = \vec{\nabla}(\vec{M} \cdot \vec{B})$, in addition to the Van der Waals forces. The change in the MFM phase signal $\delta\phi$ is related to the change in the force applied on the tip when it moves. In linear oscillating mode, the tip oscillates in z, the out-of-plane axis, thus $\delta\phi \propto \frac{\partial^2 B_i}{\partial z^2}$, where i is the magnetization axis of the tip[15].

As a consequence, the MFM does not give a measurement of the magnetic field. It can only be used as a measurement of the dimension of the magnetic domains. Figure 3.11 displays several MFM images obtained for the chosen Co/Pt multilayered structure. For these structures, two depositions techniques were used, corresponding to two different e-beam evaporators. The first one contains two e-beam guns (when the second contains only one), enabling a faster deposition of the layers. For both evaporators the deposition pressure is around 1×10^{-6} mbar. We can already observe that the quality of the image depends greatly on the quality of the deposition and of the MFM tip. We measure domains of typical width $p = 100 - 200$ nm.

To study the persistence of the domains in an external magnetic field, it is possible to do MFM measurements while applying a field. We did such measurements with Karim Bouzehouane, at UMR CNRS-Thales, as shown in figure 3.12. The probe is mostly sensitive to a dipolar signal that appears at 100 mT, coming from the tilting of the domains' magnetization with the external field (as we can see in the simulations presented later on in figure 3.13; it is visible there as magnetic charges at the edges of the structures, generating a magnetic field). Figure 3.12 (b) shows the raw MFM image at 800 mT, dominated by the dipolar signal. We can subtract it to observe the signal associated with the presence of domains, under an increasing magnetic field (c). We see that the domains persist at least up to 800 mT, with a decreasing size. Taking cuts

[15] To avoid being sensitive to the sample topography, $\delta\phi$ is measured at a fixed elevation over the surface, typically $20 - 30$ nm

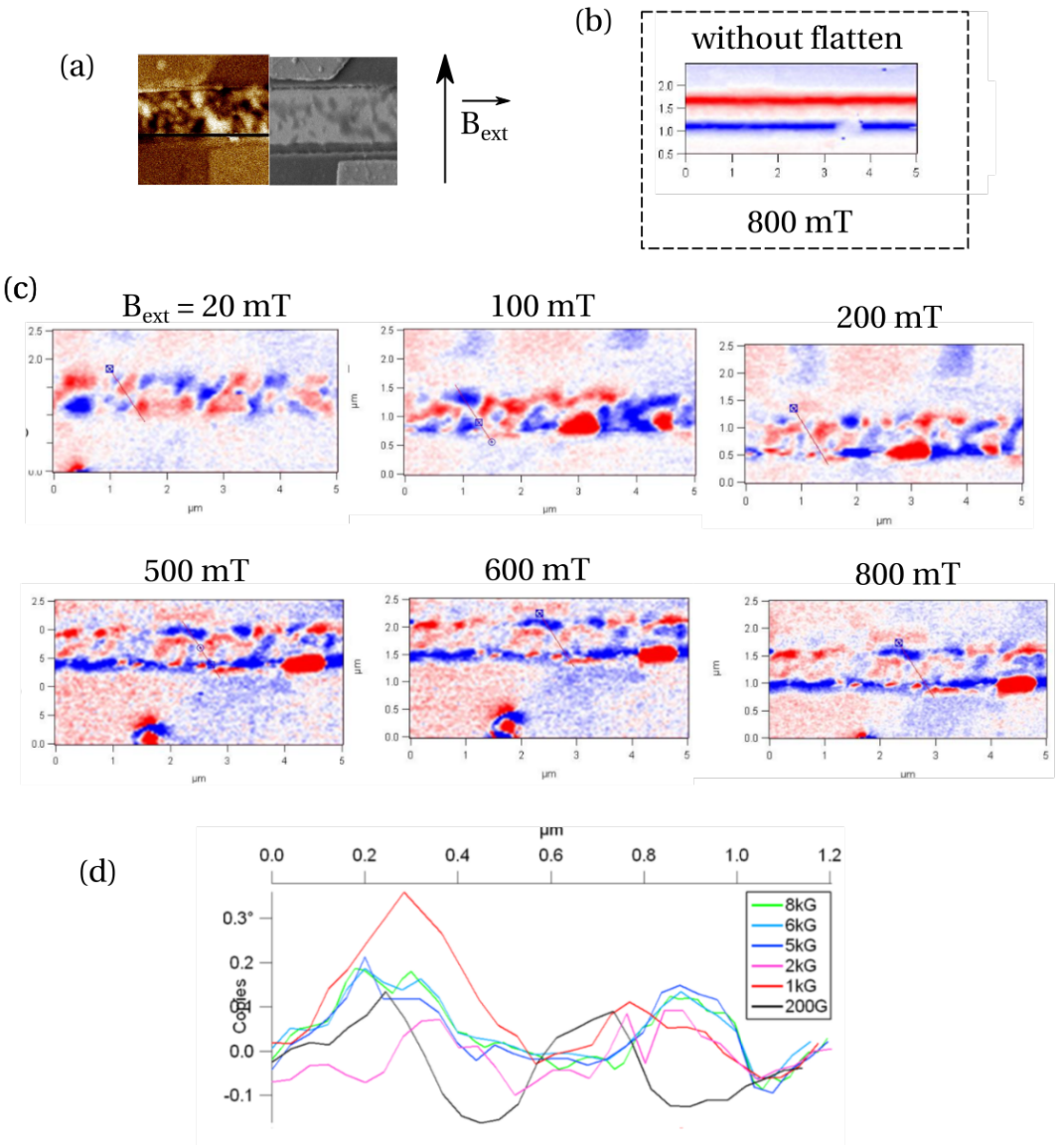

FIGURE 3.12: **MFM characterization at several external magnetic fields:** (a) MFM and SEM image of the same region of sample MU9TRd, showing the location of the CNT. (b,c) MFM measurement of the same region under a magnetic field, with a field MFM. We do not have as good a resolution of the domains with the field MFM. The tip is at about $20 - 30$ nm above the structure. (b) Raw MFM image at 800 mT. The out-of-plane component of the dipolar signal dominates over the domain signal. (c) MFM images where the dipolar contribution is removed ("flattened" images), at increasing magnetic field. (d) Cuts of the MFM signal along the position of the CNT as measured in the topographic images (the position of the cut is indicated on the above images). The scale for the phase signal is 0.6° for the field 20, 100 and 200 mT, 0.3° for fields 500, 600 and 800 mT, and 3° for image (b).

along the approximate position of the CNT shows very slow variations of the oscillating field with an applied external field (d). As said before, these MFM images cannot give us any quantitative information about the oscillating stray field above the structure, but is shows at least that the domains can persist up to high magnetic fields. It also seems to indicate that the domain size tend to decrease until all the magnetization has been

transferred to the in-plane direction.

We enhance here that the strong signal of the dipolar contribution does not necessarily mean that the corresponding field is strong. Indeed, the MFM can artificially enhance a feature compared to another [229]. To evidence this, we can consider a simple case where the magnetic field above the texture is written $B_z(x,z) = B_0 \sin(kx)e^{-kz} + B_0 \sin(k'x)e^{-k'z}$ (the tip is oriented along z)[16]. Then the MFM is sensitive to

$$\frac{d^2B_z}{dz^2} = B_0k^2 \sin(kx)e^{-kz} + B_0k'^2 \sin(k'x)e^{-k'z}.$$

Depending on the elevation z at which the measurement is done and the values of k and k', both frequencies of the magnetic field will not give the same phase contrast in the MFM signal[17].

SQUID (superconducting quantum interference device) measurement and magnetic simulations

To supplement our estimate of the saturation field of the structure, we performed SQUID measurements for both a plain chip of Co/Pt multilayers and a nano-structured chip: see figure 3.13. SQUID measurements enable the study of the evolution of the magnetization when an external magnetic field is applied. From these measurements we can extract both the saturation field and the magnetization at saturation, which in turn can be used to simulate numerically the magnetic texture. A drawback of this measurement technique is that the measured sample needs to have a sufficiently large magnetization: we can only measure plain Co/Pt multilayers, or chips full of nanostructured Co/Pt gates (similar to the ones of the real mesoscopic circuit) which may behave slightly differently than a given transport device of interest. Indeed, differences in the fabrication process will lead to differences in the disorder, which greatly affect the saturation field as will be shown by the numerical simulations.

Whatever the orientation of the applied magnetic field or the magnetic history, no remanence is found. It indicates that the sample spontaneously demagnetizes, as expected for a material with domains. When applying a magnetic field, the magnetization first increases sharply before slowly saturating. The saturation field seems to be slightly larger for the nano-structured chip, although the measurement of this value is not very precise; we estimate it between 1.5 T and 2 T.

[16] For a simple mode where the field only depends on x and z with an oscillatory behavior in x, Maxwell equations yield a decay length in z equal to the oscillation period in x

[17] Note that depending on the tip size and measurement elevation, the signal can also be sensitive to the first derivative $\frac{dB_z}{dz}$, which does not impact the argument.

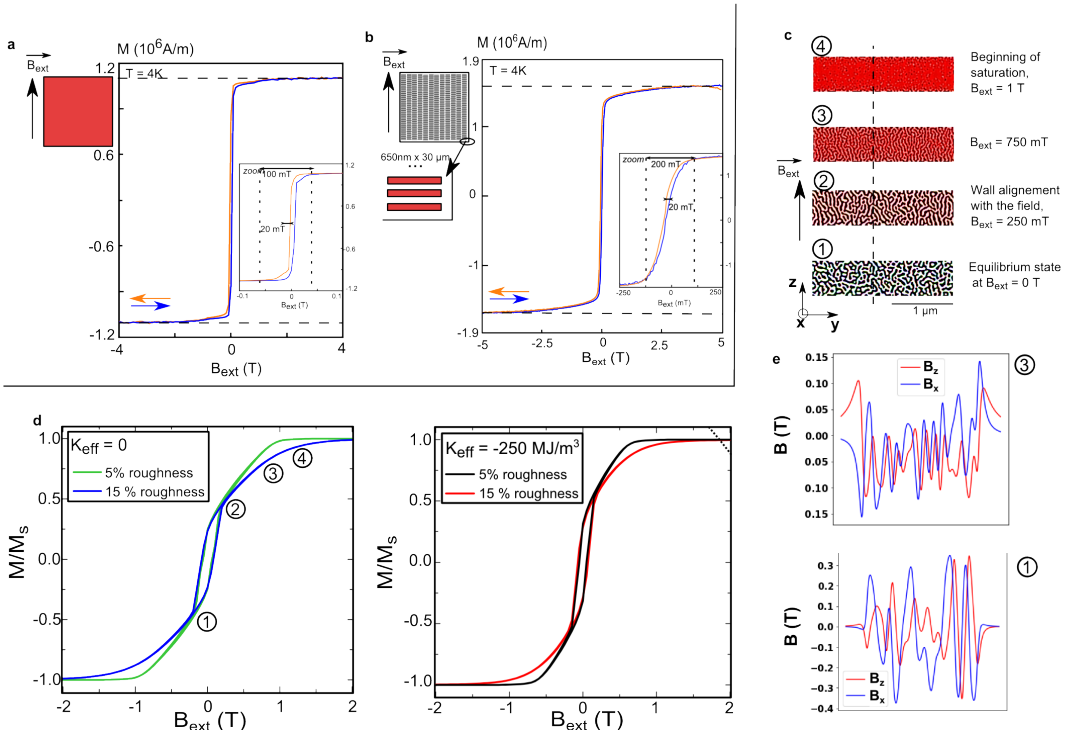

FIGURE 3.13: **Characterization of the magnetic texture using SQUID measurements and magnetic simulations:** (a) SQUID measurement at 4K of a 5mm x 5mm chip covered with the CoPt multilayer (as sketched above). The magnetization saturates at about 1.5T. Inset: Zoom on the SQUID measurement showing the opening of a hysteresis at about +/-50mT, of width 20 mT. (b) Same measurement, for a chip covered with an array of the nanoscale Co/Pt stripes (such as the ones used in the transport experiment, see the layout above). The magnetization saturates at higher magnetic field. Inset: Zoom on the SQUID measurement showing the opening of a hysteresis at about ±100 mT, of width 20 mT. (c) Magnetization texture for zero effective anisotropy and 15% roughness. The white and black pixels correspond respectively to up and down magnetization, the colored pixels represent the in-plane magnetization, colored according to a color wheel to represent their different orientation (red correspond to the applied field direction, see the arrow). The bottom image, numbered 1, corresponds to a virgin demagnetized state; the following are successive images from 0.25 T to 1 T (numbered 2 to 4). Images are 768 nm x 2304 nm, similar to the experimental Co/Pt gate dimensions. (d) Calculated hysteresis loops for in-plane magnetic field, for two anisotropy hypotheses and two magnitude of roughness. (e) Cuts of the magnetic field along the dashed line in c, obtained from the same magnetic simulation. The B_x (resp. B_z) field is represented in blue (resp. red), at a height $x = 10$ nm.

To further understand the magnetization processes in the sample, our collaborator Stanislas Rohart performed micro-magnetic simulations, using the MuMax3 code [230]. As the magnetic parameters are not exactly known, the purpose was not to reproduce exactly the sample under study, but to understand qualitatively the processes, and in particular explain the field strength needed to saturate magnetization as observed in the SQUID measurement. The saturation magnetization used ($M_s = 1.2 \times 10^6$ A/m) has been extracted from the SQUID measurements and the exchange ($K_s = 10$ pJ/m^2) is the one of bulk cobalt. As the magnetic anisotropy could not be measured, he explored two

hypotheses: zero effective magnetic anisotropy, meaning an exact compensation between shape and interface induced anisotropies, and a small negative effective anisotropy favoring in-plane magnetization orientation for homogeneous magnetized states, with an effective anisotropy $K_{eff} = \frac{K_s}{t} - \frac{1}{2}\mu_0 M_s^2 = -250 \times 10^6$ J/m^3, where t is the Co thickness. These hypotheses are in agreement with literature for the interface anisotropy at the Co/Pt interface [231]. For both cases, whatever the magnetic history is, the ground state corresponds to a demagnetized state with periodic stripes [232] (with a period of about 100 nm). Upon applying a magnetic field, the stripes first reorient progressively with a propagation vector orthogonal to the magnetic field to minimize the Zeeman energy in the domain walls (the domain walls being Bloch-type, their magnetization lies in the wall plane). For larger fields, the magnetization in the domains progressively rotates toward the applied magnetic field direction and saturates at about 1 T. Note that textures are still observed up to the saturation. The saturation field value is to be compared to the anisotropy field $\mu_0 H_K = 2K_{eff}/M_s$, which is close to zero. In usual magnetic system with a low demagnetizing strength (low magnetization systems or low thickness), this would cause a saturation at field values close to H_K. Here, the large magnetization and the ten repetitions, both favoring stripe phases, make the saturation much more difficult and therefore result in a saturation field which scales with the magnetization value. The simulation closest to the experimental results is the one with zero effective anisotropy.

Comparing the calculated and the experimental loops we note that the saturation is slower in the sample than in the calculation for a disorder of 5%. Indeed, due to the fabrication process the quality of the substrate could not be optimized, which results in a significant roughness before the deposition. While typical roughness in good magnetic samples is about 2-5%, here larger values could be expected. He also calculated the magnetic loop with increasing roughness up to 15% thickness variation. While the loops are not much changed at small field, we note that due to the disorder, saturation occurs at much larger magnetic fields and the images show that magnetic textures may survive up to 2 T. Since the disorder plays such an important role in the saturation field, one should be careful when comparing measurements done on a test sample designed for the SQUID and the mesoscopic circuit sample.

The MFM measurements and the micromagnetic simulations seem to agree on the evolution of the magnetic domains with an external magnetic field, although the domains are smaller in the simulations than in the MFM images. The tilting of the domains' magnetization along the external field, starting at about 100 mT is seen in the MFM by the apparition of the dipolar signal (see figure 3.12), as well as in the simulations (presence of magnetic charges at the edges of the domains). The domains size then seems to slightly shrink in the MFM images, with a change in the MFM signal coherent with the reduction of the stray field observed in the simulations. These measurements

were used to support a simple modeling of the evolution of the spin-orbit interaction with an external magnetic field.

Hall bar measurement

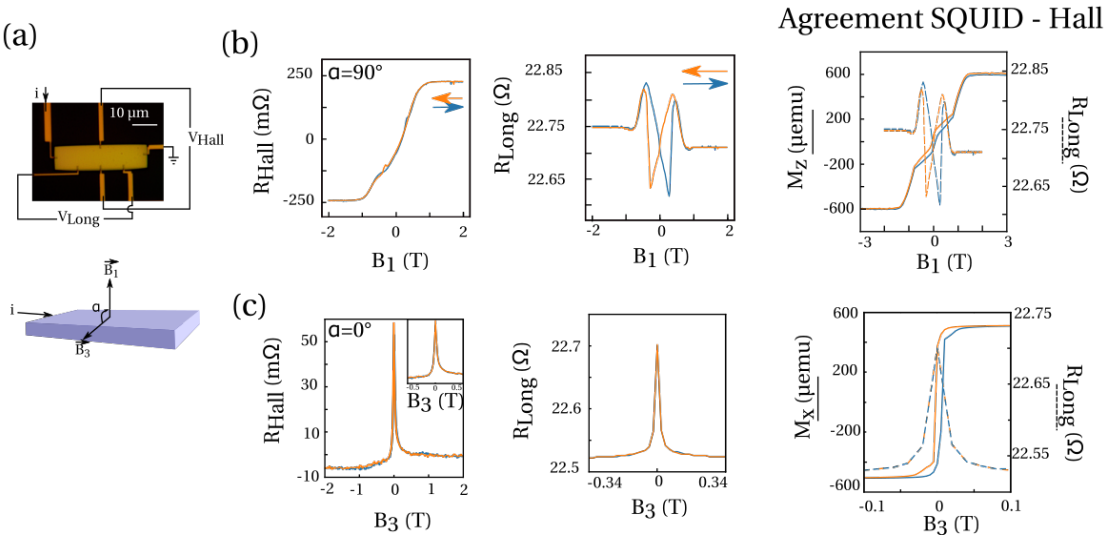

FIGURE 3.14: **Hall bar characterization of the magnetic texture:** Hall bar measurements of the Co/Pt multilayers, with a bar of dimensions 10 µm × 40 µm. (a) Image of the Hall bar with the measurement setup, and orientation of the magnetic fields. (b,c) Evolution of the Hall resistance and longitudinal resistance as a function of an external magnetic field applied in-plane (perpendicular to the current) and out-of-plane. A comparison between SQUID measurements (of a full plate of Co/Pt multilayer) and longitudinal resistance is shown.

We finally performed Hall bar measurements with the Co/Pt magnetic textures, with a sample visible in figure 3.14 (a). The magnetic field orientation is measured with a Hall probe attached to the sample holder. The longitudinal and Hall resistance are represented as a function of an applied external magnetic field along two different field directions. The Hall bar measurements are compared to SQUID measurements of a plain Co/Pt chip to show the good agreement between both methods. The fabrication and measurement details can be found in Appendix C. In both these samples, the quantitative behavior of the magnetic texture is measured to be different than for the transport device of chapter 4. For example, the in-plane saturation field visible in figure 3.14 is lower than in measurements presented in figure 3.13, which is supported by the MFM measurements of figure 3.12 (it is also lower than the out-of-plane saturation field). This seems to indicate that in this sample, the magnetization axis for the domains was close to the horizontal axis (similarly to weak stripes in Ni). We understand these differences as a consequence of differences in the fabrication process: in the transport device, the Co/Pt multilayer is fabricated over a very rough substrate (due to the presence of

trenches). There could also be variations in the deposition process, or in the trilayer resist development.

In figure 3.14 (b) we show the Hall and longitudinal resistances as a function of an out-of-plane magnetic field B_1. The Hall resistance signal is typical of anomalous Hall effect (AHE). AHE occurs in magnetic materials with spin-orbit interaction, and translates as $R_{Hall} \propto M$ where M is the out-of-plane magnetization. This measurement can thus inform us on the out-of-plane saturation field of the structure, of about 1 T in this sample. The longitudinal resistance as a function of B_1 displays a strong, hysteretic modulation (of about 30% of the total Hall resistance). This effect is linked to the presence of domains: if the two longitudinal probes are positioned over domains of opposite magnetization, the voltage drop will contain the Hall signal (this effect is described in more details in Appendix C)[18]. The disappearance of this signal coincides with the closing of the hysteresis loop in the SQUID measurement. Both measurements thus give a value for the disappearance of the domains under an out-of-plane field. Panel (c) gives us information about the in-plane saturation, with a magnetic field perpendicular to the structure. The longitudinal resistance contains a term $R_{long} \propto -M^2$ where M is again the out-of-plane magnetization. This term corresponds to an anisotropic magnetoresistance (AMR); the resistance is reduced when the magnetization is perpendicular to the current flow. In a similar fashion, the longitudinal resistance as a function of a magnetic field applied parallel to the current displays an increase of the a resistance of 100 mΩ over the same magnetic field range (not shown). The Hall resistance is more complicated to interpret. The Hall resistance probably contains a small replica of the out-of-plane signal (corresponding to an angle of $\alpha \sim 1°$), and possibly a replica of the longitudinal resistance although this would correspond to a misalignment in the contacts of 4 µm (which does not appear to be the case). In this measurement again, the longitudinal resistance and the SQUID measurements are in agreement, and enables us to measure the in-plane saturation field.

We have thus shown that Hall bar measurements can also indirectly give us information on the saturation of the magnetic domains. The interest of this measurement is that it can be done with the same setup as the one used to measure the mesoscopic circuit, and does not necessitate additional equipment such as a SQUID or a field MFM.

Summary of the magnetic characterization

The combination of these magnetic measurements enabled us to better understand our Co/Pt multilayered structure. We can summarize its main characteristics:

[18] This signal could alternatively be linked to the domain wall magnetoresistance [233], which also depends on the presence of domains.

- The domain formation and axis is strongly dependent on substrate roughness and/or fabrication cleanliness
- At $B_{ext} = 0$, the texture present domains of typical size of $100 - 150$ nm,
- The domain magnetization is out-of-plane, and results in a stray field of about 400 mT above the structure,
- The in-plane saturation field depends greatly on disorder, but is about $B_{sat} = 1 - 2$ T (and $B_{sat} > 800$ mT according to MFM measurements on the transport device of chapter 4),
- Under an external magnetic field, a dipolar field appears at around 100 mT due to the alignment of the domains with the field. The domain size tends to reduce until complete saturation.

In the end, all these measurements gave us access to complementary information, and enabled us to gain some understanding on the formation of domains in our structure as well as their evolution in an external magnetic field. As a consequence, we were able to propose a simple model for the evolution of the spin-orbit coupling strength with the magnetic field in chapter 4, to take it into account in the interpretation of our transport measurements.

3.4 Superconducting contacts

In experiments exploring the physics of Majorana quasiparticles, one needs to be able to form a good contact between a CNT and a superconductor: a large tunnel rate is necessary to allow for second order processes in the tunneling, such as Andreev reflections. Another way to formulate this need is to say that the induced gap in a proximized nano-conductor is proportional to the coupling rate [234] (at $\Gamma \ll \Delta$).

With the stamping technique, it was possible to obtain good contacts with aluminum (Al(100 nm)/Pd(4 nm)). This is shown for example in ref [235], where an induced superconducting gap of the order of the one of bulk aluminum is measured ($\Delta_{ind} = 150$ µV vs typically $\Delta_{bulk} = 340$ µV[19]), indicating a large tunnel rate between the superconducting electrode and the CNT. During this thesis, we were also able to obtained Nb superconducting contacts (made out of Nb(40 nm)/Pd(4 nm)), as will be shown in chapter 4, in a Fabry-Pérot regime (corresponding to tunnel rates of the order of the level spacing δE of the confined CNT, $\Gamma_s \sim \delta E \sim 1$ meV).

[19] For thin films of Al this value is reduced

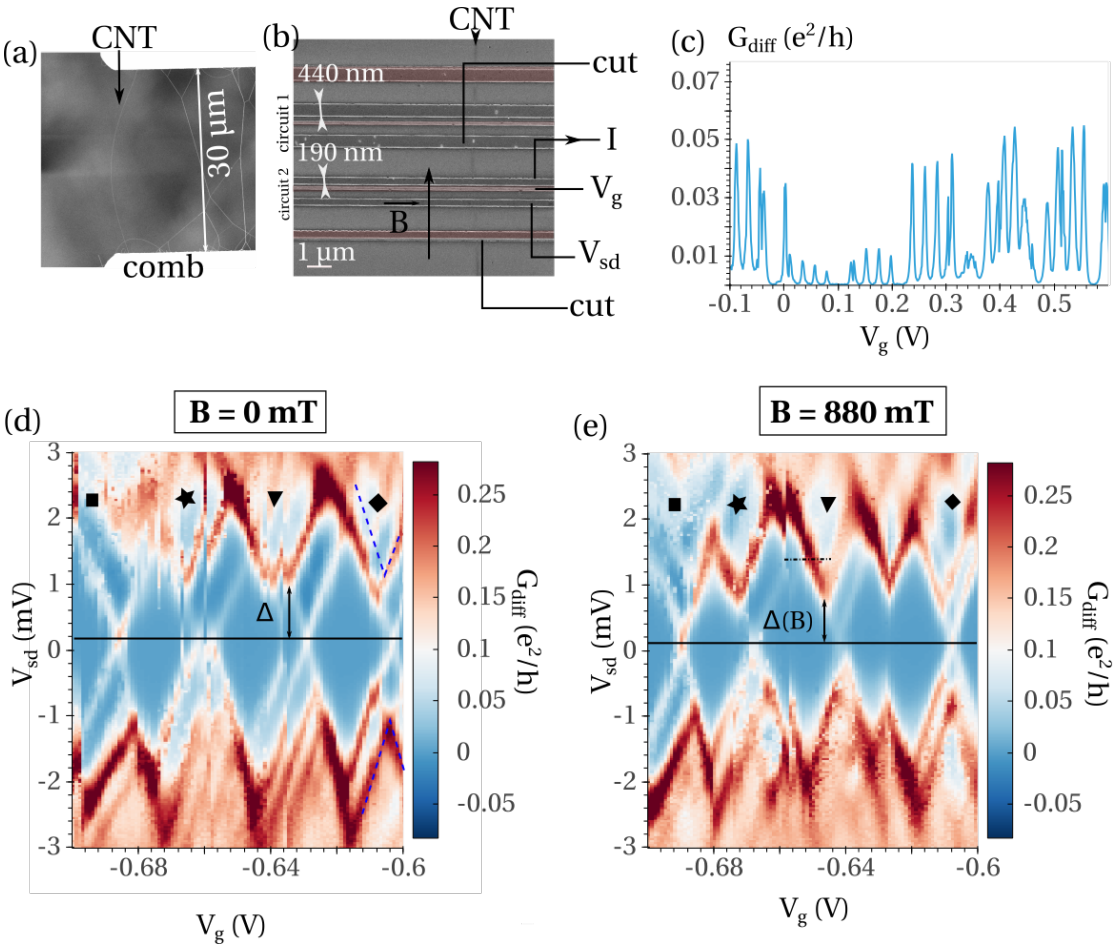

FIGURE 3.15: **Measurement of a circuit with superconducting contacts:** (a) SEM image of the CNT chosen for stapling when observing the comb. (b) False-colors SEM image of the electrical circuit after stapling. Two active regions (labeled circuit 1 and 2) can form a single quantum dot circuit, with contacts of width 190 nm and 440 nm. Additional electrodes (red) are used to cut the outer CNT segment, improving the CNT-electrode interface. An Al/Alox gate (light brown) can tune the chemical potential in the QD. (c) Differential conductance G_{diff} as a function of gate voltage V_g at finite biais voltage $V_{sd} = 240$ µV, showing 4-fold periodicity. (d, e) $V_g - V_{sd}$ map of the differential conductance G_{diff}, at $B = 0$ T (d) and $B = 0.88$ T (e). The pattern is slightly changed due to charge noise, but similar diamonds are identified by the markers ■, ▼, ★ and ♦. The measurement of $\Delta(B)$ on the Coulomb diamond labeled ▼ is shown, the horizontal black line indicating zero-bias. The dashed line in (e) indicates the peak on which the tunnel coupling Γ_1 and Γ_2 are estimated.

An open question was whether the stapling technique allowed for good superconducting contacts as well. We designed simple test circuits to investigate this possibility, and the possible influence of the contact width. During these tests, we have stapled a CNT over the electric circuit shown in figure 3.15 (a); we cut both exterior segments of the transferred CNT with the electrodes labeled cut, as described in section 3.2.1, without any additional annealing process. At room temperature, we did not observe any trend in the contact resistance value as a function of the electrode width (four width were tested: 190, 300, 440, 520 nm). We obtained room-temperature resistances of the order

of 250 kΩ−1 MΩ (measured at low bias voltage, $V_{\text{bias}} \sim 10\text{mV}$ which will be the relevant energy scale for low-temperature measurement). However, for too small contacts, flowing a current through the CNT can be more difficult, and can prevent us from cutting the exterior CNT segment. This was observed in another sample as the one presented here, with contact width of about 200 nm.

At low temperature, we managed to obtain a good superconducting contact for the circuit 2 of figure 3.15 with electrodes of width 190 nm, made out of Ti(15 nm)/Nb(45 nm)/Pd(10 nm). Post-measurement AFM and Raman characterization are indicative of a metallic 1.1 nm SWNT. The transport characteristics of this circuit are shown in figure 3.15, and was obtained with the typical DC transport measurement techniques described in 3.6.2, with $V_{ac} = 50$ μV (after the voltage divider) and $f_{ac} = 77.77$ Hz. A magnetic field can be applied in the sample plane.

The transport measurement is characteristic of a S-dot-N device (see Appendix A), for example in the Coulomb diamond labeled ▼ of figure 3.15 (d) and (e). We can note that for the diamond labeled ♦, we measure not only the conductance peaks expected for a S-QD-N device but also those of a S-QD-S devices (blue dashed line in (d)); this is illustrative of a superconducting contacts with a residual density of states at the Fermi energy. Indeed, if this residual density of states is too high in one contact, the $V_g - V_{sd}$ map will resemble one of a S-QD-N system. During this thesis, we have observed a varying quality for our superconducting contacts over several devices. The contacts often present a residual density of states at the Fermi level. This is the case for the samples presented in chapter 4. In the most extreme case, the two superconducting contacts effectively behave as normal contacts, as was seen in Ref [198], as well as in other platforms [**?**].

From the stability diagrams of figure 3.15 (d) and (e), we can extract the superconducting gap at two values of magnetic field: $\Delta(B = 0)$ and $\Delta(B = 0.88\text{ T})$, corresponding to a critical field of

$$B_c = B\frac{1}{\sqrt{1-(\Delta(B)/\Delta(0))^2}} \sim 1.2\text{ T}. \tag{3.2}$$

We extract the gap values and B_c for two different diamonds:

Coulomb diamond	$\Delta(0)$ in meV	$\Delta(0.88\text{ T})$ in meV	B_c
▼	0.8±0.1	0.55 ±0.1	1.2
♦	0.7±0.1	0.5±0.1	1.3

We can also estimate the tunnel rates to the two electrodes using the simple sequential transport picture, yielding $\Gamma_1/2\pi = 7$ GHz and $\Gamma_2/2\pi = 80$ GHz[20].

Another metallic thin film, Ti/Nb/Al/Au, was tested with no good contact at low temperature. This was possibly due to resist residues after the trench etching process, or to a bad interface between the metallic layers.

As a conclusion, this test shows that it is possible to obtain good superconducting contacts with the stapling technique, with high superconducting gap and large coupling rates, even though the quality of the superconducting contact (and notably its residual density of state at the Fermi energy) can depend on the fabrication process. We can now envision more complicated devices, to study superconductivity in mesoscopic physics and its interplay with, for example, a magnetic texture.

3.5 Device nanofabrication

We now present the specific steps for the nano-fabrication of the circuits presented in this thesis. We will first introduce some generic concepts and recipes, before describing the fabrication steps for both the stamping and the stapling techniques, putting the emphasis on the transfer of the CNT in the new stapling process.

3.5.1 Generic processes

A few generic processes are used several times during the nano-fabrication. They are summarized once and for all here.

Lithography process The principle of a lithography is represented in figure 3.16: it enables the fabrication of an electrical circuit according to a specific drawing. In very general terms, a resist is first deposited on a chip, and spread using a spin-coater down to a uniform thickness of typically less than 1 µm (depending on the resist). The resist can be degraded at specific locations, as given by the circuit drawing using an electron beam, a laser beam or a uniform light source combined with an opaque mask[21]. The degraded resist is soluble (and thus can be removed) in an appropriate solution called the developer. Metal can then be evaporated over the chip, before the remaining resist is

[20] The gate lever arm is 0.014 V/meV. Since there is a superconducting gap, we cannot take the conductance at zero bias. We still use the formula for the resonant tunnelling regime ($\Gamma > k_B T$), $G = \frac{e^2}{h} \frac{\Gamma_1 \Gamma_2}{(\frac{\Gamma_1+\Gamma_2}{2})^2}$ at finite bias, along the dashed line in figure 3.15 (e) to get an order of magnitude of the tunnel coupling rates.

[21] The resist consist in long polymer chains that break down under these beams

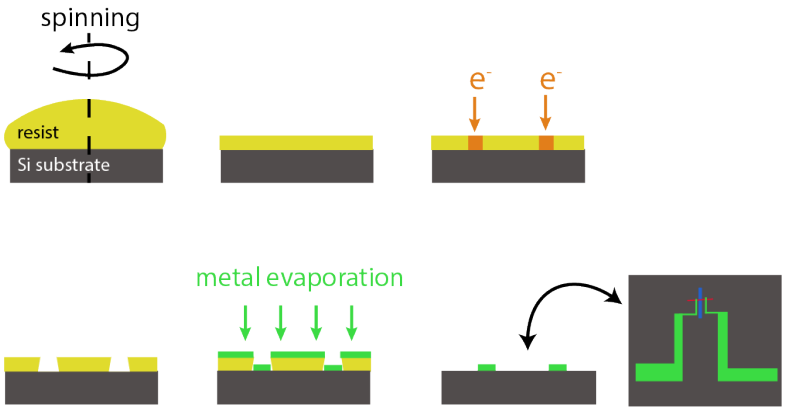

FIGURE 3.16: **Lithography process**

removed using an adequate solution. Instead of depositing metal, one can alternatively do an etching process (for example a reactive ion etching, RIE), thus obtaining trenches or removing metal at desired positions on the chip.

RIE processes Several reactive ion etching (RIE) processes are used during fabrication. The specific parameters are described below: the gas flow d, the working pressure P, the RF excitation power $\mathrm{P_{RF}}$. For all the process, the reproducibility in the etching rates is improved if the gas lines are purged before the process, and the chamber is flushed with the process gas for 2 minutes before turning on the RF excitation.

- Stripping recipe: $d = 100$ sccm of O_2, $P = 100$mTorr, $\mathrm{P_{RF}} = 30$ W,
- Nb etching recipe: $d = 25$ sccm of SF_6, $P = 7$mTorr, $\mathrm{P_{RF}} = 70$ W,
- SiO_2 etching recipe: $d = 50$ sccm of CHF_3, $P = 20$mTorr, $\mathrm{P_{RF}} = 70$ W,
- Si etching recipe: $d = 25$ sccm of SF_6 and 4 sccm of O_2, $P = 80$mTorr, $\mathrm{P_{RF}} = 100$ W.

CNT growth As stated before, the CNTs are grown using CVD in a home made furnace.

As a catalyst, we use the following solution: 39 mg of $Fe(NO_3)_3 - 9H_2O$, 7.9 mg of MoO_2 and 39 mg of Al_2O_3 nanoparticles, diluted in 20 mL of isopropyl alcohol (IPA).

Before using the catalyst, we sonicate it for one hour to break down potential particles cluster and we let it rest for 45 minutes. The top of the solution is then taken off using a pipette. One or two drops are deposited on the chip, which can be rinsed in IPA to make the deposition more homogeneous. The IPA is dried-off using nitrogen.

Once the catalyst is deposited onto the growth chip, they are positioned in the center of the furnace. The specific CNT growth recipe can be found in J.J. Viennot PhD thesis [236].

3.5.2 Specific fabrication steps

Both fabrication techniques start with a 10 mm x 10 mm chip of undoped, high resistivity (10 kΩcm), Si(500 µm)/SiO_2(500 nm).

Nano-fabrication ensues, to obtain the desired mesoscopic circuit in a microwave cavity, with either the stamping process of the stapling process.

At the end of the process, the chip is cut in two halves to fit in the sample holder shown in figure 3.8 and 3.1. It is glued using PMMA (dried for 1h), and wire bonded so that it can be connected onto the cryostat. At the beginning of this thesis, the cryostat were wired using sheathed electric cable of diameter 0.4 mm. We are now in the process of switching to nano-D connectors, which are more rigid thus less prone to triboelectric effects.

Below, we summarize all the fabrication steps for both transfer techniques used during this thesis.

3.5.2.1 Device made with the stamping technique

The final device that one gets when using the stamping is represented in figure 3.17.

Cavity preparation Prepare the microwave cavity, with a ground plane opening to position a mesoscopic circuit:

- Clean the Si chip with acetone (rinsed with IPA)
- Prepare Ti/Au alignment crosses by e-beam lithography
- Evaporate 150 nm of Nb
- Do the cavity lithography, using e-beam lithography
- Etch away the Nb to define the cavity, and clean the chip with acetone
- Do any pre-stamping lithographies and metal depositions of the mesoscopic circuit

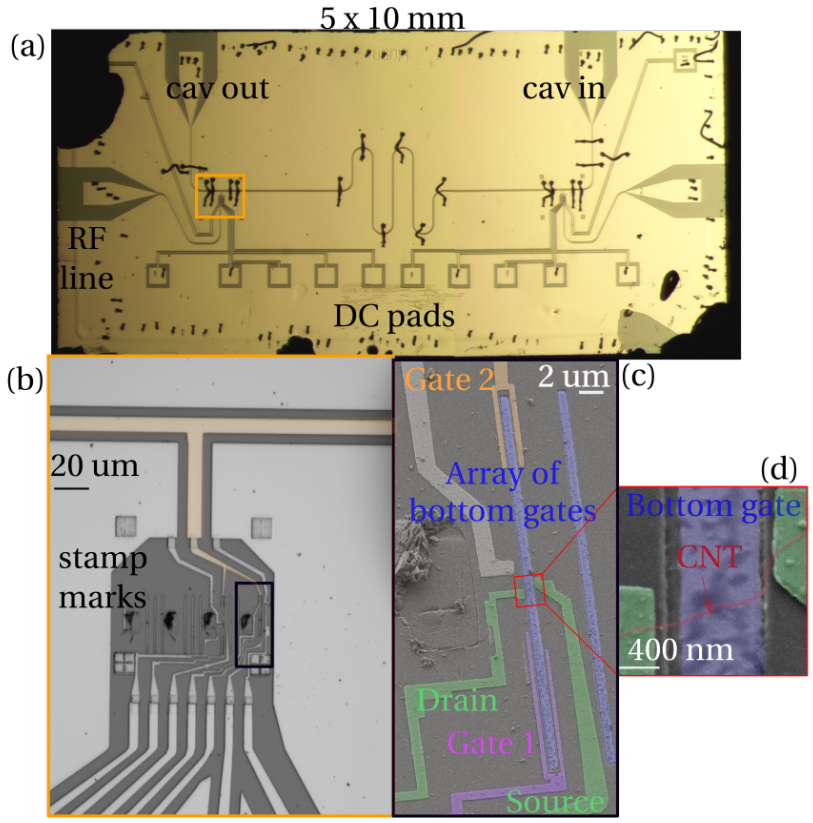

FIGURE 3.17: **Example of a device made with the stamping technique:** (a) Device picture where the CPW is visible. (b) Zoom-in on the ground plane opening, where the stamp marks are visible. (c, d) False-colored SEM image, zooming-in on the mesoscopic circuit. An array of magnetic bottom gates (blue) is fabricated before CNT stamping. After stamping, superconducting contacts (green), as well as DC (purple) and AC (orange) gates are fabricated around the selected CNT, visible in (d). The AC and DC line are capacitively coupled to a floating magnetic gate (blue). The AC gate is connected onto the central conductor of the cavity, as visible in (b).

The gold crosses are made with e-beam lithography, and allow for coarse and fine re-alignement on the chip, which is necessary for the fabrication of the mesoscopic circuit. The Nb deposition is done in a Plassys electron-beam evaporator, equipped with a cryogenic pump. During deposition the evaporator walls are cooled-down with liquid nitrogen, which enables us to deposit Nb at a rate of 10 Å/s at a pressure below 5×10^{-10} mbar. The cavity is defined using e-beam lithography, followed by the dry etching process described in 3.5.1. The resist residues are cleaned using acetone, rinsed with IPA. For the sample MU9TRd described in chapter 4, buried magnetic gates were fabricated before stamping, in a two step process (fabricating trenches by e-beam lithography and RIE etching, and fabricating a thinner Co/Pt multilayer gates by e-beam lithography using a tri-layered resist stack and metal evaporation at LPS Orsay), as described in the PhD thesis of M.M. Desjardins [206].

Quartz pillars To prepare the quartz pillars :

- Fabricate several quartz pillars (typically 4 per ground plane opening of the cavity), of about 4 µm high and 10 µm × 5 µm of surface starting from a 10 mm x 10 mm quartz chips. This pillars are formed using a dry etching process with a Ni mask.
- Grow CNTs over these pillars as described in section 3.5.1.
- Stamp the pillars over the ground plane opening of the cavity chip.

This process is described in more details in the PhD thesis of J.J. Viennot [236], and L.E. Bruhat for the quartz process using Ni [237].

Finishing the CNT circuit around one stamped CNT

- Localize the transferred CNTs with an SEM (at low acceleration voltage to protect the CNT) and choose one,
- Draw the schematics of the needed electrodes,
- For each metal, do a lithography followed by a metal deposition and a lift-off, with the fine lithography parameters below.

Fine lithography parameters: The resist used is PMMA A6, with a thickness of about 500 nm. It is spin-coated during 30 s at 4000 rpm, and baked during 15 min at 165°C. It is exposed with e-beam lithography at 20 kV at a current of about 30 pA and a typical dose of 450 µC/cm^2. The development is made using a solution of MIBK/IPA (3/1) during 2 minutes, rinsing in IPA. The metal is deposited in our Plassys e-beam evaporator with typical pressures of the order of 1×10^{-9} mbar. The lift is done using acetone, rinsed with IPA. When no CNT is present, the chip can be cleaned in an oxygen plasma for 1 minute with the stripping RIE recipe.

During this thesis, we started using Nb superconducting contacts. Since this is a very refractive metal, the resist heats up a lot during the deposition. To prevent that, the evaporator sample holder is cooled down to 0°C, using liquid nitrogen. The lift is done in acetone heated up to 50°C. The Nb layer is covered by a Pd buffer, to prevent oxidation and to ensure a good contact with the CNT. It is best to wait 30 minutes in the evaporator chamber between the two metal deposition. In one occurrence where this was not done, we observed a peeling of the Pd top layer.

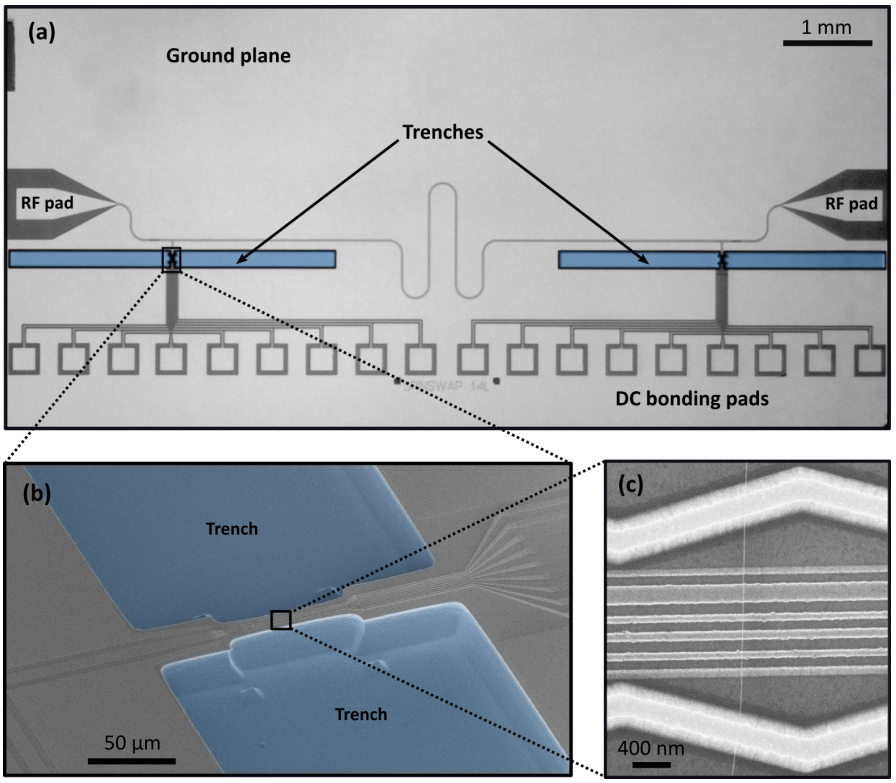

FIGURE 3.18: **Example of a device made with the stapling technique:** (a) Picture of the CPW cavity. The trenches needed for stapling are highlighted in blue. (b) False-colored SEM image zooming-in on the trenches surrounding the mesoscopic circuit. The central conductor of the cavity is visible on the left, as well as the DC lines leading to the bonding pads on the right. (c) Zoom-in on a circuit where a CNT was transferred. The circuit consists in two metallic electrodes (external lines) and an array of Al/Alox gates in the center. One of the gate is connected to the central conductor of the cavity to capacitively couple the circuit to cavity photons. Here the cut electrodes are not shown. Source: [2].

3.5.2.2 Devices made with the stapling technique

General remarks on the stapling devices geometry A typical device made with the stapling technique is shown in figure 3.18. Due to the finite precision in positioning the comb over the cavity chip, the mesoscopic circuit need to be at least 20 µm long, and for safety can be made even longer. Another new fabrication constraint is that the electrodes surface now need to be very flat. For the Nb deposition, we started using a MMA(110nm)/PMMA(300nm) bilayer to avoid resist remains at the edge of the electrodes.

During the stapling, the presence of a CNT is monitored using the electrical circuit shown in figure 3.19 (d). In this circuit, we see that in addition to the QD circuit, there are two external electrodes. These electrodes are necessary to cut the CNT outer sections by flowing a large current (typically > 10 µA) between the cut electrode and the circuit electrode on each side of the QD circuit. During this process, the contact

between the circuit electrode and the CNT is improved, without having to flow a current in the central region of the CNT[22].

It is possible to obtain a suspended CNT with the stapling technique, provided that the height of the metallic electrodes is sufficient. We observed that the CNT tends to be suspended when the distance between two electrodes is no more than ten times bigger than the electrode height. However for the experiment presented in the next chapters, we want the CNT to be as close as possible to the bottom gate made out of the Co/Pt texture, thus we do not fabricate thick electrodes.

Comb preparation The combs used are commercial cantilevers bought at Micromotive Mikrotechnik (see figure 3.19 (a)). They are 3 mm × 4 mm $Si/SiO_2/Si$ chips on which 5 µm thick cantilevers are etched over a length of 500 µm.

CNTs are grown on it as described in section 3.5.1, with the comb arms oriented perpendicular to the gas flow. After growth, some CNTs are suspended between two successive cantilevers of the comb, as visible in 3.19 (c).

Circuit and cavity fabrication

- Prepare the alignment crosses and the cavity as for the stamping technique,
- Finish the mesoscopic circuit by e-beam lithography with one lithography step per desired metal,
- Fabricate trenches for the stapling.

During this thesis, we started using laser lithography for the cavity lithography. This process is much faster than the e-beam lithography, and its lower resolution (about 1 µm) is still sufficient for the CPW, with dimensions no smaller than 2 µm. Compared to a mask aligner (that has the same resolution), it is more flexible since the design can be changed without having to fabricate a new mask. The resist used is Microposit S1805, spin coated straight out of the fridge with the same process as PMMA, and baked for 1 minute at $115°C$. The dose used is typically 170 mJ/cm^2. It is developed in a Merck MIF 760 solution for 40 seconds, and rinsed with distilled water.

Compared to the stamping technique, all of the mesoscopic circuit electrodes as well as the transfer trenches can be fabricated before transferring the CNT. The parameters used are the same as for the stamping, except that the PMMA baking was done at

[22]Flowing a large current can degrade the CNT, notably by heating up and facilitating chemical reactions

175°C for 5 min, and developed during 1 minute in MIBK/IPA (rinsed with IPA, followed by 10 s of stripping). The lithography for the Nb contact was done using a MAA(110 nm)/PMMA(300 nm) resist bilayer to ensure a smooth electrode surface, developed during 30 s only.

The trenches are fabricated with laser lithography with a 1 µm thick resist (AZ) followed by a dry etching, in two steps: about 30 minutes of the SiO_2 process (the etching can be followed by laser interferometry), and between 5 and 10 minutes of Si etching, to obtain at least 10 µm deep trenches. Too long a Si process risks etching through all the resist, and degrading the chip. The chip has to be carefully cleaned after such a long etching, in a bath of hot acetone with ultrasounds, rinsed in IPA, and cleaned using an oxygen plasma for 5 minutes (with the RIE stripping process).

Stapling Before stapling, both the circuit and CNT chips must be positioned in the stapler. The comb is glued onto the attocube micromanipulator using PMMA. The cavity chip is similarly glued onto the vacuum-compatible sample holder and wire-bonded. It it connected to the chamber electrical rack. The holder cover is held in the moving arm.

The chamber is pumped with a turbo pump below $P = 1 \times 10^{-6}$ mbar.

The circuit electrodes are cleaned using Ar ion milling, during 30 seconds, at a voltage $V_{acc} = 5$ kV. Then, the comb is positioned above the cavity chip using micrometric and nanometric manipulators. The presence of an electrical contact between the circuit electrodes (when a CNT is present) is monitored using the circuit shown in figure 3.19 (d).

The comb is lowered first using the attocube continuous displacement mode, and at the end of the approach using the step displacement mode with parameters $f = 30$ Hz and $V_{step} = 30$ V. As soon as an electrical contact is detected, typically with a resistance of 1 GΩ (ranging from 50 MΩ to 50 GΩ), we stop lowering the comb and we cut the outer segments of the CNT using the circuit shown in figure 3.19 (e). This process improves the resistance contact of the CNT to the central electrodes. We can then measure the room temperature resistance (typically of the order of 200 kΩ, up to tens of MΩ at $V_{app} = 10$ mV) and the gate dependence of the central region. If the obtained resistance seems too high for the desired application, one can try and flow a relatively high current in the central region of the CNT. However, this can also irremediably degrade the CNT.

In this case, one can definitely remove the CNT using the ion miller (retracting the comb to protect it) and repeat the stapling process[23].

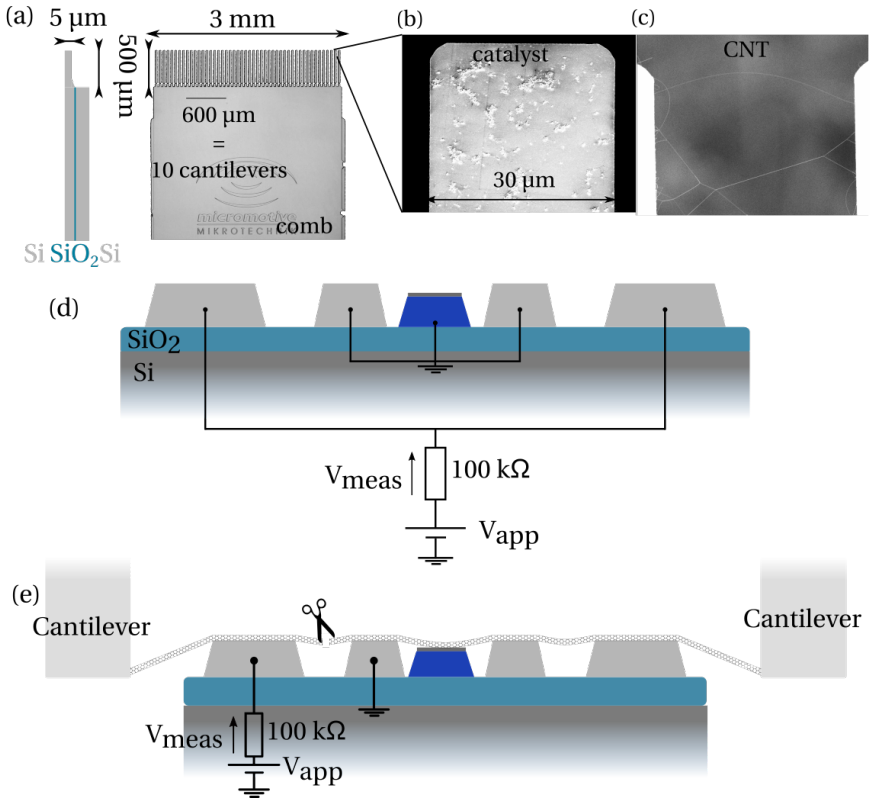

FIGURE 3.19: **Details on the stapling technique:** (a) Picture of the comb used to grow suspended CNTs. On the left, a schematic side view of the $Si/SiO_2/Si$ structure shows the relevant comb dimensions. (b,c) Zoom in on a cantilever after growth, with different contrast so that either the nanotubes on the cantilever are visible (b) or the CNT suspended between the cantilever (c). (d) Electrical setup used during the lowering of the comb, to detect the presence of a CNT. We typically apply a voltage $V_{app} = 0.5$ V. (e) Electrical setup used to cut the outer CNT segments. We increase V_{app} by steps of 2 mV, measuring the increase in V_{meas} until the CNT breaks and it falls to zero.

3.6 Low temperature measurements

Most of the measurements presented in this thesis were obtained in a dry dilution refrigerator with a base temperature of 20 mK. Some of the test measurements were done in a ^{3}He cryostat with a base temperature of 250 mK. These temperatures are necessary to observe coherent effect in the mesoscopic circuit, and to avoid thermal occupation of the microwave cavity.

[23]Note that the ion milling does not remove the CNT per se: with SEM imaging they are still present at the same position. It simply transform it into amorphous carbon, as one can see with Raman spectroscopy.

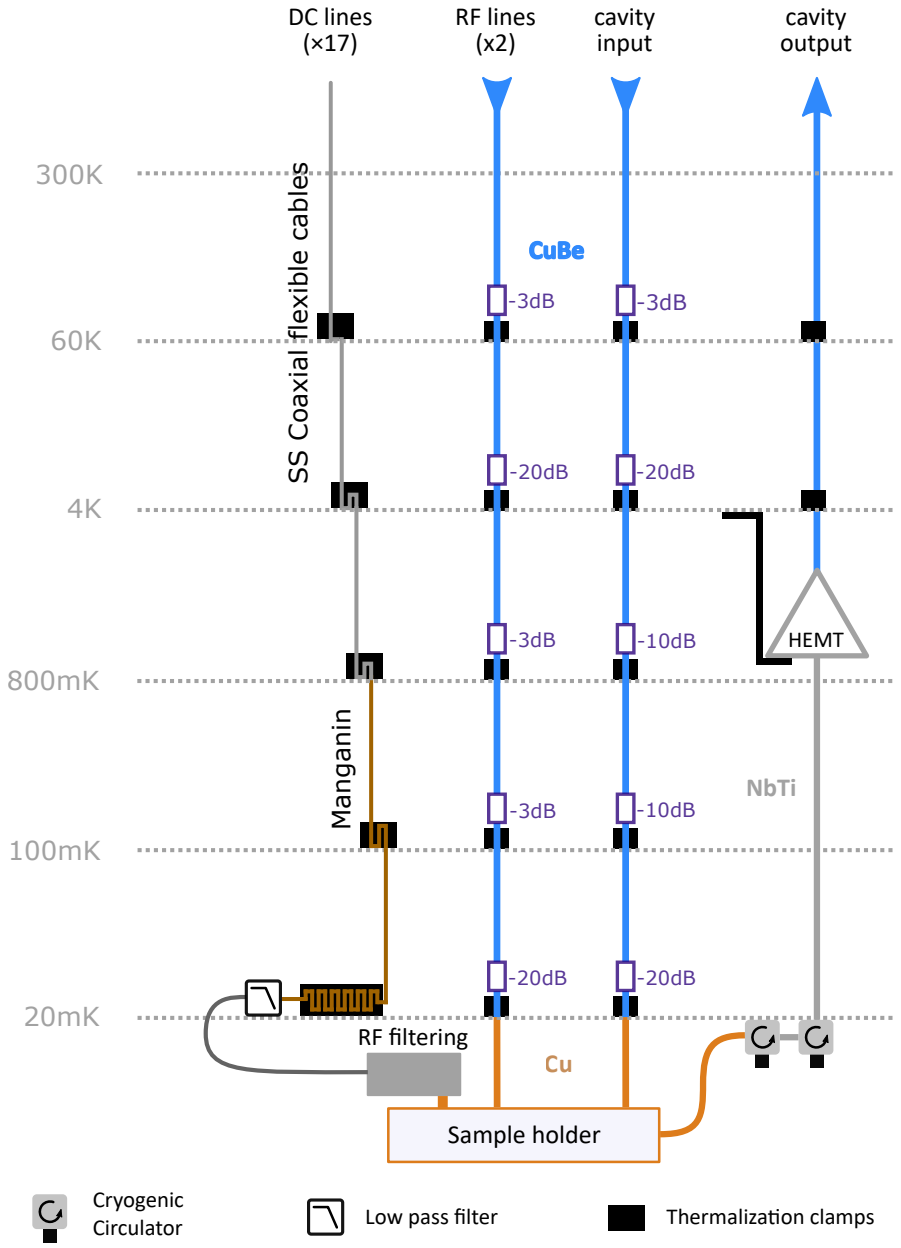

FIGURE 3.20: **Schematics of the cryostat wiring**. The HEMT amplifier provides an amplification of 62 dB.

3.6.1 Fridge wiring

The fridge wiring is shown in figure 3.20. Details about the wiring and the calibration of the line attenuation are given in the PhD thesis of L.E. Bruhat [237].

3.6.2 DC measurement techniques

The transport measurements presented in this thesis are either current or differential conductance measurement. Differential conductance can directly reveals the hole and

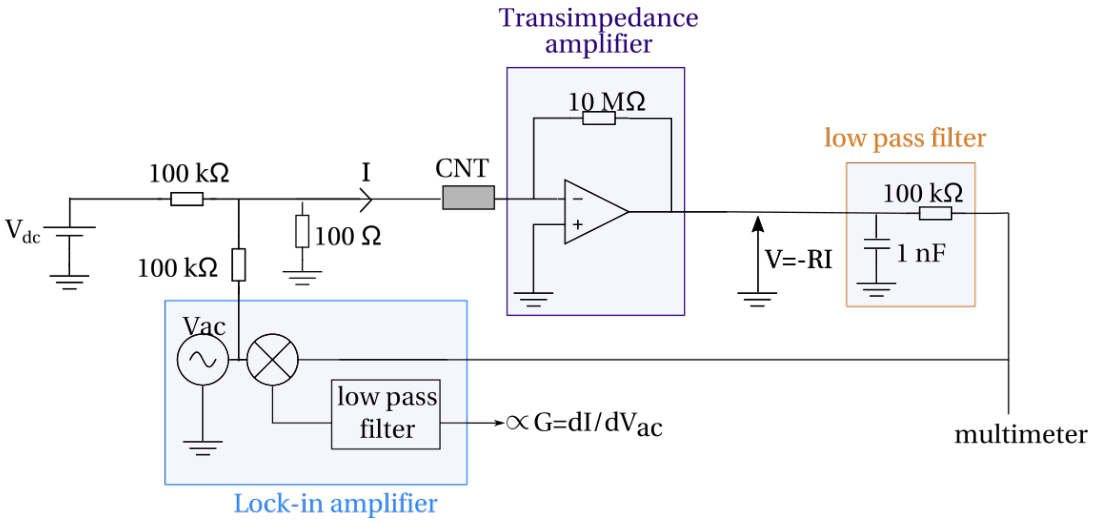

FIGURE 3.21: **Schematics of the DC measurement setup-up**

electron density of states of a quantum dot. In addition, the lock-in technique is very efficient to filter out the noise in the measurement. However, for very low signals (currents of the order of 10 pA), the signal cannot be measured with our lock-in anymore, and the density of states can be inferred from the current measurement.

A typical setup for the DC (and lock-in) measurements presented in this thesis is shown in figure 3.21. A DC and AC voltages (typical frequency of $f_{ac} = 77.777$ Hz) are combined on a voltage divider (factor 1000) and applied to the CNT. The output current is amplified using a home-made transimpedance amplifier. A multimeter measures the current and the lock-in measures the output voltage V_{out}^{ac} at f_{ac} which is related to G_{diff} through

$$G_{\text{diff}} = \frac{dI}{dV} = \frac{10^{-7} V_{out}^{ac}}{10^{-3} V_{ac}} = 10^{-4} \frac{V_{out}^{ac}}{V_{ac}}$$

The parameters f_{ac} and V_{ac} are chosen so that the lock-in measurement does not affect the current measurement (meaning high enough frequency[24] and low enough voltage), with still a strong enough signal (ie high enough voltage) and not too many capacitive effects due to the low-pass RC filters (ie low enough frequency).

[24] Which is also favorable to reduce the 1/f noise.

Chapter 4

Synthetic spin-orbit interaction for Majorana devices

We have described in chapter 1 how Majorana Zero Modes (MZM) can emerge in a one-dimensional condensed matter circuit that combines spin-orbit interaction and induced superconductivity, subject to an external magnetic field. We then discussed in chapter 2 how the effect of a magnetic field oscillating in space along a nanoconductor is equivalent to both a synthetic spin-orbit interaction and a constant magnetic field for the electron bands. In Chapter 3, we presented the magnetic characterization of a Co/Pt multilayered structure that presents small domains of magnetization and generates an oscillating stray field with a period of about 100 nm. We now describe more in details a device integrating this magnetic structure to a CNT-based mesoscopic circuit, and its transport study. Current is measured through one superconducting contact and one tunnel probe, and is carried by ABS below the superconducting gap. We present the evolutions of these ABS when an external magnetic field is applied, whose main effect is to modify the structure of the magnetic domains. The first section briefly describes the transport regimes in such a device, and reproduces experimental results presented in Ref [179]. The second section presents additional details on the experiment.

4.1 Synthetic spin-orbit interaction

We start by describing the different transport signatures of ABS in CNT-based mesoscopic circuits. We then propose a non-interacting picture to understand the impact of a spatially varying magnetic field, that is of interest in the large tunnel coupling limit, using the same tight-binding formalism as introduced in chapter 2. Finally, we present transport measurement in a CNT-based device with superconducting contacts, in proximity to a magnetic texture.

4.1.1 Transport regimes for QD with superconducting contacts

At the interface between a BCS superconductor and a normal metal, ordinary Andreev reflections can occur where an incoming electron of momentum (spin) $\vec{k}, (s)$ is reflected into a hole of momentum (spin) $-\vec{k}, (-s)$. When two superconductors are separated by a short ballistic conductor ($L < \xi \equiv \frac{\hbar v_F}{\Delta}$ where v_F is the fermi velocity of the conductor and Δ the superconductors' gap), bound states can form thanks to Andreev reflections occurring on each interface. They are called Andreev Bound States (ABS).

Several experiments have been conducted combining a quantum dot with one or two superconducting contacts to study the emergence of superconducting correlations in an ideal 1D system [238]. It has notably enabled a better understanding of the phenomenon of Andreev reflections in a ballistic nanoconductor with few conduction channel. Carbon

nanotubes are particularly well suited for such a study due to their well-understood band structures and strong 1D confinement, yielding a conductor with effectively only four conduction channels.

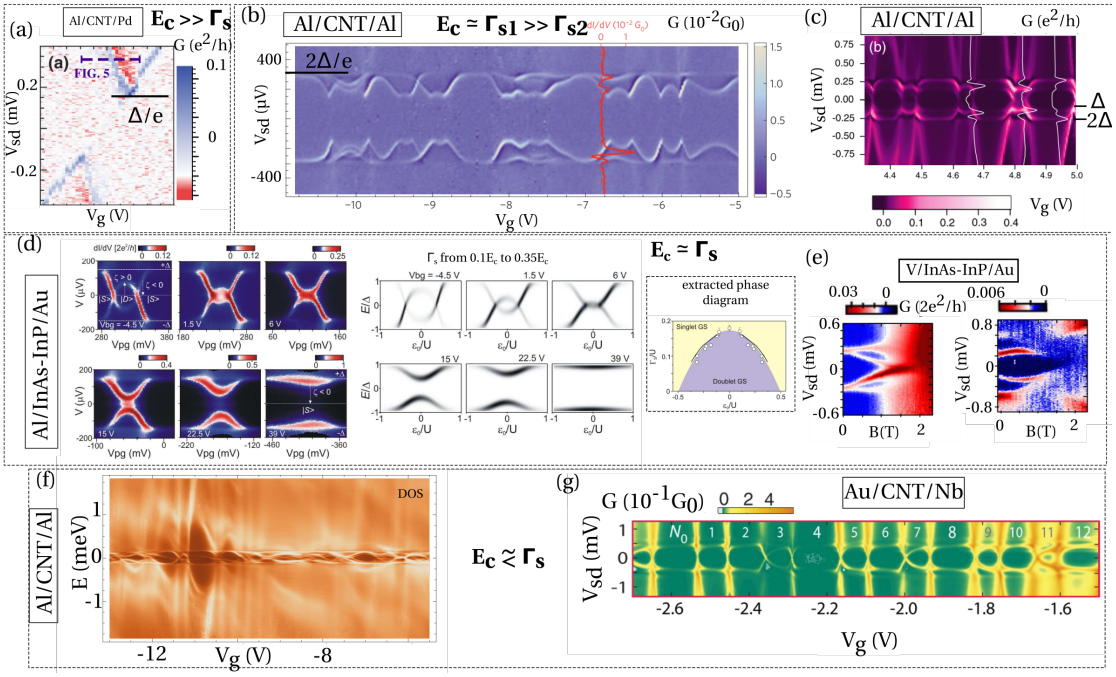

FIGURE 4.1: **Overview of experimental studies of a quantum dot with superconducting contacts, for different couplings to the superconducting lead Γ_s** (a) $V_g - V_{sd}$ conductance map for a **S/QD/N device with weak** Γ_s where no ABS are formed. The Coulomb diamond is simply shifted (and its contrast modulated around the BCS peak) due to the BCS-like density of states of the superconducting tunnel probe. Parameters: $E_c \sim 1.8$ meV, $\Delta = 0.17$ meV (from measurements) and $\Gamma_s = 0.003\Delta$ (from simulations) Source: [197]. (b) $V_g - V_{sd}$ conductance map for a **S/QD/S device with an intermediate coupling,** Γ_s. A first superconducting contact is weakly coupled and acts as a tunnel probe. The second one gives rise to ABS in the nanoconductor, visible between $eV_{sd} = \Delta$ and 2Δ. Parameters: $\Delta \sim 125$ μeV, $\Gamma_s \sim 1 - 2\Delta$. Source: [98]. (c) $V_g - V_{sd}$ conductance map for a **S/QD/S device with one large** Γ_s. Replica of the transport at $eV_{sd} = 2\Delta$ is visible at $eV_{sd} = \Delta$, characteristic of a residual density of states in one of the superconducting contact. Parameters: $\Gamma_{s1} = 0.2$ meV, $\Gamma_{s2} = 4$ μeV, $\Delta = 135$ μeV and $E_c = 2 - 5$ meV. Source: [239]. (d) Evolution of ABS around the degeneracy point for different values of the tunnel coupling to the superconductor Γ_s in a **N/QD/S device**. At low Γ_s, the ground state changes from a singlet $|S\rangle$ to a doublet $|D\rangle$ state. Left panel: $V_g - V_{sd}$ conductance map for various Γ_s. Center panel: NRG simulations of the DOS of the QD proximitized by its superconducting contact. Right panel: extracted phase diagram for the singlet/doublet ground state as a function of Γ_s and ϵ_0, the detuning of the dot level. Source: [240]. (e) Effect of a magnetic field on ABS similar to the ones shown in (e), either in the singlet or doublet ground state. The doublet state energy degenerescence is lifted linearly. Source: [100]. (f) DOS of the proximitized QD (deconvoluted from the DOS of the superconducting probe) for a large Γ_s. Source: [98]. (g) $V_g - V_{sd}$ conductance map of a **S/QD/N device with large** Γ_s. Parameters: $E_c = 5$ meV, $\Gamma_s = 0.4E_c$, $\Delta = 0.5$ meV. Source: [241].

When two superconducting contacts have a large tunnel coupling to a conductor ($\Gamma \sim \Delta$)

with a low Coulomb repulsion ($E_c < \Delta$), multiple Andreev reflections (MAR)[1] can be observed when applying a bias between the two superconductors: see for example ref [242, 243], both with CNTs. A supercurrent can be measured across the device at $eV_{sd} = 0$[2] [244].

Alternatively, the nanoconductor can have a strong asymmetry in its tunnel couplings to two superconductors. In this case, the contact to the "good" superconductor dresses the bound states in the nanoconductor, whereas the weakly coupled contact only acts as a tunnel probe with a semiconductor-like density of states [98, 245] as visible in figure 4.1 (b,c) (Andreev reflection processes at this interface can be neglected). The experimental observations are similar to the ones of a S/QD/N system in terms of Andreev processes. We will call a device in such a parameter regime a S/QD/S' device.

In addition, several experiments have studied S/QD/N devices. In such devices, the effect of the superconducting interface (of tunnel coupling rate Γ_s) can be again understood as an induced proximity effect. Depending on the value of Δ and E_c, various effects compete with this proximity effect. When Coulomb interactions are strong, the energetic cost of the formation of a pair of electrons (E_c at the degeneracy point) can be larger than the cost of a doublet ground state ($\Delta_{ind} \propto \Gamma$ being the cost of an unpaired electron at the charge degeneracy point when $\Gamma \leq \Delta$), suppressing any proximity effect. The transport signature is only affected by the semiconductor-like DOS of the superconducting probe : there is an additional $\pm\Delta/e$ bias gap in the conductance signal, and negative differential conductance (NDC) as visible in figure 4.1 (a). On the opposite, when Coulomb interactions are weak, the ground state can present superconducting pairing (figure 4.1 (f) and (g)). In the intermediate regime, the evolution of the conductance peaks as a function of the nanoconductor chemical potential can be successfully modeled by NRG calculations: see figure 4.1 (d), (e). They illustrate the competition between Coulomb interactions and superconductivity in the CNT, favoring either a doublet of a singlet ground state [100, 240].

We can summarize the different transport regimes as follows:

- Very strong Coulomb interactions, $\Gamma_s \ll E_c$: no effect of the superconducting pairing (figure 4.1 (a)). Coulomb diamonds are observed, shifted by the BCS-like DOS of the superconducting probe(s); transport can be described using the semiconductor representation for the superconductor(s) [197],
- Strong Coulomb interactions $\Gamma_s \sim E_c$: competition between superconductivity and the Kondo effect (figure 4.1 (d) and (e)), the ground state is either doublet

[1] MAR give rise to conductance peaks at $eV_{sd} = \frac{2\Delta}{n}$, corresponding to a n-th order tunneling terms
[2] A supercurrent can also be seen in intermediate regimes, see the review [238] for example.

or singlet depending on the dot level. As a consequence, the conductance can vary strongly around the charge degeneracy points as shown in figure 4.1 (d), for various ratio of Γ_s/E_c, enabling the outline of the phase diagram [100, 240],

- Weak Coulomb interactions $\Gamma > E_c$: the ground state hosts superconducting correlations (figure 4.1 (f)); several ABSs can be visible below the gap, while above the gap the transport is typical of the Fabry-Pérot regime, as expected for $\Gamma > E_c$ [98]. Supercurrent can flow across the device with two superconducting contacts if $\Gamma_{s1} + \Gamma_{s2} > \Delta$[3].

We can note that in the majority of experiments with superconducting contacts, a finite conductance below the gap is measured, indicating a residual density of states in one or both the superconducting contacts [103, 239, 246–249], as visible for example in figure 4.1 (c), where the peaks at $eV_{sd} = \pm 2\Delta$ are replicated at $eV_{sd} = \pm\Delta$.

Few experimental results show the evolution of ABS with a magnetic field, notably because aluminum contacts are often used, and they have a very low critical field (it is of 10 mT for bulk Al, up to about $B = 100$ mT for thin films). When applying a magnetic field, the energy levels of the nanoconductor become spin-split, modifying the transport measurement. Ref [100, 248] show the evolution of the conductance as a function of a magnetic field in the regime of competition between superconductivity and Kondo effect, either with a singlet (right) or a doublet (left panel) ground state. Under a magnetic field, the doublet state's energy splits and linearly evolves with the magnetic field while the singlet state energy stays constant, resulting in the transport maps of figure 4.1 (e).

4.1.2 Theoretical descriptions

In most of the transport regimes described in the previous section, strong Coulomb interactions are present. However taking them into account in a theoretical modeling is challenging; one needs for example to resort to NRG calculations. Alternatively, it was shown in several papers that a non-interacting QD picture (using Green functions' formalism) can accurately describe many experimental observations [98, 197]. In the first paper, a phenomenological energy difference between the two spin orientations was added to the dot description. It mimics the effect of charging energy on the energy of the singlet state. In the second one, Andreev reflections being negligible (due to the low Γ_s), the two spin states are treated on an equal footing and the obtained results correspond to a sequential tunneling transport. Another non-interacting formalism, useful to take into account spatial variations of physical parameters is the scattering formalism.

[3] The Cooper pair coherence needs to last longer than the tunneling time.

Side note on the Keldysh Green functions' formalism, and the link between the density of states and the conductance

When using a superconducting probe, the link between the density of states and the differential conductance signal is not direct. In the strong Coulomb interactions regime, transport does not involve the BCS condensate, and the transport signature can be understood using a semiconductor representation for the S contact(s). However, when Andreev reflections are allowed, the density of states of the quantum dot is modified by this proximity effect. The bound states that form are addressed in transport by the BCS condensate, yielding transport below the superconducting gap, while the transport above the gap is also greatly modified. This is illustrated in figure 4.2, which represents the DOS and conductance of a S/QD/N system as calculated using the Keldysh formalism introduced in Ref [197]. The Keldysh formalism allows us to obtain non-equilibrium quantities such as the conductance of a 0D non-interacting voltage-biased quantum dot. Following Ref [98], we added to the orbital energy ϵ a phenomenological Zeeman splitting $\epsilon_{s=\pm1} = \frac{1}{2} s B_{\text{eff}}$ (where s is the spin index) to lift the degeneracy between both spin orientations and mimic the charging energy.

We consider three parameters regime: on the one hand, panels (a,d) describe the very strong Coulomb interactions regime (it corresponds to the parameters of [197]). We recover a transport gap of $eV_{sd} = \pm\Delta$, and negative differential conductance along the transport line associated with the S contact, as well as a replica of the transport signatures below the gap due to a residual density of states at the Fermi energy in the superconducting probe (introduced as a Dynes parameter in the superconducting contact DOS, $\eta = 0.15\Delta$). On the other hand, panels (b,e) and (c,f) describe a regime with a stronger tunnel coupling Γ_S, for two values of the splitting B_{eff}. The density of states of the quantum dot is strongly modified by the superconducting contact : a superconducting gap is visible, as well as subgap states made out of a mixture of electrons and holes. The two values of B_{eff} used in panels (b,e) (respectively (c,f)) effectively implement two ratio of Γ_S/E_c, corresponding to the presence (respectively absence) of a loop in the density of states. They yield similar results as the more rigorous NRG calculations presented in figure 4.1 (d).

Adequacy of the scattering formalism

In this thesis we wanted to study the effect of a spatially varying field along the nanoconductor, preventing us from using this 0D quantum dot picture. For simplicity, we started by looking at the effect of the field with either a scattering or a tight-binding formalism, neither of which takes into account Coulomb interactions. The finite-size

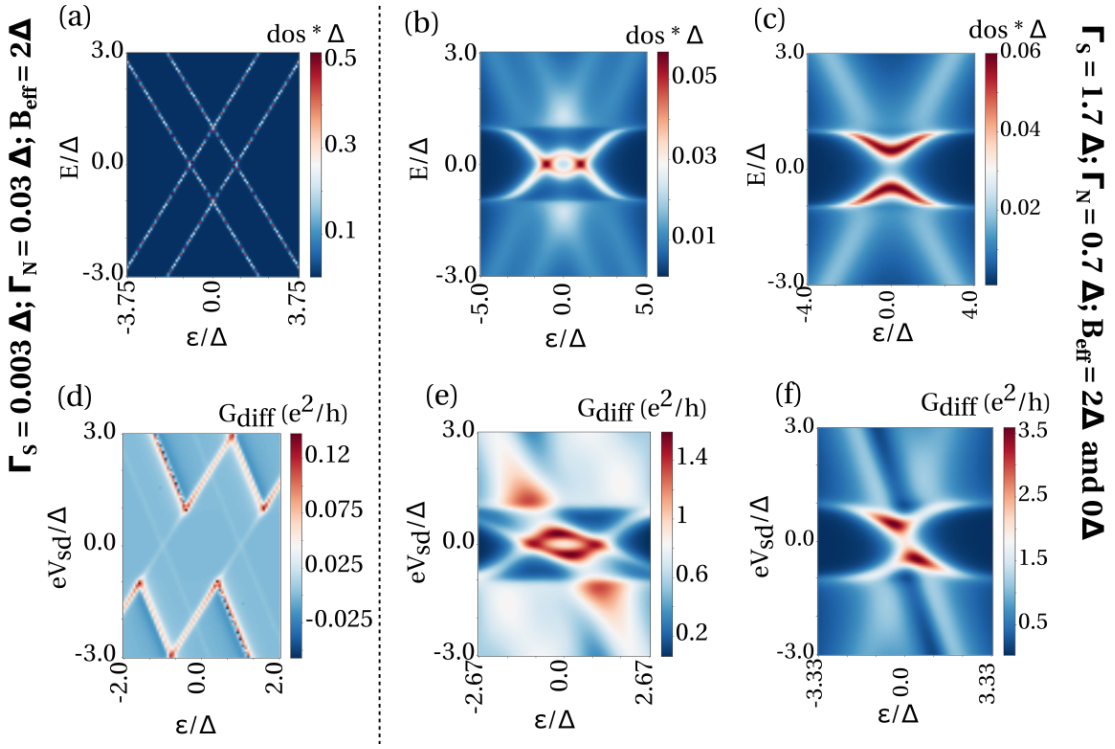

FIGURE 4.2: **Link between the density of states and the differential conductance for different parameters regime** for a S/QD/N system. In the following plots, we plot as the density of states (DOS) the sum of the density of states of electrons and holes with both spin orientations. (a,d) DOS and conductance for $\Gamma_S = 0.003\Delta$, $\Gamma_N = 0.03\Delta$, $B_{\text{eff}} = 2\Delta$, $\eta = 0.15\Delta$, illustrating the regime of very strong Coulomb interactions. Transport can be modeled using the semiconductor representation for the S contact. A small conductance peak can be seen at the position of the Coulomb diamond for a N/QD/N system due to the residual density of states at the Fermi energy in the S contact. (b,c,e,f) DOS and conductance for $\Gamma_S = 1.7\Delta$, $\Gamma_N = 0.7\Delta, \eta = 0.1\Delta$, and two values of B_{eff} : $B_{\text{eff}} = 2.7\Delta$ (b,e) and $B_{\text{eff}} = 0\Delta$ (c,f) corresponding to the two regimes of competition between Coulomb interactions and superconductivity. The Γ parameters used in panels (b-f) correspond to the experimental values of Ref [239] (although in this reference, the second contact is also superconductor). The simulations are done with an electronic temperature of $T = 60$ mK and a symmetric voltage drop along S/QD/N circuit.

effects will give rise to discrete orbitals, but they are spin-degenerate, thus there is no competing effect to superconductivity. Still, this modeling should describe the transport regime $\Gamma > E_c$. To get an intuitive picture of what happens when E_c increases, one could compare the energy of the different states in the obtained spectrum by adding by hand the charging energy, as was done in the study presented in figure 4.1 (b).

4.1.3 Non-interacting picture for proximity effect with a magnetic field

We now present the numerical study of the formation of ABS in the non-interacting limit, using the tight binding formalism introduced in section 2.3.1. The goal of this study is to help us understand how the presence of a cycloidal field will affect the spectrum of

our nanoconductor, and how we can reveal this effect. In the experiments, several knobs can affect the ABS: first, the chemical potential of the nanoconductor, as used in figure 4.1 (a-d,f,g). In the large coupling limit, Γ_s, the ABS are less sensitive to this parameter (as visible in figure 4.2 (f)). Then, the phase difference between two superconducting contacts also matters, and can be controlled in a SQUID geometry. Finally, an external magnetic field also changes the ABS energy by Zeeman effect. The external magnetic field can have an additional effect, which is to modify the domains of the magnetic texture, as discussed in section 3.3.3.

In figure 4.3, we compare three different scenarii for the evolution of ABS in a uniform external magnetic field B_{ext}.

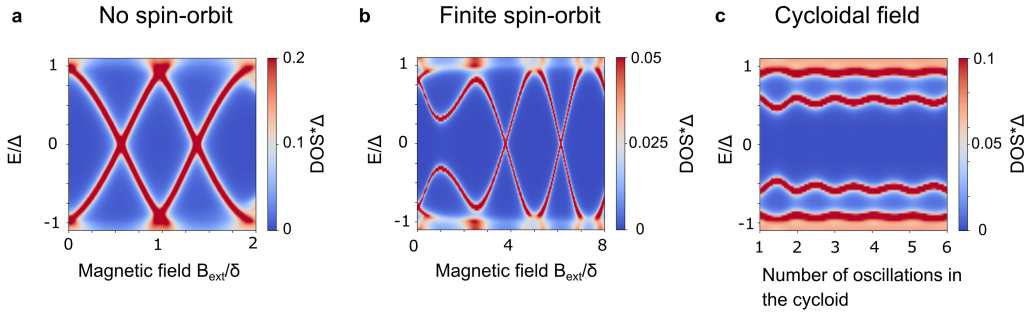

FIGURE 4.3: **Oscillations of Andreev Bound States in various scenario** The colorscale map displays the density of states (DOS) of the first site as a function of the energy eV/Δ in an N/S device. Panel (a) (resp. (b)) displays the evolution of Andreev Bound states as a function of a homogeneous magnetic field B_{ext} without (resp. with) a spin-orbit interaction in the chain (scenario labeled a and b). Panel (c) displays the evolution of ABS with respect to the number of oscillations of a cycloidal field in the normal N part. The density of states in (c) shows non-crossing oscillations of the ABS energy as a function of the number of oscillations of an oscillating field B_{osc} (scenario c).

A nanoconductor subject to a rotating magnetic field, coupled to a superconductor is described by the following discrete hamiltonian:

$$H = \sum_{n\in[1,N_1]} \hat{d}_n^\dagger \left(-\mu\hat{s}_0 + B_{osc,z}(n)\hat{s}_z + B_{osc,x}(\mathrm{n})\hat{s}_x + B_{osc,y}(\mathrm{n})\hat{s}_y\right)\hat{d}_n - t(\hat{d}_n^\dagger\hat{d}_{n+1} + \hat{d}_n^\dagger\hat{d}_{n-1})\hat{s}_0 + \sum_{n\in[N_2,N_{tot}|k} t_{kn}\hat{d}_n^\dagger\hat{c}_k\hat{s}_0 + h.c. + H_s \tag{4.1}$$

where $\hat{d}_n^\dagger \equiv \left\{\hat{d}_{n\uparrow}^\dagger, \hat{d}_{n\downarrow}^\dagger\right\}$ and $\hat{d}_{ns}^\dagger$ is the creation operator of an electron with spin s at site n, $\hat{c}_k^\dagger \equiv \left\{\hat{c}_{k\uparrow}^\dagger, \hat{c}_{k\downarrow}^\dagger\right\}$, with $\hat{c}_{ks}^\dagger$ the creation operator of an electron in the superconductor with momentum k, spin s, and H_s the superconductor's hamiltonian. The chain with sites label by n is along the z-axis. A superconductor is coupled to the chain only between sites N_2 and N_{tot}. For the sake of simplicity, we take $t_{kn} = t_s$. A normal

part between sites 1 and N_1 is subject to a magnetic field $B_{(osc,x,y,z)}(n)$, as represented schematically in figure 4.4. We then calculate the density of states (DOS) on each site.

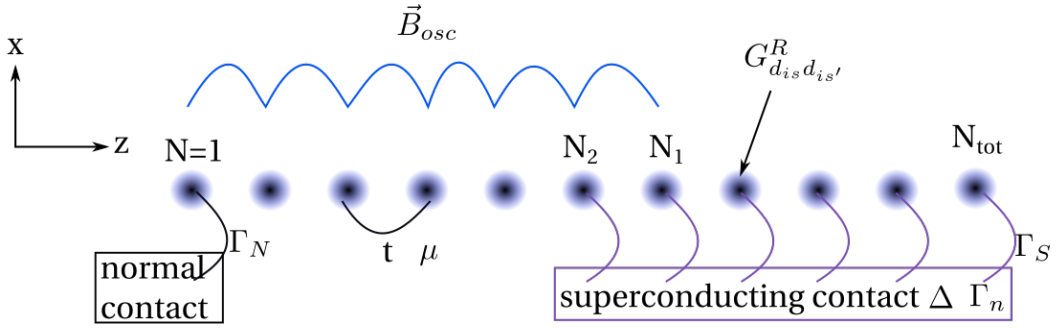

FIGURE 4.4: Schematics of the chain of N sites described using tight-binding formalism. A superconductor (normal lead) is coupled to sites N_2 to N_{tot} (N_1). An oscillating field spans sites 1 to N_1.

figure 4.3 displays three different scenarii :

Scenario a The oscillating field is set to zero, $B_{osc}(n) = 0$ and we look at the evolution of the density of states at the first site, as a function of a homogeneous field B_{ext} applied along the whole chain. In the short junction limit (level spacing δ larger than the superconducting gap Δ), there is one ABS that is pinned at the superconducting gap at $B = 0$. When varying the magnetic field, the Andreev bound states display crossings at zero energy, with a period set by the energy level spacing δ. In figure 4.3 (a), we show a simulation for

$$N_{tot} = 60, N_1 = 30, N_2 = 30, t = 100, \Delta = 1, t_s = 100, \Gamma_N = 0, \gamma_n = 0.1, \mu = 0$$

Scenario b We look at the evolution of the ABS with respect to an external magnetic field but with a finite spin-orbit energy in the chain, modeled in the discrete Hamiltonian by an additional term : $\sum_{n\in[1,N_{tot}]} \Lambda \hat{d}^\dagger_n \hat{s}_y \hat{d}_{n+1} + h.c.$. At $B_{ext} = 0$, the ABS are now separated from the superconducting gap. The ABS display anti-crossing at small magnetic field on a period which is bigger than the energy level spacing δ. At large magnetic field, the effect of the spin-orbit coupling becomes negligible and we recover crossing oscillations. In figure 4.3 (b), we show a simulation for

$$N_{tot} = 60, N_1 = 40, N_2 = 20, t = 100, \Lambda = 20, \Delta = 1, t_s = 1, \Gamma_N = 0,$$
$$\gamma_n = 0.1, \mu = -0.99 * 2t.$$

Scenario c We finally consider the scenario where the external magnetic field shifts the number of oscillations of a cycloidal field in the normal part: $B_{osc,x}(n) = B_{osc} \cos(2\pi n\alpha)$

and $B_{osc,z}(n) = B_{osc}\sin(2\pi n\alpha)$. We take into account the stray field out of the magnetic texture by implementing a homogeneous field in the superconducting part with amplitude 0.5 B_{osc}. The ABS show oscillations with a period defined by the change in the number of field oscillations. In figure 4.3 (c), we show a simulation for

$$N_{tot} = 60, N_1 = 40, N_2 = 20, t = 100, \Delta = 1, t_s = 1, \Gamma_N = 0, \gamma_n = 0.1, \mu = -0.85 * 2t,$$
$$B_{osc} = 1.$$

For these three cases, we see that depending on the effect of the external magnetic fields, ABS oscillate with or without crossing but with very different periods, which will enable us to discriminate between these possible effects. In the third scenario, the number of oscillations is directly linked to the variation in the number of magnetic domains, enabling us a measurement of the spin-orbit energy from equation (2.10). This comparison will help us understand the experiment presented in the following section.

4.1.4 Synthetic spin-orbit interaction: S/QD/S' device with a magnetic texture

We will now discuss one of the main experimental result obtained during this thesis. This section is adapted from the article [179]. The labeling Subgap States (SGS) has been replaced by Andreev Like States which we felt to be more specific. It presents the experimental study of the combined effect of a spatially varying magnetic field and superconductivity on a nanoconductor. Indeed, as discussed in chapter 1, the interplay of superconductivity with a non-trivial spin texture holds promises for the engineering of non-abelian Majorana quasi-particles. A wide class of systems expected to exhibit exotic correlations are based on nanoscale conductors with strong spin-orbit interaction, subject to a strong external magnetic field. The strength of the spin-orbit coupling is a crucial parameter for the topological protection of Majorana modes as it forbids other trivial excitations at low energy [11, 12]. The spin-orbit interaction is in principle intrinsic to a material. As a consequence, experimental efforts have been recently focused on semiconducting nano-conductors or spin-active atomic chains contacted to a superconductor [15, 49, 58, 250, 251]. Alternatively, we show how both a spin-orbit and a Zeeman effect can be autonomously induced by using a magnetic texture coupled to any low dimensional conductor, here a carbon nanotube. Transport spectroscopy through superconducting contacts reveals oscillations of Andreev like states[4] under a change of the magnetic texture. These oscillations are well accounted for by a scattering theory

[4] We use the terminology Andreev like states to bring forward the fact that we deal with spinful Andreev bound states

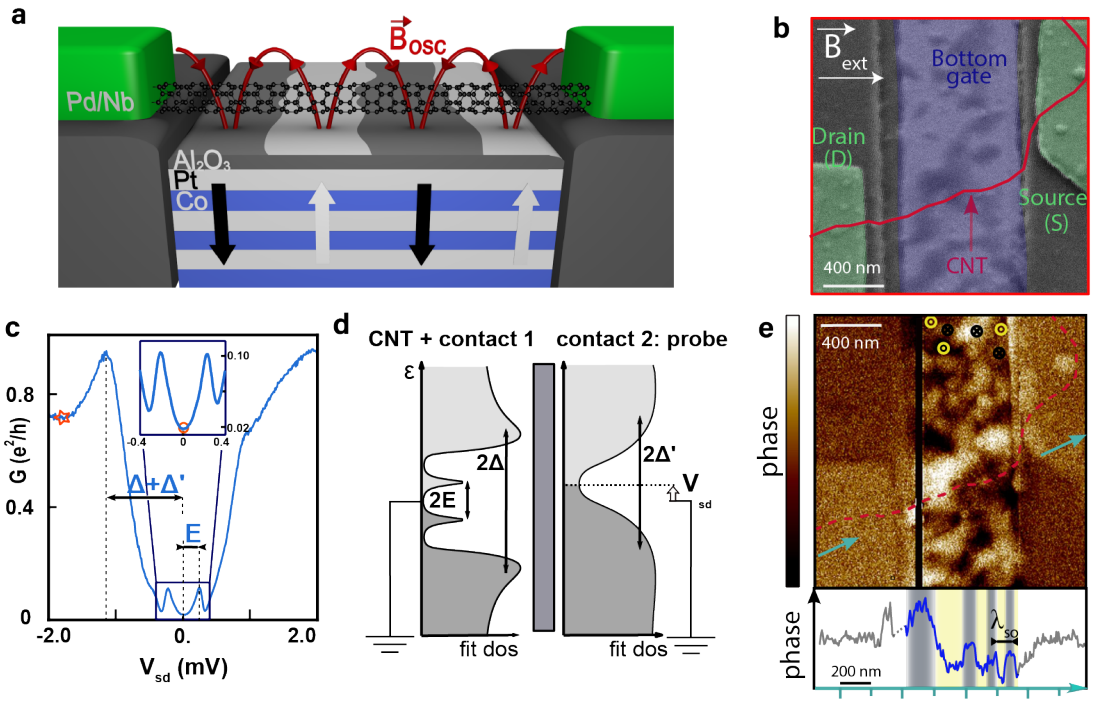

FIGURE 4.5: **Hybrid superconductor-nanotube-magnetic texture setup** (a) Schematic picture of the multilayer magnetic texture with up and down domains (white and black arrows) inducing the rotating magnetic field in space (B_{osc}, red line) leading to the synthetic spin-orbit interaction. (b) Zoom on the device showing the single wall carbon nanotube (in red). The bottom gate is made from a multilayer of Co/Pt. The source and drain superconducting electrodes are made out of Pd/Nb. (c) Conductance of the device as a function of source-drain bias displaying a well-defined gap with two symmetric ALSs at energy E, shown again in the inset. The "hardness" of the gap is measured by the ratio of the conductance values marked by the star and the circle. (d) Density of states of the probe contact and of the NT, with the Andreev-like states arising from the coupling between the nanotube and the left superconductor, as fitted by Usadel equations (see section 4.2.4.1). The right superconductor has a residual density of states at zero bias allowing for a direct spectroscopy of the ALSs. (e) Magnetic Force Microscope (MFM) micrograph of the device showing the magnetic texture of the bottom gate. The cut of the magnetic signal indicating field modulations (yellow and grey) along the nanotube on a scale of about 200 nm is shown at the bottom.

and are absent in a control device with no magnetic texture. A large synthetic spin-orbit energy of about 1.1 meV, larger than the intrinsic spin orbit energy in many other platforms, is directly derived from the number of oscillations. Furthermore, a robust zero energy state, the hallmark of devices hosting localized Majorana modes, emerges at zero magnetic field. Our findings synthetize all the features for the emergence of Majorana modes at zero magnetic field in a controlled, local and autonomous fashion. It could be used for advanced experiments, including microwave spectroscopy and braiding operations, which are at the heart of new schemes of topological quantum computation.

Here, we present experimental results on a transport device composed of a single wall carbon nanotube (our 1D conductor) connected to two superconducting electrodes and

coupled to a proximal magnetically textured gate. Within the superconducting gap, we observe Andreev-like States (ALSs) whose energy oscillates as a function of the external magnetic field. This is direct evidence that we have induced a large synthetic spin orbit interaction in the nanotube and observed its interplay with spinful Andreev bound states. We finally observe a zero bias conductance peak stable in magnetic field, and discuss its compatibility with the emergence of Majorana modes in our setup.

Our device is shown in figure 4.5 (b) and (e). A single wall nanotube is stamped onto a magnetic Co/Pt bottom gate bottom gate which is capacitively coupled to two gate electrodes, Gate 1 and Gate 2. The Co/Pt is expected to have a small pitch and an out of plane anisotropy, giving rise to several domains over the length of the nanotube, with a strong stray field of about 0.4 T as supported by the magnetic characterization and simulations shown in section 3.3.3. The Magnetic Force Microscope (MFM) picture shown in figure 4.5 (e) evidences magnetic domains in the bottom gate, which have a typical size of about $100 - 150$ nm. An external magnetic field B_{ext} changes the magnetic structure and can therefore reveal the existence of the synthetic spin orbit interaction.

Superconducting correlations are induced by connecting the nanotube to two Nb/Pd superconducting electrodes. We address the discrete spectrum induced by the superconductor by transport spectroscopy. The typical measurement of the differential conductance G as a function of source-drain bias V_{sd} is shown in figure 4.5 (c). The conductance displays a well-defined energy gap of about 550 μeV containing two peaks, symmetric with respect to zero bias. These two peaks signal ALSs arising from superconducting correlations. As sketched in figure 4.5 (d), our measurements are equivalent at low energy to conventional tunnel experiments as a consequence of the finite density of states at the Fermi energy in one of the two superconducting contacts (contact 2). Such a residual density of states in the superconducting leads is systematically observed in our devices and has also been reported by other groups (see for example Ref. [248]). The global shape of the conductance curve is well accounted for by the quasi-classical description of superconductivity in the electrodes, based on Usadel equations and reveals that contact 1 displays a well-defined superconducting hard gap. The large subgap slope is shown to arise mainly from a residual pair-breaking in one of the superconductor (contact 2 in figure 4.5 (d); see section 4.2.4.1 for details on the Usadel formalism). The ratio between the high bias conductance and the zero bias conductance which measures the "hardness" of the gap is of about 45 which compares favorably with the recently reported figures in semiconducting nanowires [49].

One of the main findings of our experiments is displayed in figure 4.6 (b). In this color-scale map of G as a function of V_{sd} and the external magnetic field B_{ext}, we observe the evolution of the ALSs under an external magnetic field. Strikingly, they display

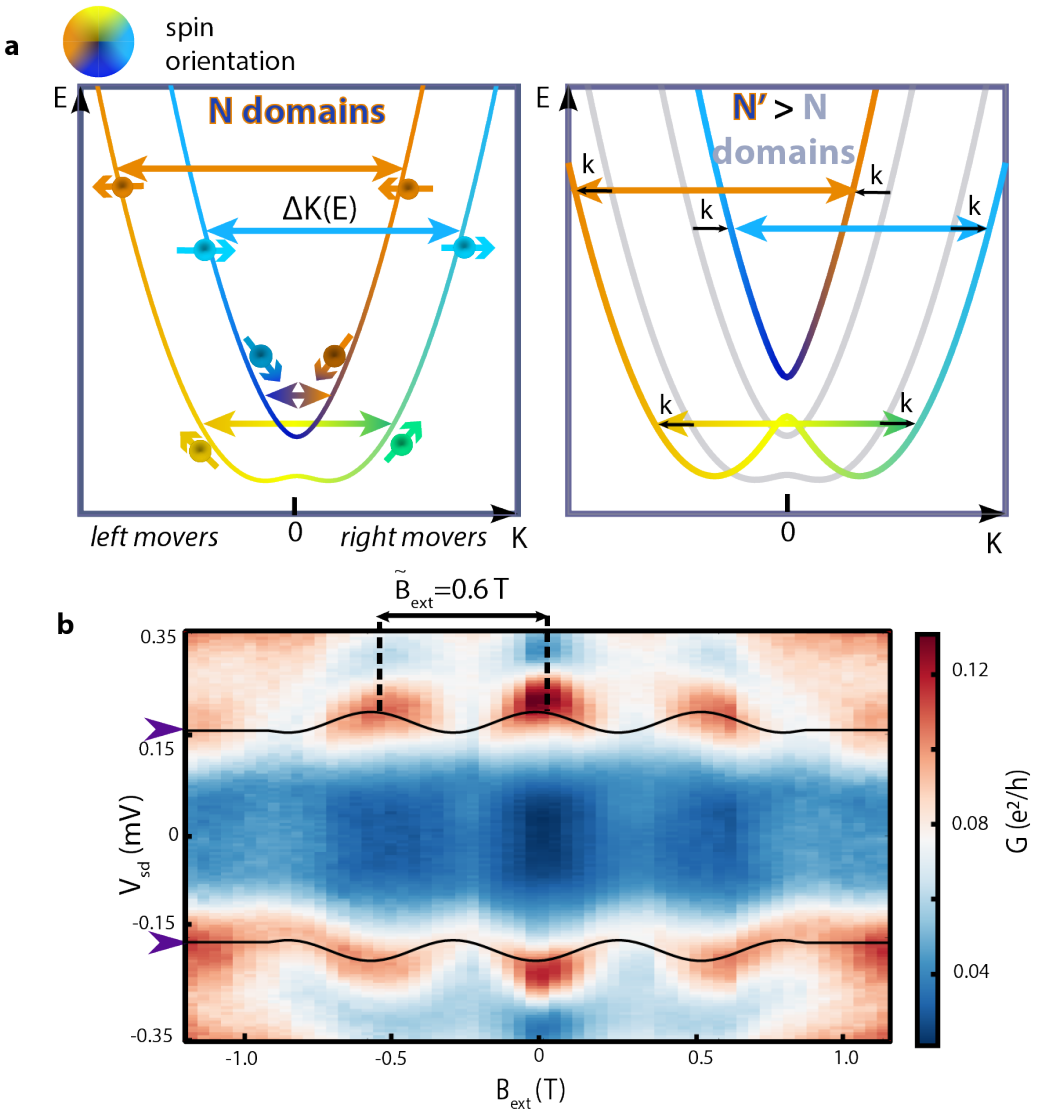

FIGURE 4.6: | **Oscillations of the subgap states and synthetic spin-orbit interaction** (a) Left panel: Band structure arising from the synthetic spin orbit interaction with N domains. The allowed interferences in the finite length system are represented with arrows. Right panel: Schematics of how the band structure can be tuned by changing the spin orbit energy (with N' domains, the bands are shifted by k). b. Low bias conductance G map in the $V_{sd} - B_{\text{ext}}$ plane showing the oscillations of the ALSs (indicated by purple arrows) as a function of the magnetic field. The black lines are the fit to the theory, as described in more details in section 4.2.2.

oscillations with a period of about 0.6 T (±10% from one magnetic sweep to another). We can resolve up to three oscillations around the mean energy of 220 μeV, together with the expected slow reduction of the superconducting gap as shown in 4.7 (a)[5]. Such a behavior is unusual for ALSs and has not been observed in any other system. It stems from the progressive alignment of the magnetic domains with the global magnetic

[5]Note that here this reduction is not seen on a coherence peak but on the gap edge due to the small bias window. Its evolution can be fitted by the usual formula, $\Delta(B) = \Delta(0)\sqrt{1-(B/B_c)^2}$, as will be shown below

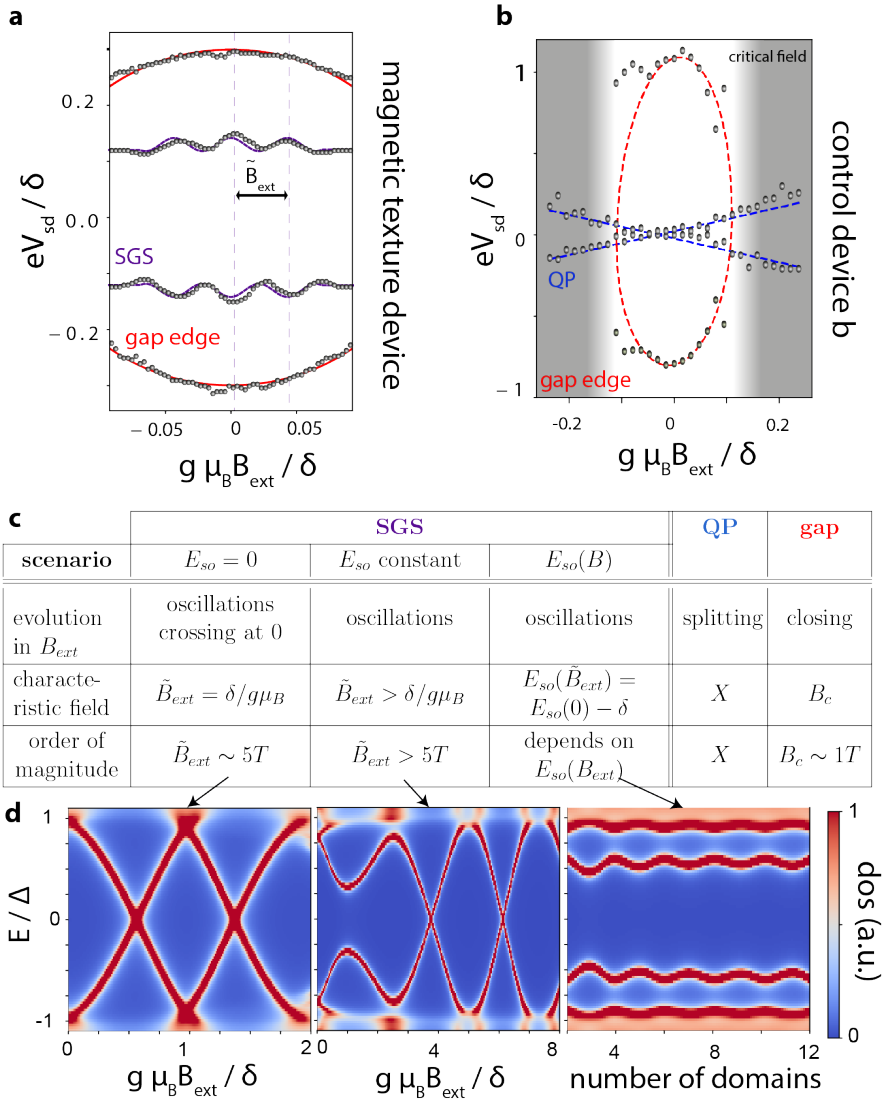

scenario	SGS: $E_{so}=0$	SGS: E_{so} constant	SGS: $E_{so}(B)$	QP	gap
evolution in B_{ext}	oscillations crossing at 0	oscillations	oscillations	splitting	closing
characte-ristic field	$\tilde{B}_{ext}=\delta/g\mu_B$	$\tilde{B}_{ext}>\delta/g\mu_B$	$E_{so}(\tilde{B}_{ext})=E_{so}(0)-\delta$	X	B_c
order of magnitude	$\tilde{B}_{ext}\sim 5T$	$\tilde{B}_{ext}>5T$	depends on $E_{so}(B_{ext})$	X	$B_c\sim 1T$

FIGURE 4.7: **Control experiment and phenomenology of Andreev-like states under a magnetic field** (a) Conductance resonances energies with respect to $V_{sd}-B_{\text{ext}}$, extracted from figure 4.6 (b) (grey points). Theory fits are represented in purple and red respectively (see 4.2.2). (b) Same plot as in (a), for the control experiment presented in section 4.1.5. A quasiparticle resonance (QP, blue) appears within the gap, with a linear blue fit. (c) Table of the evolution of transport signatures as a function of an external magnetic field in different scenario. (d) Corresponding DOS, from tight-binding simulations as presented in section 4.1.3.

field. This can be understood more precisely from the energy dispersion of electrons subject to a rotating magnetic field, $E(K)$ with K the wave vector, shown in figure 4.6 (a). The interference conditions defining the energies of the ALSs are set by the wavevectors difference ΔK between right-moving and left-moving-electrons with non-orthogonal spins eigenstates. A variation of the magnetic domains induces a shift k in the wavevectors K. Near the helical gap, where the spin states are not orthogonal, it

adds a term $2kL$ to the interference condition :

$$E_{ALS} \approx \pm E_{ALS,0}\left(1 + a\cos\left[2\Delta K\left(B_{\text{ext}}\right)L\right]\right) \tag{4.2}$$

with $\Delta\text{K}\left(B_{\text{ext}}\right) = \Delta K\left(B_{\text{ext}} = 0\right) + 2\text{k}\left(B_{\text{ext}}\right)$, $E_{ALS,0}$ the ALS energy at $B_{\text{ext}} = 0$ and a the relative amplitude of the oscillations. The ALSs magnetic field dependence is well accounted for by this formula, under the assumption that the spin orbit strength decays linearly as the field increases, up to a saturation field of about 1 T. Such an evolution of the synthetic spin orbit energy is supported by magnetic measurements as well as micromagnetic simulations (see sections 3.3.3 and 4.2.3).

The number of oscillations N sets the range of modulation of $k(B_{\text{ext}})$ and therefore allows us to give a lower bound for the induced spin orbit energy at zero magnetic field: $E_{so} \geqslant \delta N/2$ (see section 4.2.2). From the number of oscillations in figure 4.6 for $B_{\text{ext}} > 0$ ($N \sim 1.5$) and the extracted level spacing ($\delta \sim 1.5$ meV see figure 4.18) we deduce $E_{so} \geqslant 1.1$ meV. This is of the order of the simple estimate for a linear spectrum [170, 171] $E_{so} = \frac{hv_F}{2\lambda} = \delta\frac{L}{\lambda}$ with $\frac{L}{\lambda} \sim 2$ (5 domains), inferred from the MFM picture in figure 4.5 (e). Strikingly, this spin orbit energy is larger than the ones found in InSb or InAs nanowires (respectively $0.25 - 1$ meV and $0.015 - 0.135$ meV [252]). Moreover, we can reproduce the ALSs oscillations with simulations based on the scattering theory, with δ and $\Delta \sim 0.6$ meV extracted from the data, an amplitude of the stray field B_{osc} of 400 mT extracted from the magnetic simulations and a chemical potential close to the helical regime (see section 4.2.2). These oscillations are robust to disorder in the magnetic texture, as studied numerically in figure 4.15. They can also be qualitatively reproduced from the spatial field evolution inferred from the MFM data of figure 4.5 (see figure 4.15). These simulations will be discussed in more details in section 4.2.6.

Figure 4.7 (c) summarizes possible behaviors for the ALSs under a magnetic field, illustrating the presented transport measurement of a magnetic device, as well as measurement of a control device with no magnetic texture (that will by discussed in more details in section 4.1.5). They are illustrated in figure 4.7 (d) with tight-binding simulations of the density of states in a 1D conductor connected to a superconductor. These simulations were already presented in more details in section 4.1.3. The left and central panels describe the evolution of ALSs in a conductor with no (left) and intrinsic (center) spin-orbit interaction as a function of an external magnetic field. The right panel describes the evolution of ALSs subject to a cycloidal magnetic field under a variation of its period. In the magnetic device, the period of the oscillations with the external field is only compatible with a modulation of the induced spin-orbit interaction, through the progressive alignment of the magnetic domains. Indeed, the magnetic field period corresponding to the other scenarii is too large. The oscillations thus point

unambiguously to the non-trivial character of the observed ALSs. On the contrary, in the control device, we see a simple closing of the superconducting gap and a ZBP of a trivial origin (a residual density of states in both S contacts), whose energy linearly evolves in magnetic field.

The large measured value of spin-orbit interaction is an important prerequisite for driving a hybrid device into the topological regime, where zero energy Majorana modes can emerge. In all the devices experimentally investigated so far, this has only been pursued by applying a large external magnetic field, with severe constraints on network designs, Majorana mode lifetimes, and coupling to superconducting quantum circuits. In contrast, our magnetic texture is equivalent to both a finite and large spin orbit interaction and an external magnetic field: our device could host Majorana modes without any external magnetic field, thus lifting these constraints.

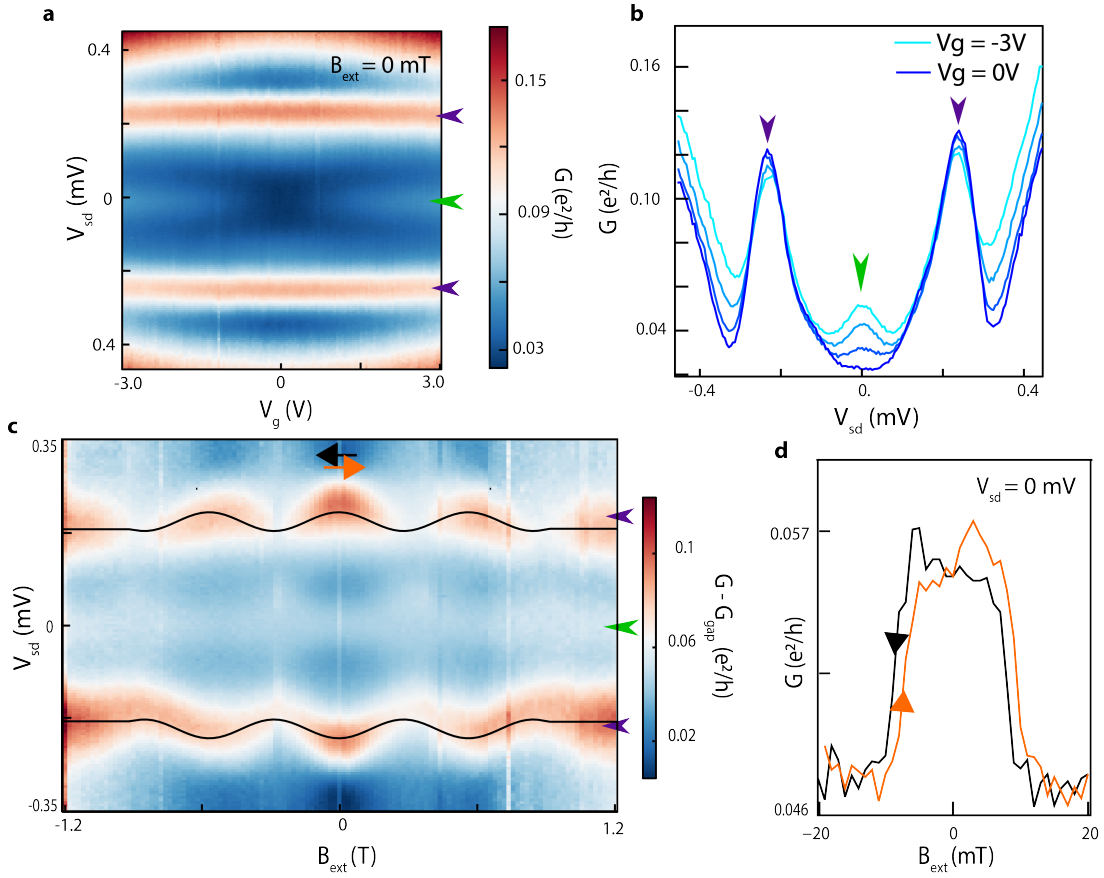

FIGURE 4.8: **Zero bias peak** (a) Conductance G map in the $V_{sd} - V_g$ plane showing the appearance of a zero bias peak when the distant gate of the wire is tuned. (b) Linecuts at gate voltage $V_g = 0, -1, -2, -3$V. (c) Conductance G map at $V_g = -3$ V in the $V_{sd} - B_{\text{ext}}$ plane showing the evolution of the zero energy peak as a function of the in-plane magnetic field. The overall background arising from the superconducting gap has been subtracted for clarity (see figure 4.19). The black lines correspond to the same fit as figure 4.6 (b). (d) Low magnetic field conductance G map in the $V_{sd} - B_{\text{ext}}$ plane for $V_g = -3$ V displaying the large magnetoresistance of the zero bias peak.

In our setup, superconductivity is induced from the side into the helical region, through superconducting proximity effect. Although this is a slight difference compared to other experiments, it can in principle lead to Majorana modes [188, 252, 253] (see also section 4.2.7 for a more developed discussion about this possibility). In figure 4.8, at zero external field, a zero bias conductance peak emerges, simply upon tuning Gate 2 at $V_g > 0.5 - 0.6$ V. We note that this gate does not affect the ALSs nor the superconducting gap but only the appearance of the ZBP along with a slight increase of the conductance background. The ZBP has a width of about 150 μeV as shown in figure 4.8(b), and a height of about $0.05\frac{e^2}{h}$, comparable to the recent findings in semiconducting nanowires (see e.g. ref [15]). In addition, in our case the finite slope of the probe contact density of states affects the conductance height which cannot be mapped directly on the spectral weight of the states in the nanotube. In figure 4.8(d), we measure a large magnetoresistance of 20% for this zero bias peak, accompanied by a hysteretic behavior which is a signature of the effect of the magnetic texture. This strong dependence at small magnetic field could come from local reconfiguration of the magnetic domains, consistent with the expected spatial localization of the state corresponding to a Majorana peak, contrary to the finite energy ALSs which are not affected by a small magnetic field (see figure 4.21 and 4.16). Finally, figure 4.8(c) displays a conductance map where the zero bias peak is robustly pinned at zero energy at large external magnetic field. These features are compatible with the zero bias peak indicating the presence of a Majorana zero modes.

As a conclusion, we have demonstrated a device with a synthetic spin orbit interaction induced by a proximal ferromagnetic multilayer producing an inhomogeneous local magnetic field. This spin orbit interaction deeply modifies the superconducting correlations induced by superconducting contacts and allows us to observe a zero bias peak suggestive of a Majorana mode without any external magnetic field. By relaxing the constraint of an external magnetic field, our setup is suitable for advanced experiments that would unambiguously [68, 70, 254] characterize Majorana modes with the tools of cQED circuits [141, 143, 255, 256]. The use of a magnetic texture also enables the obtention of Majorana modes in any conductor, such as CNTs but also graphene, Si/SiGe 2DEG... The built-in 2D pattern of our magnetic textures could also be interesting for braiding schemes [257] which will require networks of Majorana modes with local and autonomous generation of topological superconductivity.

4.1.5 S/QD/S' devices with no magnetic texture

We now show experimental results on several control S/QD/S devices with no magnetic texture, in order to understand further the specificity of our observations beyond the

comparison to the existing studies of ABS shown in section 4.1.1. The first control device was realized with the same fabrication technique as the magnetic texture device (the stamping technique) while the two other control devices were done with the stapling technique.

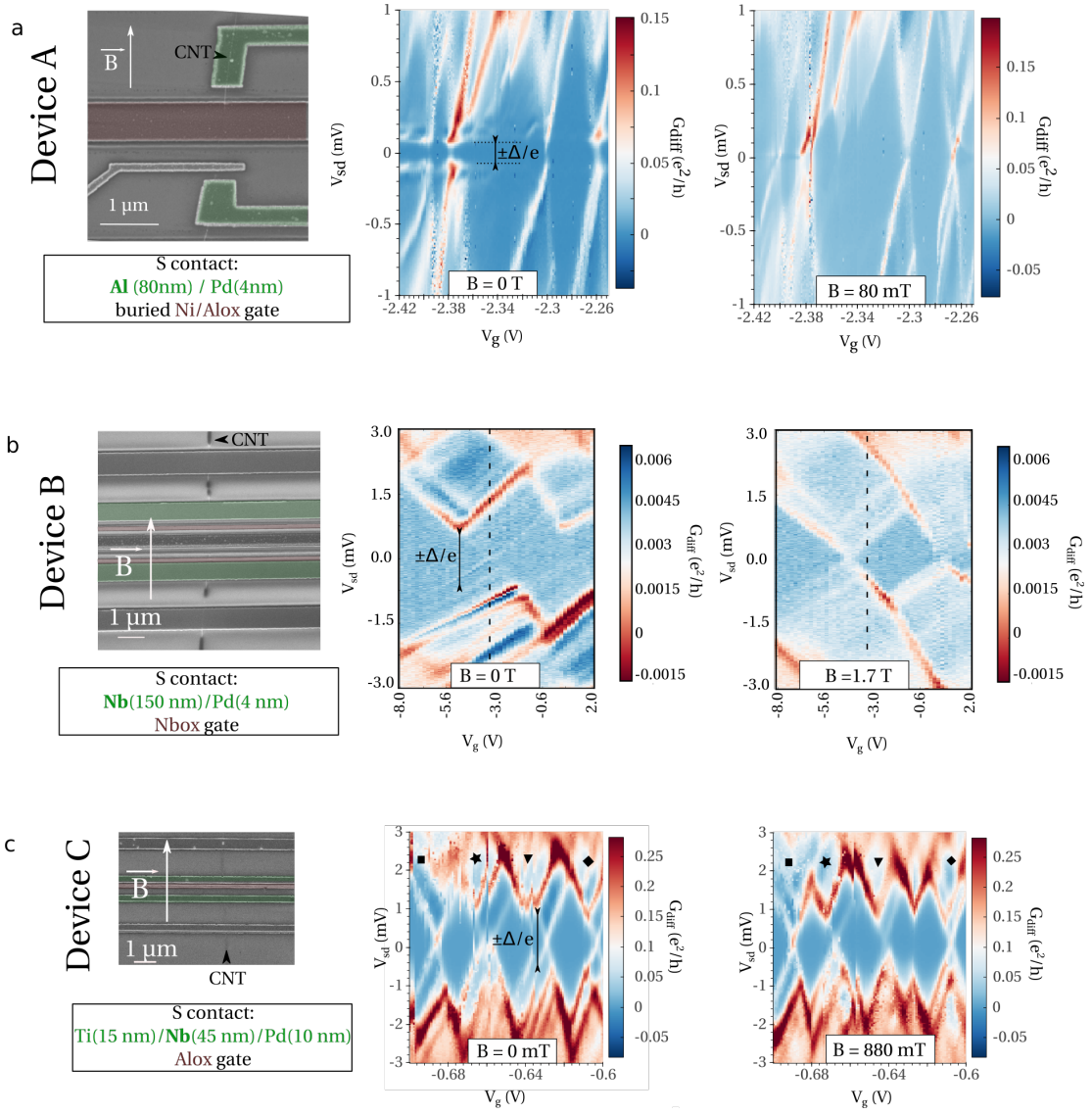

FIGURE 4.9: **Three control devices with superconducting contacts** (a) False-color SEM image and $V_g - V_{sd}$ conductance map for an Al/QD/Al device with a bottom Ni/Alox gate (device A), made with the stamping technique, at 0 and 80 mT (where the Al gap closes). The superconducting contacts are represented in green, the gate V_g in brown. (b) False-color SEM image and $V_g - V_{sd}$ conductance map for a Nb/QD/Nb device with a bottom Nbox a made with the stapling technique (device B), at 0 and 1.7 T (corresponding to the closing of the Nb gap). The dashed line indicates a reference gate voltage, to illustrate the shift in the Coulomb peaks due to Zeeman effect. (c) False-color SEM image and $V_g - V_{sd}$ conductance map for a Nb/QD/Nb device with a bottom Alox gate a made with the stapling technique (device C), at 0 and 0.88 T, as shown already in section 3.4. The markers indicate the correspondence between the Coulomb diamond in the two maps.

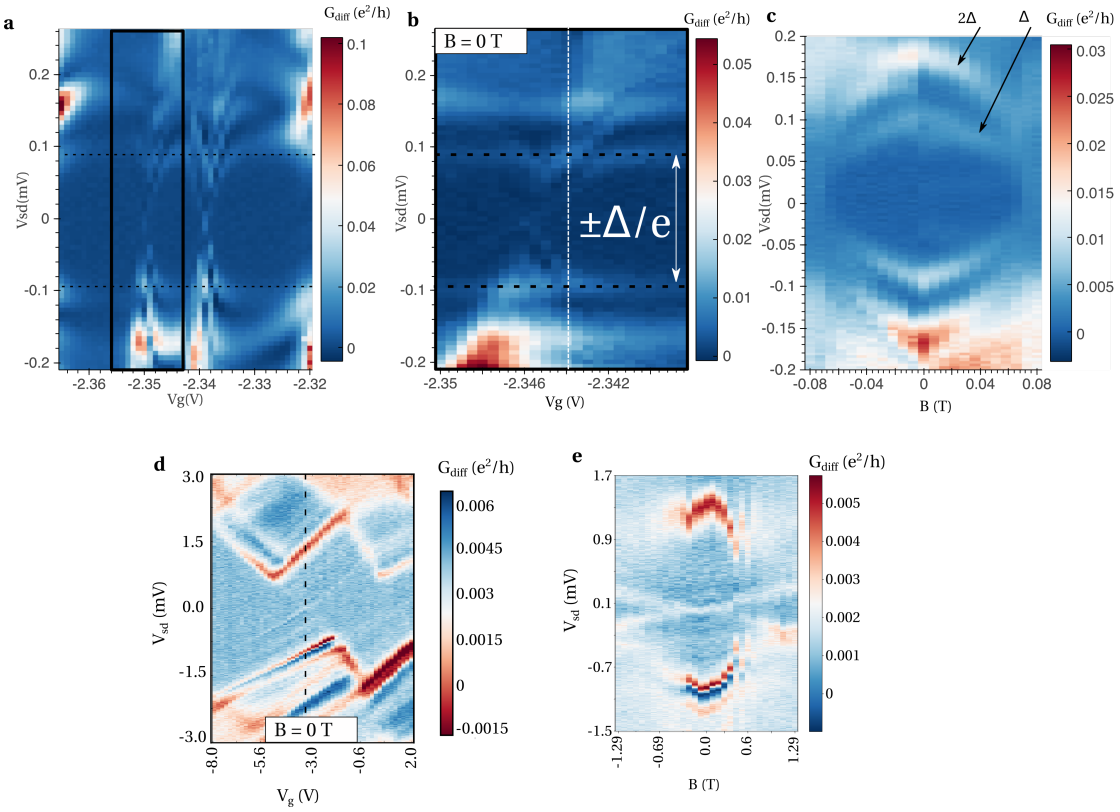

FIGURE 4.10: **Magnetic field dependence of the control devices** (a,b) Zoom-in onto the $V_g - V_{sd}$ conductance map for the control device A (after a gate jump). (c) $B - V_{sd}$ conductance map at the position of the dashed line in (b), showing the closing of the superconducting gap at $B = 80$ mT. (d,e) Similar plots for the control device B. We observe the QP peak splitting and the closing of the superconducting gap reported in figure 4.7.

Figure 4.9 shows the $V_g - V_{sd}$ conductance map for three different devices at two values of magnetic field, while figure 4.10 shows the evolution of conductance as a function of an external magnetic field B for devices A and B.

We observe two parameter regimes. First, in figure 4.9 (a), device A displays a conductance similar to the one of figure 4.1 (b), illustrative of transport through ABS below the superconducting gap, between $eV_{sd} = \Delta$ and 2Δ. In figure 4.10 (a-c) we show that in this device, away from the charge degeneracy point, the subgap states are fixed at $eV_{sd} = \Delta$. Looking at their evolution in magnetic field, we only observe the closing of the superconducting gap. Indeed, in this device we have a zero or weak constant spin-orbit interaction. From the scenarii a and b of section 4.1.3, ABS should display crossing oscillations with a period $\tilde{B}_{\text{ext}}$ of the order of $\delta/g\mu_B$ (as discussed in section 4.1.3) where μ_B is the Bohr magneton. This corresponds to $\tilde{B}_{\text{ext}} = 5$ T for our parameters, which explains why they stay pinned to the superconducting gap until it closes. We observe two square-root-like decrease of the gap with B_{ext} for both a peak at $V_{sd} = \Delta$ and $V_{sd} = 2\Delta$, expected for a S/QD/S device with a S contact with a residual density of states at the

Fermi energy (figure 4.10 (c)). At higher bias, we observe Coulomb diamond, indicating an an important charging energy in the system.

Secondly, in the devices presented in figure 4.9 (b) and (c), we observe clear Coulomb diamonds similar to the conductance map of figure 4.1 (a). Although both contact electrodes are made of superconductors, the conductance maps can be interpreted as transport signatures through a S/QD/S' system, as defined in section 4.1.1. This shows that frequently one of the S contact has a large depairing parameter which yields a smoothly varying density of states (mimicking a N contact with a reduced density of states around the Fermi energy), as already discussed for device C in section 3.4. There is also a residual density of states in the "good" superconducting contact S, which gives rise to a weak quasiparticle peak below the superconducting gap. Figure 4.10 (d,e) shows the evolution in magnetic field of device B. We observe the closing of the superconducting gap, but also the linear splitting of the quasi-particle resonance. The quasiparticle resonance simply splits in B_{ext} with a slope $g\mu_B$ (giving a Landé factor $g \sim 3.5$), and the superconducting gap closes over $B_c = 500$ mT. We can use a constant interaction model to obtain the stability diagram equations for a S/QD/N system, that was used for the fits in figure 4.7 (b) (the dashed blue QP lines and the dashed red gap lines). The quasiparticle peaks positions is given by $eV_{sd} = \frac{\epsilon(B_{\text{ext}})}{\alpha}$ and $eV_{sd} = -\frac{\epsilon(B_{\text{ext}})}{1-\alpha}$, where α is the contact asymmetry and $\epsilon(B) = \left(\epsilon_0 - \frac{1}{2}g\mu_B B\right)$ is the chemical potential of the dot (for a spin down electron, in agreement with the diamond shifting to the left with magnetic field as seen in figure 4.9 (b)). The superconducting gap peaks positions are given by $eV_{sd} = \frac{\Delta(B_{\text{ext}})-\epsilon(B_{\text{ext}})}{1-\alpha_2}$ (at positive bias) and $eV_{sd} = -\frac{\Delta(B_{\text{ext}})+\epsilon(B_{\text{ext}})}{1-\alpha}$ (at negative bias), with $\Delta(B) = \Delta\sqrt{1-(B/B_c)^2}$. We took two different contact asymmetries for positive (α) and negative (α_2) bias, in agreement with the slopes of the Coulomb diamonds[6].

The fit parameters are:

$$\Delta = 0.68 \text{ meV }, B_c = 0.6\text{T}, \epsilon_0 = -0.02\text{meV}, \text{g} = 3.8, \alpha = 0.31, \alpha_2 = 0.47.$$

4.2 Further experimental details

4.2.1 Methods

We briefly give the fabrication details and measurement techniques used in the experiments presented above. The precise recipe parameters can be found in section 3.5.2.1. A 150 nm thick Nb film is first evaporated on a high resistivity Si substrate at rate of

[6] One can note that since the diamonds shift in energy, at fixed detuning the lowest energy peak changes equation and should be piecewise-defined. However in our case the critical field is reached before this is needed.

$1nm/s$ and a pressure of 10^{-9} mbar. A microwave cavity is made subsequently using photolithography combined with reactive ion etching. An array of bottom gates is then made with two e-beam lithography steps in a 100 µm × 100 µm square opening of the ground plane near the cavity central conductor. First, we etch 750 nm × 36 µm trenches of 60 nm depth with reactive ion etching (Si RIE recipe). Second, we deposit inside the trenches the Co/Pt multilayer

$$\text{Ta(40 Å)/Pt(50 Å)[Co(15 Å)/Pt(10 Å)]}_{\times 10}\text{/Pt(40 Å)/Al(40 Å)},$$

100 nm narrower. This magnetic stack has been chosen to promote spontaneously magnetic textures, consisting of magnetic stripes with up and down magnetization with a narrow period. The Co/Pt interfaces induce a perpendicular anisotropy energy that partially compensates for the shape anisotropy which would induce an in-plane magnetization. The Co thickness as well as the number of repetitions have been chosen to increase the dipolar energy, the driving force of the stripes formation, and to maximize the stray field above the sample to about ±400 mT. All the layers in the sample are strongly coupled through their magnetic stray field and belong to a single and continuous magnetic texture. Carbon nanotubes are grown with Chemical Vapor Deposition technique (CVD) at about 900°C using a methane process on a separate quartz substrate, and subsequently stamped above the bottom gates. The quartz substrate was previously processed so that a few pillars of height 4 µm and surface 10 µm × 5 µm are aligned with the cavity openings and come in contact when stamping (see the stamping marks in figure 4.5 (a)). The nanotubes are then localized and those which correctly lie on a bottom gate are contacted with Pd(4 nm)/Nb(40 nm). The Nb layer is evaporated at a rate of 1 nm/s and pressure of 10^{-9} mbar while the substrate is cooled down at 0°C. During this last e-beam lithography and evaporation step, gate electrodes are also patterned in order to couple capacitively the bottom gate to a DC gate voltage V_{g1} (named Gate 1 in the following) and to the AC potential of the central conductor of the cavity. An additional gate, Gate 2 is capacitively coupled to the central conductor of the cavity, and a voltage V_g can be applied.

The DC measurements are carried out using standard lock-in detection techniques with a modulation frequency of 137 Hz and an amplitude of 10 µV. The base temperature of the experiment is 18 mK. An external magnetic field can be applied along the direction of the tube.

Three control devices were fabricated (and are presented in figure 4.9); device A was fabricated with the stamping technique as well, with a Ni/Alox bottom gate and Pd/Al superconducting contacts. Device B and C were fabricated with a slightly different fabrication technique (the stapling technique, see section 3.5.2.2), and the Co/Pt gate

was replaced by an Ti(5 nm)/Al(100 nm) bottom gate, and the superconducting contacts are done with Nb/Pd.

Device B conductance peaks are reproduced in figure 4.7. The chemical potential is tuned through an additional (Nb/NbOx) gate that forms a fork around the bottom gate, noted V_g in the characterization. In a similar fashion, the carbon nanotube was connected to two Nb(150 nm)/Pd(4 nm) superconducting electrodes. The DC measurement are carried at a modulation frequency of 77.77 Hz and an amplitude of 15 µV since the signal is smaller.

4.2.2 Fit parameters for the oscillations in the scattering formalism

We introduced in section 2.2.2 a scattering description of a nanoconductor subject to an oscillating magnetic field. We discussed in section 4.1.1 that although such a description neglects charging effect, it is useful to study the Fabry-Pérot transport regime $\Gamma \sim E_c$, the transport regime in which the magnetic texture device falls as illustrated by the gate dependence shown in figure 4.18 (a) and (b).

In order to refine the model and take into account the two end sections with homogeneous stray field as measured from the MFM, we allow two sections before and after the oscillating field region to be partially polarized by a magnetic field. The full transfer matrix of the 1D system depicted in figure 4.11 now reads, with the notations of (2.27):

$$\begin{aligned} T_{tot} = {} & R_0\left(0,\mu_L,E\right)^{-1} R_0\left(B_{pol},\mu_L,E\right) \exp\left\{iK_L L_L\right\} R_0\left(B_{pol},\mu_L,E\right)^{-1} \\ & R_0(B_{osc},\mu,E) exp\{i(K+k_\alpha \mathcal{A})L\} R_0(B_{osc},\mu,E)^{-1} R_0\left(-B_{pol},\mu_R,E\right) \exp\left\{iK_R L_R\right\} \\ & R_0\left(-B_{pol},\mu_R,E\right)^{-1} R_0\left(0,\mu_R,E\right) \end{aligned} \tag{4.3}$$

with

$$R_0\left(B,\mu,E\right) = \begin{pmatrix} \frac{1}{\sqrt{k_\uparrow}} & 0 & \frac{1}{\sqrt{k_\uparrow}} & 0 \\ 0 & \frac{1}{\sqrt{k_\downarrow}} & 0 & \frac{1}{\sqrt{k_\downarrow}} \\ \sqrt{k_\uparrow} & 0 & \sqrt{k_\uparrow} & 0 \\ 0 & \sqrt{k_\downarrow} & 0 & \sqrt{k_\downarrow} \end{pmatrix}, k_s = \sqrt{\frac{2m}{\hbar^2}(E+\mu+s\frac{1}{2}g\mu_B B)} \tag{4.4}$$

In this modeling, we have assumed that we have two sections around the cycloidal region in which the electrons propagate under a homogeneous magnetic field, of length L_L and L_R, chemical potential μ_L and μ_R and subject to a polarization field B_{pol} (as had been done in figure 2.6). In accordance with the magnetic simulations which shows two

opposite magnetic charges at the end of the cycloidal section (due to the contribution of the in-plane component of the domains magnetization), we take these fields to be of the same magnitude but opposite. The transfer matrix T_{tot} allows us to determine the scattering matrix $S(E)$ of the 1D section in the absence of superconductivity and terminated by a wall (see figure 4.11 (a)). In the presence of a superconducting reservoir, the Andreev Like states energies E_{ALS} may then be found using the following identity, stemming from the secular equation of the system [187]:

$$\det\left(\mathbb{1} - \exp\left(-2i\,\mathrm{acos}\left(\frac{E}{\Delta}\right)\right)S(E)S^*(-E)\right) = 0 \tag{4.5}$$

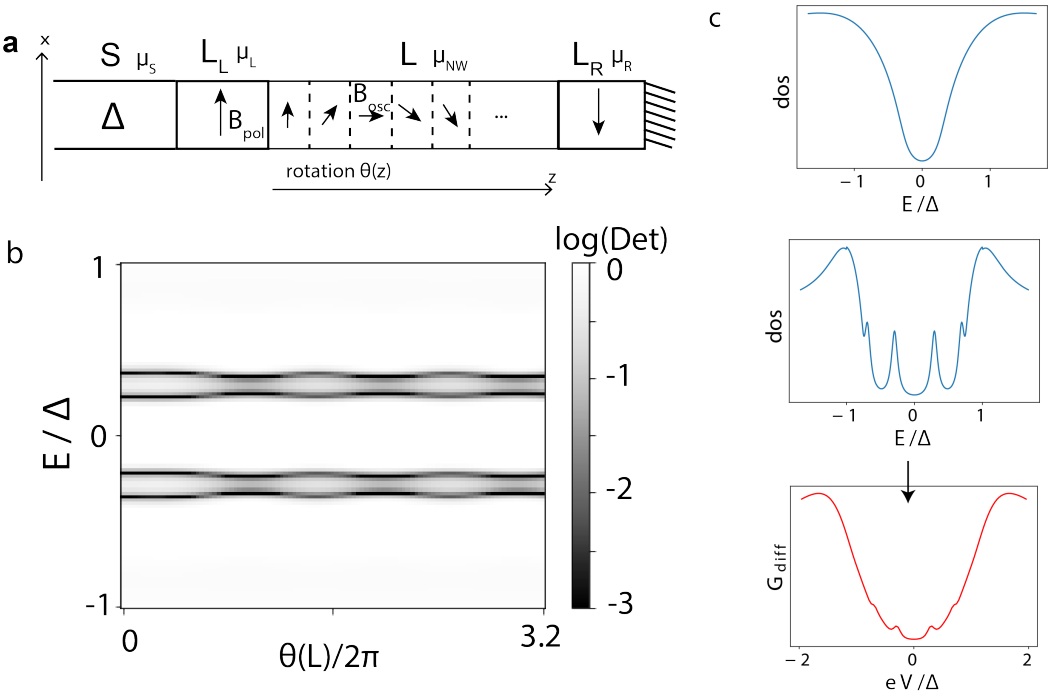

FIGURE 4.11: **Analysis of the Andreev Like states oscillations** (a) Schematic of the scattering representation of the device. The magnetic texture is modeled by a field helix over a length L_1, and is surrounded by two short segments of length L_2 with a uniform magnetic field. It is connected to a superconductor on one side. (b) Energy levels of the system as given by equation (2), as a function of energy and number of field oscillations, which is directly linked to the spin-orbit energy E_{so}. With parameters coherent with our experiments, we are able to reproduce several oscillations of the ALSs emergent in this device. (c) Convolution of the density of states of a device with 2 pairs of ALSs (with energies corresponding to 0.3Δ and 0.7Δ, a spacing that can be obtained with a slightly higher B_{osc}) and a degraded superconducting density of states (as schematized in figure 4.5). One pair of ALSs is hidden in the slope of the conductance as a function of applied bias.

Figure 4.11 (b) shows the energy of the Andreev Like states, as obtained from the secular equation as a function of the total magnetization angle $\theta(L)$ (for simplicity, the zeros of the determinant are plotted). The number of field oscillations is $\frac{\theta(L)}{2\pi} = \frac{k_\alpha L}{2\pi}$; it is related to the number of domains N_{dom} through $N_{dom} = 2\frac{\theta(L)}{2\pi}$ (two domains per oscillation).

We are able to reproduce the oscillations of the Andreev Like states observed in the magnetic texture device with reasonable physical parameters using the model described above and depicted in figure 4.11. The parameters used are the following (assuming a Landé factor of $g = 3.5$, a similar value as the one of the control device (b) described in section 4.1.5):

$$B_{osc} = 0.47T, \quad B_{pol} = 1.5B_{osc}, \quad \Delta = 600\mu eV$$
$$\delta = \frac{\hbar^2}{2mL^2} = 0.6\text{meV}, \quad L_L = L_R = L, \quad \mu = 0.4\Delta, \quad \mu_L = \mu_R = 0.5\Delta$$

We see that we recover the simple rule of thumb stating that the number of oscillations of the ALSs corresponds to the variation in the number of oscillations of the magnetic field, in agreement with the tight-binding simulations that were presented in section 4.1.3.

We note that there are twice as many ABS (four subgap peaks) as what we experimentally observed (two subgap peaks). One possibility is that the second pair of ABS is hidden in the conductance slope of the superconducting gap, as illustrated in figure 4.11 (c). Another one is that it is separated in energy from the first pair of ABS by a small charging energy that is neglected in this modeling.

The oscillations in figure 4.11 (b) are well fitted by a simple sinusoidal function. As a consequence, we fit our oscillation data with the following heuristic formula, derived from the fact that they stem from interference effect and considering that the number of domains decreases linearly with the applied magnetic field up to a saturation value B_{sat}:

$$eV_{sd} = \pm E_{ALS,0}(1 + a\cos[2\Delta k(B)L]) = \pm E_0\left(1 + a\cos\left(\frac{2\pi B}{\tilde{B}_{ext}} + \phi_0\right)\right) \qquad (4.6)$$
$$\text{for } B < B_{sat}$$

where $\tilde{B}_{ext}$ is the oscillation period. The fitting parameters are

$$B_{sat} = 0.9\text{T}, \quad \tilde{B}_{ext} = 0.56\text{T}, \quad a = 0.018\text{meV}, \quad E_0 = 0.195\text{meV}, \quad \phi_0 = 0.04$$

We also include in the fit the closing of the superconducting gap at a critical field B_c (as measured not on the coherence peak, but on their side at energy $eV_{sd} = \Delta_{edge}$ due

to the finite measurement window):

$$eV_{sd} = \Delta_{edge}\sqrt{1 - \left(\frac{B}{B_c}\right)^2} \tag{4.7}$$

with $\Delta_{edge} = 0.45$ meV and $B_c = 1.9$ T.

Large doping limit (Zeeman induced oscillations) In the large doping regime which allows us to linearize the dispersion relation: $k_s^e \sim k_F + \frac{E}{\hbar v_F} - s\frac{g\mu_B B_{osc}}{2\hbar v_F}$ for the electrons and $k_s^h \sim k_F - \frac{E}{\hbar v_F} + s\frac{g\mu_B B_{osc}}{2\hbar v_F}$, where k_0 is the Fermi wave vector. In this limiting case, equation (4.5) becomes, for each spin s:

$$1 = \gamma^2 e^{2i(k_s^e - k_s^h)L} \tag{4.8}$$

Specifically, this equation yields the following implicit equation:

$$E_{ALS} = \pm\Delta\cos\left[2\pi\left(\frac{E_{ALS}}{\delta} + s\frac{1}{2}\frac{g\mu_B B_{osc}}{\delta}\right)\right] \tag{4.9}$$

In the limit of large level spacing $\delta \gg \Delta$, the above equation simply becomes:

$$E_{ALS} = \pm\Delta\cos\left(\pi\frac{g\mu_B B_{osc}}{\delta}\right) \tag{4.10}$$

In case the Andreev like states are only subject to an external magnetic field B_{ext} (pure Zeeman effect), their evolution is obtained by making the substitution $B_{ext} = B_{osc}$. The ALSs oscillate as a function of the external magnetic field and cross at zero energy when $g\mu_B B_{ext} = \delta/2 + n\delta, n \in \mathbf{Z}$. In our case, one oscillation would require a field of 5T, an order of magnitude larger than the observed period of 600 mT.

4.2.3 Estimate of the synthetic spin-orbit energy from ALSs oscillations

We here describe in more details the estimate for the spin-orbit energy from the conductance oscillations of figure 4.6 (c). According to the picture of figure 4.6 (a) and (b), we understand these oscillations as a change in the interference condition when the number of domains $N_{dom}(B)$ changes. The variation $E_{so}^{B_{max}} - E_{so}^{B=0}$ of the synthetic spin-orbit energy induced by $N_{dom}(B=0) \to N_{dom}(B_{max})$ is related to N, the number of the ALSs oscillations by the simple formula: $E_{so}^{B_{max}} - E_{so}^{B=0} = \delta N/2$, where δ is the level spacing in the nanotube.

This formula is derived by considering the interference condition setting the energies of the ALSs. We model our system by a 1D conductor of dispersion relation $E(K)$

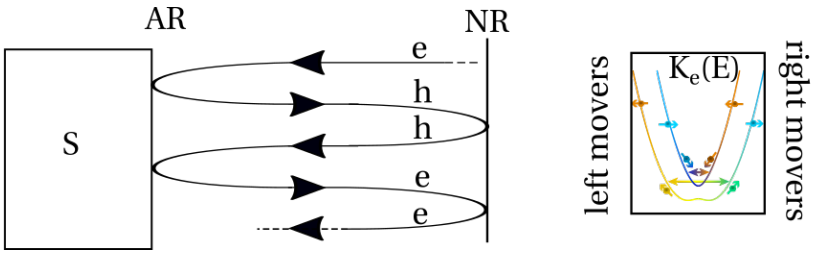

FIGURE 4.12: **Schematic representation of the interference processes** responsible for the formation of ALSs below the superconducting gap, for a nano-conductor confined by an infinite potential barrier and a superconducting contact. The electrons follow Andreev reflections at the superconducting interface on the left (AR), and normal reflections at the potential barrier on the right (NR). In the conductor, the wavevectors for the right and left-moving electrons are defined by the relation dispersion represented on the right. These considerations do not take into account the spin eigenvalue, which can add selection rules for the interferences.

and length L, connected at one end to an opaque barrier and at the other end to an s-wave superconductor. The ALSs can be derived as electronic interferences between left-moving electrons, right-moving holes, (both having a wavevector K_-) and right-moving electrons, left-moving holes (with wavevector K_+), as represented in figure 4.12. This figure shows how the presence of the superconducting interface doubles the length of the trajectories to consider to build the electronic interferences, which leads to the factor 2 in equation (4.2). The interference condition is hence defined by the equation $2K_+(E) - 2K_-(E) = 2\pi n/L$. In the main text, we define $\Delta K = K_+ - K_-$.

In absence of any polarization, $K_- = -K_+$. If the central conductor has a non-trivial dispersion with the spin, as shown in figure 4.6(a), interferences happen only between non-orthogonal spins eigenstates. Moving the domains with the magnetic field implies that the dispersion $E(K)$ is modified. The motion of the domains shifts the wave-vectors from $\Delta K^{B=0}$ to $\Delta K^{B_{max}}$. For large K, away from the helical gap, the two electronic bands are orthogonal and the only possible interference is such that $\Delta K^{B_{max}} - \Delta K^{B=0} = 0$ (orange and blue arrows in figure 4.6(a)). Near the helical gap, the spin eigenstates are not orthogonal anymore between the two bands and $|\Delta K^{B_{max}} - \Delta K^{B=0}| = 2k$, where k is the wave-vector shift induced by the changes in the domains. If N oscillations of the ALSs energies are detected, it means that $\Delta K^{B_{max}} - \Delta K^{B=0} = \pi N/L$, ie that $k = \pi N/2L$. For a linear dispersion such as (2.16): $E_s = \pm\hbar v_F k + sE_{so}$, a monotonic variation of the number of domains implies that $E_{so}^{B_{max}} - E_{so}^{B=0} = \hbar v_F k = \frac{hv_F N}{4L} = \delta N/2$[7]. This sets a lower bound for the synthetic orbit energy, $E_{so} \geq \delta N/2$.

Comparing with the formula given by the unitary transformation $E_{so} = \frac{hv_F}{2\lambda} = \frac{\delta L}{\lambda}$, N oscillations of the ALSs correspond to a change in the number of domains $N_{dom} = L/\lambda$ of $N_{dom} = N/2$. This is in qualitative agreement with the numerical results both with

[7] After one oscillation, a resonant level goes back to the same energy, indicating that the change in spin-orbit energy has been compensated by a change in the k wavevector.

the scattering and the tight-binding formalism, where we observe three oscillations of the ALSs when the number of domains change by three.

The linear spectrum is easier to deal with due to its constant level spacing. However, we can also do a similar calculation for a parabolic dispersion relation and obtain this relation at the bottom of the band. For the parabolic dispersion relation, the bands are roughly given by $E = \frac{\hbar^2}{2m}(k + sk_{so})^2 - \mu$ (at low B_{osc}). Similarly to the linear dispersion case, we consider one of the interference condition that changes with the number of domains, as represented in figure 4.6(a) (green-yellow arrow). For simplicity, we consider the situation where $E_{so}(B_{max}) = 0$, and we note $K_0 = \frac{n_0\pi}{L}$ the wavevector of the ALS resonant level n_0 measured at B_{max}. Between $B = 0$ and B_{max}, there are N oscillations corresponding to a change in energy of N levels with level spacing δ_j:

$$\Delta E = \sum_{j=n_0}^{n_0+N} \delta_j \equiv N\bar{\delta} \tag{4.11}$$

On the other hand, this corresponds to a change in the wavevector entering in the interference condition of $K_0 - k_{so} \rightarrow K_0$ with k_{so} the spin-orbit momentum at $B = 0$. We can relate it to the spin-orbit energy through $E_{so} = \frac{\hbar^2 k_{so}^2}{m}$. By comparing these quantities, we obtain

$$\Delta E_{so} = \frac{N\bar{\delta}}{2}\left(1 - \frac{n_0}{n_0 + N/2}\right) \tag{4.12}$$

At the bottom of the band (corresponding to $n_0 \sim 0$ given that we measure $\delta \sim$ meV) we obtain the same result as for the linear dispersion.

Discussion about the magnetic evolution in B In the fit of the ALSs energy oscillations presented in figure 4.6 and described in section 4.2.2, we assumed a linear decrease of the magnetic domain size up to saturation (with no change in the magnetic axis). This is a pretty simplified image. Indeed, we only know that the number of domains goes to zero when the external magnetic field completely saturated the Co/Pt magnetization, but it could first increase at low B_{ext}. This could be in better agreement with the magnetic simulations, where the domain size rather tends to reduce at first. However, the important point is that even in this case we can still extract a lower bound for the maximum of the spin orbit energy from the number of oscillations.

4.2.4 Mapping between the density of states and the conductance

This section describes the modeling of the superconducting contacts introduced in figure 4.5. The conductance fit is described in more details, and is shown to be in good agreement with the experiment. We also comment on the effect of what we call a S'

probe (i.e. a probe with a superconducting density of states with strong depairing), and notably the fact that the differential conductance contrast is different from that of the density of states.

4.2.4.1 Usadel equations used to characterize the asymmetry between the superconducting contacts

We present in this section the theory which allows us to account well for the shape of the full conductance curves based on the quasiclassical theory of superconductivity in the diffusive regime (Usadel equations). We use a superconducting bilayer of Nb(40nm)/Pd(4nm) to make a superconducting contact on the nanotube. The density of states in these bilayers are in general non BCS because of the interface resistance between the superconducting slab and the normal slab and inverse proximity effect. In addition, in our case, the dipolar helicoidal-like field can induce a pair-breaking which can be taken into account via an Abrikosov-Gorkov general term. The Usadel equations yields the evolution of the density of states as a function of z (the depth from the superconducting interface). It reads:

$$\frac{\hbar D}{2}\partial_z^2\vartheta(z) - (-iE+\gamma)\sin\vartheta(z) - 2\Gamma_{AG}\sin\vartheta(z)\cos\vartheta(z) + \Delta(z)\cos\vartheta(z) = 0 \quad (4.13)$$

where E is the energy, D is the diffusion constant, Γ_{AG} is the Abrikosov-Gorkov pair-breaking parameter, γ is the Dynes parameter and $\Delta(z)$ is the gap function. The pairing angle $\vartheta(z)$ is related to the normal and anomalous Green's functions, G and F respectively, via the relation: $G(z) = \cos\vartheta(z)$ and $F(z) = \sin\vartheta(z)$. The density of states is given by

$$N(z,E) = \mathrm{Re}(\cos\vartheta(z)) \quad (4.14)$$

An important energy scale controlling the physics of proximity effect in the bilayer is the Thouless energy $E_{Th} = \frac{\hbar D}{d^2}$, where d is the thickness of the normal (Pd) slab. In our case, this energy is much larger than the superconducting gap Δ of the homogeneous superconductor, and the interface is not too opaque. Neglecting the self-consistency of the superconducting gap, one may approximate the pairing angle in the Pd slab by an homogeneous solution which obeys the following implicit equation:

$$\tan\vartheta_0 = \frac{\Delta}{-iE+\gamma+2\Gamma_{AG}\cos\vartheta_0} \quad (4.15)$$

The above equation may be solved numerically and the gap appearing in it has the meaning of an effective gap in the normal slab. The density of states in each Nb/Pd

bilayer contacting our nanotube is therefore

$$N(\Delta, \gamma, \Gamma_{AG}, E) = \mathrm{Re}(\cos\vartheta_0) \tag{4.16}$$

In order to compute the current I flowing through our device and the corresponding differential conductance G, one may use the above density of states. As explained in section 4.1.4, one of the two contact is a tunnel probe and the nanotube is only in good contact with the other. One can therefore approximate the measured density of states as that of the well connected Nb/Pd bilayer which induces the superconducting correlation in the CNT and a sum of two lorentzians describing the Andreev Like states in the CNT:

$$N_{NT}(E) \approx N\left(\Delta, \gamma, \Gamma_{AG}, E\right) + \beta \sum_{i=+/-} \frac{\eta}{\left(E - i \times E_{ALS}\right)^2 + (\eta/2)^2} \tag{4.17}$$

This equation is an approximation since it neglects the transfer of spectral weight from the density of states of the slab to the Andreev states and is only valid as long as $\frac{4\beta}{\eta} \ll 1$. The tunnel current can be expressed using the usual tunnel spectroscopy formula:

$$I = \frac{G_N}{e} \int_{-\infty}^{+\infty} dE N_{NT}(E) N\left(\Delta, \gamma_2, \Gamma_{AG,2}, E + eV_{sd}\right) \left\{f(E) - f\left(E + eV_{sd}\right)\right\} \tag{4.18}$$

where $f(E)$ is the Fermi function. The above formula is the one used to fit the cut in figure 4.8 (a). We allow the Abrikosov-Gorkov Γ_{AG} and the Dynes parameter γ to be different for the good contact (no indice) and the tunnel probe (indice 2).

From equation (4.18), we can derive the equation on the conductance:

$$\begin{aligned} G = G_N \int_{-\infty}^{+\infty} dE N_{NT}(E) N(\Delta, \gamma_2, \Gamma_{AG,2}, E + eV_{sd})(-\frac{\partial f}{\partial E}(E + eV_{sd})) + \\ G_N \int_{-\infty}^{+\infty} dE \frac{\partial N}{\partial E}(\Delta, \gamma_2, \Gamma_{AG,2}, E + eV_{sd}) N_{NT}(E)(f(E) - f(E + eV_{sd})) \end{aligned} \tag{4.19}$$

The fit presented in figure 4.18 (d) was obtained with

$$\begin{aligned} &E_{ALS} = 210\ \mu\mathrm{eV},\ \eta = 79\ \mu\mathrm{eV},\ \Delta = 716\ \mu\mathrm{eV},\ \Gamma_{AG,1} = 51\ \mu\mathrm{eV},\ \Gamma_{AG,2} = 318\ \mu\mathrm{eV}, \\ &\gamma_1 = 16\ \mu\mathrm{eV},\ \gamma_2 = 82\ \mu\mathrm{eV},\ \frac{4\beta}{\eta} = 0.74\ , T = 150\ \mathrm{mK} \text{ and } G_N = 0.61\frac{e^2}{h}. \end{aligned}$$

We note that the spectral weight of the Andreev Like states is not completely negligible (as is also visible in figure 4.5), which may account for small mismatches between the fit and the experimental curves.

This fit leads to the two density of states N_{NT} (contact 1) and N (contact 2), plotted in figure 4.5(d). It also shows that we can safely remove a background conductance from the bare curves shown in figure 4.19 to plot those of figure 4.8, so that the ZBP is more visible.

4.2.4.2 Effect of a S' type probe

From the fit, contact 2 has a large residual density of states at the Fermi energy (which we call later on a S' contact). Since its density of states $N(E)$ is non constant in energy, the second term in the conductance equation (4.19) is non-zero.

As a consequence, the height of the ALSs conductance peaks is not directly linked to their spectral weight (as it would for a normal tunnel probe). This effect explains why the oscillations of the ALSs energies leads to the variation of the ALSs conductance height seen in figure 4.6. Importantly, this also shows that the very low value of conductance associated to the two ALSs does not imply low spectral weights in $N_{NT}(E_{ALS})$. This is best seen on figure 4.5(d) where the peak height of the two ALS peaks amounts to about 0.74 of the normal state density in the nanotube. Similarly, the zero bias peak has a spectral weight much larger than its height in conductance. From the comparison with the height of the ALSs which are roughly twice as large, we can estimate that the actual peak height of the zero bias peak is about 0.35 of the normal state density of states in the nanotube.

4.2.5 Control experiments

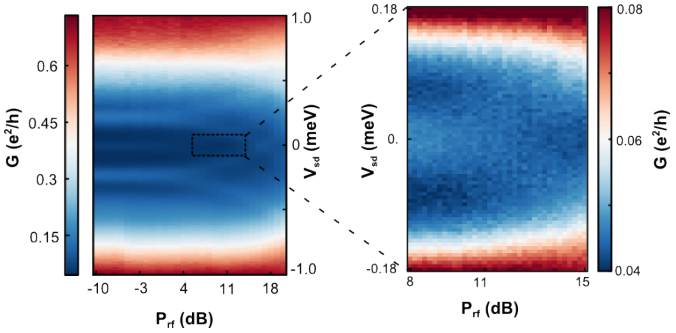

FIGURE 4.13: **Microwave power dependence of Andreev-like states and zero bias peak** Evolution of the Andreev Like peaks as a function of the microwave power applied at the input of the cavity.

In this section, we present two control experiments. In the first, we apply a large microwave power to the input port of the microwave cavity in order to test whether the zero bias peak may arise from a weak Josephson effect. In the adiabatic limit where

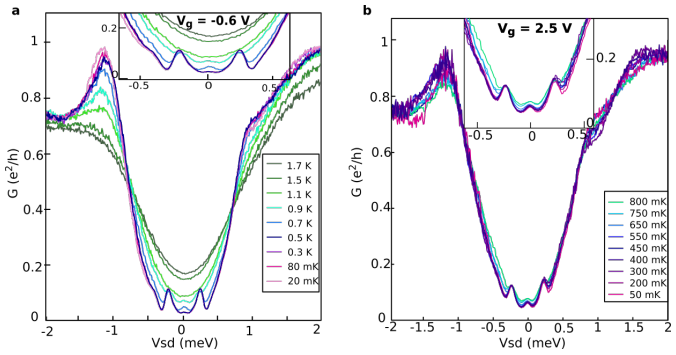

FIGURE 4.14: **Temperature dependence of Andreev Like states and zero bias peak** (a) Evolution of the Andreev Like peaks as a function of the temperature from 20 mK to 1.7 K for $V_g = -0.6$ V. We interpret the higher peak for $T = 700$ mK as a small gate switch because the gate setting is close to the transition at which the zero bias peak emerges. Such a switch is absent in panel (b) which is for a gate setting further into the gate region where the zero bias peak appears. (b) Evolution of the Andreev Like peaks as a function of the temperature from 50 mK to 800 mK for $V_g = 2.5$ V.

the frequency of the applied tone to the cavity $f_{rf} = 5.6$ GHz is much smaller than the relevant relaxation rates of the states in the device, the differential conductance G is modulated by the cavity photons as:

$$G(t) = G\left(V_{sd} + V_{AC}\cos\left(2\pi f_{rf} t\right)\right) \tag{4.20}$$

The conductance can be fit by three lorentzians centered around each of the peak energies as shown in the section devoted to the finite bias conductance. The phenomenology of the above equation is simply a splitting of each conductance peaks if V_{AC} bias larger than their width. As shown in figure 4.13, the two finite energy Andreev Like states as well as the central peak split at the same power and in the same way. This shows that they all correspond to electronic states characterized by a lorentzian like spectral density. In particular, these measurements are not consistent with the zero bias peak being a well-developed Josephson supercurrent branch which would display Shapiro steps. The case of a weak Josephson branch which does not display Shapiro steps would be very quickly washed out by temperature (at the temperature scale given by the Josephson energy, ie a supercurrent of 1 nA corresponds to 140 mK) and is not consistent with the temperature dependence of the zero bias peak which is described below.

Finally, we present in figure 4.14 the temperature dependence of our measurements which is fully consistent with a gradual filling of the gap which starts to be effective only at about 1K. In particular, as one can see in panel (a) of figure 4.14, we observe that the zero bias peak and the Andreev Like states disappear at the same temperature (about 1K). Therefore, we can exclude a thermal occupation origin for the zero bias peak that would be indicated by a continuous increase of the zero bias peak as a function of temperature.

4.2.6 Andreev Like States with a spin helix, impact of disorder

We now investigate the effect of disorder in the oscillating magnetic field, using the tight-binding model introduced in section 4.1.3. We take two models for the disorder in the magnetic field. Figure 4.15 illustrates the result of this study.

First, we consider a field that evolves in space in the same fashion as the MFM cut of figure 4.5, reproduced in figure 4.15 (a). This MFM phase signal contains various frequencies, as shown by the discrete Fourier transform given in figure 4.21 (b). We construct a cycloidal magnetic field from the Fourier coefficients a_f associated with the spatial frequency f of the MFM signal in the following way:

$$B_{osc,z}(i) = B_{osc} \sum_f a_f \sin(2\pi f i), B_{osc,x}(i) = \sum_f a_f \cos(2\pi f i). \tag{4.21}$$

We model the domains evolution under an external magnetic field by a simple shift of the frequency of each coefficient of the Fourier transform. The effect of B_{ext} is:

$$a_f\left(B_{\text{ext}}\right) = a_{f+\delta f(B_{\text{ext}})} \tag{4.22}$$

With $\delta f\left(B_{ext}\right) \propto B_{ext}$. We then plot in figure 4.15 (c) the density of states at the first site of the chain, as a function of energy and B_{ext} using this model. We observe oscillations of a pair of ALSs, as measured experimentally. The discrete Hamiltonian parameters for this simulation are:

$$N_{tot} = 60, N_1 = 40, N_2 = 20, t = 100, \Delta = 1, t_s = 1, \Gamma_N = 0.2, \gamma_n = 0.15, \mu = -0.82 * 2t,$$

and the amplitude of the oscillating field B_{osc} is normalized at each B_{ext} such that the maximal amplitude is 1 (in units of the superconducting gap Δ).

Second, If we consider a situation where there is only one oscillation frequency, we obtain the density of states of figure 4.15 (e), which is very similar to that of figure 4.15 (c), namely oscillations of a pair of ALSs. We conclude that disorder in the magnetic field does not strongly affect the oscillations of the ALSs predicted for a periodic magnetic field, and observed in the experiment.

As a third alternative approach, we use the magnetic simulations of section 3.3.3 from which we can directly extract the magnetic field in all three directions above the Co/Pt structure, and its evolution as a function of the external magnetic field. This is shown in figure 4.15 (d,f). We use as the parameters for the discrete Hamiltonian:

$$N_{tot} = 60, N_1 = 40, N_2 = 20, t = 100, \Delta = 1, t_s = 1, \Gamma_N = 0, \gamma_n = 0.15, \mu = -0.85 * 2t.$$

The amplitude of the oscillating field is taken as:

$$B_{osc}(\text{ units of } \Delta) = 2B_{\text{magnetic simulations(T)}} \tag{4.23}$$

in order to have a qualitative agreement with the measured oscillations, for this set of parameters. The micro-magnetic simulations give the spatial evolution of the field vector B_{osc} for seven values of B_{ext}: 0, 0.2, 0.4, 0.6, 0.8, 1 and 1.2T. We interpolate linearly the evolution of each component of the field in between these values. We plot the density of states at the first site as a function of energy and B_{ext}, and observe oscillations of the ALSs energies, under this more realistic evolution of the magnetic texture. The simulations reproduce qualitatively the evolution of B_{osc} in the three direction of space, when a magnetic field is applied to the magnetic texture, and at different cut positions we can obtain different realizations for B_{osc}. The simulated fields used for this study may not perfectly fit our sample's stray field; notably it seems to contain more domains than what the MFM signal indicates.

To conclude, this shows that the analysis of the oscillations of the ALSs is robust considering more realistic models of our system, build either from a realistic stray field profile extracted from the MFM data, or from micro-magnetic simulations.

4.2.7 Discussion on the zero bias peak

The emergence of a ZBP in the experiment is compatible with the emergence of a MZM in our experiment, although the signatures are not sufficient to discriminate against other unfathomed scenarii. Besides, we could not give a precise modeling of certain characteristics of the peak, such as the magnetoresistance measured in presence of the peak (figure 4.21), and the effect of Gate 2 (V_g). Finally, in the simplified picture of the unitary transformation of the oscillating magnetic field, the field period is also present in a chemical shift. As a consequence, changing the domain size could change the parameter regime from a topological region (a priori very small due to the small g-factor in our system) to a trivial region, which would be inconsistent with the persistence of the ZBP observed experimentally.

The ZBP measured in the experiment has a small conductance height. However, we use a superconductor with a finite density of states at low bias to probe the zero bias peak, which apparently lowers the spectral weight of the zero bias peak with respect to the finite energy subgap states. Besides, while the Delft group has reported a quantized conductance, the Copenhagen group has reported also clear zero bias peaks but which a very small amplitude (typically $0.02 - 0.08\frac{e^2}{h}$ [15]). We think that similar reasons as the

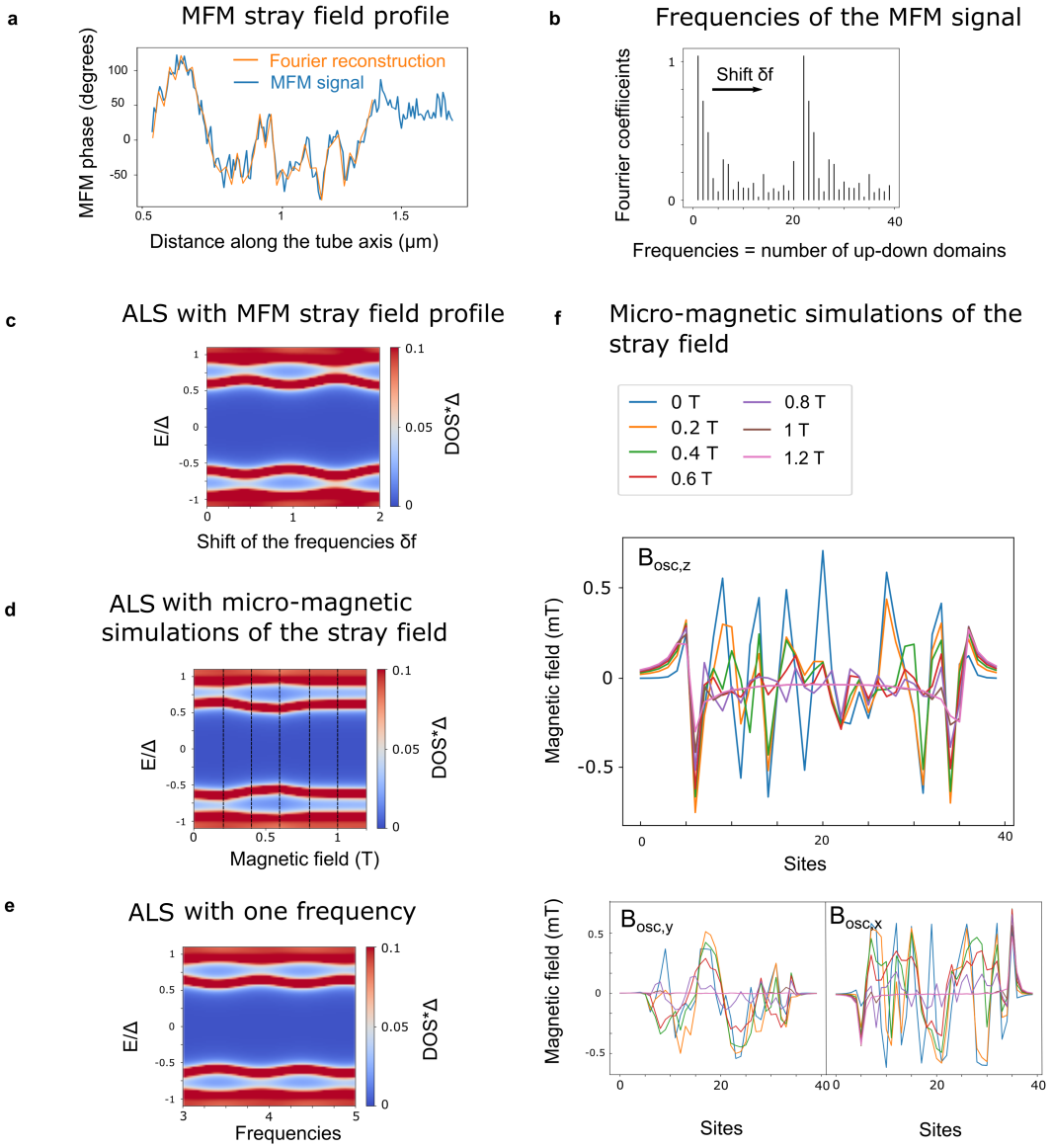

FIGURE 4.15: **Effect of disorder in the oscillating magnetic field** (a) Cut of the MFM image along the CNT as represented in figure 4.5 (in blue), and reconstructed signal containing the $N = 40$ top-most frequencies of the discrete Fourier transform of the raw data (orange). (b) Modulus of the Fourier coefficients of the MFM signal of (a). A given discrete frequency can be thought of as the number of up and down domains in the magnetic texture. To mimic the effect of the external magnetic field, we shift the coefficients' frequency as shown in equation (4.22). For example, the coefficient corresponding to 5 oscillations at the beginning will, at $\delta f = 2$, correspond to 7 oscillations. (c) Density of states of a one-dimensional wire as a function of the energy showing Andreev Like States. The oscillating field is given by the orange curve of panel (a) and evolves under a shift of it Fourier coefficients. The x axis corresponds to shifting frequencies. (d) The oscillating magnetic field is now taken from the magnetic simulations, in all three directions of space. (e) Similar plot, with only one coefficient in the discrete Fourier transform. (f) Oscillating magnetic field in all three directions of space, extracted from the magnetic simulations, along the dashed line in 4.21. It is given for different external magnetic fields, at a height $x = 0$ nm.

ones invoked in this reference could also be used to explain the small amplitude of our ZBP. Finally, since the geometry for this experiment is different than the one proposed in the original proposals [11], we do not expect a quantized conductance for the ZBP [72, 188].

Beyond this discussion, it also came to our attention that the question whether Majorana could or not emerge in such a setup was still under debate, as discussed in section 2.3. In this section, we described the scenario for apparition of a MZM with an intrinsic spin-orbit interaction. We now turn to the situation where Majorana zero modes can potentially emerge in our setup. We model both a finite superconducting contact ("on the side", as opposed to a superconducting contact extended over the whole conductor) and the magnetic field helix. In figure 4.16, we study the variations of the density of states (DOS), the singlet pairing and the triplet pairing as a function of the number of magnetic domains (which are tuned by the external magnetic field in the experiment). The parameters of the model are:

$$N_{tot} = 20, N_1 = 16, N_2 = 15, t = 12, \Delta = 1, t_s = 12, \Gamma_N = 0.1, \gamma_n = 0.05,$$
$$\mu = -0.33 * 2t, B_{osc} = 8.$$

Note that here we take larger magnetic fields than in previous modeling, since we want to discuss whether this geometry can host MZM rather than quantitatively describe the experimental results.

The density of states shown in figure 4.16 (a) displays oscillations of Andreev Like states at non zero energy but more importantly a zero bias peak emerging when the number of domains increases. In order to characterize the Andreev Like states, it is instructive to plot the singlet and triplet pairing amplitudes (in panel (b) and (c)) for the same parameters. Interestingly, before the emergence of the zero bias peak, one sees both singlet and triplet pairing amplitudes as expected for superconductivity in the presence of homogeneous spin polarization. However, the emerging zero bias peak is solely made out of triplet correlations, as required for a Majorana zero mode. The singlet and triplet pairing amplitude are defined by equation (2.41) and (2.42).

We now show another important feature of this zero mode: its spatial localization and sensitivity to the local configuration of the magnetic field, as illustrated in panels (e), (f) and (g). These colormaps show the density of states as a function of the position in the chain and energy, for a system with the same parameters as panel (a) and with 7 magnetic field oscillations (14 domains). As expected, we see that the zero bias peak corresponds to two localized states located at the interface between the magnetic texture and the superconductor and the magnetic texture and the left hard wall. On

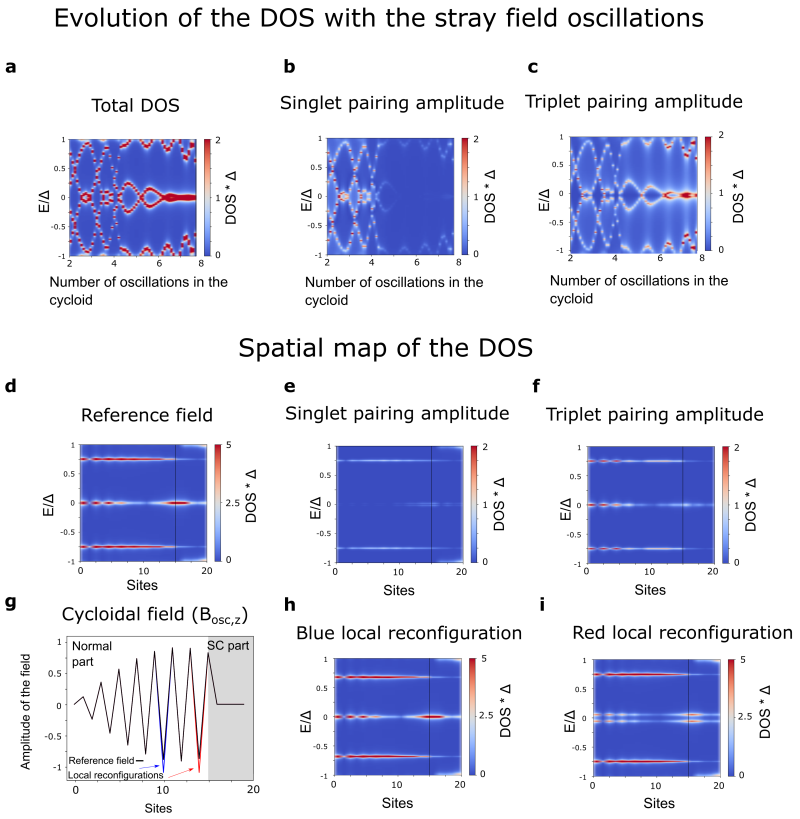

FIGURE 4.16: **Emergence of Majorana excitations in our experimental setup** (a) Density of states at the first site of the chain (site 0), computed using a discretized tight-binding Hamiltonian, showing the emergence of a zero-bias peak for a large number of up and down domains. (b)-(c). shows the singlet and triplet pairing amplitude for the same parameters. Singlet and triplet pairing amplitude are defined in equation (2.41) and (2.42). The numerical simulation is realized by considering a normal part with a cycloidal field, as illustrated in (d) for the component along the axis of the chain (z-axis). The field is not perfectly sinusoidal because of the high ratio between the number of oscillations (7) and the number of sites (16) for the cycloid. A superconductor is connected to the chain from sites 15 to 20. Two local reconfigurations of the field are shown in red and blue. (d), (h) and (i) display the spatial dependence of the density of states for the three different configurations of the field (black, red and blue). The dotted line shows the separation between the normal part and the superconducting part. (e) and (f) show the singlet and triplet pairing amplitudes for the DOS (d). The zero bias peaks have a larger triplet pairing amplitude.

the contrary, the non-zero energy Andreev Like States are fully delocalized on the entire wire length. Importantly, a change in the magnetic texture has barely any effect on the later irrespectively of the position of this change (figure 4.16 (e) and (f)). This is completely different from the case of the Majorana zero mode which is insensitive to a local reconfiguration in the middle of the magnetic texture (figure 4.16 (g)) whereas it splits for a reconfiguration close to the superconducting/wire interface, where its wave function is non-zero (figure 4.16 (f)). All these features reproduce qualitatively our experimental findings and show that localized Majorana zero modes can emerge when superconductivity is induced from the side of the wire, in a different manner than the initial propositions for engineering Majorana bound states in one dimensional conductor. In summary, our numerical study confirm the robustness of the oscillations of the ALSs at non-zero energy to disorder, and substantiate the Majorana zero mode interpretation of the observed zero bias peak.

4.2.8 Additional data on the magnetic device

Large scale device layout and microwave environment The large scale device layout and microwave environment is shown in figure 4.17. The whole device is embedded into a microwave cavity which has a fundamental resonance frequency of about 7.5 GHz. For the magnetic device presented, this particular mode was not coupled to the device but other modes of the electromagnetic environment were coupled. We use here these modes to couple our device with a distant gate Gate 2 (with gate voltage V_g) which is the one used in figure 4.8. The device is also coupled via the bottom gate to Gate 1 with gate voltage V_{g1}. Although the specific resonant mode of the cavity was not coupled to our device, the coplanar waveguide resonator could be used to convey a microwave signal in the GHz range to study its dynamical response (see below).

The two gates have different effects on the device. Gate 1 has a larger capacitance to the bottom gate than Gate 2, thus sets mainly the potential of the bottom gate. The effect of V_{g1} is to tune the energy level in the NT, as shown by figure 4.17. V_g does not affect neither the ALSs, nor the gap and only controls the appearance of the ZBP in the conductance signal, which goes along with a small increase of the conductance background. This points towards a more specific effect of Gate 2 that could locally change the wavefunction in the CNT, finely tuning the overlap of the ZPB wavefunction to the contact electrodes.

Gate maps of Andreev Like states We present the gate map of the Andreev Like states when Gate 2 is kept at 0V and Gate 1 (which is directly coupled to the bottom gate as shown in 4.17) is swept from 0.2V to 1V in 4.18. The Andreev Like states

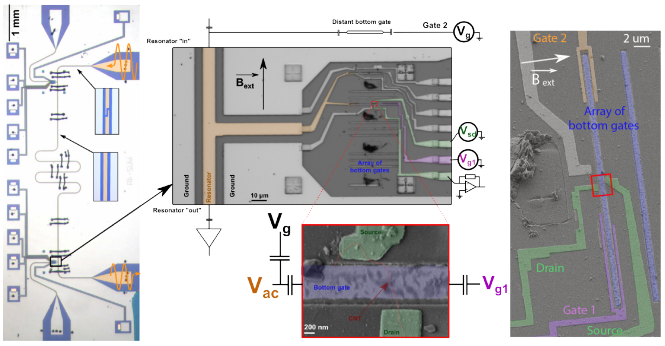

FIGURE 4.17: **Microwave environment of the device** The whole device is embedded in a microwave cavity with a resonance frequency of about 7.5 GHz.

remain visible essentially in all the map. A parity crossing is observed at $V_{g1} \sim 0.7$ V. Importantly, the high bias conductance, close to $\frac{e^2}{h}$ displays only weak features. In particular, no Coulomb blockade diamond is observed which signals that our experiment is in the Fabry-Pérot regime. From the smooth checkerboard pattern, one can extract an estimate of the level spacing $\delta \sim 1.5$ meV.

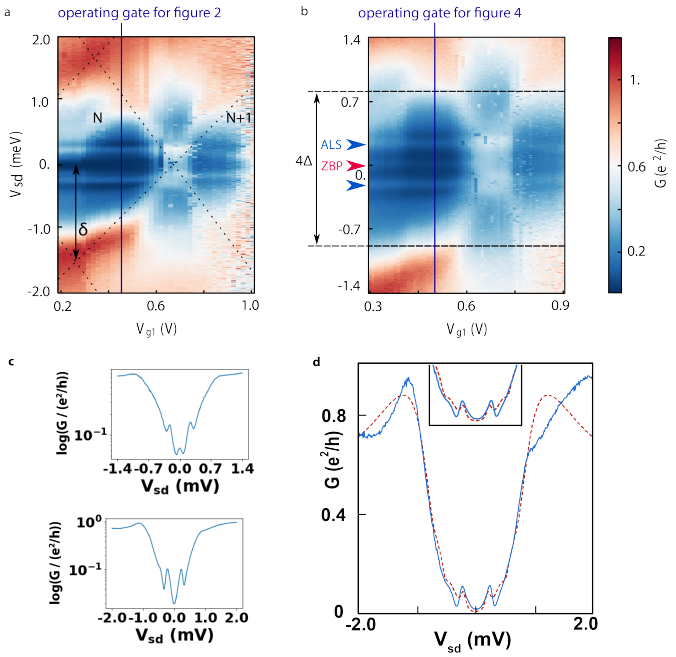

FIGURE 4.18: **Gate map of the Andreev Like states.** (a,b) Conductance as a function of bias V_{sd} and Gate 1 V_{g1} showing the evolution of the Andreev Like states as a function of Vg1 for two values of Gate 2 $V_g = 0$ V (panel a) and $V_g = -3$ V (panel b) such that the Zero Bias Peak is present. In panel a, the shape of the Fabry-Pérot modulations of the conductance is highlighted by the dotted black lines, and N and $N+1$ indicates the equilibrium charge on the dot. The level spacing δ for our quantum dot can be roughly estimated, as shown by the black arrow. In panel b, the edge of the superconducting gap and the position of the different peaks studied are outlined. The values of Gate 1 for the different figures of the article are shown by the blue lines. (c) Corresponding superconducting gap in log scale, at $V_g = 0$ V (bottom) and $V_g = -3$ V (top). (d) Comparison between the conductance measurement as a function of bias (blue line) and the corresponding fit using the Usadel equations (red dashes).

Conductance maps with background and gap closure at high magnetic field We present here two additional conductance maps as a function of magnetic field for the magnetic device.

In figure 4.19, we present the raw data corresponding to figure 4.8. In this map, one can see that there is a strong depression of the conductance as a consequence of the superconducting gap. After fitting the above curves with the theory presented above, one can extract the contribution arising only from the Andreev Like states which allows one to observe more clearly the magnetic field dependence of these states. Nevertheless, as one can see in figure 4.19, all the features presented in figure 4.5 are visible in the raw data.

Finally, it is interesting to study the magnetic field map of the conductance up to large fields where the superconducting gap of the electrodes starts to weaken substantially. In figure 4.20, we present such a map where the magnetic field is swept from 0T to 2T and back to 0T. As expected, we observe a gradual "square root like" decrease of the gap edge.

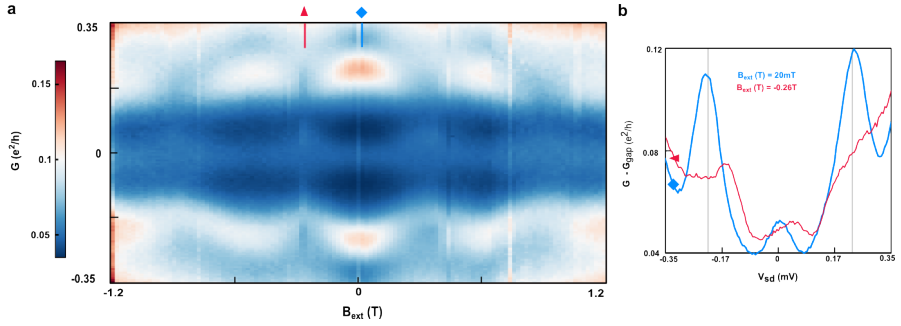

FIGURE 4.19: **Conductance map with background, similar to the map of figure 4.5** Raw data of the conductance as a function of bias V_{sd} and the external magnetic field B_{ext} at $V_g = -3$ V. As shown in the map and the cuts corresponding to those of figure 4.8, the Andreev Like resonances as well as the zero bias peak are clearly visible also in the raw data. The background originates from the peculiar shape of the density of states in the proximized Pd/Nb bilayer.

Magneto-resistance and hysteresis at different gate voltages V_g Figure 4.21 displays a panel of the conductance maps $V_{sd} - B_{\text{ext}}$ for different gate voltages between 0 and -3 V. We observe that the ALS are insensitive to small magnetic fields, whereas the zero bias peak and the background shows a magneto-resistance provided the zero bias peak is present. These two different behaviors are also observed in the Gate 2 dependence that leaves the ALS unchanged. However we cannot match this magnetoresistance with a shift in gate voltage. We also present the emergence of the hysteresis of the zero bias peak with the gate voltage which is directly linked to the emergence of the peak.

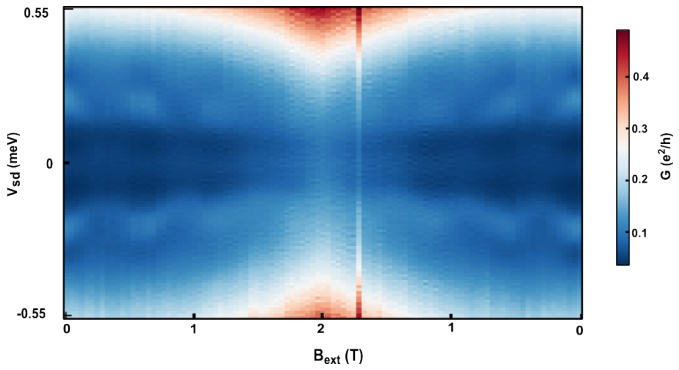

FIGURE 4.20: **Gap closure at high magnetic field** Conductance map in the $V_{sd} - B_{\text{ext}}$ plane from 0T to 2T and back showing the gradual decrease of the superconducting gap. The map is taken at $V_g = 3$ V.

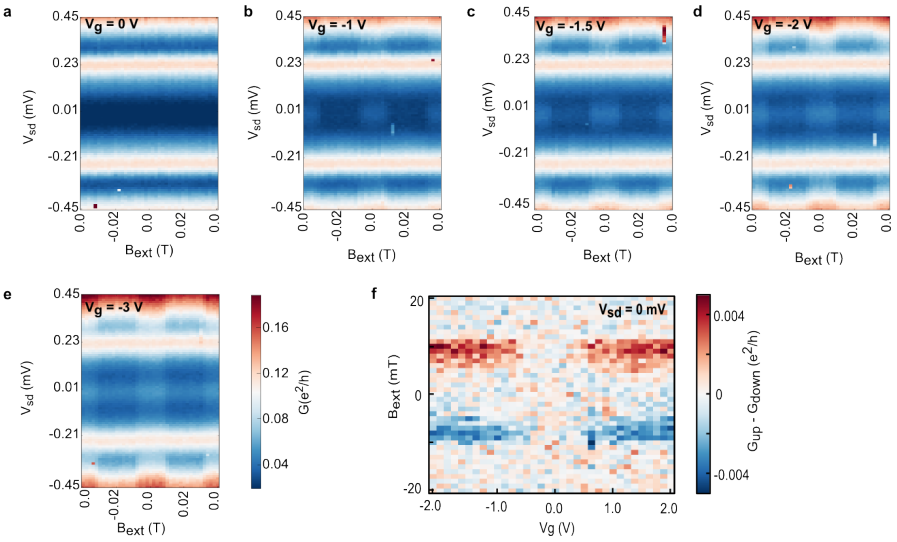

FIGURE 4.21: **Evolution of the magnetoresistance with gate voltage** Conductance map $B_{\text{ext}} - V_{sd}$ at small magnetic field for different gate voltages. The presence of the vertical stripe corresponding to the magnetoresistance is correlated to the emergence of the zero bias peak. f. Difference in conductance between upward and downward field sweeps at zero bias showing the gate voltage dependence of the hysteresis.

Chapter 5

Sensing a spin texture with cavity photons

The next geometry that we would like to study is a double quantum dot where each dot is subject to a synthetic spin-orbit interaction, with a central superconducting contact (and two normal leads). This geometry would realize two copies of the previous device, and would give us new tools to study the interplay of a spin texture with superconductivity. For example, in very open devices, it could be possible to localize differently the potential MZM when tuning each of the dots' chemical potential. In closed devices, the microwave signal could give additional information of the DQD spectrum.

A first step was to investigate the coupling of such a DQD to a microwave cavity, and the microwave signature of the magnetic textures. This study can be realized without the central superconducting contact, instead replaced by a gate electrode. We will present here experimental results obtained during this thesis on such a device. We will first briefly introduce the physics of a DQD with no magnetic texture, with special focus on the information accessible though microwave measurements of a coupled cavity. We then present the study of the DQD where each dot is formed in proximity to a magnetic texture, coupled to a microwave cavity. We have measured the energy of the DQD internal transitions through the change in the microwave signal, and used this spectroscopic tool to characterize the magnetization of the dot electrons. We have observed strong distortions of the microwave signal compared to what is expected for a normal DQD, which is due to the large renormalization of the Landé g-factor in each dot by the magnetic texture.

5.1 DQD stability diagram and microwave measurement

Figure 5.1 (a) shows the stability diagram of a DQD, meaning the current flowing through the whole device as a function of two gates, tuning primarily one dot each [258]. Depending on the parameters regimes, and especially the interdot coupling and the tunnel couplings to the leads, different signals are measured. Current at zero bias is only measured at the triple points (where both dots are aligned with the leads' fermi level) in very closed DQD, whereas co-tunelling lines are visible (where only one dot is aligned with the leads' fermi level) when the tunnel couplings are large.

Coupling a microwave resonator to a DQD enables us to study its internal degrees of freedom [193], and to measure transitions that are not accessible though transport measurements. Indeed, if the cavity field mainly affects the chemical potential on one of the dot, the cavity signal will be strongly modified at the resonant condition $\omega_{cav} = \omega_{DQD}$ where ω_{DQD} is the transition energy between the DQD ground state and excited state(s). Formally, if a cavity is coupled to a mesoscopic circuit with energy levels indexed by i, j, the normalized transmission T of the cavity can be written as a function

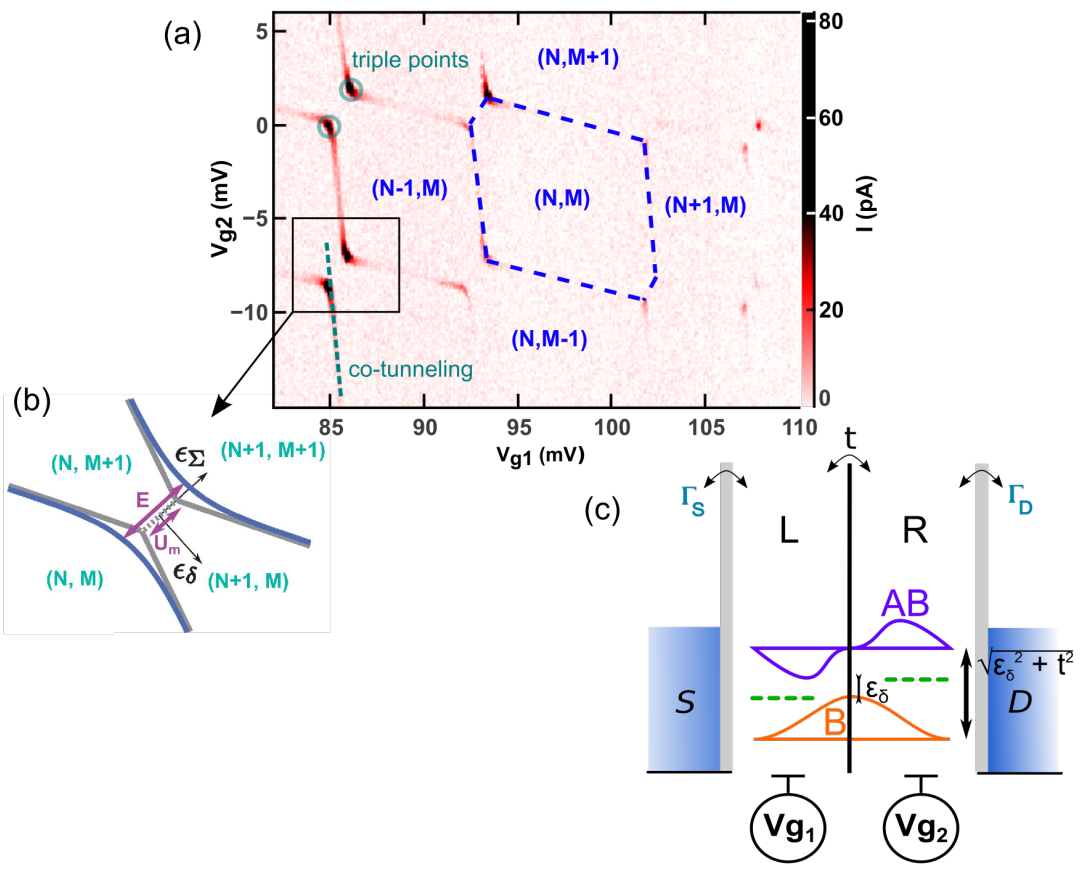

FIGURE 5.1: **Stability diagram for a DQD** (a) Experimental stability diagram: current through the DQD as a function of the two gate voltages V_{g1} and V_{g2}. The charge number on the left and right dots are written over each region. Co-tunneling lines are visible on the bottom left (2^{nd} order tunneling event). (b) Zoom in on the so-called "triple point area" where the interdot tunneling modifies the tunneling lines. The strength of the anti-crossing depends on t the inter-dot hopping and U_m, the mutual charging energy. (c) Schematics of the DQD levels close to zero detuning ϵ_δ. The former dot levels (in green) hybridize to form bonding (B) and anti-bonding (AB) orbitals. Source: [237].

of the drive (resonant) frequency f_d (f_{cav}), the cavity linewidth κ, the level populations n_i, their coupling to the cavity (which is a geometric factor) g_{ij}, the decoherence rate $\Gamma_{ij} = \frac{\Gamma_1}{2} + \Gamma_\phi$ and the drive-transition detuning $\Delta_{ij}/2\pi = f_i - f_j - f_d$:

$$T = \frac{\kappa/2}{2\pi(f_{cav} - f_d) - i\kappa/2 - \sum_{i,j,f_i>f_j} \chi_{ij}(n_i - n_j)} \tag{5.1}$$

$$\chi_{ij} = \frac{g_{ij}^2}{-i\Gamma_{ij} + \Delta_{ij}} \tag{5.2}$$

From this expression, we indeed notice that the cavity signal is strongly modified at the resonant condition $f_{cav} = f_i - f_j$, when the cavity is resonant with an internal transition of the mesoscopic circuit.

Finally, the typical resolution of the microwave signal is of the order of its resonant frequency: 6 GHz $\sim$ 25 µeV. The microwave signal is thus sensitive to smaller changes than the transport measurement, whose resolution is limited by the tunnel couplings to the leads.

5.1.1 A simple DQD: the charge qubit

The first typical system on which one can study the microwave response is a trivial spinless DQD, also known as the charge qubit. In such a system, the two spin eigenvalues are degenerate in both dots, and independent from one another.

We can calculate the transition energies of this DQD by explicitly writing the Hamiltonian of the closed DQD (neglecting the coupling to the leads), considering only one orbital in each dot (of electron number operator $\hat{n}_L$ and $\hat{n}_R$):

$$H = \epsilon_L \hat{n}_L + \epsilon_R \hat{n}_R + (t\hat{c}_L^+ \hat{c}_R + h.c.) \tag{5.3}$$

In the simple case of a total occupancy of one (in the $N \equiv N_L + N_R = 1$ subspace), the energy levels of the system correspond to an electron localized on the right (left) dot, or bonding (anti-bonding) superposition of these two orbitals when they hybridize, at low detuning.

The energy levels are the eigenvalues of:

$$H = \begin{pmatrix} \epsilon_L & t \\ t & \epsilon_R \end{pmatrix}, \text{ ie } E_\pm = \frac{\epsilon_\Sigma}{2} \pm \frac{1}{2}\sqrt{\epsilon_\delta^2 + 4t^2} \tag{5.4}$$

with the following notations: $\epsilon_\Sigma = \epsilon_L + \epsilon_R$ and $\epsilon_\delta = \epsilon_L - \epsilon_R$. Figure 5.1 (c) represents these eigenenergies (labeled B and AB, for bonding and anti-bonding), made out of the two isolated dot's resonant levels (represented in green) detuned by ϵ_d.

In order for the resonant condition $\omega_{cav} = \omega_{DQD}$ to occur at a certain value of detuning, one needs $2t \lesssim \omega_{cav}$[1]. An example of the typical microwave measurement of such a charge qubit is shown in figure 5.2. We can already notice that the energy scale is very different from the one for the transport measurement.

For more complex DQD systems, the microwave signal can have a more complex shape: for example, there can be a dependence on ϵ_Σ, as was seen when the central tunnel gate of the DQD was replaced by a superconducting contact [235]. The spin-degeneracy can be

[1] Note that in case of a large coupling, there will still be a measureable dispersive signal even at $2t > \omega_{cav}$.

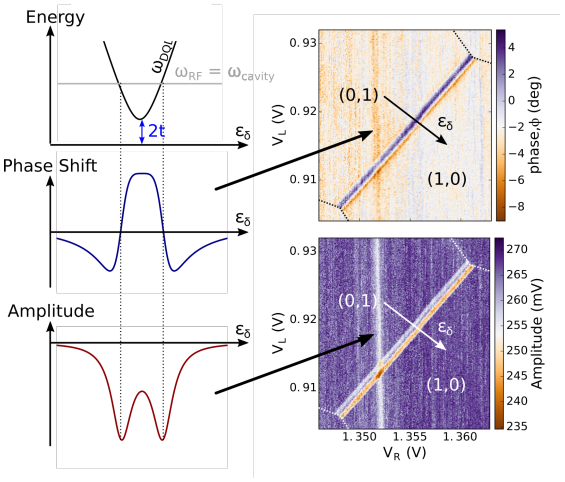

FIGURE 5.2: **Microwave measurement of a CNT based charge qubit**. Left column represents the pulsation of a charge qubit internal transition ω_{DQD} and the cavity pulsation ω_{cavity} as a function of the detuning ϵ_δ. The resulting phase shift and amplitude signals are plotted below. The right column presents the microwave response of the cavity which reveals the internal transitions of the charge qubit. The DQD stability diagram is highlighted with dashed lines. Source: [2].

lifted, for example through exchange-interaction, by using non-collinear ferromagnetic contacts [3, 185] or micromagnets [259], or finally by relying on the interplay of a magnetic field with spin-orbit coupling [260, 261]. In this case, the two levels that couple to the cavity can have different spin eigenvalues; the transition energy can then vary with an external magnetic field B_{ext} and with the detuning as we will show in the next section. Finally, for total occupancy $N_{tot} > 1$, the ground state becomes a singlet state over the two DQD, whereas the excited states are triplet states. The microwave signal can be affected by spin blockade effect in this parity region [262].

5.1.2 Magnetic field dependence of known DQD

In the following we will show a magnetic field dependence for the spin-textured DQD that reveals the effect of the magnetic texture. First, we show what can be expected for the microwave signal when the magnetic field varies in several DQD geometries. In figure 5.3 (a), we show the magnetic field dependence of a charge qubit. As already mentioned, in such a DQD system the two spin sectors are independent. The microwave cavity is only sensitive to transitions between states of equal spin, thus the transition energy does not change with a magnetic field B_{ext}. On the other hand, in presence of an inhomogeneous magnetic field, the circuit internal transitions can vary with the external magnetic field. This was seen for example in figure 5.3 (b) through an inhomogeneous Zeeman effect[2] or in figure 5.3 (c) through the effect of the field on the magnetization

[2]The detuning changes the localization of the two probed states, from a left/right hybridization at zero detuning to a more localized state at strong detuning.

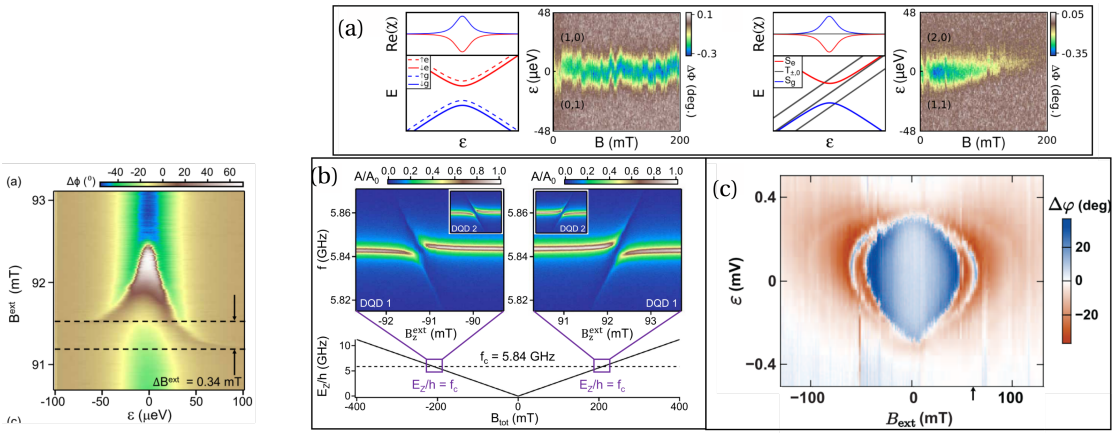

FIGURE 5.3: **Phase shift as a function of detuning and external magnetic field for known DQD** (a) Phase shift of the microwave signal as a function of an external magnetic field and detuning. The two charge qubit transitions studied correspond to an odd (left) or even (right) total occupancy in the two dots. The corresponding energy levels are represented on the left. For even occupancy, they correspond to singlet or triplet states. Source: [262]. (b) Study of a spin qubit where the charge and spin degree of freedom are mixed by the combination of a inhomogeneous magnetic field (a Co micromagnet stray field), non collinear with the external one. The colormap represents the amplitude of the coupled microwave cavity as a function of external magnetic field and probe frequency. An distorsion of the cavity signal is visible when a spin transition is at resonance, indicating a strong coupling between the cavity and the spin qubit. The bottom panel shows the spin transition frequency as a function of the external magnetic field. Source: [263]. (c) Effect of an external magnetic field on a spin qubit made with two non collinear ferromagnetic leads. The colormap represents the evolution of the phase shift as a function of an external magnetic field and detuning. Here the magnetic field modifies the magnet axis. This effect can be modeled to numerically reproduce the data. Source: [3].

axis of two non-collinear magnets. In this last example, additional transitions are visible due to the valley degree of freedom of the CNT. In both situations, the dependence of the transition energies on both the detuning and an external magnetic field indicates a spin transition.

5.2 Sensing a spin texture induced by the magnetic texture

A challenge in DQD physics is to address the spin degree of freedom of the electron with microwave photons, for example as a tool to read or couple distant spin qubits[3]. The magnetic coupling strength of a single spin to a CPW is typically $g_{spin} = 10$ Hz for our devices [264]. A road to enhance this small native coupling is to hybridize the position and spin degree of freedom of the electron, either by relying on an intrinsic spin-orbit interaction or on inhomogeneous magnetic fields. Our magnetic texture also provides all the necessary ingredients for coupling spin transitions to the microwave cavity. As

[3]The electron spin degree of freedom being less coupled to the environment than its charge, thus having better coherence properties

mentioned above, the cavity measurement can also probe small changes compared to transport measurement, and is a powerful tool to measure the perturbative effect of the magnetic texture over our DQD spectrum. We now present preliminary results on a DQD with a magnetic texture below each dot, probed through both current and microwave measurements.

5.2.1 Experimental results

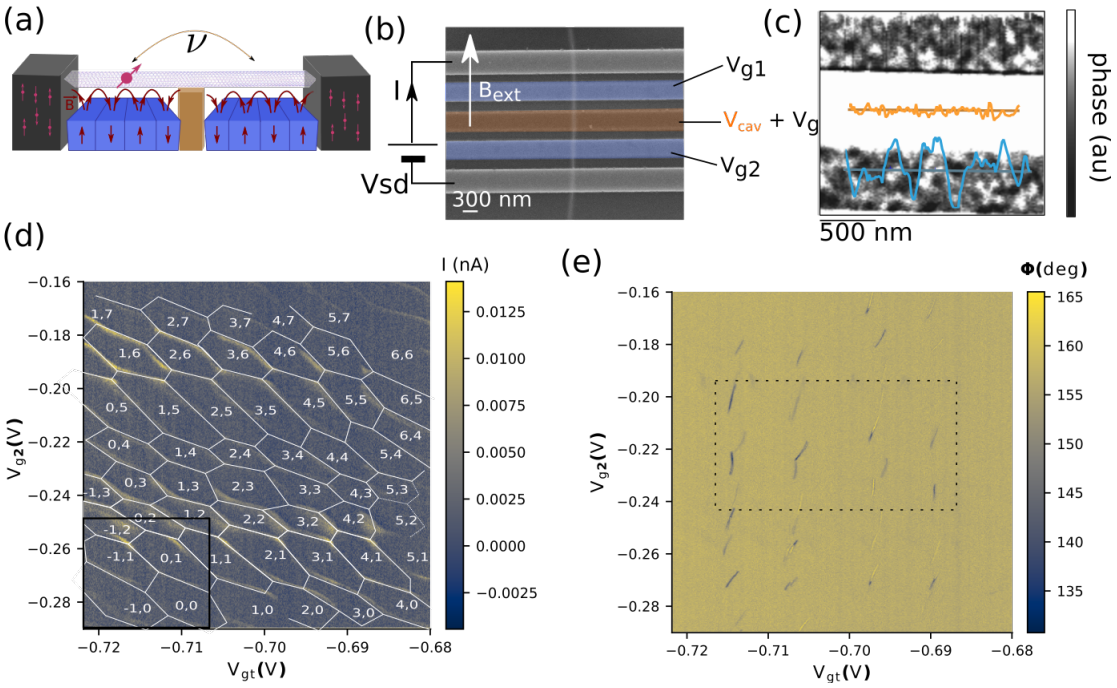

FIGURE 5.4: **Schematics of the device and stability diagram** (a) Schematics of the DQD with a magnetic texture below each dot. Cavity photons ν are coupled to the position of the electron. (b) SEM picture of the device. The DQD is made out of a CNT (highlighted in white) coupled to two normal Pd leads (grey) over which a voltage difference V_{sd} is applied, one Co/Pt gate under each dot (blue) and a central Al/Alox electrode (orange). The cavity is galvanically coupled to the central gate. An external magnetic field can be applied along the CNT axis. The device is characterized through both current (I) and microwave signal. (c) MFM phase signal on the same Co/Pt multilayer as the one above. Two cuts are extracted, above the magnetic texture (blue) and above the Si substrate (orange). (d) Stability diagram of the DQD device: current I as a function of two gates, V_{gt} and V_{g2} at bias $eV_{sd} = 200$ µeV. The electron filling number on each dot (up to a constant) is labeled in white. The black rectangle indicates the gate range for figure 5.5. (e) Corresponding microwave phase signal Φ. The dashed black line delimits the set of transitions studied in figure 5.6.

The device under study is a DQD made out of a CNT, stapled over a mesoscopic circuit using the stapling technique described in chapter 3. The CNT is positioned over two magnetically textured gates, and a central Al/Alox gate that is also galvanically connected to a microwave cavity of resonant frequency $f_{cav} = 6.42$ GHz. It is connected to two Pd electrodes, through which a current can be measured. Schematics and SEM

picture of the device are shown in figure 5.4 (a,b). From figure 5.4(c), the MFM measurement of the same Co/Pt multilayered structure displays oscillations of the MFM phase signal, with a period of about 400 nm. Current through the device is typical of a DQD with a large interdot coupling t, as visible in panel (d). The electron filling numbers in the left and right dots are labeled in each blockade region, up to a constant offset for each dot.

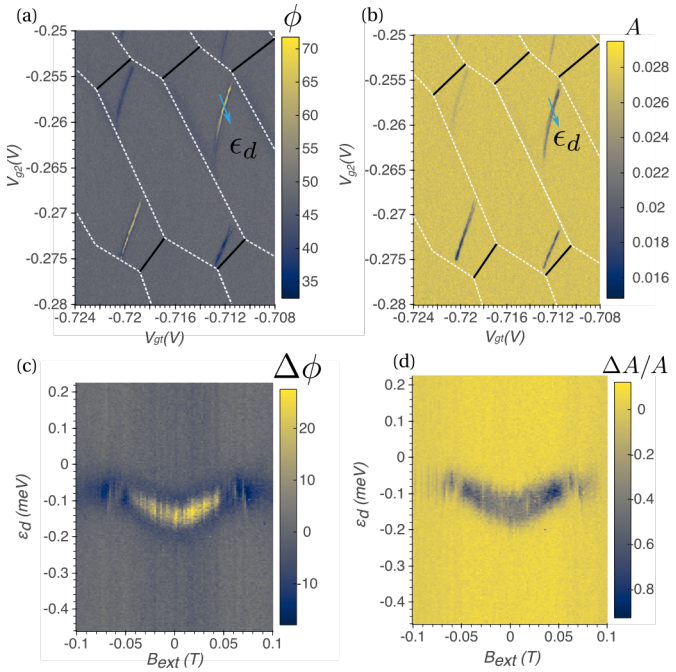

FIGURE 5.5: **Evolution of the cavity signal in magnetic field** (a) Phase and (b) amplitude of the cavity transmission in a small region of the stability diagram shown in figure 5.4 (d). The blue arrow indicates the orbital detuning axis for the following panels, the white dashed lines the limits of the stability diagram and the black line the zero-detuning line for the DQD charge transitions. As opposed to the other dots presented before, in section 5.1, the cavity signal is not centered between the DQD triple points. (c) Phase variation $\Delta\phi$ and (d) microwave amplitude relative variation $\Delta A/A$ for this signal (upper right transition), as a function of detuning ϵ_d and external magnetic field B_{ext}. The transition energy evolves non-monotonically with these parameters, as well as the DQD tunnel coupling (as indicated by the change in contrast).

In the cavity signal, we observe strong distortions of the transmission, as visible in figure 5.4 (e) and 5.5 (a,b). Although the cavity is contacted to the central gate, it is mostly coupled to one dot, thus our measurement is sensitive to internal transitions in the DQD (indeed, in the stability diagram we see that the effect of this central gate is primarily to tune one dot). Strikingly, this signal is shifted from the zero-detuning line, which is highlighted by the black lines in figure 5.5 (a,b). The zero detuning line at constant filling factor $N \equiv N_L + N_R$ is defined by $\epsilon_d = \epsilon_L - \epsilon_R = 0$ where $\epsilon_{L(R)}$ is the chemical potential of the left (right) QD. Over a larger gate range, as shown in figure 5.4 (e), we

also notice that the the position of the resonances seems to be determined by a more complex condition than $\epsilon_d = 0$ (or a constant offset), and is primarily controlled by V_{gt}.

Figure 5.5 (c,d) shows the evolution of the phase and amplitude signals as a function of an external magnetic field and detuning for the upper right transition of 5.5 (a). We see a non-trivial dispersion of these signal: the transition energy shifts with B_{ext}, with a slope that changes sign. Similarly the $B_{ext} - \epsilon_d$ evolution of the cavity signal for all the transitions enclosed in the black rectangle in figure 5.4 (e) are shown in figure 5.6. The mapping between the stability diagram and the indexes n_1, n_2 can be found in figure 5.13; these indexes do not represent the filling of the left and right dots, but are associated with a change in the field-dependence of the associated transitions. We observe four behaviors for the field dependence: either a monotonic decrease of the transition energy ($n_2 = 1$), a monotonic increase ($n_2 = 4$) or a change in the direction of change (from increasing to decreasing, $n_2 = 2$ or the opposite, $n_2 = 3$). This behavior is similar for all values of n_1, although there are quantitative changes in the slopes and contrast of the phase signal. At these values of magnetic field, we do not expect the magnetization of the texture to be much affected. This is substantiated by MFM measurements of a magnetic texture made during the same deposition, on the same substrate, presented in section 5.2.3.

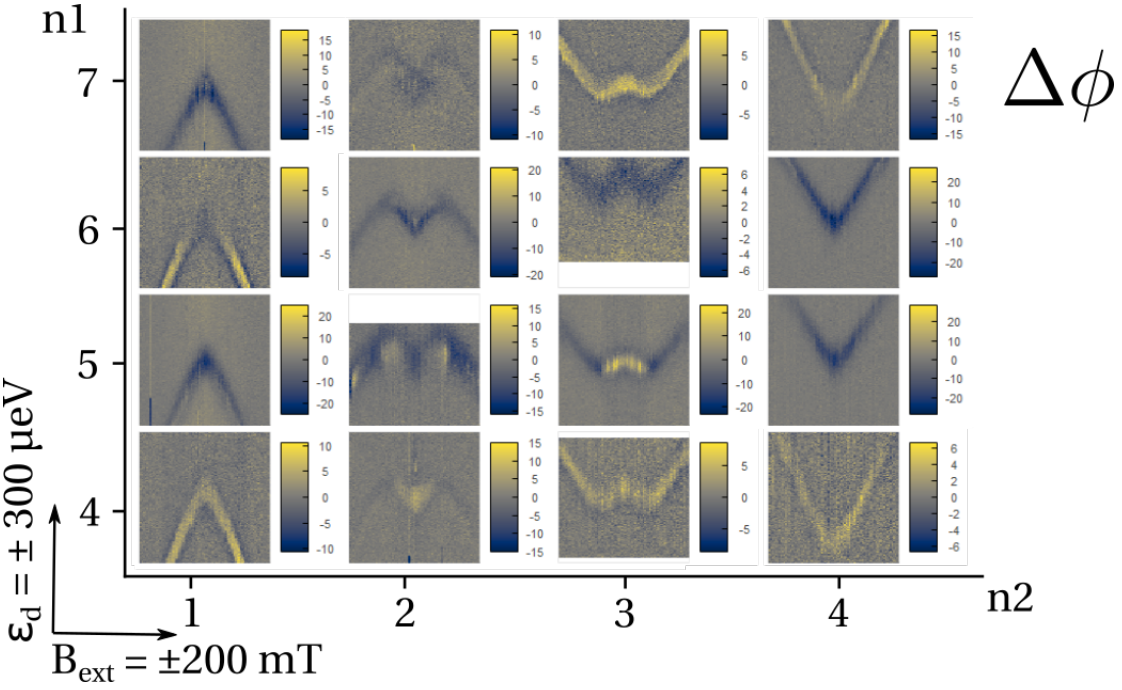

FIGURE 5.6: **Phase signal dispersion in the $B_{ext} - \epsilon_d$ space, for several transitions** Phase signal as a function of $B_{ext} - \epsilon_d$ for a few transitions shown in the stability diagram of figure 5.4 (e) (the correspondence between the stability diagram and the indices (n_1, n_2) is shown in figure 5.13). The axes for these plots are $B_{ext} = \pm 200$ mT (horizontal) and $\epsilon_d = \pm 300$ µeV.

A simple figure of merit to evidence a non-trivial effect of the magnetic texture is to extract from these dispersions the slope of the transition energy with B_{ext}[4]. The energy conversion for the gate voltages is presented in appendix D. The ensemble of values is represented in figure 5.7, sorted as a function of n_2 (ie the different dispersion behaviors; for non-monotonic dispersions both the slopes of the inner and outer branches are represented). We measure several dispersions whose slopes correspond to Landé g factors of up to 60, much larger than expected for a CNT (even taking into account the orbital effect of the field). Although these slopes are not a direct measure of the Landé factor in the dots, we will show in section 5.2.2 that in a simple model, they are related to the difference in Landé factor between the right and left dots. Thus our measurements seem to indicate very large and orbital-dependent g factors in the DQD. We propose that this effect is linked to the presence of the magnetic texture: in heavy materials, the spin-orbit interaction can lead to a strong renormalization of the g factor. In our situation, the synthetic spin-orbit interaction could similarly renormalizes the effect of an external magnetic field on each of the dots' energy levels.

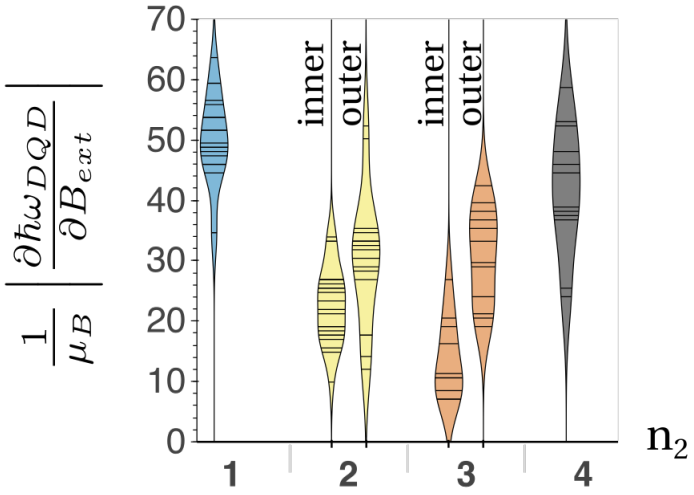

FIGURE 5.7: **Extracted slopes for the magnetic field dispersion** Extracted slopes for the change in the microwave phase shown in figure 5.6, represented as a violin plot. Each line represents a data point asssociated with a given (n_1, n_2). These data points are enclosed in a colored envelope representative of a probability density (estimated from the dataset). For columns $n_2 = 2, 3$, two slopes are measured per transition (*i.e.* per value of n_1), labeled "inner" (for the slope between $B = 0T$ and the value of B at which the direction of change reverses) and "outer" (at large magnetic fields).

5.2.2 Theoretical description

We have measured a rich range of behavior for the internal transitions in our magnetically textured DQD. Notably, the resonant condition $\omega_{DQD} = \omega_{cav}$ can be very far from the

[4]For a pure spin transition, this slope is of $2g$, where g is the Landé factor. In addition a magnetic field parallel to the CNT can also contribute to the dispersion through an orbital effect.

zero-detuning line, and changes in a non-monotonic way with the external magnetic field.

We first consider a simple model, to try and shed light on the minimal effects that can capture this behavior. We then try and describe the effect of the magnetic texture.

5.2.2.1 A DQD with inhomogeneous g and inhomogeneous stray field

We start by considering the following model, which is schematically represented in figure 5.8. We study a DQD where the left (respectively right) dot is subject to a homogeneous field B_L, (resp. B_R) (which we will call "local field"), and has a Landé g-factor g_L, (g_R). An external magnetic field B_{ext} can be applied. For simplicity, we consider B_{ext} to be orthogonal to $B_{L,R}$, so that the resulting spectrum is symmetric in $B_{ext} \to -B_{ext}$ (as our measurements are even in B_{ext}). To We also take B_L and B_R to be parallel, and we will discuss the effect of an angle between these local fields later on. Given the large measured level spacing between two electronic levels (about 2 meV, as visible in figure 5.14), we can consider only one orbital in each dot.

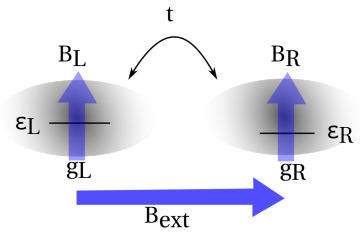

FIGURE 5.8: **Schematics of the DQD model considered** Each dot (grey region) contains one orbital, of chemical potential $\epsilon_{L,R}$, had a Landé g-factor $g_{L,R}$ and is subject to a local field $B_{L,R}$ for the left and right dot respectively. Both dots are subject to an external magnetic field B_{ext}, orthogonal to $B_L \parallel B_R$.

The energy levels for each dot $i = L,\ R$ are:

$$E_{i,s=\pm1}(\epsilon_i, B_i, g_i, B_{ext}) = \epsilon_i + \frac{s g_i \mu_B}{2}\sqrt{B_i^2 + B_{ext}^2}. \tag{5.5}$$

We then add the tunnel coupling between the two dots. Since B_L and B_R are parallel, the coupling term stays diagonal in the basis of these new energy levels:

$$H = \begin{pmatrix} E_{1,s=1} & 0 & t & 0 \\ 0 & E_{1,s=-1} & 0 & t \\ t & 0 & E_{2,s=1} & 0 \\ 0 & t & 0 & E_{2,s=-1} \end{pmatrix} \tag{5.6}$$

Under this condition, only the charge transitions will be coupled to the microwave cavity.

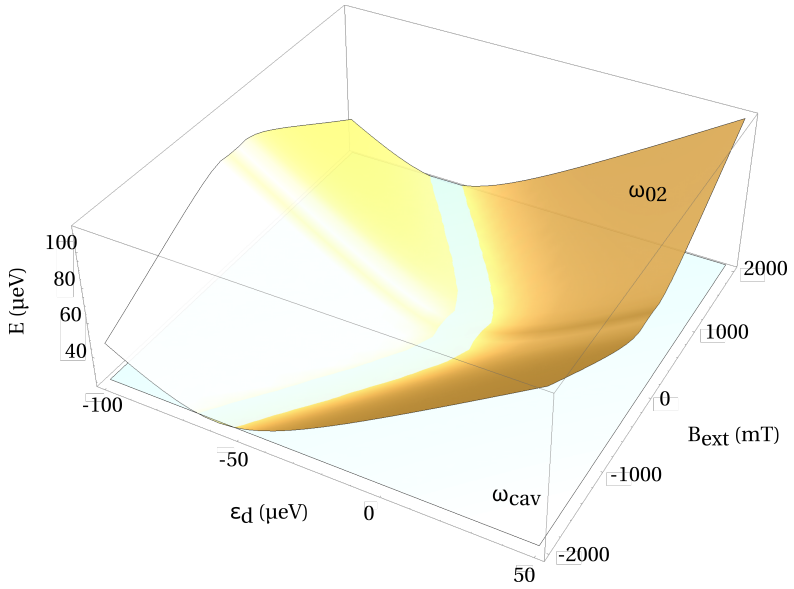

FIGURE 5.9: **Illustration of the resonant condition** $\omega_{DQD} = \omega_{cav}$ for the considered DQD.

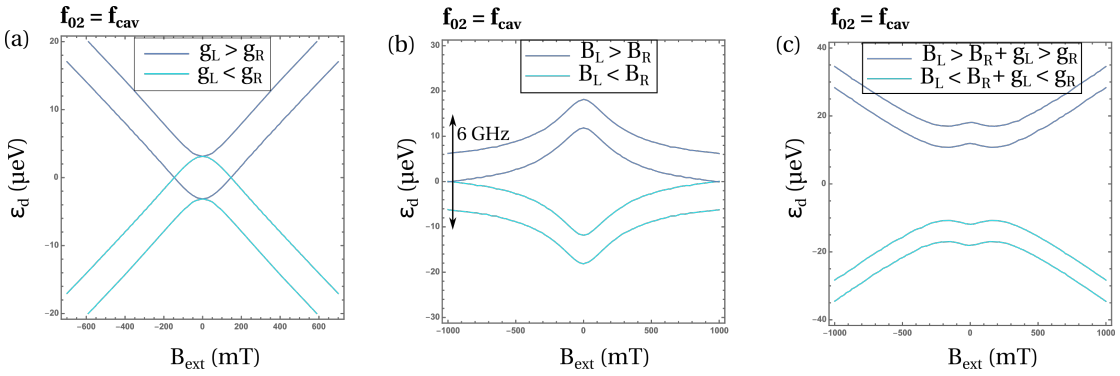

FIGURE 5.10: **Resonant condition for a DQD subject to an inhomogenous Zeeman effect**, either through inhomogeneous stray fields or inhomogeneous g-factors. (a) Resonant condition as a function of detuning ϵ_d and magnetic field B_{ext} for different Landé factors in both dots, $g_L = 3$, $g_R = 2$ (dark blue) or the opposite (light blue), with $E_z^{L,R} = 10$ μeV. (b) Resonant condition as a function of detuning ϵ_d and magnetic field B_{ext} for different stray fields in both dots, $B_L = 340$ mT ($E_z^L = 20$ μeV), $B_R = 85$ mT ($E_z^R = 5$ μeV) (dark blue) or the opposite (light blue), with $g = 2$. (c) Resonant condition as a function of detuning ϵ_d and magnetic field B_{ext} for the combination of both these effects: $g_L = 2, E_z^L = 5$ μeV, $g_R = 3, E_z^R = 20$ μeV (light blue) or the reverse (dark blue). The rest of the parameters are $f_{cav} = 25$ μeV (about 6 GHz) and $t = 12.4$ μeV. The combination of both an inhomogeneous stray field and an inhomogeneous g-factor reproduces qualitatively the measured dispersions.

We look at the transition energy $\hbar\omega_{02}$ between the bonding / anti-bonding levels with spin $s = -1$. This transition is expected to be the one most visible in the cavity signal because it starts from the DQD ground state which is in principle highly populated, and it does not flip the spin[5]. It will have a square-root function-like shape that will allow

[5]Under our working hypothesis, the two spin sectors are independent. However, a misalignment between B_L and B_R would enable the coupling of transitions between two states with different spin orientation.

for two solutions for the condition $\omega_{02} = \omega_{cav}$ (as is the case in the measurements).

The Hamiltonian (5.6) yields:

$$\begin{aligned} &\omega_{02}(\epsilon_d, B_{ext}) = \sqrt{(E_z^L - E_z^R + \epsilon_d)^2 + 4t^2} \\ &\text{with } \epsilon_d = \epsilon_L - \epsilon_R \\ &\quad E_z^i \equiv \frac{g_i \mu_B}{2} \sqrt{B_{ext}^2 + B_i^2} \end{aligned} \tag{5.7}$$

Figure 5.9 illustrates the idea that the microwave cavity provides a cut of the DQD transition energies at ω_{cav}. It represents both the transition energy ω_{02} and the plane ω_{cav}; the microwave signal will be most strongly affected at the resonant condition, given by the intersection of the two surfaces. Figure 5.10 represents the resonant condition under three scenarii. These scenario are motivated by the following observations.

First, we can already notice that an imbalance between the right and left Zeeman energies E_z^i lifts the symmetry $\epsilon_d \to -\epsilon_d$, and can move the cavity shift away from the zero-detuning line. It can either come from an asymmetry in the fields B_i or in the g-factors. In addition, this transition energy will change with an external magnetic field if such an asymmetry is present. The sign of the imbalance determines the direction of change of the condition $f_{DQD}(B_{ext}, \epsilon_d) = f_{cav}$ in the $(B_{ext} - \epsilon_d)$ plane. The effect of an imbalance in B_i becomes negligible when $B_{ext} \gg B_L, B_R$ whereas the effect of an imbalance in g stays visible at large B_{ext}. Indeed, these two behaviors are visible in figure 5.10 (a) and (b). Panel (a) represents the evolution of the resonant condition for different values of g in the left and right dot, either $g_L > g_R$ (dark blue) or $g_L < g_R$ (light blue). Panel (b) represents the evolution of the resonant condition for different values of B in the left and right dot, either $B_L > B_R$ (dark blue) or $B_L < B_R$ (light blue). The change in the DQD transition energy does not saturate at large B_{ext} in (a) whereas it does in (b). In addition, the sign of the imbalance determines the sign of the slope $\frac{1}{\mu_B}\frac{\partial \omega_{02}}{\partial B_{ext}}$ in both cases. This simple model can even reproduce non-monotonous evolutions of the resonant condition, as was observed experimentally, when these two effects combine as represented in figure 5.10 (c).

To be more quantitative, we can study in more details the resonant condition $\omega_{02} = \omega_{cav}$. If $\omega_{cav} \geq 2t$, there are two detuning values $\epsilon_{0,\pm}$ that satisfy this condition:

$$\omega_{02}(\epsilon_0, B_{ext}) = \omega_{cav} \Leftrightarrow \epsilon_{0,\pm} = E_z^R - E_z^L \pm \sqrt{\omega_{cav}^2 - 4t^2} \tag{5.8}$$

These two values are centered around $\epsilon_{0,c}(B_{ext}) \equiv E_z^R - E_z^L$. We can thus look at the change of this value with B_{ext}:

$$\frac{\partial \epsilon_{0,c}}{\partial B_{ext}} = \frac{\mu_B B_{ext}}{2}\left(\frac{g_R}{\sqrt{B_{ext}^2 + B_R^2}} - \frac{g_L}{\sqrt{B_{ext}^2 + B_L^2}}\right) \tag{5.9}$$

From these equations, we can now understand better the dispersions presented in figure 5.10:

- There is a change in the direction of change of $\epsilon_{0,c}$ when $\frac{\partial \epsilon_{0,c}}{\partial B_{ext}} = 0$, *i.e.* at $B_{ext} = 0$ and, if it exists, at
$$B_{ext} = \sqrt{\frac{(g_R B_R)^2 - (g_L B_L)^2}{g_L^2 - g_R^2}}, \tag{5.10}$$
- The large magnetic field slope is:
$$\lim_{B_{ext} \gg B_L, B_R}\left(\frac{\partial \epsilon_{0,c}}{\partial B_{ext}}\right) = \frac{\mu_B}{2}(g_R - g_L), \tag{5.11}$$
- The low magnetic field slope is:
$$\lim_{B_{ext} \ll B_L, B_R}\left(\frac{\partial \epsilon_{0,c}}{\partial B_{ext}}\right) = \frac{\mu_B B_{ext}}{2}\left(\frac{g_R}{B_R} - \frac{g_L}{B_L}\right), \tag{5.12}$$
- The offset from zero detuning at $B_{ext} = 0$ is
$$\epsilon_{0,c}(0) = \frac{\mu_B}{2}\left(g_L B_L - g_R B_R\right) \tag{5.13}$$

Note that a misalignment between the local fields B_L, B_R would not change these results, but instead it would enable a coupling between the cavity and spin-full transitions (this is the working principle of the DQD based spin qubits). In addition, adding a component along the B_{ext} axis to the local fields would remove the symmetry $B_{ext} \to -B_{ext}$.

We can now compare this model with our experimental setup. In the experiment, the imbalance in local magnetic fields $B_{L,R}$ could come from a difference in the two magnets (inhomogeneities in the deposition, or a difference in the magnet axis resulting in a different decay with elevation)[6]. On the other hand, the imbalance in Landé factor could come from a change in the CNT nature (which is unlikely given its clean spectrum), or again a difference in the orientation of the effective fields $B_{L,R}$ resulting in different orbital effects on the left/right dots. However, as noted above, we would need local fields perpendicular to the tube axis to reproduce our B_{ext}-symmetric data, so orbital effects

[6]However we do not expect a large imbalance since the two magnetic textures are fabricated simultaneously.

would be small. With only these ingredients, in order to reproduce our experimental data, we need much larger g factors than $g \sim 2$ in each dot. Indeed, we have measured slopes of up to 60 (see figure 5.7), which has to be compared to $\frac{1}{2}(g_R - g_L)$ according to equation (5.11) !

In the end, this simple model enables us to discriminate between the effect of two non-collinear fields and our experimental results. Our results cannot simply be explained by the presence of a local magnetic field below each dot[7]. In addition, we can point out that lifting the constraint of a low-electronic g-factor, this model can accurately reproduce our measurements with g factors of the order of 100. The magnetic texture, with its oscillating magnetic field, could be responsible for such a large renormalization of the bare electronic g-factor.

5.2.2.2 Modeling of the effect of the magnetic texture

We now try and describe how the magnetic texture could induce a large renormalization of the g-factor. We first consider its effect on one dot, modeled as a confined electron in a segment of size L in 1D (oriented along z), with a parabolic dispersion relation.

The magnetic texture stray field and the external magnetic field can be written as follows, with $k_\lambda \equiv \frac{2\pi}{\lambda}$ where λ is the spatial period of the texture:

$$\vec{B}_{osc} = B_{osc} \begin{pmatrix} \sin(k_\lambda z) \\ 0 \\ \cos(k_\lambda z) \end{pmatrix}, \vec{B}_{ext} = \begin{pmatrix} 0 \\ 0 \\ B_{ext} \end{pmatrix} \tag{5.14}$$

In the absence of a magnetic texture, the dot orbitals are given by

$$\psi_{n,s} = \sqrt{\frac{2}{L}} \sin(k_{n,s} z), \text{ with } k_n \equiv \frac{n\pi}{L} \tag{5.15}$$

of eigenenergies $E^{(0)}_{n,s} \equiv E_n + s\frac{1}{2} g\mu_B B_{ext}$ ($E_n \equiv \hbar v_F k_n$).

We describe the effect of $\vec{B}_{osc}$ by considering it as a small perturbation. The eigenenergies, up to second order can be written:

$$E^{(2)}_{n,s} = E^{(0)}_{n,s} + \langle \psi_{n,s} | \frac{1}{2} g\mu_B \vec{B}_{osc} \cdot \vec{\hat{s}} | \psi_{n,s} \rangle + \sum_{n' \neq n, s'} \frac{\left| \langle \psi_{n,s} | \frac{1}{2} g\mu_B \vec{B}_{osc} \cdot \vec{\hat{s}} | \psi_{n',s'} \rangle \right|^2}{E_n - E_{n'} + \frac{1}{2} g\mu_B B_{ext}(s - s')} \tag{5.16}$$

[7] This stays valid taking into account the valley degree of freedom of the CNT, using the effective Hamiltonian of Ref [201].

We can calculate the coupling induced by the oscillating magnetic field:

$$\langle\psi_{n,s}|\frac{1}{2}g\mu_B\vec{B}_{osc}\cdot\vec{\hat{s}}|\psi_{n',s'}\rangle = \frac{1}{2}g\mu_B\left(B_{eff,z}(n,s,n',s')\langle s|\hat{s}_z|s'\rangle + \right. \tag{5.17}$$

$$\left. B_{eff,x}(n,s,n',s')\langle s|\hat{s}_x|s'\rangle\right) \tag{5.18}$$

with:

$$B_{eff,z}(n,s,n',s') \equiv \frac{B_{osc}}{2}\left(\frac{\sin\left[(k_\lambda - k_n + k_{n'})L\right]}{(k_\lambda - k_n + k_{n'})L} + \frac{\sin\left[(k_\lambda + k_n - k_{n'})L\right]}{(k_\lambda + k_n - k_{n'})L}\right) \tag{5.19}$$

$$B_{eff,x}(n,s,n',s') \equiv \frac{B_{osc}}{2}\frac{1-\cos\left[(k_\lambda - k_n + k_{n'})L\right]}{(k_\lambda - k_n + k_{n'})L} + \frac{B_{osc}}{2}\frac{1-\cos\left[(k_\lambda + k_n - k_{n'})L\right]}{(k_\lambda + k_n - k_{n'})L} \tag{5.20}$$

Note that we have neglected the terms $\pm k_\lambda + k_n + k_{n'}$, that are small assuming we are not at the bottom of the band.

For a given n, we suppose there is one n' such that either $(k_\lambda + k_n - k_{n'})L \in [\pi/2, \pi]$ or $(k_\lambda - k_n + k_{n'})L \in [\pi/2, \pi]$, and we define $\alpha_n \equiv (k_\lambda + k_n - k_{n'})L$ or $(k_\lambda - k_n + k_{n'})L$ accordingly.

In that case, the renormalisation of the energy writes:

$$E^{(2)}_{n,s} = E^{(0)}_{n,s} + \langle\psi_{n,s}|\frac{1}{2}g\mu_B\vec{B}_{osc}\cdot\vec{\hat{s}}|\psi_{n,s}\rangle + \left(\frac{1}{2}g\mu_B B_{osc}\right)^2\left[\left(\frac{\sin\alpha_n}{\alpha_n}\right)^2\frac{1}{E_n - E_k} + \left(\frac{1-\cos\alpha}{\alpha}\right)^2\frac{1}{E_n - E_k + sg\mu_B B_{ext}}\right] \tag{5.21}$$

This calculation illustrates how an oscillating magnetic field can renormalize the external magnetic field dependence of confined electrons, and thus the Landé g-factor of our quantum dots. However, more work is still needed to provide a complete theoretical description of our experimental observations.

5.2.3 Supplementary information

We now present additional measurements of the DQD presented in section 5.2.1, as well as the estimate of the coupling strength to the microwave cavity.

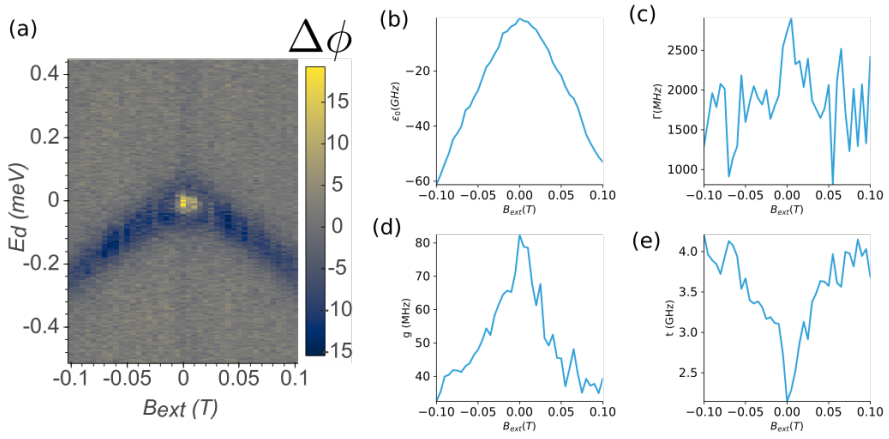

FIGURE 5.11: **Fit of the cavity signal on one transition** (a) Phase variation as a function of B and ϵ_d for the considered transition. (b-e) Fit values as a function of B for the following parameters: ϵ_0 (panel (b)), γ (panel (c)) g (panel (d)) and t (panel (e)). The transition considered is centered around $V_{gt} = -0.719$ V, $V_{g2} = -0.153$ V.

5.2.3.1 Estimate of the coupling strength

We can extract from the cavity signal an estimate of the coupling strength of the cavity to the DQD. For simplicity, we extract effective parameters, assuming the same detuning-dependence for our DQD transitions as for the charge qubit (see equation (5.4)). We show in figure 5.11 the fit of the cavity transmission (given by equation (5.1)):

$$f_{DQD}(\epsilon_d) = \sqrt{(\epsilon_d - \epsilon_0)^2 + 4t^2} \tag{5.22}$$

The remaining fit parameters are:

$$\kappa = 5.5 \text{ MHz},\ f_{cav}(B) = 6.42 - 6.427 \text{ GHz},\ f_d = f_{cav}$$

With this sample, we obtain a coupling strength of up to $g = 2\pi \times 80$ MHz. The decoherence for this transition is of the order of $\Gamma \sim 2$ GHz, and may be quite high due to the relatively large coupling to the DQD leads (see figure 5.4(d)), in addition to charge noise. For these measurements, the cavity was driven with a low-power tone, with an estimated photon number of about $n \sim 2$.

The extracted coupling strength can be favorably compared to recent experimental results on strong charge-photon coupling: $\frac{g}{2\pi} = 7$ MHz [202], $\frac{g}{2\pi} = 5$ MHz [235], or $\frac{g}{2\pi} = 119$ MHz with a high-impedance resonator [265]. In addition, it corresponds to a cooperativity $C \equiv \frac{g^2}{\kappa\Gamma}$ well above 1, enabling a coherent exchange between the two systems. However, here the relaxation rate is too strong to reach the strong coupling regimes. Overall, most experiments on coupling a charge qubit to a typical microwave

cavity obtained coupling constants in the range of $\frac{g}{2\pi} = 10 - 50$ MHz [3, 185, 266]. One factor that could contribute to the large measured coupling strength is the size of the mesoscopic circuit (of about 1.5 µm, yielding a large capacitive lever arm to the gate), which is made possible by the use of a very clean CNT.

Note that here the fit seems to indicate that there is a magnetic field dependence of the interdot coupling t. This is possibly an artefact of the simple picture we have adopted for the dispersion relation of the DQD (taken as the one of the charge qubit). Alternatively, for a DQD subject to two non-collinear fields $B_{L,R}$ the cavity signal will change with B_{ext} : An angle of θ between the two fields will change the value of the hopping rate without spin flip: $t \to t\cos(\theta)$ at $B_{ext} = 0$. At strong magnetic field $B_{ext} \gg B_{L,R}$, we recover a rate t.

5.2.3.2 Additional measurements

In chapter 4, we have presented the effect of a change in the magnetic texture on a single quantum dot bound states, over a magnetic scale of 1.2 T. In this chapter, on the other hand, we have studied the evolution of a DQD internal transitions over a much smaller range of magnetic field, at most ±200 mT (at higher magnetic field, the cavity resonance is too degraded by the Zeeman effect of the field on the Nb superconducting sheet). Thus we expect that the magnetic texture is not very affected by the magnetic field over this field range. This approximation is substantiated by field MFM measurements, shown in figure 5.12. Those MFM measurements were performed on an identical DQD circuit fabricated with the same technique as the sample measured in the previous section. Its topographic image is shown in panel (a). The remaining images represent the MFM phase over one magnetic texture, under increasing magnetic fields, from $B_{ext} = 0$ to $B_{ext} = 400$ mT. Each image is approximately taken at the same position. A dipolar contribution to the phase signal is removed in these MFM images (as was done in section 3.3.3). However, the phase range is the same for all plots, and give an idea of which fraction of the zero-magnetic field signal is transferred to the dipolar signal. We notice that the realization for the magnetic domains is slightly different for each value of the magnetic field, but the signal is overall of the same strength, with a similar characteristic length over the range $0 - 100$ mT, and its strength is slightly reduced over the range $100 - 150$ mT. At higher magnetic fields, the signal is strongly reduced, as can be seen from the measurement at 400 mT.

In the following we present additional transport measurements of the DQD circuit. Figure 5.13 shows the mapping between the indices (n_1, n_2) and the stability diagram, as well as $B - \epsilon_d$ dispersions of the phase contrast for additional transitions. Figure 5.14

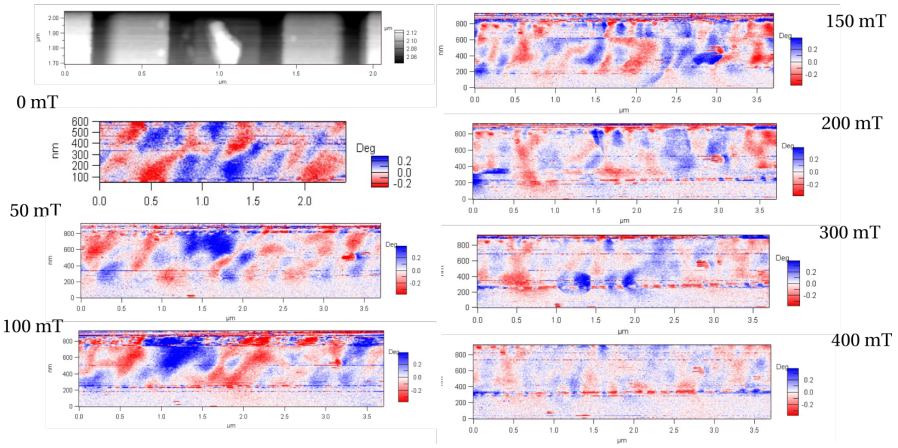

FIGURE 5.12: **Field MFM characterization of the Co/Pt texture**. (a) AFM image of the device. We measure the MFM phase signal on one of the side magnetic gates of the DQD circuit, subject to external in-plane magnetic field (in the same axis as in the transport experiment) of $0, 50, 100, 150, 200, 300$ and 400 mT. The phase contrast is the same on each plot. The decrease in signal comes from the transfer of part of the magnetization to the in-plane axis, and becomes particularly noticeable at $B > 200$ mT. Courtesy of W. Legrand.

reproduces Coulomb diamonds when gates V_{gt} and V_{g2} are swept over a few orbitals. Figure 5.15 shows current as a function of external magnetic field and two gate axes defined in order to primarily tune one or the other dot, labeled μ_1 and μ_2.

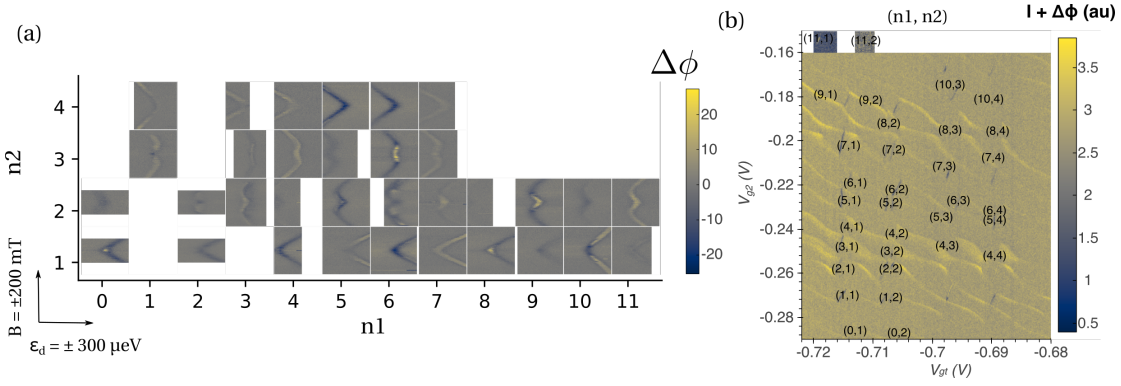

FIGURE 5.13: **Phase signal dispersion in $B - \epsilon_d$ for additional transitions** (a) Phase signal as a function of $B - \epsilon_d$ for the transitions shown in the stability diagram of figure 5.5. The axes for these plots are $B_{ext} = \pm 200$ mT (horizontal) and $\epsilon_d = \pm 300$ µeV. The colorbar spans the range $\Delta\phi = \pm 25°$. (b) Superposition of the current and phase signals of the stability diagram shown in figure 5.4 (d,e). To be precise, we plot $2\frac{I-I_{min}}{max(I-I_{min})} + 3\frac{\Phi-\Phi_{min}}{max(\Phi-\Phi_{min})}$. The labels (n_1, n_2) indicate the position of the transitions shown in panel (a).

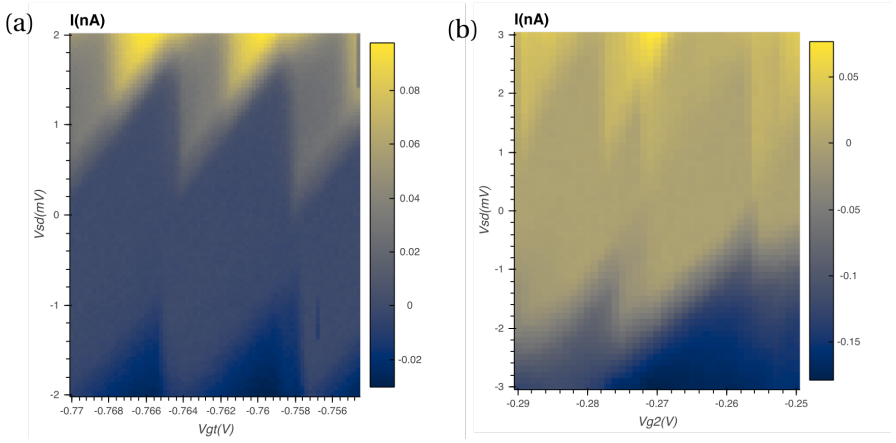

FIGURE 5.14: **Coulomb diamond for each dot**. (a) $V_{sd} - V_{gt}$ current map. We can extract the lever arm for gate V_{gt} and the level spacing for dot 1, primarily tuned by gate V_{gt}. (b) Same plot as (a) with gate voltage V_{g2}, tuning primarily dot 2.

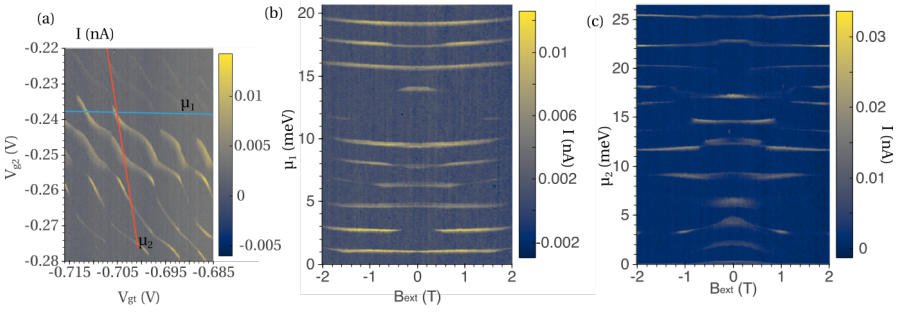

FIGURE 5.15: **Magnetic field evolution at large** B_{ext}. (a) $V_{gt} - V_{g2}$ current map. It enables to define new axes, μ_1 (blue) and μ_2 (red) corresponding to the chemical potential on each dot. (b) $B_{ext} - \mu_1$ map and (c) $B_{ext} - \mu_2$ map of the current over about 10 dot orbitals, over a magnetic field range of ± 2 T.

Conclusion and perspectives

Summary and conclusion

In this thesis, we have addressed the effect of a spin texture on confined electrons in CNT based nanocircuits through both current measurements in the circuit and the microwave transmission of a cavity, in two separate experiments. The experimental setup allows for both measurements simultaneously, but the cavity was not functioning in the first experiment. In these experiments, the CNT is placed above a Co/Pt multilayer presenting magnetization domains. The stray magnetic field rotates in space and is equivalent to both a synthetic spin-orbit interaction and a Zeeman splitting.

In the first experiment, we have shown that adding a very transparent superconducting contact to the CNT dresses the confined electronic states. We have measured the presence of two states below the superconducting gap. Their energies oscillate when an external magnetic field slowly aligns the magnetic domains in the texture, with a relatively small period. These oscillations stem from the change in the electronic bands when the synthetic spin-orbit decreases. This enabled us to extract an estimate for the spin-orbit energy induced in the CNT by the magnetic texture. Such a device regroups all the ingredients enabling the emergence of Majorana quasiparticles in the CNT. We have studied numerically how these Majorana quasiparticles can emerge in the specific geometry where superconductivity is added in one section on the nanoconductor, and a synthetic spin-orbit interaction in the remaining section. The presence of Majorana quasiparticles is suggested by a zero-bias conductance peak appearing in specific regions of the (μ, B_{ext}) phase diagram. However, more information is necessary to prove unambiguously the presence of MZM, because other effects can lead to the appearance of trivial ZBP. On the contrary, cavity photons can reveal their self-adjointness, and are a promising tools for manipulating them.

In the second experiment, we have rather studied two spin-textured quantum dots, positioned above a Co/Pt gate each. We have measured the cavity photons signal, which is strongly modified when the energy of the internal transitions between the two

dots matches the photons energy. The DQD transition energies change when a small external magnetic field is applied due to Zeeman effect, with large g-factors. Such high g-factors are most likely due to their renormalization by the synthetic spin-orbit interaction. This effect is strongly dependent on the dots' orbital filling as expected for a spin-orbit interaction. We have also observed a strong evolution of the effective interdot hopping t with the magnetic field, which can also be due to the effect of the synthetic spin-orbit interaction. Indeed, the use of a magnetic texture with a semiconducting CNT has been proposed as an alternative way to build a spin qubit.

Perspectives

Both experiments presented in this thesis have improved our understanding of the effect of a magnetic texture on confined electrons in a CNT circuit, both at low external magnetic field (where the magnetic domains are not affected) and at large magnetic fields, which align the domains.

The magnetic texture provides directly the two non-collinear magnetization axes needed to build a spin-qubit. This could be investigated in a SQD geometry, coupled to the cavity.

Our work on the texture characterization shows that the texture characteristics could be improved by changing its composition. Among the changes, in future experiments we could reduce the Co height, and use an asymmetric structure (Pt/Co/Au/Co for example) to make the domains more robust to an external in-plane field. We could also replace the Co by an Co/Fe alloy, and increase the number of repetitions to increase the amplitude of the oscillating magnetic field.

Increasing the amplitude of the magnetic field would be very beneficial in the search for Majorana quasiparticles. From the numerical simulations of our particular geometry, we now understand better the shape of the zero-modes' wavefunction. New circuit geometries, such as the DQD geometry of the second experiments, would potentially accomplish a greater separation of two MZMs.

Finally, the study of light-matter coupling in our specific geometry could be pushed further to show how cavity photons can reveal the self-adjoint property of MZMs.

Appendix A

Constant interaction model for a S/QD/N device

A.1 General equations

As mentioned in section 4.1.5, we use a constant interaction model in the strong Coulomb blockade regime ($\Gamma \ll E_c$) to interpret the conductance maps of the control devices B and C, presented in figures 4.7 and 4.9. We start by recalling how the constant interaction models yields the Coulomb diamond lines for a N/QD/N device before describing a S/QD/N device.

A.1.1 N/QD/N device

We here give the general equations that are used to understand the stability diagram of a N/QD/N device.

The model is based on two assumptions. First, the electronic interactions both inside the dot and between the dot and the circuit are constant, and can be parametrized by the relative capacitances between the circuit elements (dot, leads, gates). Then, the dot spectrum consist in a series of single-particle energy levels ϵ_i, that are not modified by interactions [267].

One can calculate the energy of the N and $N-1$ occupancy of the dot, and thus the electrochemical potential $\mu(N) = E(N) - E(N-1)$. The energy of a dot connected to two leads and coupled to a gate, occupied by N electrons is

$$E(N) = \sum_{i=1}^{N} \epsilon_i + \frac{e^2}{2C_\Sigma} \left(N - \frac{C_g V_g + C_L V_L + C_R V_R}{e} \right)^2 \tag{A.1}$$

where $C_\Sigma = C_L + C_R + C_g$ is the sum of the capacitances to the dot (left, right leads with voltages V_L, V_R and gate with voltage V_g). The second term in the right-hand side correspond to the electrostatic interaction.

The center of the Coulomb diamond associated with the occupation number N on the dot corresponds to the situation where both the leads energies ($eV_{L,R}$) are smaller than the energy cost of adding an electron to the dot (thus the charge is fixed to N):

$$\mu(N) < eV_{L,R} < \mu(N+1) \tag{A.2}$$

Combining with equation (A.1), and taking $V_L = V_{sd}, V_R = 0$, this yields the four lines of the Coulomb diamond, which can be rewritten:

$$eV_{sd} = -\frac{C_g}{C_L}(eV_g - eV_{g,N}) \text{ and } -\frac{C_g}{C_L}(eV_g - eV_{g,N+1}) \tag{A.3}$$

$$eV_{sd} = \frac{C_g}{C_\Sigma - C_L}(eV_g - eV_{g,N}) \text{ and } eV_{sd} = \frac{C_g}{C_\Sigma - C_L}(eV_g - eV_{g,N+1}) \tag{A.4}$$

where $V_{g,N}$ is a constant corresponding to the zero-bias degeneracy between the $N-1$ and N occupancies. This enables the drawing of the stability diagram represented in figure A.1.

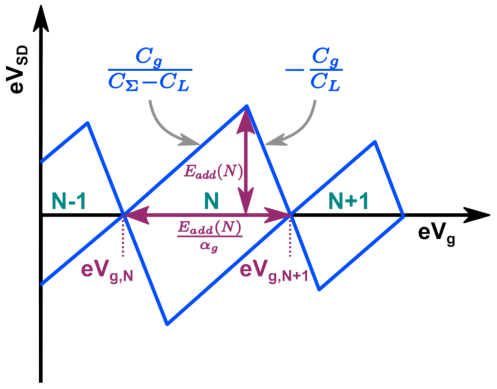

FIGURE A.1: **N/QD/N stability diagram** Source: [237].

With this picture, we see that the gate voltage tunes the electrochemical potential of the dot with a lever arm α_g:

$$\mu(N) = \epsilon_N + \frac{e^2}{C_\Sigma}(N - \frac{1}{2}) - e\alpha_g V_g \text{ with } \alpha_g = \frac{C_g}{C_\Sigma} \tag{A.5}$$

One can convert the gate axis to an energy axis by replacing $V_g \rightarrow \epsilon_d = e\alpha_g V_g$. The diamond equations then become:

$$eV_{sd} = -\frac{1}{\alpha}(\epsilon_d - \epsilon_N) \text{ and } eV_{sd} = -\frac{1}{\alpha}(\epsilon_d - \epsilon_{N+1}) \tag{A.6}$$

$$eV_{sd} = \frac{1}{1-\alpha}(\epsilon_d - \epsilon_N) \text{ and } eV_{sd} = \frac{1}{1-\alpha}(\epsilon_d - \epsilon_{N+1}) \tag{A.7}$$

with $\alpha = \frac{C_L}{C_\Sigma}$ the contact asymmetry, and ϵ_N is the zero-bias degeneracy point between the $N-1$ and N occupancies, on this new axis.

A.1.2 S/QD/N device

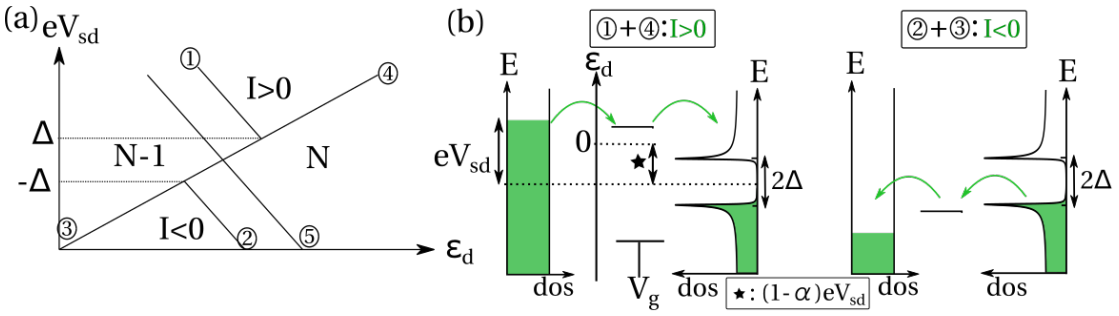

FIGURE A.2: **S/QD/N stability diagram** (a) Schematic representation of the stability diagram between the $N-1$ and N occupancy. A positive current flows through the circuit above the lines 1 and 4; a negative current does below the lines 2 and 3. Line 5 indicates the position of a small current step due to a residual DOS at the Fermi energy in the S contact. (b) Conditions for the existence of a positive or negative current, as a function of bias eV_{sd}, detuning ϵ_d and superconducting gap Δ. Compared to the previous notations we have taken $\epsilon_N = 0$. The bias potential drops along the circuit with an asymmetry α. These enable us to write the equation for the lines 2-3 ($I < 0$) and 1-4 ($I > 0$).

In a similar fashion, we can use a constant interaction model to obtain the stability diagram equations for a S/QD/N system. Since the density of states of the S contact is similar to the one of a semiconductor, the energy cost for an electron tunneling from the left contact is just increased by Δ [268]. We also add the magnetic field dependence of the dot energy levels $\epsilon_N(B) = \left(\epsilon_{N,0} + s\frac{1}{2}g\mu_B B\right)$ where s is the spin of this N-th level. In the following, we drop the N indice.

The two conditions for having a positive current are:

$$\epsilon > -(1-\alpha)eV_{sd} + \Delta \tag{A.8}$$

$$\epsilon < \alpha eV_{sd} \tag{A.9}$$

We write similar equations for $I < 0$ and we obtain the equations of the lines 1 to 4 in figure A.2:

$$eV_{sd} = \frac{\Delta(B) - \epsilon(B)}{1-\alpha} \text{ at positive bias} \tag{A.10}$$

$$eV_{sd} = -\frac{\Delta(B) + \epsilon(B)}{1-\alpha} \text{ at negative bias,} \tag{A.11}$$

where $\Delta(B) = \Delta\sqrt{1 - \left(\frac{B}{B_c}\right)^2}$.

One can note that since the diamonds shift in energy, the lower gap evolution should be piecewise-defined. However in our experiments the critical field is reached before this is needed.

A.1.3 Comment on the experimental data presented in chapter 4

We now present the specific parameters used to to fit the data presented in figure 4.9 (b) and 4.10 (d) and (e). The fit of the conductance peak energy as a function of an external magnetic field is shown in figure 4.7.

We used different contact asymmetries between positive and negative bias to fit the data, as one can see in the $V_g - V_{sd}$ conductance map that the slope does change. The positive bias asymmetry is noted α_2, the negative bias asymmetry α. The N-th level considered is the one associated with a spin down electron, as can be deduced from the shift of the Coulomb diamonds in field visible in figure 4.9 (b).

In addition to S/QD/N peaks described in the previous section, a residual density of state in the superconducting contact also gives rise to transport peaks similar to the ones of a N/QD/N devices (called quasiparticle peaks).

The quasiparticle peaks positions is thus given by $eV_{sd} = \frac{\epsilon(B)}{\alpha_2}$ and $eV_{sd} = -\frac{\epsilon(B)}{1-\alpha}$.

The fit values are the following:

$$s = -1,\ \Delta = 0.68 \text{ meV},\ B_c = 0.6\text{T},\ \epsilon_0 = -0.02\text{meV},\ \text{g} = 3.8,\ \alpha = 0.31,\ \alpha_2 = 0.47$$

.

Appendix B

Supplementary material on chapter 2

B.1 Scattering formalism with an oscillating magnetic field

In chapter 2, we demonstrated (in equation (2.29)) that the transfer matrix $\tau(L)$ for a 1D conductor of length L with an oscillating magnetic field can be written:

$$\tau(L) = \exp\left(i\kappa L + k_\alpha \frac{A}{4} L\right) \tag{B.1}$$

where $k_\alpha = \frac{\partial\theta}{\partial z}$ is the speed of variation of the magnetization angle, and A and K are 4x4 matrices defined in 2.2.2, dependent on the wave-vectors $k_\uparrow$ and $k_\downarrow$ associated with spin up and down. This transfer matrix can be converted to the scattering matrix $S^M(L)$:

$$S^M(L) = \begin{pmatrix} \tau_{12} \cdot \tau_{22}^{-1} & \tau_{11} - \tau_{12} \cdot \tau_{22}^{-1} \cdot \tau_{21} \\ \tau_{22}^{-1} & -\tau_{22}^{-1} \cdot \tau_{21} \end{pmatrix} \tag{B.2}$$

using a bloc notation for $\tau = \begin{pmatrix} \tau_{11} & \tau_{12} \\ \tau_{21} & \tau_{22} \end{pmatrix}$.

To calculate the transmission of a segment of conductor subject to an oscillating magnetic field, we considered a confined structure as drawn in figure 2.3 (that we will call an N-M-N circuit). For simplicity, we have surrounded the central segment with two potential barriers of same height. The scattering matrix of each potential barrier is then written

as:

$$S_{barrier} = \begin{pmatrix} -\sqrt{1-T} & 0 & -i\sqrt{T} & 0 \\ 0 & -\sqrt{1-T} & 0 & -i\sqrt{T} \\ -i\sqrt{T} & 0 & -\sqrt{1-T} & 0 \\ 0 & -i\sqrt{T} & 0 & -\sqrt{1-T} \end{pmatrix} \tag{B.3}$$

with $T \in [0,1]$ the barrier transmission (in energy).

The transmission of the structure is given by (noting $r = -\sqrt{1-T}$):

$$T_{NMN} = Tr[t_{NMN} \cdot t_{NMN}^{\dagger}] \tag{B.4}$$

with

$$t_{NMN} = -T(\mathbb{1} - r(S_{11}^M + rS_{12}^M \cdot (\mathbb{1} - rS_{22}^M)^{-1} \cdot S_{21}^M)^{-1} \cdot (\mathbb{1} - rS_{22}^M)^{-1} \cdot S_{21}^M \tag{B.5}$$

In chapter 2, certain values are given in reduced units (noted k, b_{osc}, L there; to avoid confusion we note them k_{red}, b_{osc}, L_{red} here) such that:

- $k_{\sigma,red} = \sqrt{E + \mu + \sigma b_{osc}}$
- $k_{red} L_{red} = kL$

which corresponds to $k = \frac{\hbar k}{\sqrt{2m}}$, $L_{red} = \frac{\sqrt{2m}L}{\hbar}$ and $b_{osc} = \frac{1}{2} g \mu_B B_{osc}$ with m the electrons effective mass.

In figure 2.6, we studied a structure surrounded by two polarized regions. The previous transfer matrix has to be sandwiched by the transfer matrices associated with such a region, $T_{pol,L}$ and $T_{pol,R}$, which can be written as:

$$T_{pol,L} = R^{-1}(0,0,\mu_L) R(B_{pol}, \theta_L^0, \mu_L) \cdot T_{prop}(L_L) \cdot R^{-1}(B_{pol}, \theta_L^0, \mu_L) R(B_{osc}, 0, \mu)$$
$$T_{pol,R} = R^{-1}(B_{osc}, \theta(L), \mu) R(B_{pol}, \theta_R^0, \mu_R) \cdot T_{prop}(L_R) \cdot R^{-1}(B_{pol}, \theta_R^0, \mu_R) R(0,0,\mu_R)$$
$$T_{prop}(L) \equiv \begin{pmatrix} e^{ik_\uparrow L} & 0 & 0 & 0 \\ 0 & e^{ik_\downarrow L} & 0 & 0 \\ 0 & 0 & e^{-ik_\uparrow L} & 0 \\ 0 & 0 & 0 & e^{-ik_\downarrow L} \end{pmatrix}$$

where the rotation matrices $R(B, \theta, \mu)$ are the same as the one defined in equation (2.24) where $k_{\uparrow,\downarrow}$ depends on B and μ through equation (2.30). The polarization segments $p = L, R$ have a length L_p, with chemical potential μ_p (equal to the chemical potential

of the reservoirs) and polarization axis θ_p^0. As before, the transfer matrix contains both a propagation and the change of coordinate system. For simplicity, in the calculation we always take $\theta_L^0 = 0$ and $\theta_R^0 = \pi$ (the opposite axes roughly reproduce a stray dipolar field).

B.2 Tight-binding formalism

$$\mathcal{H}_{1D} = \int dz \left[\Psi_\uparrow^\dagger(z)\Psi_\downarrow^\dagger(z)\right] H_{1D} \begin{bmatrix} \Psi_\uparrow(z) \\ \Psi_\downarrow(z) \end{bmatrix}$$

$$H_{1D}(z) = -\frac{\hbar^2}{2m}\frac{\partial^2}{\partial z^2} + E_z s_z - \mu - eV_\perp(z)\left(a + a^\dagger\right) - i\alpha s_y \frac{\partial}{\partial z}$$

with the same convention for the spin-orbit strength α as the one adopted in chapter 2.

We discretize the conductor of length L in N sites, separated by a length l with $\hat{\Psi}(nl) = \hat{d}_n/\sqrt{l}$, $V_\perp^n = V_\perp(nl)$:

$$\mathcal{H}_{1D} = \sum_{n\in[1,N]} \hat{d}_n^\dagger \left(-\overline{\mu} + b_{ext} s_z\right) \hat{d}_n - t\left(\hat{d}_n^\dagger \hat{d}_{n+1} + \hat{d}_n^\dagger \hat{d}_{n-1}\right) - i\hat{d}_n^\dagger \Lambda s_y \left(\hat{d}_{n+1} - \hat{d}_{n-1}\right)$$

with:

$$t = \frac{\hbar^2}{2m}\frac{1}{l^3},\ \Lambda = \frac{1}{2l^2}\alpha,\ b_{ext} = E_z$$
$$\overline{\mu} = \mu - 2t + eV_\perp^n\left(a + a^\dagger\right)$$

We can try and relate the level spacing in the continuous hamiltonian with this discretized version. In the simple case of a chain with no spin-orbit interaction and $E_z = 0$, the tight-binding formalism results in a dispersion relation of

$$E_{E_z,\Lambda=0}(k) = -\bar{\mu} - 2t\cos(kl) \tag{B.6}$$

Around the bottom of the band, we can develop the cosine to obtain a relation dispersion similar to the one of free electrons.

In presence of spin-orbit and Zeeman energy, the bands are non degenerate. The dispersion relation is given by the eigenvalues of H_{1D}, rewritten using the identity $d_n^\dagger = \frac{1}{\sqrt{N}}\sum_k e^{-i\vec{k}\vec{r_n}} c_k^\dagger$:

$$H_{1D} = \sum_{k,s} \begin{pmatrix} -2t\cos(ka) - \bar{\mu} + E_z & -2\Lambda\sin(ka) \\ 2\Lambda\sin(ka) & -2t\cos(ka) - \bar{\mu} - E_z \end{pmatrix} d_{k,s}^\dagger d_{k,s}. \tag{B.7}$$

We get the following dispersion relation:

$$E_s(k) = -\bar{\mu} - 2t\cos(ka) + s\sqrt{E_z^2 + (2\Lambda\sin(ka))^2} \tag{B.8}$$

Again, we can develop this expression at the bottom of the band. We can then deduce the level spacing in a confined chain through the condition $kL = 2\pi n$, $n \in \mathbb{Z}$.

Appendix C

Additional information on the experimental methods

C.1 Hall bar fabrication and measurements

C.1.1 Remarks on the fabrication of the different samples for the magnetic characterization

As was mentioned in chapter 3, the magnetic texture in the transport device is deposited over a rough substrate due to the presence of trenches. This roughness affects the domains formation and their magnetic evolution, as shown by the magnetic simulations.

In order to try and reproduce this roughness, we performed a full-flake etching of the Si chips used for the various characterization samples, with the same etching parameters (with the exception of the SQUID measurements presented in figure 3.14).

C.1.2 Hall bar measurements

Hall bar fabrication

The Hall bar presented in section 3.3.3 were fabricated as follows. The $Si/Si0_2$ is etched for 3min40s (with the $Si0_2$ RIE recipe) to try and reproduce the transport devices' roughness. The metallic structures are defined in two steps. The measurement pads and lines are lithographically defined in Ti(5nm)/Au(45nm), before evaporating the Co/Pt multilayer.

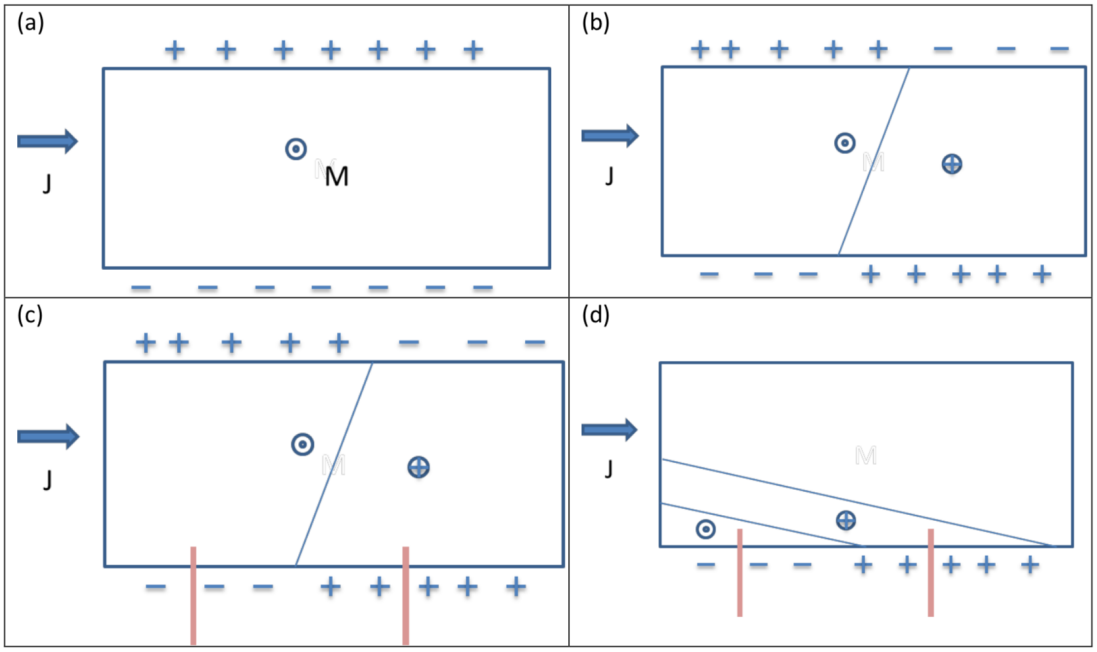

FIGURE C.1: **Effect of domains on the longitudinal resistance** Magnetic texture with different configurations. When a current J is applied, the magnetization M results in the accumulation of charge on both sides of the sample (as marked by the plus and minus signs), which can be measured as a transverse voltage drop. In presence of domains, this charge accumulation is modified. In the two scenario (c) and (d), this voltage drop would be measured simultaneously with the longitudinal resistance through the two pink electrodes. Courtesy of A. Thiaville.

The Hall bar measurement is performed at $T = 4$ K, using two synchronized lock-in at $f = 77.7$ Hz. A voltage of $V = 5$ V is applied on a 10 kΩ resistance in series with the texture. A zero-field Hall resistance of about 53 mΩ is measured, which would correspond to a misalignment of the electrodes of about 50 nm (given the longitudinal resistance). It is subtracted in the Hall bar resistance plots of figure 3.14.

Details on the domain contribution to the Hall signal

Figure C.1 shows how the hall signal can be read in the longitudinal resistance if the sample contains domains larger than the measurements electrodes, in a sample with a few domains.

C.2 Detailed HFSS simulations parameters

We summarize here the important parameters for the HFSS simulations presented in section 3.1.2. In our simulations, the chip is simulated as a 10 mm × 5 mm × 500 µm Si volume topped by 0.5 µm of SiO_2 and then vacuum. All the thin films are represented as

2D metallic planes made out of a perfect conductor. The wire bonds are 3D volumes, also represented as perfect conductors (in the experiments they are made out of aluminum, superconducting at the measurements' temperature). A CNT circuit is positioned in both ground openings of the cavity, in an antinode of the cavity mode.

To simulate accurately the different volumes, we can specify the maximal meshing length on the different circuit elements. This is defines as :

- 5 µm on the central conductor of the cavity,
- 20 µm on the SiO_2 in the ground plane opening, around the CNT circuit,
- 100 µm elsewhere.

To refine the results, we could increase the meshing of the cavity central conductor at the positions of the input/outuput capacitances, where the field amplitude is strong.

All the DC and RF ports are connected to the ground through a dissipative 50 Ω resistance.

The HFSS parameters are:

- Solution type: Eigenmode,
- Modes of frequency $f > 5$ GHz,
- Maximum 10% variation on each adaptative pass and 8 passes maximum,
- Do lambda refinement with maximum 20% variation, with minimum 2 converged passes
- Order of basis functions: mixed order.

C.3 Details on the second pad studied

In table 3.1, a large DC pad is mentioned but not shown. It is visible in figure C.2.

C.4 Cavity resonance without the galvanic pad

We also performed simulations on the influence of the CNT circuit on the cavity resonance in the absence of the a galvanic pad connected on the central conductor of the cavity.

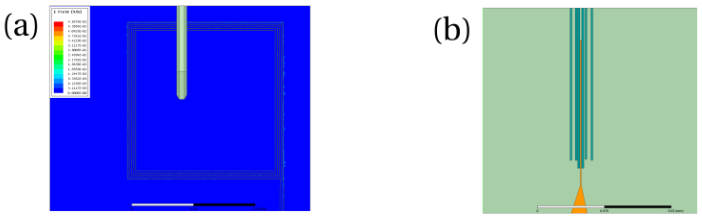

FIGURE C.2: **Additional details on the HFSS simulations** (a) Details of the "large DC pad" geometry. (b) Details of the shorter CNT circuits geometry: the cavity line overlaps with the DC lines over 30 µm.

It tends to show that a shorter circuit degrades less the quality factor of the cavity, and that the width of the element also influence a lot the resonance, as summarized in table C.1. These simulations consider all metals as non-dissipative. The dissipative nature of the metals used in the CNT circuit could strongly affect the resonance, seeing how the field is concentrated in this region. Surprisingly, we find that the presence of one instead of two circuits in the cavity (in either one or both the mode antinode) does not always improve the quality factor. We did not investigate this effect in more details.

Geometry	f_c (GHz)	simulated Q	Measured Q
No DC circuit	6.8	42 000	$\sim$ 50 000
Two DC circuits of 70 µm long	6.5	4900	
One DC circuit of 70 µm long	6.5	5400	
Two DC circuits of 30 µm long	6.5	15500	
One DC circuit of 30 µm long	6.5	11300	

TABLE C.1: Quality factor Q and resonant frequency f_c for some of the additional cavity geometries tested. The geometry for the 30 µm long circuits is shown in figure C.2.

Appendix D

Supplementary material on chapter 5

D.1 Unit conversion for the detuning axis

The detuning is defined as

$$\epsilon_\delta = \mu_1 - \mu_2 \tag{D.1}$$

where μ_i is the electrochemical potential of dot i. The two gate voltages act on each μ_i with different lever arms, defined as:

$$\mu_1 = \alpha_{11} V_{g1} + \alpha_{12} V_{g2} \tag{D.2}$$

$$\mu_2 = \alpha_{21} V_{g1} + \alpha_{22} V_{g2} \tag{D.3}$$

The α_{ii} can be measured from the stability diagram at finite bias (the co-tunelling lines only depend on the alignment of one dot with the leads). They can also be measured from Coulomb diamond measurements[1].

The slope of co-tunneling lines associated with a dot yields the ratio between the two lever arms associated with this dot.

[1] In theory both lever arms can be deduced from the Coulomb diamonds, if we can distinguish the two dots by their different slopes.

D.2 Frequency dependence

We show in figure D.1 the evolution of the cavity resonance when a DQD transition is tuned to resonance with the cavity frequency. The cavity signal is strongly distorted by the DQD transition (around $\epsilon_d = 100$), indicating a high coupling strength.

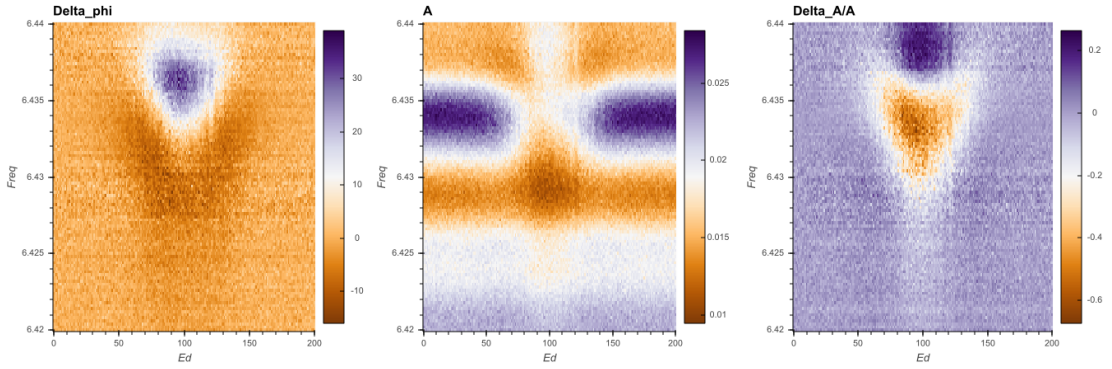

FIGURE D.1: **Effect of the DQD on the cavity signal** (a) Phase variation $\Delta\phi$, (b) amplitude A and (c) amplitude relative variation $\Delta A/A$ as a function of drive tone f_d and detuning ϵ_d.

D.3 Stability diagram represented in figure 5.5

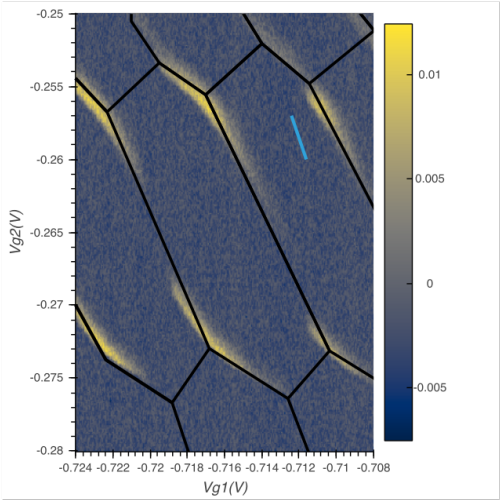

FIGURE D.2: **Effect of the DQD on the cavity signal** Current as a function of V_{gt} and V_{g2} in the same gate region as in figure 5.5. The co-tunnelling current lines enable us to draw the stability diagram, and identify the zero-detuning lines.

Bibliography

[1] J. H. Bruning, SPIE **3051**, 14 (1997).

[2] T. Cubaynes, PhD Thesis , December (2018).

[3] J. J. Viennot, M. C. Dartiailh, A. Cottet, and T. Kontos, Science **349**, 408 (2015).

[4] E. Majorana, in *Nuovo Cimento*, Vol. 5 (Springer Berlin Heidelberg, Berlin, Heidelberg, 1937) p. 171.

[5] G. Moore and N. Read, Nuclear Physics B **360**, 362 (1991).

[6] A. Y. Kitaev, Physics-Uspekhi **44**, 131 (2001).

[7] L. Fu and C. L. Kane, Physical Review Letters **100**, 096407 (2008).

[8] M. Sato, Y. Takahashi, and S. Fujimoto, Physical Review Letters **103**, 020401 (2009).

[9] J. D. Sau, R. M. Lutchyn, S. Tewari, and S. Das Sarma, Physical Review Letters **104**, 040502 (2010).

[10] J. Alicea, Physical Review B **81**, 125318 (2010).

[11] Y. Oreg, G. Refael, and F. von Oppen, Physical Review Letters **105**, 177002 (2010).

[12] R. M. Lutchyn, J. D. Sau, and S. Das Sarma, Physical Review Letters **105**, 077001 (2010).

[13] V. Mourik, K. Zuo, S. M. Frolov, S. R. Plissard, E. P. a. M. Bakkers, and L. P. Kouwenhoven, Science **336**, 1003 (2012).

[14] A. Das, Y. Ronen, Y. Most, Y. Oreg, M. Heiblum, and H. Shtrikman, Nature Physics **8**, 887 (2012).

[15] M. T. Deng, S. Vaitiekėnas, E. B. Hansen, J. Danon, M. Leijnse, K. Flensberg, J. Nygård, P. Krogstrup, and C. M. Marcus, Science **354**, 1557 (2016).

[16] A. Murani, A. Chepelianskii, S. Guéron, and H. Bouchiat, Physical Review B **96**, 165415 (2017).

[17] Z. Su, A. B. Tacla, M. Hocevar, D. Car, S. R. Plissard, E. P. A. M. Bakkers, A. J. Daley, D. Pekker, and S. M. Frolov, Nature Communications **8**, 585 (2017).

[18] L. P. Rokhinson, X. Liu, and J. K. Furdyna, Nature Physics **8**, 795 (2012).

[19] F. Nichele, A. C. C. Drachmann, A. M. Whiticar, E. C. T. O. Farrell, H. J. Suominen, A. Fornieri, T. Wang, G. C. Gardner, C. Thomas, A. T. Hatke, P. Krogstrup, M. J. Manfra, K. Flensberg, and C. M. Marcus, Physical Review Letters **136803**, 136803 (2017).

[20] S. Jeon, S. Nadj-Perge, H. Chen, A. Yazdani, B. A. Bernevig, I. K. Drozdov, J. Seo, J. Li, and A. H. MacDonald, Science **346**, 1259327 (2014).

[21] R. Pawlak, M. Kisiel, J. Klinovaja, T. Meier, S. Kawai, T. Glatzel, D. Loss, and E. Meyer, npj Quantum Information **2**, 16035 (2016).

[22] G. C. Ménard, S. Guissart, C. Brun, R. T. Leriche, M. Trif, F. Debontridder, D. Demaille, D. Roditchev, P. Simon, and T. Cren, Nature Communications **8**, 2040 (2017).

[23] C. Nayak, S. H. Simon, A. Stern, M. Freedman, and S. Das Sarma, Reviews of Modern Physics **80**, 1083 (2008).

[24] D. Aasen, M. Hell, R. V. Mishmash, A. Higginbotham, J. Danon, M. Leijnse, T. S. Jespersen, J. A. Folk, C. M. Marcus, K. Flensberg, and J. Alicea, Physical Review X **6**, 031016 (2016).

[25] C. Beenakker and L. Kouwenhoven, Nature Physics **12**, 618 (2016).

[26] G. E. Volovik, Journal of Experimental and Theoretical Physics Letters **70**, 609 (1999).

[27] T. Senthil and M. P. Fisher, Physical Review B **61**, 9690 (2000).

[28] N. Read and D. Green, Physical Review B **61**, 10267 (2000).

[29] C. Chamon, R. Jackiw, Y. Nishida, S. Y. Pi, and L. Santos, Physical Review B **81**, 224515 (2010).

[30] S. R. Elliott and M. Franz, Reviews of Modern Physics **87**, 137 (2015).

[31] R. Aguado, Rivista del Nuovo Cimento **40**, 523 (2017).

[32] C. W. Beenakker, Reviews of Modern Physics **87**, 1037 (2015).

[33] S. Ryu, A. P. Schnyder, A. Furusaki, and A. W. Ludwig, New Journal of Physics **12**, 065010 (2010).

[34] F. von Oppen, Y. Peng, and F. Pientka, in *Topological Aspects of Condensed Matter Physics* (Oxford University Press, 2017) pp. 387–450.

[35] J. Alicea, Reports on Progress in Physics **75**, 076501 (2012).

[36] C. Beenakker, Annual Review of Condensed Matter Physics **4**, 113 (2013).

[37] M. Leijnse and K. Flensberg, Semiconductor Science and Technology **27**, 124003 (2012).

[38] F. L. Pedrocchi, N. E. Bonesteel, and D. P. DiVincenzo, Physical Review B **92**, 115441 (2015).

[39] D. A. Ivanov, Physical Review Letters **86**, 268 (2001).

[40] J. Alicea, Y. Oreg, G. Refael, F. von Oppen, and M. P. A. Fisher, Nature Physics **7**, 412 (2011).

[41] P. Bonderson, M. Freedman, and C. Nayak, Annals of Physics **324**, 787 (2009).

[42] F. Hassler, A. R. Akhmerov, and C. W. J. Beenakker, New Journal of Physics **13**, 095004 (2011).

[43] L. A. Landau, S. Plugge, E. Sela, A. Altland, S. M. Albrecht, and R. Egger, Physical Review Letters **116**, 050501 (2016).

[44] S. Vijay and L. Fu, Physical Review B **94**, 235446 (2016).

[45] S. Plugge, A. Rasmussen, R. Egger, and K. Flensberg, New Journal of Physics **19**, 012001 (2017).

[46] C. Malciu, L. Mazza, and C. Mora, Physical Review B **98**, 165426 (2018).

[47] S. Das Sarma, J. D. Sau, and T. D. Stanescu, Physical Review B **86**, 220506 (2012).

[48] K. Zuo and V. Mouirk, *Signatures of Majorana fermions inhybrid superconductor-semiconductor nanowire devices* (PhD Thesis, 2016).

[49] S. M. Albrecht, A. P. Higginbotham, M. Madsen, F. Kuemmeth, T. S. Jespersen, J. Nyg, P. Krogstrup, and C. M. Marcus, Nature **531**, 206 (2016).

[50] A. Murani, B. Dassonneville, A. Kasumov, J. Basset, M. Ferrier, R. Deblock, S. Guéron, and H. Bouchiat, Physical Review Letters **122**, 076802 (2019).

[51] B. Jäck, Y. Xie, J. Li, S. Jeon, B. A. Bernevig, and A. Yazdani, Science **1444**, eaax1444 (2019).

[52] H. Zhang, Ö. Gül, S. Conesa-Boj, M. P. Nowak, M. Wimmer, K. Zuo, V. Mourik, F. K. de Vries, J. van Veen, M. W. A. de Moor, J. D. S. Bommer, D. J. van Woerkom, D. Car, S. R. Plissard, E. P. Bakkers, M. Quintero-Pérez, M. C. Cassidy, S. Koelling, S. Goswami, K. Watanabe, T. Taniguchi, and L. P. Kouwenhoven, Nature Communications **8**, 16025 (2017).

[53] M. T. Deng, C. L. Yu, G. Y. Huang, M. Larsson, P. Caroff, and H. Q. Xu, Nano Letters **12**, 6414 (2012).

[54] H. O. H. Churchill, V. Fatemi, K. Grove-Rasmussen, M. T. Deng, P. Caroff, H. Q. Xu, and C. M. Marcus, Physical Review B **87**, 241401 (2013).

[55] J. Chen, P. Yu, J. Stenger, M. Hocevar, D. Car, S. R. Plissard, E. P. Bakkers, T. D. Stanescu, and S. M. Frolov, Science Advances **3**, 1701476 (2017).

[56] Ö. Gül, H. Zhang, J. D. S. Bommer, M. W. A. de Moor, D. Car, S. R. Plissard, E. P. A. M. Bakkers, A. Geresdi, K. Watanabe, T. Taniguchi, and L. P. Kouwenhoven, Nature Nanotechnology **13**, 192 (2018).

[57] S. Gazibegovic, D. Car, H. Zhang, S. C. Balk, J. A. Logan, M. W. A. de Moor, M. C. Cassidy, R. Schmits, D. Xu, G. Wang, P. Krogstrup, R. L. M. Op het Veld, K. Zuo, Y. Vos, J. Shen, D. Bouman, B. Shojaei, D. Pennachio, J. S. Lee, P. J. van Veldhoven, S. Koelling, M. A. Verheijen, L. P. Kouwenhoven, C. J. Palmstrøm, and E. P. A. M. Bakkers, Nature **548**, 434 (2017).

[58] H. Zhang, C.-X. Liu, S. Gazibegovic, D. Xu, J. A. Logan, G. Wang, N. van Loo, J. D. S. Bommer, M. W. A. de Moor, D. Car, R. L. M. Op het Veld, P. J. van Veldhoven, S. Koelling, M. A. Verheijen, M. Pendharkar, D. J. Pennachio, B. Shojaei, J. S. Lee, C. J. Palmstrøm, E. P. A. M. Bakkers, S. D. Sarma, and L. P. Kouwenhoven, Nature **556**, 74 (2018).

[59] P. Lafarge, P. Joyez, D. Esteve, C. Urbina, and M. H. Devoret, Physical Review Letters **70**, 994 (1993).

[60] B. Van Heck, R. M. Lutchyn, and L. I. Glazman, Physical Review B **93**, 235431 (2016).

[61] R. M. Lutchyn and L. I. Glazman, Physical Review Letters **119**, 057002 (2017).

[62] F. Qu, J. van Veen, F. K. de Vries, A. J. A. Beukman, M. Wimmer, W. Yi, A. A. Kiselev, B.-M. Nguyen, M. Sokolich, M. J. Manfra, F. Nichele, C. M. Marcus, and L. P. Kouwenhoven, Nano Letters **16**, 7509 (2016).

[63] F. K. De Vries, J. Shen, R. J. Skolasinski, M. P. Nowak, D. Varjas, L. Wang, M. Wimmer, J. Ridderbos, F. A. Zwanenburg, A. Li, S. Koelling, M. A. Verheijen, E. P. Bakkers, and L. P. Kouwenhoven, Nano Letters **18**, 6483 (2018).

[64] R. M. Lutchyn, G. W. Winkler, B. van Heck, T. Karzig, K. Flensberg, L. I. Glazman, and C. Nayak, Arxiv preprint (2018).

[65] D. J. van Woerkom, A. Proutski, B. van Heck, D. Bouman, J. I. Väyrynen, L. I. Glazman, P. Krogstrup, J. Nygård, L. P. Kouwenhoven, and A. Geresdi, Nature Physics **13**, 876 (2017).

[66] L. Tosi, C. Metzger, M. F. Goffman, C. Urbina, H. Pothier, S. Park, A. L. Yeyati, J. Nygård, and P. Krogstrup, Physical Review X **9**, 011010 (2019).

[67] B. Van Heck, J. I. Väyrynen, and L. I. Glazman, Physical Review B **96**, 075404 (2017).

[68] J. Liu, A. C. Potter, K. T. Law, and P. a. Lee, Physical Review Letters **109**, 267002 (2012).

[69] Z. Cao, H. Zhang, H.-F. Lü, W.-X. He, H.-Z. Lu, and X. C. Xie, Physical Review Letters **122**, 147701 (2019).

[70] D. Rainis, L. Trifunovic, J. Klinovaja, and D. Loss, Physical Review B **87**, 024515 (2013).

[71] F. Domínguez, J. Cayao, P. San-Jose, R. Aguado, A. L. Yeyati, and E. Prada, npj Quantum Materials **2**, 13 (2017).

[72] J. Danon, E. B. Hansen, and K. Flensberg, Physical Review B **96**, 125420 (2017).

[73] F. Pientka, G. Kells, A. Romito, P. W. Brouwer, and F. von Oppen, Physical Review Letters **109**, 227006 (2012).

[74] E. Prada, P. San-Jose, and R. Aguado, Physical Review B **86**, 180503 (2012).

[75] T. D. Stanescu and S. Tewari, Arxiv preprint (2016).

[76] A. Vuik, B. Nijholt, A. R. Akhmerov, and M. Wimmer, Arxiv preprint (2018).

[77] C. Reeg, D. Loss, and J. Klinovaja, Physical Review B **96**, 125426 (2017).

[78] A. E. Antipov, A. Bargerbos, G. W. Winkler, B. Bauer, E. Rossi, and R. M. Lutchyn, Physical Review X **8**, 031041 (2018).

[79] B. D. Woods, T. D. Stanescu, and S. Das Sarma, Physical Review B **98**, 035428 (2018).

[80] A. E. G. Mikkelsen, P. Kotetes, P. Krogstrup, and K. Flensberg, Physical Review X **8**, 031040 (2018).

[81] M. W. De Moor, J. D. Bommer, D. Xu, G. W. Winkler, A. E. Antipov, A. Bargerbos, G. Wang, N. V. Loo, R. L. Op Het Veld, S. Gazibegovic, D. Car, J. A. Logan, M. Pendharkar, J. S. Lee, E. P. M Bakkers, C. J. Palmstrom, R. M. Lutchyn, L. P. Kouwenhoven, and H. Zhang, New Journal of Physics **20**, 103049 (2018).

[82] C. Reeg, D. Loss, and J. Klinovaja, Physical Review B **97**, 165425 (2018).

[83] A. C. Potter and P. A. Lee, Physical Review Letters **105**, 227003 (2010).

[84] A. C. Potter and P. A. Lee, Physical Review B **83**, 094525 (2011).

[85] T. D. Stanescu, R. M. Lutchyn, and S. Das Sarma, Physical Review B **84**, 144522 (2011).

[86] T. D. Stanescu and S. Tewari, Journal of Physics: Condensed Matter **25**, 233201 (2013).

[87] M. J. Biercuk, S. Ilani, C. M. Marcus, and P. L. Mceuen, Carbon Nanotubes, Topics Appl. Physics **111**, 455 (2008).

[88] K. Flensberg, Physical Review B **82**, 180516 (2010).

[89] D. Bagrets and A. Altland, Physical Review Letters **109**, 227005 (2012).

[90] D. I. Pikulin, J. P. Dahlhaus, M. Wimmer, H. Schomerus, and C. W. Beenakker, New Journal of Physics **14**, 0 (2012).

[91] E. M. Stoudenmire, J. Alicea, O. A. Starykh, and M. P. Fisher, Physical Review B **84**, 014503 (2011).

[92] S. Gangadharaiah, B. Braunecker, P. Simon, and D. Loss, Physical Review Letters **107**, 036801 (2011).

[93] B. Béri and N. R. Cooper, Physical Review Letters **109**, 156803 (2012).

[94] B. Béri, Physical Review Letters **110**, 216803 (2013).

[95] M. Papaj, Z. Zhu, and L. Fu, Physical Review B **99**, 014512 (2019).

[96] D. Goldhaber-Gordon, H. Shtrikman, D. Mahalu, D. Abusch-Magder, U. Meirav, and M. a. Kastner, Nature **391**, 156 (1998).

[97] N. Roch, S. Florens, V. Bouchiat, W. Wernsdorfer, and F. Balestro, Nature **453**, 633 (2008).

[98] J.-D. Pillet, C. H. L. Quay, P. Morfin, C. Bena, a. L. Yeyati, and P. Joyez, Nature Physics **6**, 965 (2010).

[99] J.-D. Pillet, P. Joyez, R. Žitko, and M. F. Goffman, Physical Review B **88**, 045101 (2013).

[100] E. J. H. Lee, X. Jiang, M. Houzet, R. Aguado, C. M. Lieber, and S. De Franceschi, Nature nanotechnology **9**, 79 (2014).

[101] E. J. H. Lee, X. Jiang, R. Aguado, G. Katsaros, C. M. Lieber, and S. De Franceschi, Physical Review Letters **109**, 186802 (2012).

[102] M. T. Deng, C. L. Yu, G. Y. Huang, M. Larsson, P. Caroff, and H. Q. Xu, Scientific Reports **4**, 7261 (2015).

[103] S. Li, N. Kang, P. Caroff, and H. Q. Xu, Physical Review B **95**, 014515 (2017).

[104] M.-T. Deng, S. Vaitiekėnas, E. Prada, P. San-Jose, J. Nygård, P. Krogstrup, R. Aguado, and C. M. Marcus, Physical Review B **98**, 085125 (2018).

[105] E. Prada, R. Aguado, and P. San-Jose, Physical Review B **96**, 085418 (2017).

[106] L. S. Ricco, V. L. Campo, I. A. Shelykh, and A. C. Seridonio, Physical Review B **98**, 075142 (2018).

[107] D. Chevallier, P. Szumniak, S. Hoffman, D. Loss, and J. Klinovaja, Physical Review B **97**, 045404 (2018).

[108] C. X. Liu, J. D. Sau, T. D. Stanescu, and S. Das Sarma, Physical Review B **96**, 075161 (2017).

[109] Y. Peng, F. Pientka, E. Berg, Y. Oreg, and F. von Oppen, Physical Review B **94**, 085409 (2016).

[110] P. San-Jose, E. Prada, and R. Aguado, Physical Review Letters **112**, 137001 (2014).

[111] D. Laroche, D. Bouman, D. J. van Woerkom, A. Proutski, C. Murthy, D. I. Pikulin, C. Nayak, R. J. J. van Gulik, J. Nygård, P. Krogstrup, L. P. Kouwenhoven, and A. Geresdi, Nature Communications **10**, 245 (2019).

[112] A. Murani, A. Kasumov, S. Sengupta, Y. A. Kasumov, V. T. Volkov, I. I. Khodos, F. Brisset, R. Delagrange, A. Chepelianskii, R. Deblock, H. Bouchiat, and S. Guéron, Nature Communications **8**, 15941 (2017).

[113] A. Fornieri, A. M. Whiticar, F. Setiawan, E. Portolés, A. C. C. Drachmann, A. Keselman, S. Gronin, C. Thomas, T. Wang, R. Kallaher, G. C. Gardner, E. Berg, M. J. Manfra, A. Stern, C. M. Marcus, and F. Nichele, Nature **569**, 89 (2019).

[114] H. Ren, F. Pientka, S. Hart, A. T. Pierce, M. Kosowsky, L. Lunczer, R. Schlereth, B. Scharf, E. M. Hankiewicz, L. W. Molenkamp, B. I. Halperin, and A. Yacoby, Nature **569**, 93 (2019).

[115] W. Mayer, M. C. Dartiailh, J. Yuan, K. S. Wickramasinghe, A. Matos-Abiague, I. Žutić, and J. Shabani, Arxiv preprint (2019).

[116] J. Li, S. Jeon, Y. Xie, A. Yazdani, and B. A. Bernevig, Physical Review B **97**, 125119 (2018).

[117] M. Ruby, Y. Peng, F. von Oppen, B. W. Heinrich, and K. J. Franke, Physical Review Letters **117**, 186801 (2016).

[118] B. W. Heinrich, J. I. Pascual, and K. J. Franke, Progress in Surface Science **93**, 1 (2018).

[119] S. Nadj-Perge, I. K. Drozdov, B. A. Bernevig, and A. Yazdani, Physical Review B **88**, 020407 (2013).

[120] M. M. Vazifeh and M. Franz, Physical Review Letters **111**, 206802 (2013).

[121] J. Klinovaja, P. Stano, A. Yazdani, and D. Loss, Physical Review Letters **111**, 186805 (2013).

[122] M. Ruby, F. Pientka, Y. Peng, F. von Oppen, B. W. Heinrich, and K. J. Franke, Physical Review Letters **115**, 197204 (2015).

[123] S. Jeon, Y. Xie, J. Li, Z. Wang, B. A. Bernevig, and A. Yazdani, Science **358**, 772 (2017).

[124] M. Ruby, B. W. Heinrich, Y. Peng, F. von Oppen, and K. J. Franke, Nano Letters **17**, 4473 (2017).

[125] G. C. Ménard, C. Brun, R. Leriche, M. Trif, F. Debontridder, D. Demaille, D. Roditchev, P. Simon, and T. Cren, The European Physical Journal Special Topics **227**, 2303 (2019).

[126] D. Chevallier, D. Sticlet, P. Simon, and C. Bena, Physical Review B **85**, 2 (2012).

[127] T. D. Stanescu, R. M. Lutchyn, and S. Das Sarma, Physical Review B **87**, 094518 (2013).

[128] C. Moore, T. D. Stanescu, and S. Tewari, Physical Review B **97**, 165302 (2018).

[129] C. Moore, C. Zeng, T. D. Stanescu, and S. Tewari, Physical Review B **98**, 155314 (2018).

[130] J. D. Sau and S. D. Sarma, Nature Communications **3**, 964 (2012).

[131] I. C. Fulga, A. Haim, A. R. Akhmerov, and Y. Oreg, New Journal of Physics **15**, 045020 (2013).

[132] J. P. T. Stenger, B. D. Woods, S. M. Frolov, and T. D. Stanescu, Physical Review B **98**, 085407 (2018).

[133] P. Bonderson, M. Freedman, and C. Nayak, Physical Review Letters **101**, 010501 (2008).

[134] T. Hyart, B. Van Heck, I. C. Fulga, M. Burrello, A. R. Akhmerov, and C. W. J. Beenakker, Physical Review B **88**, 035121 (2013).

[135] G. C. Paul, A. Saha, and S. Das, Physical Review B **97**, 205446 (2018).

[136] K. N. Nesterov, M. Houzet, and J. S. Meyer, Physical Review B **93**, 174502 (2016).

[137] C. J. Bolech and E. Demler, Physical Review Letters **98**, 237002 (2007).

[138] T. Jonckheere, J. Rech, A. Zazunov, R. Egger, A. L. Yeyati, and T. Martin, Physical Review Letters **122**, 097003 (2019).

[139] S. Smirnov, Physical Review B **99**, 165427 (2019).

[140] M. Trif and Y. Tserkovnyak, Physical Review Letters **109**, 257002 (2012).

[141] A. Cottet, T. Kontos, and B. Douçot, Physical Review B **88**, 195415 (2013).

[142] O. Dmytruk, M. Trif, and P. Simon, Physical Review B **92**, 245432 (2015).

[143] M. C. Dartiailh, T. Kontos, B. Douçot, and A. Cottet, Physical Review Letters **118**, 126803 (2017).

[144] E. Rashba and V. Sheka, Fiz. Tverd. Tela: Collected Papers **2**, 162 (1959).

[145] R. Winkler, *Spin-Orbit Coupling Effects in Two-Dimensional Electron and Hole Systems*, Springer Tracts in Modern Physics, Vol. 191 (Springer Berlin Heidelberg, Berlin, Heidelberg, 2003).

[146] M. C. Hels, B. Braunecker, K. Grove-Rasmussen, and J. Nygård, Physical Review Letters **117**, 276802 (2016).

[147] J. Klinovaja, M. J. Schmidt, B. Braunecker, and D. Loss, Physical Review B **085452**, 085452 (2011).

[148] J. Klinovaja and D. Loss, Physical Review X **3**, 011008 (2013).

[149] P. Stano, C.-H. Hsu, M. Serina, L. C. Camenzind, D. M. Zumbühl, and D. Loss, Physical Review B **98**, 195314 (2018).

[150] E. a. Laird, F. Kuemmeth, G. Steele, K. Grove-Rasmussen, J. N. Rd, K. Flensberg, and L. P. Kouwenhoven, Reviews of Modern Physics **87**, 703 (2015).

[151] T. Ando, Journal of the Physical Society of Japan **69**, 1757 (2000).

[152] W. Izumida, K. Sato, and R. Saito, Journal of the Physical Society of Japan **78**, 074707 (2009).

[153] F. Kuemmeth, S. Ilani, D. C. Ralph, and P. L. McEuen, Nature **452**, 448 (2008).

[154] T. S. Jespersen, K. Grove-Rasmussen, K. Flensberg, J. Paaske, K. Muraki, T. Fujisawa, and J. Nygard, Physical Review Letters **107**, 186802 (2011).

[155] G. a. Steele, F. Pei, E. a. Laird, J. M. Jol, H. B. Meerwaldt, and L. P. Kouwenhoven, Nature communications **4**, 1573 (2013).

[156] A. Manaselyan, A. Ghazaryan, and T. Chakraborty, Solid State Communications **181**, 34 (2014).

[157] J. D. S. Bommer, H. Zhang, Ö. Gül, B. Nijholt, M. Wimmer, F. N. Rybakov, J. Garaud, D. Rodic, E. Babaev, M. Troyer, D. Car, S. R. Plissard, E. P. A. M. Bakkers, K. Watanabe, T. Taniguchi, and L. P. Kouwenhoven, Physical Review Letters **122**, 187702 (2019).

[158] C. H. L. Quay, T. L. Hughes, J. a. Sulpizio, L. N. Pfeiffer, K. W. Baldwin, K. W. West, D. Goldhaber-Gordon, and R. de Picciotto, Nature Physics **6**, 336 (2010).

[159] J. Kammhuber, M. C. Cassidy, F. Pei, M. P. Nowak, A. Vuik, O. Gül, D. Car, S. R. Plissard, E. P. Bakkers, M. Wimmer, and L. P. Kouwenhoven, Nature Communications **8**, 478 (2017).

[160] B. Braunecker, G. I. Japaridze, J. Klinovaja, and D. Loss, Physical Review B **82**, 045127 (2010).

[161] D. Huertas-Hernando, F. Guinea, and A. Brataas, Physical Review B **74**, 155426 (2006).

[162] D. Marchenko, A. Varykhalov, M. R. Scholz, G. Bihlmayer, E. I. Rashba, A. Rybkin, A. M. Shikin, and O. Rader, Nature Communications **3**, 1232 (2012).

[163] C. Kloeffel, M. Trif, and D. Loss, Physical Review B **84**, 195314 (2011).

[164] X.-J. Hao, T. Tu, G. Cao, C. Zhou, H.-O. Li, G.-C. Guo, W. Y. Fung, Z. Ji, G.-P. Guo, and W. Lu, Nano Letters **10**, 2956 (2010).

[165] A. P. Higginbotham, F. Kuemmeth, T. W. Larsen, M. Fitzpatrick, J. Yao, H. Yan, C. M. Lieber, and C. M. Marcus, Physical Review Letters **112**, 216806 (2014).

[166] F. Pientka, L. I. Glazman, and F. Von Oppen, Physical Review B **88**, 155420 (2013).

[167] B. Braunecker, P. Simon, and D. Loss, Physical Review B **80**, 165119 (2009).

[168] C. H. Hsu, P. Stano, J. Klinovaja, and D. Loss, Physical Review B **92**, 235435 (2015).

[169] J. Klinovaja, P. Stano, and D. Loss, Physical Review Letters **109**, 236801 (2012).

[170] M. Kjaergaard, K. Wölms, and K. Flensberg, Physical Review B **85**, 020503 (2012).

[171] R. Egger and K. Flensberg, Physical Review B **85**, 235462 (2012).

[172] A. Matos-Abiague, J. Shabani, A. D. Kent, G. L. Fatin, B. Scharf, and I. Žutić, Solid State Communications **262**, 1 (2017).

[173] S. Turcotte, S. Boutin, J. C. Lemyre, I. Garate, and M. Pioro-Ladrière, Arxiv preprint (2019).

[174] N. Mohanta, T. Zhou, J. Xu, J. E. Han, A. D. Kent, J. Shabani, I. Zutic, and A. Matos-Abiague, Arxiv preprint **1** (2019).

[175] J. D. Sau and S. Tewari, Physical Review B **88**, 054503 (2013).

[176] J. Klinovaja, S. Gangadharaiah, and D. Loss, Physical Review Letters **108**, 196804 (2012).

[177] M. Marganska, L. Milz, W. Izumida, C. Strunk, and M. Grifoni, Physical Review B **97**, 075141 (2018).

[178] T. P. Choy, J. M. Edge, A. R. Akhmerov, and C. W. Beenakker, Physical Review B **84**, 195442 (2011).

[179] M. M. Desjardins, L. C. Contamin, M. R. Delbecq, M. C. Dartiailh, L. E. Bruhat, T. Cubaynes, J. J. Viennot, F. Mallet, S. Rohart, A. Thiaville, A. Cottet, and T. Kontos, Arxiv preprint (2019).

[180] P. Jarillo-Herrero, S. Sapmaz, C. Dekker, L. P. Kouwenhoven, and H. S. Van Der Zant, Nature **429**, 389 (2004).

[181] J. Cao, Q. Wang, and H. Dai, Nature Materials **4**, 745 (2005).

[182] G. A. Steele, G. Gotz, and L. P. Kouwenhoven, Nature Nanotechnology **4**, 363 (2009).

[183] J. Waissman, M. Honig, S. Pecker, A. Benyamini, A. Hamo, and S. Ilani, Nature nanotechnology (2013).

[184] M. Jung, J. Schindele, S. Nau, M. Weiss, A. Baumgartner, and C. Schönenberger, Nano Letters **13**, 4522 (2013).

[185] T. Cubaynes, M. R. Delbecq, M. C. Dartiailh, R. Assouly, M. M. Desjardins, L. C. Contamin, L. E. Bruhat, Z. Leghtas, F. Mallet, A. Cottet, and T. Kontos, Arxiv preprint (2019).

[186] J.-D. Pillet, PhD Thesis (2011).

[187] C. W. J. Beenakker, in *Quantum Dots: a Doorway to Nanoscale Physics. Lecture Notes in Physics*, Vol. 667, edited by H. Springer, Berlin (Dieter Heiss W., 2005).

[188] P. San-Jose, J. Cayao, E. Prada, and R. Aguado, Scientific Reports **6**, 21427 (2016).

[189] D. Sticlet, C. Bena, and P. Simon, Physical Review Letters **108**, 096802 (2012).

[190] D. I. Pikulin and Y. V. Nazarov, JETP Letters **94**, 693 (2012).

[191] J. Cayao, E. Prada, P. San-Jose, and R. Aguado, Physical Review B **91**, 024514 (2015).

[192] J. Cayao, A. M. Black-Schaffer, E. Prada, and R. Aguado, Beilstein Journal of Nanotechnology **9**, 1339 (2018).

[193] A. Cottet, M. C. Dartiailh, M. M. Desjardins, T. Cubaynes, L. C. Contamin, M. Delbecq, J. J. Viennot, L. E. Bruhat, B. Douçot, and T. Kontos, Journal of Physics: Condensed Matter **29**, 433002 (2017).

[194] M. Trif and P. Simon, Physical Review Letters **122**, 236803 (2019).

[195] T. L. Schmidt, A. Nunnenkamp, and C. Bruder, Physical Review Letters **110**, 107006 (2013).

[196] T. L. Schmidt, A. Nunnenkamp, and C. Bruder, New Journal of Physics **15**, 025043 (2013).

[197] L. E. Bruhat, J. J. Viennot, M. C. Dartiailh, M. M. Desjardins, T. Kontos, and A. Cottet, Physical Review X **6**, 021014 (2016).

[198] M. M. Desjardins, J. J. Viennot, M. C. Dartiailh, L. E. Bruhat, M. R. Delbecq, M. Lee, M.-S. Choi, A. Cottet, and T. Kontos, Nature **545**, 71 (2017).

[199] A. Emmert, PhD Thesis , February (2006).

[200] M. Göppl, A. Fragner, M. Baur, R. Bianchetti, S. Filipp, J. M. Fink, P. J. Leek, G. Puebla, L. Steffen, and A. Wallraff, Journal of Applied Physics **104**, 113904 (2008).

[201] M. Dartiailh, PhD Thesis , November (2017).

[202] X. Mi, X. Mi, J. V. Cady, D. M. Zajac, P. W. Deelman, and J. R. Petta, Science **355**, 156 (2017).

[203] L. Milz, W. Izumida, M. Grifoni, and M. Marganska, Arxiv preprint (2018).

[204] M. Marganska, P. Chudzinski, and M. Grifoni, Physical Review B **92**, 075433 (2015).

[205] J. J. Viennot, J. Palomo, and T. Kontos, Applied Physics Letters **104**, 113108 (2014).

[206] M. Desjardins, PhD Thesis , December (2018).

[207] F. Pei, E. A. Laird, G. A. Steele, and L. P. Kouwenhoven, Nature Nanotechnology **7**, 630 (2012).

[208] J. Gramich, A. Baumgartner, M. Muoth, C. Hierold, and C. Schönenberger, physica status solidi (b) **252**, 2496 (2015).

[209] S. Blien, P. Steger, A. Albang, N. Paradiso, and A. K. Hüttel, physica status solidi (b) **255**, 1800118 (2018).

[210] M. S. Dresselhaus, A. Jorio, A. G. Souza Filho, and R. Saito, Philosophical Transactions of the Royal Society A: Mathematical, Physical and Engineering Sciences **368**, 5355 (2010).

[211] D. M. S. Jorio, A., Pimenta M.A., Zouza Filho A.G, Saito R, Dresselhaus G, New Journal of Physics **5**, 139 (2003).

[212] M. Paillet, T. Michel, J. C. Meyer, V. N. Popov, L. Henrard, S. Roth, and J. L. Sauvajol, Physical Review Letters **96**, 257401 (2006).

[213] Z. Yu and L. Brus, The Journal of Physical Chemistry B **105**, 1123 (2001).

[214] M. Y. Sfeir, Science **312**, 554 (2006).

[215] A. Moschel and K. D. Usadel, Physical Review B **51**, 16111 (1995).

[216] S. H. Lee, F. Zhu, C. Chien, and N. Marković, Physical Review B **77**, 132408 (2008).

[217] C. Canedy, X. Li, and G. Xiao, Physical Review B **62**, 508 (2000).

[218] F. E. Spada, F. T. Parker, C. L. Platt, and J. K. Howard, Journal of Applied Physics **94**, 5123 (2003).

[219] M. Yu, H. Ohguchi, A. Zambano, I. Takeuchi, J. P. Liu, D. Josell, and L. A. Bendersky, Materials Science and Engineering B: Solid-State Materials for Advanced Technology **142**, 139 (2007).

[220] M. Carbucicchio, R. Ciprian, and L. Nasi, Journal of Physics D: Applied Physics **43**, 405001 (2010).

[221] Y. Shirahata, E. Wada, M. Itoh, T. Taniyama, Y. Shirahata, E. Wada, M. Itoh, and T. Taniyama, Applied Physics Letters **104**, 032404 (2014).

[222] J. E. Davies, O. Hellwig, E. E. Fullerton, G. Denbeaux, J. B. Kortright, and K. Liu, Physical Review B **70**, 224434 (2004).

[223] D. B. Gopman, C. L. Dennis, P. J. Chen, Y. L. Iunin, P. Finkel, M. Staruch, and R. D. Shull, Scientific Reports **6**, 27774 (2016).

[224] M. Tekielak, M. Dbrowski, M. Kisielewski, A. Maziewski, and V. Zablotskii, Journal of Applied Physics **107**, 083911 (2010).

[225] R. Allenspach, Journal of Magnetism and Magnetic Materials **129**, 160 (1994).

[226] I. Dzialoshinskii, Soviet Physics JEPT **5**, 1259 (1957).

[227] A. Fert, in *Materials Science Forum*, edited by A. C. Hillairet and J. (Trans Tech Publications Ltd, 1990) pp. 439–480.

[228] M. Bode, M. Heide, K. von Bergmann, P. Ferriani, S. Heinze, G. Bihlmayer, A. Kubetzka, O. Pietzsch, S. Blügel, and R. Wiesendanger, Nature **447**, 190 (2007).

[229] A. Thiaville, J. Miltat, and J. Garcia, *Magnetic Force Microscopy: Images of Nanostructures and Contrast Modeling, in Magnetic Microscopy of Nanostructures*, edited by H. Hopster and H. Oepen (Springer, 2005) p. 225.

[230] A. Vansteenkiste, J. Leliaert, M. Dvornik, M. Helsen, F. Garcia-Sanchez, and B. Van Waeyenberge, AIP Advances **4**, 107133 (2014).

[231] P. Beauvillain, C. Chappert, V. Grolier, R. Mégy, S. Ould-Mahfoud, J. P. Renard, and P. Veillet, Journal of Magnetism and Magnetic Materials **121**, 503 (1993).

[232] M. Tekielak, R. Gieniusz, M. Kisielewski, P. Mazalski, A. Maziewski, V. Zablotskii, F. Stobiecki, B. Szymański, and R. Schäfer, Journal of Applied Physics **110**, 043924 (2011).

[233] M. Labrune and A. Thiaville, The European Physical Journal B **23**, 17 (2001).

[234] S. E. Nigg, R. P. Tiwari, S. Walter, and T. L. Schmidt, Physical Review B **91**, 094516 (2015).

[235] L. E. Bruhat, T. Cubaynes, J. J. Viennot, M. C. Dartiailh, M. M. Desjardins, A. Cottet, and T. Kontos, Physical Review B **98**, 155313 (2018).

[236] J. J. Viennot, PhD Thesis , September (2014).

[237] L. Bruhat, PhD Thesis , April (2016).

[238] S. De Franceschi, L. Kouwenhoven, C. Schönenberger, and W. Wernsdorfer, Nature nanotechnology **5**, 703 (2010).

[239] A. Eichler, M. Weiss, S. Oberholzer, C. Schönenberger, A. L. Yeyati, J. C. Cuevas, and A. Martín-Rodero, Physical Review Letters **99**, 126602 (2007).

[240] E. J. Lee, X. Jiang, R. Žitko, R. Aguado, C. M. Lieber, and S. De Franceschi, Physical Review B **95**, 180502 (2017).

[241] J. Schindele, A. Baumgartner, R. Maurand, M. Weiss, and C. Schönenberger, Physical Review B **89**, 045422 (2014).

[242] M. R. Buitelaar, W. Belzig, T. Nussbaumer, B. Babić, C. Bruder, and C. Schönenberger, Physical Review Letters **91**, 57005 (2003).

[243] B. K. Kim, Y. H. Ahn, J. J. Kim, M. S. Choi, M. H. Bae, K. Kang, J. S. Lim, R. López, and N. Kim, Physical Review Letters **110**, 076803 (2013).

[244] P. Jarillo-Herrero, J. a. van Dam, and L. P. Kouwenhoven, Nature **439**, 953 (2006).

[245] J. Rowell, Physical Review Letter **30**, 167 (1973).

[246] Y. Kanai, R. S. Deacon, A. Oiwa, K. Yoshida, K. Shibata, K. Hirakawa, and S. Tarucha, Phys. Rev. B **82**, 54512 (2010).

[247] A. Kumar, M. Gaim, D. Steininger, A. L. Yeyati, A. Martín-Rodero, A. K. Hüttel, and C. Strunk, Physical Review B **89**, 075428 (2014).

[248] Z. Su, A. Zarassi, J.-F. Hsu, P. San-Jose, E. Prada, R. Aguado, E. J. H. Lee, S. Gazibegovic, R. L. M. Op het Veld, D. Car, S. R. Plissard, M. Hocevar, M. Pendharkar, J. S. Lee, J. A. Logan, C. J. Palmstrøm, E. P. A. M. Bakkers, and S. M. Frolov, Physical Review Letters **121**, 127705 (2018).

[249] Y. Ma, T. Cai, X. Han, Y. Hu, H. Zhang, H. Wang, L. Sun, Y. Song, and L. Duan, Physical Review B **99**, 035413 (2019).

[250] A. Das, Y. Ronen, M. Heiblum, D. Mahalu, A. V. Kretinin, and H. Shtrikman, Nature Communications **3**, 1165 (2012).

[251] S. Nadj-Perge, I. K. Drozdov, J. Li, H. Chen, S. Jeon, J. Seo, A. H. MacDonald, B. A. Bernevig, and A. Yazdani, Science **346**, 602 (2014).

[252] T. Yokoyama, M. Eto, and Y. V. Nazarov, Journal of the Physical Society of Japan **82**, 054703 (2013).

[253] F. Keidel, P. Burset, and B. Trauzettel, Physical Review B **97**, 075408 (2018).

[254] Y.-Y. Liu, J. Stehlik, X. Mi, T. R. Hartke, M. J. Gullans, and J. R. Petta, Physical Review Applied **9**, 014030 (2018).

[255] J. I. Väyrynen, G. Rastelli, W. Belzig, and L. I. Glazman, Physical Review B **92**, 134508 (2015).

[256] D. J. van Woerkom, P. Scarlino, J. H. Ungerer, C. Müller, J. V. Koski, A. J. Landig, C. Reichl, W. Wegscheider, T. Ihn, K. Ensslin, and A. Wallraff, Physical Review X **8**, 041018 (2018).

[257] G. L. Fatin, A. Matos-Abiague, B. Scharf, and I. Žutić, Physical Review Letters **117**, 077002 (2016).

[258] R. Hanson, L. P. Kouwenhoven, J. R. Petta, S. Tarucha, and L. M. K. Vandersypen, Reviews of Modern Physics **79**, 1217 (2007).

[259] T. Nakajima, A. Noiri, J. Yoneda, M. R. Delbecq, P. Stano, T. Otsuka, K. Takeda, S. Amaha, G. Allison, K. Kawasaki, A. Ludwig, A. D. Wieck, D. Loss, and S. Tarucha, Nature Nanotechnology **14**, 555 (2019).

[260] S. Nadj-Perge, S. M. Frolov, E. P. A. M. Bakkers, and L. P. Kouwenhoven, Nature **468**, 1084 (2010).

[261] C. Kloeffel, M. Trif, P. Stano, and D. Loss, Physical Review B **88**, 241405 (2013).

[262] M. D. Schroer, M. Jung, K. D. Petersson, and J. R. Petta, Physical Review Letters **109**, 166804 (2012).

[263] X. Mi, M. Benito, S. Putz, D. M. Zajac, J. M. Taylor, G. Burkard, and J. R. Petta, Nature **555**, 599 (2018).

[264] Y. Kubo, F. R. Ong, P. Bertet, D. Vion, V. Jacques, D. Zheng, A. Dréau, J. F. Roch, A. Auffeves, F. Jelezko, J. Wrachtrup, M. F. Barthe, P. Bergonzo, and D. Esteve, Physical Review Letters **105**, 140502 (2010).

[265] A. Stockklauser, P. Scarlino, J. V. Koski, S. Gasparinetti, C. K. Andersen, C. Reichl, W. Wegscheider, T. Ihn, K. Ensslin, and A. Wallraff, Physical Review X **7**, 011030 (2017).

[266] X. Mi, S. Kohler, and J. R. Petta, Physical Review B **98**, 161404 (2018).

[267] T. Fujisawa, T. Hayashi, and S. Sasaki, Reports on Progress in Physics **69**, 759 (2006).

[268] S. Pfaller, A. Donarini, and M. Grifoni, Physical Review B **87**, 155439 (2013).

RÉSUMÉ

Dans cette thèse, nous avons étudié des nanocircuits à base de nanotubes de carbone intégrées dans une cavité micro-onde. Notre dispositif permet de réaliser simultanément des mesures de transport et des mesures micro-ondes, qui donnent des informations complémentaires sur le nanocircuit. Dans les deux expériences réalisées durant cette thèse, un nanotube de carbone est placé au-dessus d'un matériau magnétique qui présente plusieurs domaines d'aimantation. L'axe du champ magnétique de fuite résultant oscille le long du nanotube. Pour les électrons confinés, il est équivalent à un couplage spin-orbite synthétique et à un effet Zeeman.
Cet effet synthétique est mis en évidence de deux manières. Dans une première expérience, nous avons mesuré l'évolution des niveaux d'énergie de la boîte quantique quand le matériau magnétique est progressivement aimanté par un champ extérieur, ce qui détruit le champ oscillant. Dans cette expérience, le nanotube a un très bon contact avec un métal supraconducteur en supplément des effets spin-orbite et Zeeman synthétique, qui sont les pré-requis pour obtenir des quasiparticules de Majorana dans un nanoconducteur 1D. De telles quasiparticules sont activement recherchées pour leur utilisation pour le calcul quantique.
Dans un second temps, nous avons réalisé une double boîte quantique, dans laquelle chaque boîte est constituée d'un segment de nanotube, situé au-dessus du même champ magnétique oscillant que dans la première expérience. Les transitions internes de ce système sont mesurées à l'aide de la cavité micro-onde. Nous avons mis en évidence une très forte dispersion de l'énergie de la transition interne avec un faible champ magnétique extérieur, qui peut être expliqué par un effet Zeeman pour lequel le facteur de Landé, g, a été fortement renormalisé par l'interaction spin-orbite synthétique.

MOTS CLÉS

Electrodynamique quantique, Etats topologiques, Nanotubes de carbone, Cavité microondes, Couplage spin-orbite.

ABSTRACT

In this thesis, we have studied carbon nanotube-based nanocircuits integrated in a microwave cavity architecture. Our device is compatible with the simultaneous measurement of both the current through the nanocircuit and the frequency shift of the cavity. These two signals give complementary information about the device. In the two experiments presented in this thesis, the carbon nanotube was positioned above a magnetic material containing several magnetization domains. The resulting magnetic stray field's axis oscillates along the carbon nanotube length. For the confined electrons, this is equivalent to both a synthetic spin-orbit interaction and a Zeeman effect. This synthetic effect is evidenced in two ways. In a first experiment, we have measured the evolution of the nanotube's energy levels when the magnetic material is progressively magnetized by an external magnetic field, thus destroying the oscillations of the stray field. In this experiment, the carbon nanotube had a very transparent contact to a superconducting metal, in addition to the synthetic spin-orbit interaction and Zeeman effect. These ingredients are a pre-requisite to observe Majorana quasiparticles in a one-dimensional nanoconductor. Those quasiparticles are under intense study for their potential use in quantum computing.
In the second experiment, we have realized a double quantum dot in which each dot similarly lays above an oscillating magnetic field. The internal transitions of this DQD are measured with the microwave cavity signal. We evidenced a strong dispersion of the energy of the double quantum dots' internal transitions with a small external magnetic field. This dispersion can be explained by a Zeeman effect in which the Landé factor, g, has been strongly renormalized by the synthetic spin-orbit interaction.

KEYWORDS

Quantum electrodynamics, Topological states of matter, Carbon nanotubes, Microwave cavity, Spin-orbit coupling.